Werasak Udomkichdecha
Thomas Böllinghaus
Anchalee Manonukul
Jürgen Lexow *Editors*

Materials Challenges and Testing for Manufacturing, Mobility, Biomedical Applications and Climate

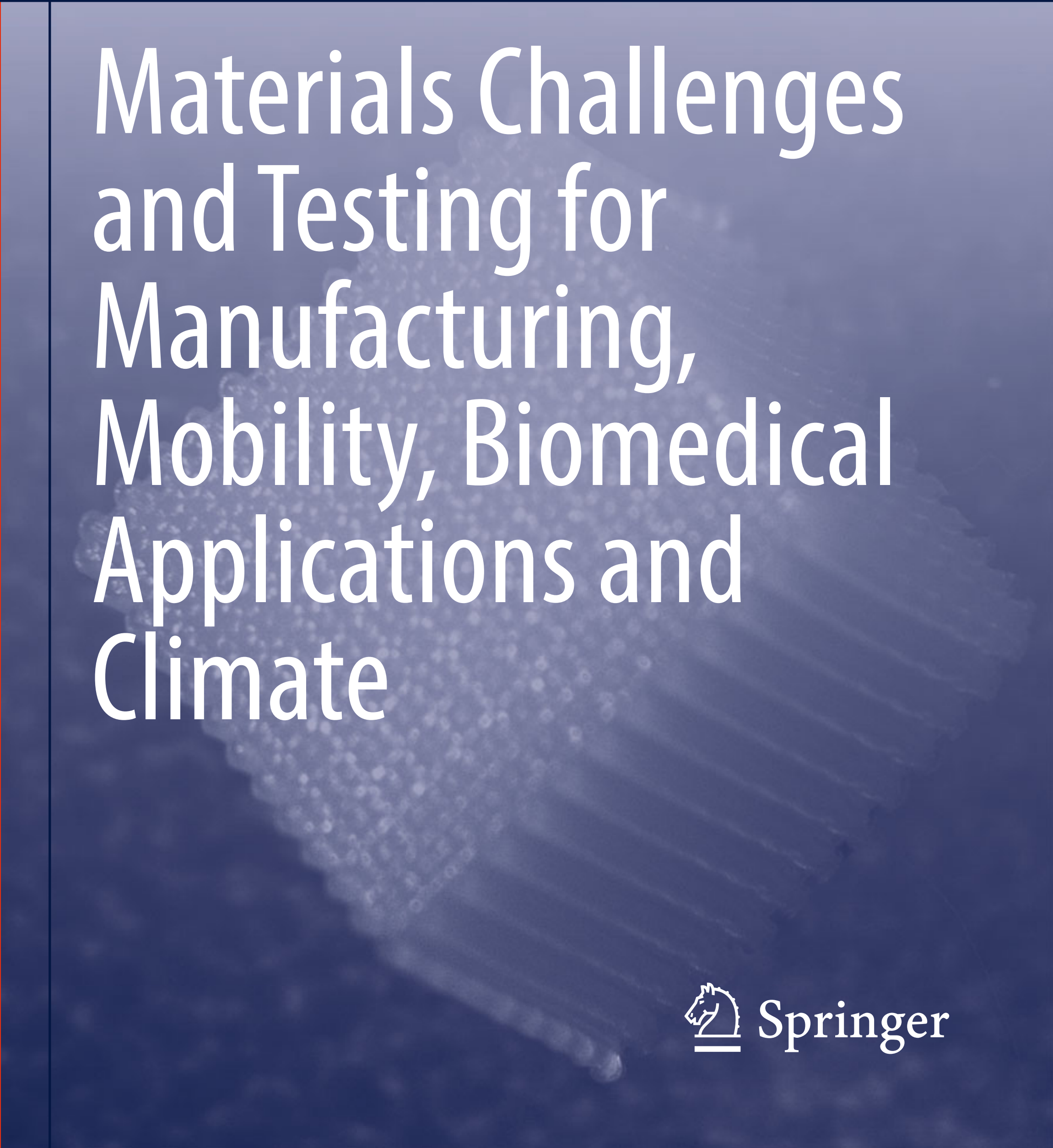

Springer

Materials Challenges and Testing for Manufacturing, Mobility, Biomedical Applications and Climate

Werasak Udomkichdecha
Thomas Böllinghaus · Anchalee Manonukul
Jürgen Lexow
Editors

Materials Challenges and Testing for Manufacturing, Mobility, Biomedical Applications and Climate

Springer

Editors
Werasak Udomkichdecha
Anchalee Manonukul
National Metal and Materials
Technology Center (MTEC)
khlong luang, Pathum Thani
Thailand

Thomas Böllinghaus
Jürgen Lexow
BAM Bundesanstalt für Material- forschung
und -prüfung
Berlin
Germany

ISBN 978-3-319-11339-5 ISBN 978-3-319-11340-1 (eBook)
DOI 10.1007/978-3-319-11340-1

Library of Congress Control Number: 2014948574

Springer Cham Heidelberg New York Dordrecht London

© Springer International Publishing Switzerland 2014
This work is subject to copyright. All rights are reserved by the Publisher, whether the whole or part of the material is concerned, specifically the rights of translation, reprinting, reuse of illustrations, recitation, broadcasting, reproduction on microfilms or in any other physical way, and transmission or information storage and retrieval, electronic adaptation, computer software, or by similar or dissimilar methodology now known or hereafter developed. Exempted from this legal reservation are brief excerpts in connection with reviews or scholarly analysis or material supplied specifically for the purpose of being entered and executed on a computer system, for exclusive use by the purchaser of the work. Duplication of this publication or parts thereof is permitted only under the provisions of the Copyright Law of the Publisher's location, in its current version, and permission for use must always be obtained from Springer. Permissions for use may be obtained through RightsLink at the Copyright Clearance Center. Violations are liable to prosecution under the respective Copyright Law.
The use of general descriptive names, registered names, trademarks, service marks, etc. in this publication does not imply, even in the absence of a specific statement, that such names are exempt from the relevant protective laws and regulations and therefore free for general use.
While the advice and information in this book are believed to be true and accurate at the date of publication, neither the authors nor the editors nor the publisher can accept any legal responsibility for any errors or omissions that may be made. The publisher makes no warranty, express or implied, with respect to the material contained herein.

Printed on acid-free paper

Springer is part of Springer Science+Business Media (www.springer.com)

Preface

The global challenges, as defined by the OECD, provide multiple requirements for all type of materials. One of the major goals of the World Materials Research Institute Forum (WMRIF) is to make young scientists aware of the materials challenges associated with the grand societal needs, like climate change, health, energy, mobility, security. The promotion of the WMRIF global ideas and knowledge exchange among young researchers represents a major accelerator to push future research and development into that direction, but also to provide a common understanding among the following researcher generation about current and future needs in materials science and engineering all over the globe. In the previous WMRIF Young Scientist Workshops already some material requirements to meet global challenges like water supply and scarce elements have been addressed. Following to the workshops in 2008 and 2010 in Tsukuba and Berlin, respectively, the 3rd WMRIF Young Materials Scientist Workshop was organized by MTEC in Thailand. During August 28th to 31st, 2012 29 young scientists from 17 institutes in 12 countries presented their work in Bangkok, Thailand, matching increasingly important subjects under the topics:

- Reliable manufacturing with advanced materials
- Materials challenges for biomedical applications
- Materials challenges in mitigation and adaption to climate change

The workshop not only found a tremendous echo among the young and senior audience from the member institutes, but also among additional scientists and governmental staff from Thailand, representing one of the highly industrialized and productive countries in the eastern hemisphere. In continuation of the previous successes, the best five presenters were awarded a two week stay at a WMRIF institute of their choice.

The present book compiles the peer reviewed and revised papers presented during this 3rd WMRIF Young Materials Scientist Workshop. The reader will find very valuable contributions to the above mentioned topics, representing in most cases cutting edge research.

In the name of all WMRIF member institutes and, in particular, in the name of the Working Group 3 members, the editors convey their sincere gratitude to all authors and to all participants at the workshop for their individual contributions, for their eager discussions and, in particular, for pushing the scientific knowledge in the four subjects further on.

Bangkok, Thailand
Werasak Udomkichdecha,
Executive Director, MTEC, Thailand
Berlin, Germany
Chairman of WMRIF Working Group 3

Berlin, Germany
Thomas Böllinghaus
Vice-president, BAM,

WMRIF President

Contents

Part I Reliable Manufacturing with Advanced Materials

Part II Material Challenges for Mobility Systems

Part III Material Challenges for Biomedical Applications

Part IV Material Challenges in Mitigation and Adaptation to Climate Change

Part I
Reliable Manufacturing with Advanced Materials

Engineering graphene superlattices with crystallographic orientation control using atomic force microscope

Clara M. Almeida[1], Pedro M. Bede[1], Benjamin Fragneaud[1] and Carlos A. Achete[1,2]

[1]Divisão de Metrologia de Materiais, Instituto Nacional de Metrologia, Normalização e Qualidade Industrial (INMETRO), 25250-020, Brasil.

[2]Departamento de Engenharia Metalúrgica e de Materiais, Universidade Federal do Rio de Janeiro, RJ, 21941-972, Brasil.

Abstract

In this work we present a route to engineer bilayer graphene superlattices via direct nanomanipulation of monolayer graphene sheets by the mean of atomic force microscopy. In order to obtain such structures we manipulate the graphene sheet using an AFM tip in contact mode by scanning it parallel to the edge direction. Since the static surface atomic potential created by the twisted bilayer structure depends on the mismatch angle between the top and bottom layers, we carried out lattice resolution images in order to determine the crystallographic orientation of the graphene and of the folded twisted bilayer.

Keywords: *graphene; superlattice; atomic force microscopy; lateral force microscopy, nanomanipulation.*

1. Introduction

With the purpose of designing a controlled periodic structure with specific properties, graphene superlattices have been lately a focus of interest. Two dimensional periodic structures have been observed in CVD grown graphene monolayers, which present a lattice mismatch as compared to the substrate [1,2]. On the other hand, some groups describe periodic defects in the graphene sheet as a possible way to tune the electronic structure of graphene [3,4]. (for a review see [5])

When two graphene sheets are placed on top of each other, the mismatch angle formed between the top and the bottom layers lead to periodic modulations of the electronic potential giving rise to Moiré patterns. A first evidence of such superlattices was observed in graphite by using scanning tunneling microscopy [6]. The electronic properties of these superlattices can be tuned by controlling the mismatch angle between layers. For instance, theoretical works done by M. Killi

W. Udomkichdecha et al. (eds.), *Materials Challenges and Testing for Manufacturing, Mobility, Biomedical Applications and Climate*,
DOI 10.1007/978-3-319-11340-1_1

et al [7] show that depending on the folding angle, some superlattices should undergo a band gap opening whenever others might behave as a metal. Furthermore Suarez Morell et. al. [8] predict by tight-binding calculation that small mismatch angle ($\approx$ 1.5º) graphene superlattices should have flat energy bands close to the Fermi level which might interesting in the field of high transition semi-conductors. The Raman signature of the superlattices formed by graphene bilayers was previously studied by Carozo et.al. It appears that an intervalley and intravalley double-resonance Raman processes respectively called R and R' bands, permits to precisely define the mismatch angle between grapheme layers [9].

Twisted bilayer graphene can be obtained by mechanical exfoliation of graphite and it has also been observed in bilayer graphene grown by CVD [10]. Moreover, spontaneously wrapped single and bilayer graphene was chemically induced by intercalation of species between graphene and the substrate thus interrupting the adhesion force between both materials [11]. In the previously mentioned cases, the synthesis of graphene superlattices occurs randomly and, as consequence, it is impossible to control the final mismatch angle.

The manipulation of objects at the nanoscale is one of the main challenges of the nanotechnology manufacturing and the atomic force microscopy appears as a candidate that fulfills the requirements to successfully manipulate nano-objects. The AFM tip has already been used to tear and to fold monolayers and few layers of carbon sp2-bonded networks at surface steps on highly oriented pyrolytic graphite. The fracture and/or folding were observed to occur along specific directions, depending on the force applied by the tip [12]. Moreover, the atomic force microscope is able to image a surface with lattice resolution by using it in lateral force microscopy mode (LFM). LFM images presenting the atomic-scale features were first obtained in graphite. The images usually reveal the periodicity of the crystal lattice of the graphite basal plane [13-15]. The direct visualization of the lattice symmetries of graphene was reported by Almeida et.al [16], where crystal edges predominantly formed by zigzag or armchair directions were identified.

In this work, we use the capabilities of the atomic force microscope to engineer graphene superlattices via nano-manipulation. To produce such structures we folded the graphene sheet using the AFM tip in contact mode, applying a controlled force and scanning the tip along a given direction. Since, the static potential created by the twisted bilayer structure depends on the mismatch rotation angle between the top and bottom layers, lattice resolution LFM images were performed in order to determine the crystallographic orientation of both graphene and folded twisted bilayer.

2. Experimental procedures

Graphene flakes were micromechanically exfoliated onto an oxidized silicon substrate by using the adhesive tape method [17]. The graphene sheets were identified using an optical microscope and the number of sheets was determined by Raman spectroscopy. The AFM nano-manipulation processes were performed using an AFM NanoWizard from JPK under ambient conditions, using a Si cantilever with normal spring constant of 0.5 N/m. In order to fold the graphene the AFM was operated in contact mode using lithography routines, as it will be described below.

Lattice resolution LFM images were performed in contact mode with a NanoscopeIIIa (Veeco) using a Si3N4 V-shaped cantilever with normal and torsional spring constants of 0.075 ± 0.001 N/m, and 68.5 ± 2.6 N/m respectively . A scanner with 1 μm^2 maximum scan range was used. The microscope gains were set close to zero and the scanning was performed at 40Hz using the constant height mode. The sample was carefully positioned in the microscope stage so that the angle between the crystal and the scanning direction was known.

2. Results

A detailed description of the routine that permit to fold graphene sheets is presented in figure 1(a-d).

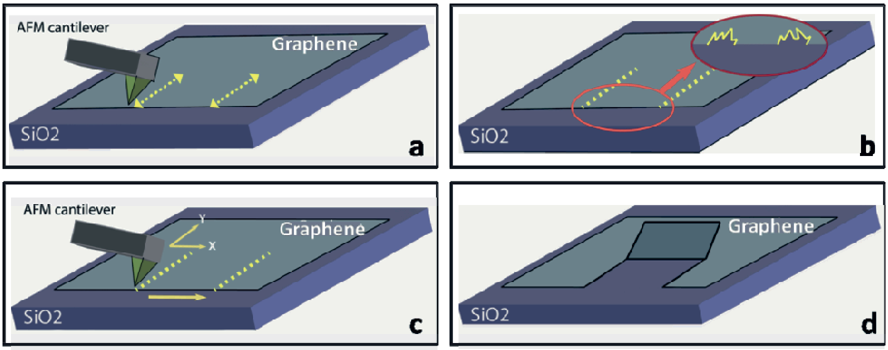

Figure 1. *Sketch of the AFM manipulation process to fold graphene sheets. (a-b) The AFM tip scratches the sheet by using low forces along two specific directions. It permits slightly disrupt the graphene sheet close to the edge, which will guide the future fold. (c-d) After the area to be folded has been 'marked', the AFM tip scans the sheet with the fast scan direction parallel to the sheet edge (x-axis, bottom to top), resulting in folding the graphene sheet at the exact position where the monolayer sheet has been previously scratched.*

Before to start the folding procedure, it was necessary to identify the edges of graphene sheets. The first AFM image was performed in tapping mode in order to avoid any pre-damaging of the material. The AFM was then set to work in contact mode. As shown in figure 1a, the tip was moved continuously along a single line, perpendicularly to the edge of the graphene sheet. This allows to slightly disrupt the edge of the atomic monolayer material (see figure 1b). After that, the scanning direction was rotated at 90º, so the fast scan direction was parallel to the graphene edge. The load applied by the tip was then increased up to 100nN while the tip scanned the sheet at a rate of 1Hz (fig. 1c). As the scanning tip reaches the defected graphene edges, the opposite forces exerted by the forward scanning of tip and the substrate tear the graphene sheet. The lateral forces applied by the tip during scanning folds the graphene sheet along the slow scanning axis direction as presented in figure 1d. Once the scan was completed, the tip was retracted. The operational mode of the AFM was switched back to tapping mode and an image of the folded graphene sheet was obtained.

An AFM image of a folded graphene sheet is shown in figure 2. The dotted lines indicate the fracture lines induced by scanning the AFM tip are described in figure 2a. In this sheet two distinct folds were induced separately. In fig. 2b, the black arrows indicate the folds that were obtained. The slow scan direction during the folding process is parallel to the arrows as indicated in figure 2b. In this sheet, an accidental folding can be observed. This unwanted fold probably occurred during the mechanical exfoliation process of the graphene (fig.2-a).

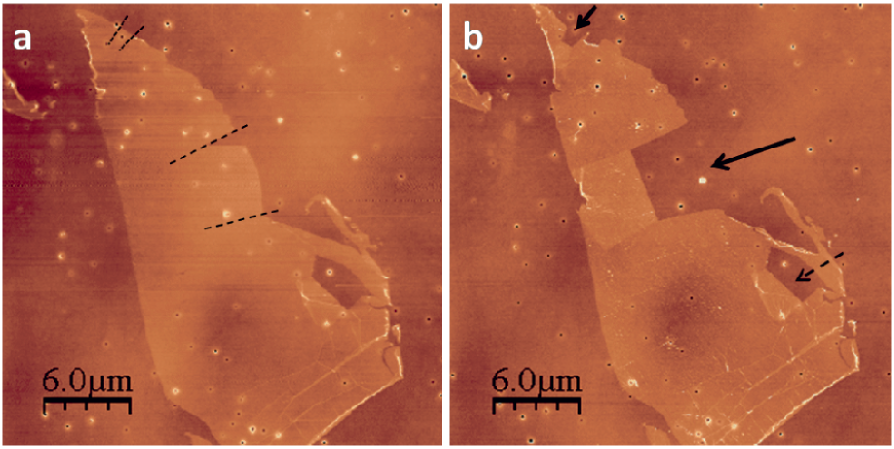

Figure 2. *(a) AFM image acquired in tapping mode of a graphene sheet. The Doted lines highlight the lines where defects were created prior to the folding procedure. (b) Folded graphene imaged by AFM (z range from 0 to 8 nm in both images). The tip scanned direction used to induce the fold was perpendicular to the arrows. The created folds, marked with a black arrow, could be seen in the middle and the top of the image. Another fold, accidentally occurred during the deposition process, can be noted in the top of the sheet (doted arrow).*

Figure 3(a-b) shows the lattice resolution LFM image of a graphene sheet. Raw data presenting the lateral force signal can be seen in fig. 3a. To reduce noise, a low pass filter was applied to the image and the periodic potential of the honeycomb lattice was observed (fig.3b). Black dots are used to highlight the hexagonal symmetry of the graphene. In fig. 3c, a sketch of the graphene crystallographic structure is shown. The same black dots seen in fig. 3b are shown and they represent the centers of the hexagons formed by the carbon atoms. The arrows in fig. 3c present the graphene crystallographic directions known as armchair (ac) and zigzag (zz). The line profile marked in fig. 3b is shown in figure 3d. The profile shows stick-slip movement of the tip while it scans the graphene surface. The intrapeak distance presented in the profile is 0.24 ± 0.02 nm. Several images were acquired at the same crystal area indicating that the friction forces between the AFM tip and the graphene sample do not produce any detectable wear at the crystal surface. No movement of the flake relative to the substrate was observed as well.

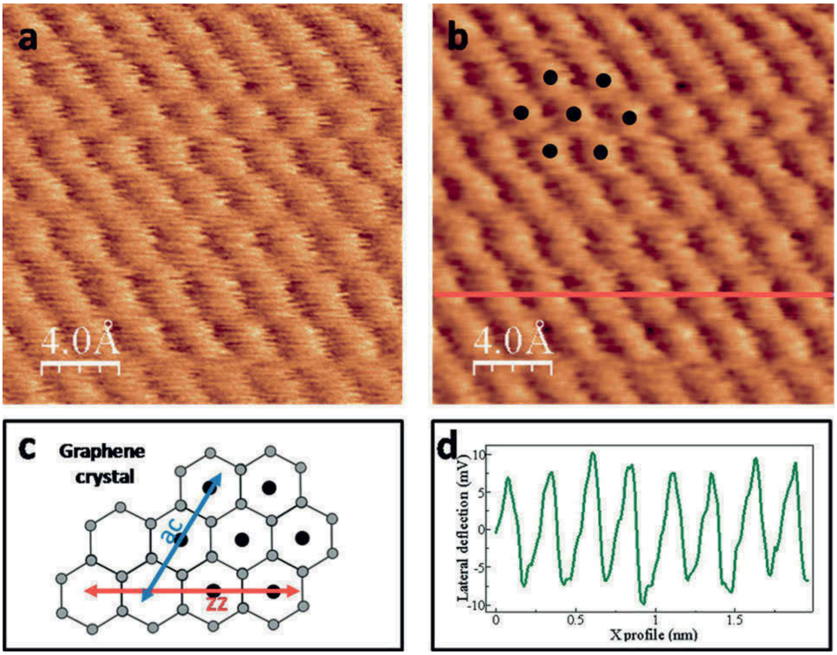

Figure 3. *(a) Raw image showing the lateral force signal when scanning graphene sheet. (b) Low-pass filtered LFM image showing the periodic potential of the lattice. Black dots represent the hexagonal periodicity of graphene as shown in the sketch (c). The zigzag (zz) and armchair (ac) crystallographic directions are indicated in the sketch, (d) is the line profile corresponding to the highlighted red line in (b). The profile presents intrapeak distance of 0.242 ± 0.02 nm.*

If the angle between the graphene sheet and the scanning direction of the tip during the LFM measurements is known, the identification of the crystallographic orientation of the graphene superlattice can be easily obtained. In figure 4, we present a folded sheet that has its crystallographic orientation previously determined by LFM imaging. An AFM image of the graphene sheet with tree folded regions marked with dotted lines is shown in fig. 4a. Lattice resolution LFM image of the graphene can be seen in the inset (I). Once identified the zigzag and armchair crystallographic directions, hexagons were drawn on the image in order to show the crystallographic orientation of the graphene flake determined by AFM. As shown in fig. 4b, by measuring the angle α between the fold line and the zigzag direction, it is possible to determine the mismatch angle between both layers (θ).

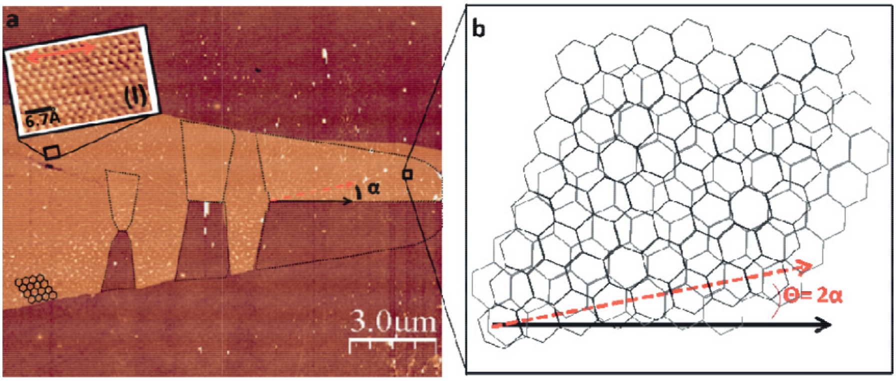

Figure 4. *(a) AFM image of the graphene sheet with tree folded regions marked with doted lines. Z scale ranges from 0 to 10.5 nm. Lattice resolution LFM image of the hexagonal arrangement of the graphene sheet is shown in inset (I). The LFM image allows the identification of the crystallographic orientation of the sheet, (b) By measuring the angle α made by the zz direction and the fold edge, it is possible to find out the mismatch angle between both layers (θ).*

3. Discussion

The experimental procedure described previously allows us to create wrapped bilayer graphene superlattice almost anywhere we want in a given sample. However some details might be discussed. We experimentally noticed that some graphene sheets were extremely hard to fold, which seems to depend on the substrate interaction and/or some uncontrolled experimental parameters, like glue residual form the tape, high shear stress while exfoliating and etc. However, the presence of a thin layer of water on top of the SiO_2 substrate seems to be decisive in the success of the folding. Some samples were dried under primary vacuum (10^{-6} Pa)and none of it could be folded

In the mechanical exfoliation process, normal and lateral forces applied between the graphite flakes and the substrates are responsible for the transfer of graphite flakes to the substrate surface. It has been observed experimentally that during this process, graphene fracture occurs preferentially along specific crystallographic directions [12], once the density of carbon-carbon covalent bonds is different along the zigzag direction as compared to the armchair direction [16]. Interestingly, in fig. 2, one can notice that the fold that accidentally occurs during the exfoliation process makes angles that are multiple of 30°, thus confirming that the fracture propagates preferentially along specific directions, following the six-fold symmetry of the graphene lattice.

As mentioned in the introduction, the mismatch angle between both graphene layers defines the periodicity of the static potential of the superlattice. As a consequence it is crucial in terms of future electronic application of the super-structure. Thus, in order to control the electronic properties of the folded graphene it is necessary to know the crystallographic orientation of the original graphene sheet and then find out the mismatch angle between the top and the bottom layers. As previously described, the crystallographic orientation of the graphene and the superlattice were obtained by the mean of lattice resolution LFM images. Scanning the cantilever perpendicularly to its main axis causes shear forces between the tip and the surface, resulting in the torsion of the cantilever. The torsion signal is highlighted and easily measured in this operational mode called lateral force microscopy. The lattice resolution LFM results from the friction of the very top atoms of the tip with the periodic hexagonal potential of the carbon network. The figure 3 shows that the AFM tip moves in a discontinuous manner on top of the graphene layer following a stick-slip friction pattern. The distances between the centers of consecutive hexagons are theoretically predicted as 0.246 nm and 0.426 nm for the zigzag and the armchair directions respectively. Figure 3(d) shows a profile taken from the image on figure 3b. The stick-slip pattern observed has a periodicity of 0.24 nm. This is close enough to the distance we should expect between the centers of graphene hexagons for a scan along the zigzag direction, and as a consequence we could precisely define the graphene crystallographic orientation

Figure 4 shows a complete set of a graphene folded by the AFM tip and its crystallographic orientation defined by LFM images. It can be observed that most of the edges are preferentially formed by a zigzag or armchair crystal directions which is in agreement with our previous observations. Once the crystallographic orientation was obtained, the mismatch angle between the top and the bottom layers of the fold has to be determined. First we calculate the angle, in here named α, between the fold edge and the zigzag direction (obtained from LFM). It comes out that the mismatch angle (θ) is twice the angle α, as can be observed in figure 5.

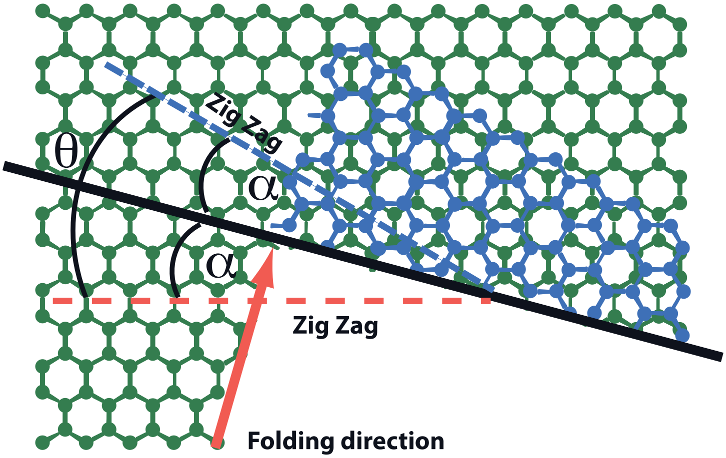

Figure 5. *Sketch of a folded graphene resulting in a twisted bilayer superlattice. The mismatch angle (θ) is the angle between the zigzag directions of the top and the bottom layers. Θ is twice the angle between the zigzag direction and the folded edge.*

When folding an object by mirror symmetry, the rotation angle (θ) between the top and the bottom pattern one might be twice the angle made by the symmetry axis and the folding direction. All our estimations of the superlattice mismatch angle are in good agreement with the one obtained by Raman spectroscopy [9].

4. Conclusion

In summary, a route to fold graphene monolayers with the AFM was presented. Graphene superlattices obtained by twisted bilayer graphene were successfully engineer via nanomanipulation. The mismatch angle has been precisely measured with lattice resolution lateral force microscopy The LFM images revealed the periodicity of the graphene hexagonal structure, allowing an accurate determination of the crystallographic orientation of the monolayer graphene One of the advantage of this process is that the grapheme monolayer did not required any special treatment prior to the synthesis of the superlattice created. The ability to design superlattices with a controlled mismatch angle opens the possibility to study the fundamental characteristics of this material from an electronic, vibrational and electric transport point of view.

References

1. B Borca, S Barja, M Garnica et al (2010) Electronic and geometric corrugation of periodically rippled, self-nanostructured graphene epitaxially grown on Ru(0001). New J Phys 12: 093018

2. M Yankowitz, J Xue, D Cormode et al (2012) Emergence of superlattice Dirac points in graphene on hexagonal boron nitride. Nature Phys 8: 382-386
3. R Martinazzo, S Casolo, G F Tantardini (2010) Symmetry-induced band-gap opening in graphene superlattices. Phys Rev B 81: 245420
4. H Şahin, S Ciraci1 (2011) Structural, mechanical, and electronic properties of defect-patterned graphene nanomeshes from first principles. Phys. Rev. B 84: 035452
5. F Guinea, T Low (2010) Band structure and gaps of triangular graphene superlattices. Phil Trans R Soc A 368: 5391-5402
6. D Tománek, S G Louie, H J Mamin, D W Abraham, R EThomson, E Ganz, J Clarke (1987) Theory and observation of highly asymmetric atomic structure in scanning-tunneling-microscopy images of graphite. Phys Rev B 35: 7790
7. M Killi,S Wu, A Paramekanti (2011) Band structures of bilayer graphene superlattices. Phys Rev Lett 107: 086801
8. E SuárezMorell, J D Correa, P Vargas, M Pacheco, Z Barticevic (2010) Flat bands in slightly twisted bilayer graphene: Tight-binding calculations. Phys Rev B 82:121407
9. V Carozo, C M Almeida, E H M Ferreira, L G Cancado, C A Achete, A Jorio (2011) Raman signature of graphene superlattices. Nano Lett 11 (11): 4527
10. R W Havener, H Zhuang, L Brown, R Hennig, J Park (2012)_Angle-Resolved Raman Imaging of Interlayer Rotations and Interactions in Twisted Bilayer Graphene. Nano Lett 12 (6): 3162–3167
11. M J Allen, M Wang, S A Jannuzzi, Y Yang, KL Wang, RB Kaner (2009) Chemically induced folding of single and bilayer graphene. Chem Commun 41:6285
12. L X Li, R P Liu, Z W Chen, Q Wang et al (2006) Tearing, folding and deformation of a carbon-carbon sp^2-bonded network. Carbon 44: 1544
13. C M Mate, G M McClelland, R Erlandsson, S Chiang (1987) Atomic-scale friction of a tungsten tip on a graphite surface. Phys Rev Lett 59: 1942
14. D R Baselt, J D Baldeschwieler (1992) Lateral Forces During Atomic Force Microscopy of Graphite in Air. J Vac Sci Technol B 10: 2316
15. W-C Lai, S-C Chin, Y-C Chang, L-Y Chen, C-S Chang (2010) Lattice-resolved frictional pattern probed by tailored carbon nanotubes. Nanotech 21: 055702
16. C M Almeida, V Carozo, R Prioli, C A Achete (2011) Identification of graphene crystallographic orientation by atomic force microscopy. J Appl Phys 110: 086101
17. K S Novoselov, A K Geim, S V Morozov, D Jiang, Y Zhang, S V Dubonos, I V Grigorieva, A A Firsov (2004) Electric Field Effect in Atomically Thin Carbon Films. Science 306: 666-669

Additive Micro-Manufacturing of Designer Materials

**Eric Duoss[1,*], Cheng Zhu[1], Kyle Sullivan[1], John Vericella[1],
Jonathan Hopkins[1], Rayne Zheng[1], Andrew Pascall[1], Todd Weisgraber[1],
Joshua Deotte[1], James Frank[1], Howon Lee[3], David Kolesky[2], Jennifer Lewis[2],
Daniel Tortorelli[2], David Saintillan[2], Nicholas Fang[3], Joshua Kuntz[1],
and Christopher Spadaccini[1,*]**

[1] *Lawrence Livermore National Laboratory, Livermore, CA, 94551, USA*
[2] *University of Illinois at Urbana-Champaign, Urbana, IL, 61801, USA*
[3] *Massachusetts Institute of Technology, Cambridge, MA, 02139, USA*

Abstract

Material properties are governed by the chemical composition and spatial arrangement of constituent elements at multiple length scales. This fundamentally limits material properties with respect to each other creating trade-offs when selecting materials for a specific application. For example, strength and density are inherently linked so that, in general, the more dense the material, the stronger it is in bulk form. Other coupled material properties include thermal expansion and thermal conductivity, hardness and fracture toughness, strength and thermal expansion, etc. We are combining advanced microstructural design, using flexure and screw theory as well as topology optimization, with new additive micro- and nano-manufacturing techniques to create new material systems with previously unachievable property combinations. Our manufacturing techniques include Projection Microstereolithography (PμSL), Direct Ink Writing (DIW), and Electrophoretic Deposition (EPD). These processes are capable of reliably producing designed architectures that are highly three-dimensional, multi-scale, and often composed of multiple constituent materials.

Keywords: *Additive manufacturing; designer materials; advanced materials.*

1. Introduction

Design of any new hardware component, regardless of the application, is constrained by both the available material set and the geometry that can be fabricated using existing manufacturing processes. Both of these limitations could be overcome through bottom-up fabrication processes if they were capable of achieving

W. Udomkichdecha et al. (eds.), *Materials Challenges and Testing for Manufacturing, Mobility, Biomedical Applications and Climate*,
DOI 10.1007/978-3-319-11340-1_2

arbitrary three-dimensional mesoscale structures with microscale architectures and sub-micron precision. These processes would have a broad impact on manufacturing if they were also compatible with a wide range of materials (e.g., metals, ceramics, and polymers), allowed for rapid translation from computer model to fabricated component, and were scalable to large numbers of components or bulk material billets. This paper describes the creation of designer materials on demand with three bottom-up micro-manufacturing processes that can meet these metrics.

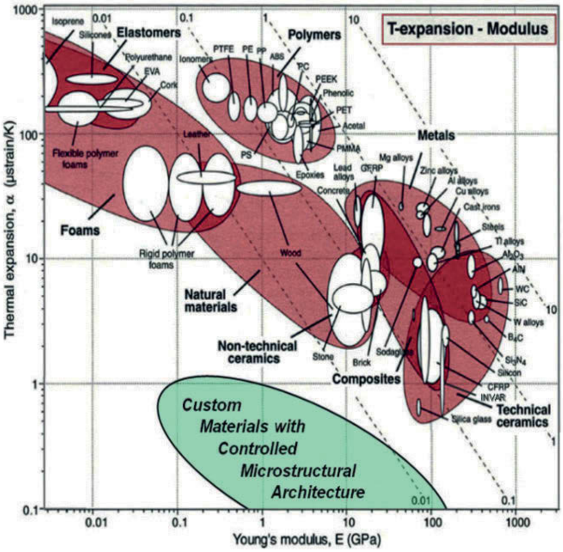

Figure 1. *Ashby chart of thermal expansion coefficient versus Young's Modulus with possible "designer materials" space indicated in green[1].*

Material properties are governed by the chemical composition and spatial arrangement of constituent elements at multiple length scales. This fundamentally limits material properties with respect to each other creating trade-offs when selecting materials for a specific application. For example, strength and density are inherently linked so that, in general, the more dense the material, the stronger it is in bulk form. Other coupled material properties include thermal expansion and thermal conductivity, hardness and fracture toughness, strength and thermal expansion, etc. This coupling can be visualized in the material selection charts such as that shown in Figure 1 for thermal expansion versus Young's modulus [1]. Such plots are also known as "Ashby" charts, being named for their originator, Prof. M.F. Ashby. The coupling between these properties creates significant unpopulated, yet potentially desirable design spaces that cannot be attained using standard manufacturing methods such as mixing and alloying.

However, structural and functional properties of materials may be decoupled via control of the micro- and nanostructure. Recently, Launey et al. demonstrated that a microscale brick and mortar structure composed of Al_2O_3 (brick) and Al–Si (mortar) exceeded the fracture toughness predicted using the rule-of-mixtures by a factor of four while reducing the weight versus pure Al_2O_3 by 25% [2]. Their fabrication process, however, is only compatible with a narrow range of materials and provides limited control over the final structure.

Similarly, there is a significant amount of theoretical work in the literature that predicts arrays of microscale bi-material lattices could dramatically reduce thermal expansion and/or density while maintaining material strength [3-6]. In principle, this type of design could provide materials with the strength of steel and the density of polymers or also zero thermal expansion with controlled stiffness. To date, no manufacturing process has demonstrated the necessary 3D microscale control and material flexibility required to fabricate these designer materials, but emerging additive manufacturing techniques may soon be able to meet these needs.

We aim to fundamentally understand and develop new additive micro-manufacturing techniques that enable designer materials on demand. To achieve these goals, the processes must: (1) be compatible with multiple materials (polymers, metals, ceramics, etc.), (2) be capable of creating heterogeneous or multi-material structures, (3) produce complex 3D mesoscale geometries with micron scale precision, and (4) be scalable to eventually achieve high manufacturing volumes at low cost. There are no current fabrication technologies which adequately address all of these needs. Therefore, we are developing three new additive micro-manufacturing processes because they have the potential to meet these needs. These techniques are: Projection Microstereolithography (PμSL), Electrophoretic Deposition (EPD), and Direct Ink Writing (DIW).

2. Results and Discussion

2.1 Designer Materials on Demand

"Designer materials on demand" refers to the ability to design and fabricate a "new" material with specified properties, either structural or functional, that exceed those attainable with bulk materials processed via traditional synthetic or manufacturing methods such as mixing and alloying. Control of these properties can be obtained by advanced design of the structural architecture at the micron scale. This capability will dramatically expand the design space for many applications ranging from aircraft to microelectronics. We are designing and manufacturing new micro-architectures based on desired structural or functional properties for particular applications. These designs have been both analytically and computationally derived. In addition, our efforts are guided by the open literature where many microstructures have been theorized, but few have been fabricated due to the relative lack of suitable manufacturing techniques. For example, materials with ultra-low or negative thermal expansion and controlled stiffness have been reported [3-6]. Typical theoretical structures which exhibit this combination of properties are bi-material lattices with void space. By carefully designing a structure with both high and low expansion materials, growth or shrinkage due to temperature changes can be accommodated locally by the void space or by small amounts of bending or twisting of a structural member.

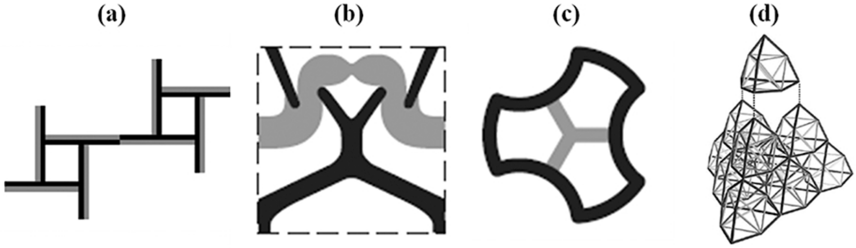

Figure 2. *Unit cells of bi-material lattice structures for low or neutral thermal expansion. Light gray indicates high thermal expansion material and black indicates low thermal expansion. These geometries have been proposed by (a) Lakes [4], (b) Sigmund and Torquato [5], and (c) Jefferson [3]. The structure in (d) is a low thermal expansion 3D lattice proposed by Steeves et al. [6].*

Unit cells of some of the designs for which thermal and mechanical properties have been derived in the literature are shown in Figure 2. Although these geometries have theoretically excellent properties, they have yet to be fabricated as the building blocks of a bulk material due to the absence of a fabrication technology with the suitable materials flexibility, three-dimensionality, and range of length scales. The high-throughput, multi-material, 3D micro- and nano-manufacturing tools being reported here are well-suited to achieving these structures. Ultimately, this combined design and manufacturing approach will result in the ability to generate volumetric lattices and truss-like structures at the microscale which exhibit these previously unobtainable property combinations.

2.2 Projection Microstereolithography (PμSL)

Projection Microstereolithography (PμSL) is a low cost, high throughput, microscale, stereolithography technique which uses a spatial light modulator, typically a digital micromirror device (DMD) or a liquid crystal on silicon (LCoS) chip as a dynamically reconfigurable digital, photomask [7-9].

PμSL is capable of fabricating complex three-dimensional microstructures in a bottom-up, layer-by-layer fashion. In this process, a computer aided design CAD) model is first sliced into a series of closely spaced horizontal planes. These two-dimensional slices are digitized as an image and transmitted to the spatial light modulator which projects the image through a reduction lens on the surface of a photosensitive polymer resin bath. The exposed liquid resin material then rapidly cures and solidifies. Next, the substrate on which the part rests is lowered to repeat the process with the next image slice.

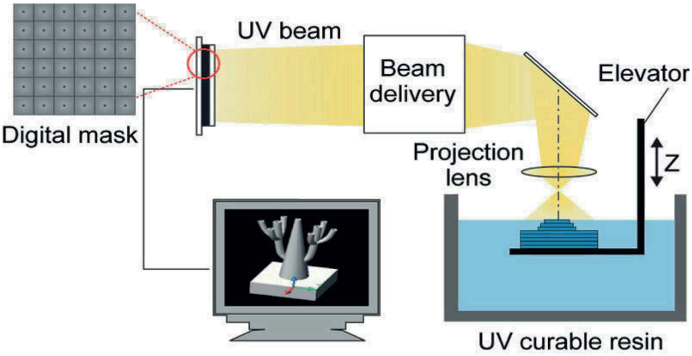

Figure 3. *Process schematic of PμSL.*

Figure 3 shows a schematic illustration of this process. The process is currently capable of rapidly generating complex 3D geometries such as those shown in Figure 4. These structures were fabricated in minutes out of hexanediol diacrylate (HDDA) and have features spanning size-scales from 10-500 μm [8].

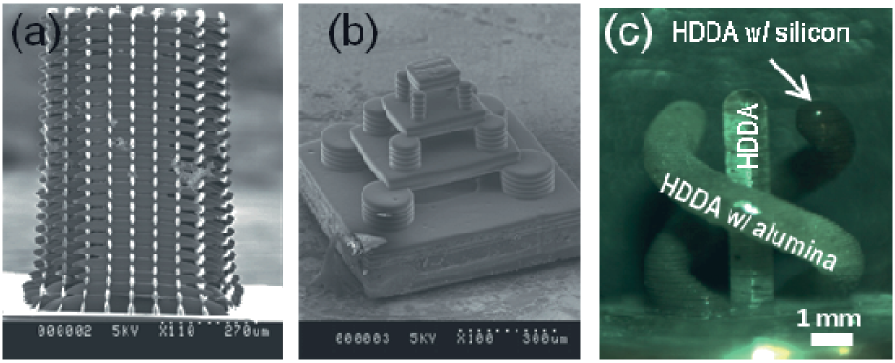

Figure 4. *SEM images of (a) lattice structures, (b) 3D components with void spaces, and (c) heterogeneous materials. For (c), the light curved helix is formed with Al_2O_3 nanoparticles in HDDA, the straight center post is pure polymer (HDDA), and the dark curved helix is silicon powder dispersed in HDDA [10].*

Currently, we are able to fabricate structures with micro or nanoparticles suspended in the photosensitive polymer resulting in a hybrid material with loadings of ~50 wt% of the nanoparticle material. An example of this is shown in Figure 4(c). A subsequent burn-out and sintering process can remove the organic polymer and densify the remaining inorganic material. It is also possible to fabricate a bi-material hybrid component with void space similar to those that may be required for a designer structural material by incorporating microfluidic material delivery systems.

The quality of a component fabricated by PμSL depends on the light uniformity at the image or polymerization plane and both the lateral and depth resolution of the system. The light uniformity is influenced by the performance and alignment of the various optical components, especially the LED array, and optimization of the projected image is achieved through careful selection and installation of these components. The fabricated resolution is limited both by the optical resolution and the physical-chemical characteristics of the exposed monomer solution. In order to optimize the fabrication procedure we have developed a process model that incorporates the chemical kinetics of photopolymerization, fluid dynamics, and optical effects. At the core of the process model is a set of differential equations that describe the evolution of the reaction in the resin during its transition from liquid resin to solid polymer. These equations include the effects of light attenuation as well as the kinetics of the various stages of polymerization coupled with heat and mass transport. In addition to improving our understanding of the underlying physics, this model also provides a means to optimize the fabrication parameters to obtain a desired resolution. For example, since the polymerization is driven by light intensity but limited by diffusion, there is a trade-off between fabrication speed and feature resolution.

2.3 Electrophoretic Deposition (EPD)

Electrophoretic deposition (EPD) is a bottom-up fabrication process that utilizes electric fields to deposit charged nanoparticles from a solution onto a substrate [11]. EPD can be used with a wide range of nanoparticles including oxides[12], metals [13], polymers [14], and semiconductors [15]. Once the particles are deposited, the green body can be post-processed (e.g., sintered, hot isostatic pressed, etc) to produce the final part. One-dimensional (1D) density and composition gradients in coatings have also been demonstrated by exchanging the nanoparticle suspension during the deposition process [16-19]. Hayward et al. demonstrated that EPD could be used to pattern particles in the plane parallel to the deposition surface, which is an important step in eventually patterning complex 3D geometries [16]. To date, this type of 2D patterning has been limited to fixed patterns and generally films only a monolayer thick.

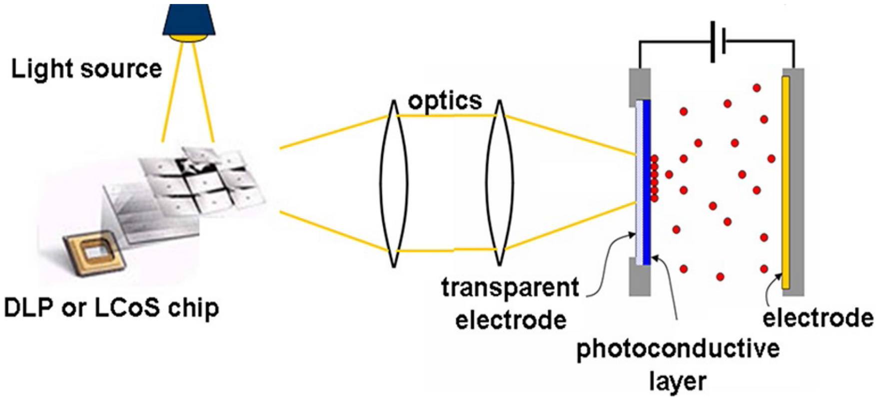

Figure 5. *Illustration of the dynamic electrode system using a spatial light modulator.*

We can precisely pattern different geometries and additively build structures on the deposition plane by modifying the electrode pattern because EPD occurs only where the field is applied. To enable this capability, we use dynamic, optically defined electrodes. The dynamic electrodes utilize a transparent photoconductive layer (such as α-H:Si) that can be illuminated in specific regions using either an optical mask or a dynamic optical pattern from a spatial light modulator as shown in Figure 5. By changing the optical mask during the deposition process, we can adjust the 2D pattern on the deposition plane to build complex 3D structures.

In order to accurately fabricate new designs, we must be able to predict the necessary process parameters to achieve the desired deposition thicknesses, feature widths, and resulting particle packing structure based on the particle material(s). To do this, we have developed a Stokesian dynamics simulation that captures the physics relevant to this process including: electrophoresis, dielectrophoresis, hydrodynamic interactions and Brownian motion of the particles during the deposition process as well as the particle-particle and particle-wall interactions (e.g., van der Waals and electrostatic interactions) that determine the resulting packing structure. Figure 6 shows simulation results of the first few layers of polystyrene particles as they deposit onto a uniform electrode surface. Additional functionality is required in this model to accurately predict 3D patterning as the electric fields generated by the electrode patterns at the surface will quickly diverge away from the surface (this is a work in progress). Using finite element modeling to capture these features in the field, we can predict the appropriate electrode spacing away from the deposition surface to maintain the desired 2D pattern at the surface.

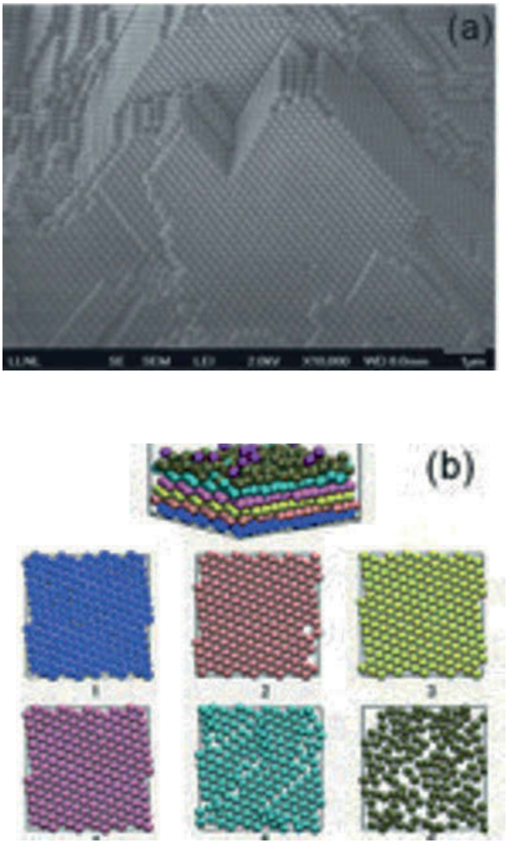

Figure 6. *Comparison of the experimentally observed (a) and predicted (b) structure for polystyrene particles deposited from an ethanol solution in an electric field of approximately 20 V/cm. The numbered images in (b) represent different layers of the deposition at a given time and correspond to the colored layers in the isometric view above.*

2.4 Direct Ink Writing (DIW)

Direct ink writing (DIW) is a layer-by-layer printing approach in which concentrated inks are deposited in planar and 3D layouts with lateral dimensions (minimum ~200 nm) that are at least an order of magnitude lower than those achieved by conventional printing methods. Paramount to this approach is the creation of concentrated inks that can be extruded through fine deposition nozzles as filament(s) which then undergo rapid solidification to maintain their shape even as they span gaps across unsupported regions (see Figure 7(a) for a schematic illustration). Direct-write techniques offer an attractive alternative to conventional manufacturing technologies due to the low-cost of the printing equipment, ease of manufacture, and flexibility in material systems, dimensions, and designs.

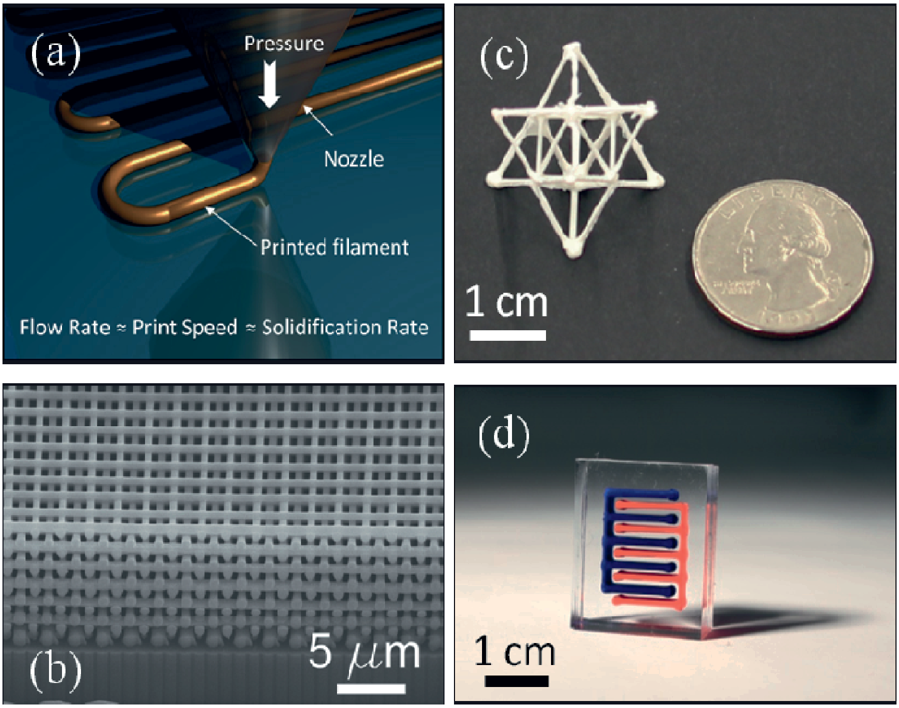

Figure 7. *(a) Schematic illustration of DIW process, (b) woodpile structure printed with a titania-based sol-gel ink [20], (c) octet-truss structure printed with an alumina-based ink with a wax support material (wax has been removed), (d) multi-material silicone structure (e.g., red and blue materials) printed with two nozzles and infilled with a third silicone material.*

The real strength of the DIW approach is the materials flexibility due to functional ink design. To date, DIW has been demonstrated with a wide variety of functional inks, including colloidal gels [21, 22], organic waxes [23], concentrated polyelectrolyte complexes [24], silk [25], sol-gel materials [20], and metallic nanoparticles [26]. In general, DIW inks are designed to exhibit shear thinning behavior so they will easily flow through micro-nozzles, but rapidly gel and solidify upon exiting the nozzles. Typically, 3D structures are assembled in a layer-by-layer build sequence with this filamentary printing technique to create scaffolds that resemble a log-pile structure (Figure 7(b)). In another approach, one may also print support materials (e.g., similar to fused deposition modeling processes) that can be subsequently removed to obtain an arbitrarily complex 3D structure (Figure 7(c)). In addition, DIW is used to pattern heterogeneous structures with the use of multiple nozzles loaded with different inks, akin to an inkjet print-head, to microfabricate composite structures from different materials (Figure 7(d)). Presently, we are developing a process model to capture the relevant physics for improved patterning capability. To achieve this, we are creating computational fluid dynamics models that capture ink rheology and flow behavior during printing as well as shape retention and uniformity after deposition.

3. Conclusions

We are developing three new additive micro-manufacturing techniques that will enable production of designer materials on demand. These techniques, Projection Microstereolithography, Electrophoretic Deposition, and Direct Ink Writing, are capable of patterning multiple materials (polymers, metals, ceramics, etc.) within a single structure to produce complex 3D mesoscale geometries with micron scale precision. These processes were selected, in part, due to their eventual scalability to high manufacturing volumes at low-cost.

Acknowledgments

This work was performed under the auspices of the U.S. Department of Energy by Lawrence Livermore National Laboratory under Contract DE-AC52-07NA27344. IM release number LLNL-CONF-567932. This work was supported by LLNL LDRD 11-SI-005 and the DARPA DSO MCMA program. *Primary author contact information: Dr. Eric Duoss, duoss1@llnl.gov. Principal investigator contact information: Dr. Christopher Spadaccini, spadaccini2@llnl.gov.

References

1. Ashby MF (2005) Materials Selection in Mechanical Design. Butterworth-Heinemann, Burlington
2. Launey ME, Munch E, Alsem DH et al (2010) A novel biomimetic approach to the design of high-performance ceramic-metal composites. J R Soc Interface 7: 741-753
3. Jefferson G, Parthasarathy TA, Kerans RJ (2009) Tailorable thermal expansion hybrid structures. International Journal of Solids and Structures 46: 2372-2387
4. Lakes R (1996) Cellular solid structures with unbounded thermal expansion. Journal of Materials Science Letters 15: 475-477
5. Sigmund O, Torquato S (1996) Composites with extremal thermal expansion coefficients. Applied Physics Letters 69: 3203

6. Steeves CA, Lucato SLdSe, He M et al (2007) Concepts for structurally robust materials that combine low thermal expansion with high stiffness. Journal of the Mechanics and Physics of Solids 55: 1803-1822
7. Cox A, Xia C, Fang N (2006) Microstereolithography: A Review. Proceedings of ICOMM: International Conference on Micro-Manufacturing, Urbana
8. Spadaccini CM, Farquar G, Weisgraber T et al (2009) High Resolution Projection Microstereolithography for 3-D Fabrication. National Nanomanufacturing Summit, Boston
9. Sun C, Fang N, Wu DM et al (2005) Projection micro-stereolithography using digital micro-mirror dynamic mask. Sensors and Actuators: A Physical 121: 113-120
10. Spadaccini CM, Farquar G, Weisgraber T et al (2009) High Resolution Projection Microstereolithography for 3-D Fabrication. National Nanomanufacturing Summit, Boston, MA
11. Besra L, Liu M (2007) A review on fundamentals and applications of electrophoretic deposition (EPD). Progress in Materials Science 52: 1–61
12. Ferrari B, Moreno R (2000) Zirconia thick films deposited on nickel by aqueous electrophoretic deposition. J. Electrochem. Soc. 147: 2987-2992
13. Li HX, Lin MZ, Hou JG (2000) Growth of metal/organism multilayer films from ligand-stabilized silver nanoparticles. J. Mat. Sci. Lett. 19: 963-964
14. Velev OD, Bhatt KH (2006) On-chip micromanipulation and assembly of colloidal particles by electric fields. Soft Matter 2: 738-750
15. Ordung M, Lehmann J, Ziegler G (2004) Fabrication of fibre reinforced green bodies by electrophoretic deposition of silicon powder from aqueous suspensions. J. Mat. Sci. 39: 889-894
16. Hayward RC, Saville DA, Aksay IA (2000) Electrophoretic assembly of colloidal crystals with optically tunable micropatterns. Nature 404: 56-59
17. Kruger HG, Knote A, Schindler U et al (2004) Composite ceramic-metal coatings by means of combined electrophoretic deposition and galvanic methods. J. Mat. Sci. 39: 839-844
18. Tabellion J, Clasen R (2004) Electrophoretic deposition from aqueous suspensions for near-shape manufacturing of advanced ceramics and glasses – applications. J. Mat. Sci. 39: 803-811
19. Uchikoshi T, Ozawa K, Hatton BD et al (2001) Dense, bubble-free ceramic deposits from aqueous suspensions by electrophoretic deposition. J. Mater. Res. 16: 321-324
20. Duoss EB, Twardowski M, Lewis JA (2007) Sol-Gel Inks for Direct-Write Assembly of Functional Oxides. Advanced Materials 19: 3485-3489
21. Lewis JA (2002) Direct-write assembly of ceramics from colloidal inks. Curr. Opin. Solid State Mat. Sci. 6: 245-250
22. Smay JE, Cesarano J, Lewis JA (2002) Colloidal Inks for Directed Assembly of 3-D Periodic Structures. Langmuir 18: 5429-5437

23. Therriault D, Shepherd RF, White SR et al (2005) Fugitive inks for direct-write assembly of three-dimensional microvascular networks. Advanced Materials 17: 395-399
24. Gratson GM, Xu MJ, Lewis JA (2004) Microperiodic structures - Direct writing of three-dimensional webs. Nature 428: 386-386
25. Ghosh S, Parker ST, Wang XY et al (2008) Direct-write assembly of microperiodic silk fibroin scaffolds for tissue engineering applications. Adv. Funct. Mater. 18: 1883-1889
26. Ahn BY, Duoss EB, Motala MJ et al (2009) Omnidirectional Printing of Flexible, Stretchable, and Spanning Silver Microelectrodes. Science 323: 1590-1593

Freely configurable Functionalization Tool for switchable Information Carriers

Melanie Ecker and Thorsten Pretsch*

BAM Federal Institute for Materials Research and Testing, Division 6.5,
Polymers in Life Science and Nanotechnology, 12205 Berlin, Germany
*Corresponding Author: Tel. +49 30 8104-3804, Fax. +49 30 8104-1617
E-mail: thorsten.pretsch@bam.de

Abstract

The selective compression of quick response (QR) and Data Matrix code carriers based on shape memory polymer (SMP) with a freely configurable steel ball type indenter and adjacent thermo-mechanical shape fixing gave notched, room temperature (23 °C) stable, temporary shapes with non-decipherable codes. The microscopic investigation of cryomicrotome sections unveiled indentation-related shape fixities of about 90%. Independent of the selected two-dimensional code, the triggering of the SM effect resulted in sufficient shape recoveries to restore the code readability so that a maximum number of characters including 122 for a QR code (version 7) and 112 in case of a Data Matrix code (version 12) could be read with a scanning and decoding device. Due to the large number of difficult to copy shapes with on demand releasable information, SMPs may serve as viable information carriers for product and brand protection applications.

Keywords: *shape memory polymer; QR code; Data Matrix code; freely configurable functionalization*

1. Introduction

Shape memory polymers (SMPs) are stimuli-responsive materials, [1-4] which can be stabilized in a temporary shape by means of thermo-mechanical treatment (also denoted as “programming” or “functionalization”). The temporary shape is kept by the SMP until the SM effect is triggered by heating the polymer above the switching temperature. As a result, the SMP returns almost completely into the original (permanent) shape. One excellent example for an SMP is phase-segregated poly(ester urethane) (PEU) based on poly(1,4-butylene adipate) (PBA) as soft segment. The physically cross-linked block copolymer combines the advantages of distinct shape memory properties[5-7] with facile surface structuring.[8]

W. Udomkichdecha et al. (eds.), *Materials Challenges and Testing for Manufacturing, Mobility, Biomedical Applications and Climate*,
DOI 10.1007/978-3-319-11340-1_3

In surface-colored SMPs, two-dimensional (2D) codes like quick response (QR) codes are affine towards distortions, which inhibit their deciphering with a scanning and decoding device.[8] Having this in mind, we prepared switchable information carriers (hereafter also called tags), by laser engraving either a QR or Data Matrix code into a dyed SMP surface and thermo-mechanically functionalized the tags to render the 2D codes temporarily non-readable. Both types of codes are widely-used and decodable in a non-distorted state with a standard scanning and decoding device (smartphone). In contrast to earlier functionalization routes, in which for instance PEU-based QR code carriers were compressed with plane steel plates to randomly distort the overall QR code (version 1) with the aim of rendering it temporarily non-readable, we herein used a freely configurable steel ball type indenter as exclusively developed for a more selective code distortion. Beyond that, we employed QR code version 7 with a much higher data capacity and analyzed the compatibility of the overall SMP Tagnologies™ concept with two versions of Data Matrix codes. In any case, the shape memory effect was finally triggered to efficiently recover the permanent shape and investigate the code readability.

2. Experiments

2.1 Materials

Desmopan DP 2795A SMP, which is a poly(ester urethane) (PEU) from Bayer MaterialScience AG, was specially developed for shape memory applications and used as received. The hard segment was composed of 4,4’-methylenediphenyl diisocyanate and a 1,4-butanediol chain extender. The soft segment was based on poly(1,4-butylene adipate) (PBA). The raw material was supplied as cuboidal, injection molded plaques with dimensions of $126 \times 52 \times 2$ mm^3.

2.2 Sample preparation

The cuboidal PEU plaques were surface-dyed with a black-colored dye solution, consisting of 2 wt% of *N*-[4-[[4-(dimethylamino)phenyl][4-(phenylamino)-1-naphthyl] methylene]-2,5-cyclohexadien-1-ylidene]-*N*-methyl-methanaminium chloride (*Victoria Blue B*; C.I. 44045; CAS 2580-56-5; Sigma Aldrich), 5.5 wt% of [4-[4-(Diethylamino) benzhydrylene]cyclohexa-2,5-dien-1-ylidene]diethylammonium hydrogen sulphate (*Basic Green 1*; C.I. 42040; CAS 633-03-4) and 5.5 wt% of 3-[1,3-dihydro-1,3,3-trimethyl-2H-indol-2-ylene)ethylidene]-9-ethyl-3H-carbazolium chloride (*Basic Red 28*; CAS 72828-

91-2), which were completely dissolved in a 1:1 mixture of ethanol (96%, Merck) and acetone (98%, AppliChem). The obtained solution had a dye concentration of 27.9×10^{-2} mol l^{-1}.

The surface-specific dyeing procedure was based on guest diffusion. In the first step, the PEU surface was cleaned with lint-free cloth, before it was pretreated with acetone for about 30 s. Adjacently the black dye solution was pipetted onto the PEU surface and uniformly distributed by means of a brush. After 30 s, the residue of the dye solution was completely removed with another lint-free cloth. In a next step, either a QR or Data Matrix code was engraved into the colored PEU surface. Basically, both code types may hold different numbers of characters, depending on the employed version. For instance, QR code version 1 may hold a maximum of 34 numeric, 20 alphanumeric (consisting of the Latin letters "A to Z" and the Arabic digits "0 to 9") or 14 (8-bit) characters (alphanumeric characters and special characters; each character is encoded as an 8-bit byte), whereas QR code version 7 may store up to 293 numeric, 178 alphanumeric or 122 (8-bit) characters.[9] Likewise, Data Matrix code version 5 may hold a maximum of 36 numeric, 25 alphanumeric or 16 (8-bit) characters, whereas Data Matrix code version 12 is able to store up to 228 numeric, 169 alphanumeric or 112 (8-bit) characters.[10] The engraved, codified information was "BAM QRM-Label" (version 1) and "BAM QRM-Label 123456789 followed by webpage URL[11]“ (version 7) for QR codes and "BAM DM-Label" (version 5) same as "BAM DM-Label followed by webpage URL[11]“ (version 12) for Data Matrix codes. The QR codes were generated by means of the free application accessible through the website "http://goQR.me“ by selecting the error correction level "M" and the Data Matrix codes via "http://www.barcode-generator.org“. For engraving the black-and-white inverted 2D codes into the colored PEU surface and cutting plaques into squarish (25 × 25 mm^2) samples, an Epilog Zing 16 laser engraver and cutting machine was used. In order to guarantee a sufficiently high surface contrast, the laser ablation depth was set to exceed the dye diffusion depth.

2.3 Functionalization and recovering

The programming (functionalization) and recovering of samples was conducted with an electromechanical testing system (MTS Insight 10), which was equipped with a thermochamber (Thermcraft). The heating of the samples was accomplished by two electrical heating elements in the back of the thermochamber. The cooling was achieved by injecting liquid nitrogen from a Dewar vessel into the thermochamber.

For compressive deformation-determined functionalization (CDDF), a freely configurable stainless steel ball type indenter was developed (Fig. 2.1).

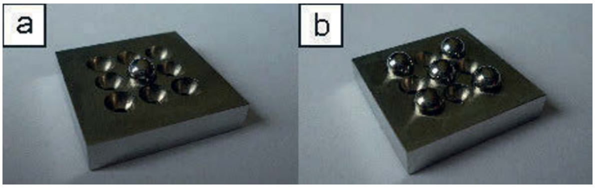

Fig. 2.1: Freely configurable stainless steel ball type indenter, occupied by one (a, center position) and five metal balls (b, arranged in an X-shape similar to the five pip side of a Western-style die).

In the stainless steel indenter with a dimensioning of $25 \times 25\ \mathrm{mm}^2$, nine indentations of identical 5 mm diameter and 2.5 mm depth were arranged in a 3×3 matrix, so that every indentation could be filled with one stainless steel ball maximum (having a radius of 2.5 mm). The horizontal and vertical distance between the maximum depths of nearby indentations was 5.5 mm. Mathematically speaking, when allocating k balls n positions, the overall number of possible indenter configurations corresponds to the binominal coefficient, indexed by n and k (eq. 2.1):

$$\binom{n}{k} = \frac{n!}{k!(n-k)!} \tag{2.1}$$

Accordingly, a maximum number of 126 configurations is obtainable both for $k = 4$ and 5 (at $n = 9$). Herein, we focused on two out of 511 possible indenter configurations. In the first one, the center position was occupied by one steel ball, whereas in the second configuration, five steel balls were arranged in an X-shape similar to the five pip side of a Western-style die (Fig. 2.1). In this regard, we would like emphasizing that the indenter dimensioning was selected in compliance with the tag size and thus with the QR and Data Matrix code areas.

In the given setup, the deformable areas of the PEU were thus predetermined by the selected number of steel balls and their positions. The PEU sample was always placed exactly in the same way atop the configurable indenter with the steel ball(s) pointing towards the colored PEU surface (Fig 2.2). In this connection, aluminum foil was used for a proper adjustment. The indenter and PEU sample were positioned between the upper and lower steel plates, which in turn were connected to the rods of the electromechanical testing system.

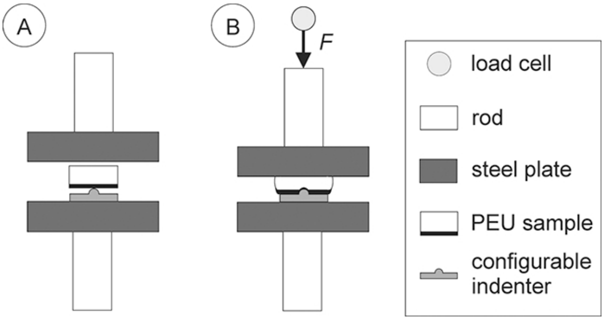

Fig. 2.2: Schematic setup for CDDF of PEU samples: (A) before and (B) after loading.

In order to assure that the PEU sample and the indenter did not alter position, an initial force of 10 N was applied prior to heating the polymer with a rate of 4.3 °C min^{-1} to 80 °C and thus above the PBA melting transition (which was close to 40 °C[8]). After 5 min at 80 °C, the sample was compressed with a rate of 100 N min^{-1} to the maximum force F_{max}, which was chosen in accordance with the selected indenter configuration (one ball: F_{max} = 60 N; five balls: F_{max} = 300 N). In order to fix the polymer in the temporary shape, F_{max} was maintained during cooling the PEU sample with a rate of 5.3 °C min^{-1} to −20 °C and thus below the PBA crystallization temperature (around 0 °C[8]). After 5 min at −20 °C, the steel ball indented (notched) PEU sample was unloaded with a rate of 500 N min^{-1} to finalize shape programming, before it was heated to 23 °C. In order to trigger the shape memory effect and recover the original shape, the PEU was reheated to 80 °C and kept at that temperature for 5 min. Finally, the sample was cooled to 23 °C.

2.4 Scanning and decoding

A Samsung Galaxy S I9000 smartphone equipped with the software “Barcode Scanner” version 4.1 from ZXing Team was used as scanning and decoding device. The 2D codes were scanned after the preparation, functionalization and recovering of the information carriers (tags).

2.5 Indentation-related shape memory properties

Microscopic investigations were carried out on cryomicrotome sections (prepared at −20 °C) of black surface-dyed PEU, both after the functionalization and recovering of the sample. For a first microscopic image, the steel ball indented (notched), programmed polymer was cut perpendicular to the dyed surface and exactly through the indentation maximum with a cryomicrotome CM1950 from Leica. Then, the polymer was heated to 80 °C and kept at that temperature for 5 min to recover the permanent shape, before one further microscopic image was taken. In any case, a Wild M5A stereo microscope with 6 times optical zoom and the associated Dietermann and Heuser Solution GmbH (dha) software (version 13) were used. From the obtained photographs the steel ball indentation depth and the dye diffusion depth were determined with the graphical program ImageJ (developed at the National Institutes of Health, USA). For latter, the darkest point at the surface was set as standard and the intensity decline down to a loss of 70% was measured. The corresponding distance to the surface was defined as dye diffusion depth.

Independent of the employed one or five steel ball type indenter, the indentation-related shape memory properties of the PEU were quantified. In the initial state, the PEU was characterized by a sample height h_0 of 2 mm. The steel ball penetration depth h_p as directly determined from crosshead displacement, the maximum indentation depth ($h_0 - h_t$), corresponding to the lowest sample height in the temporary state, the extent of indentation recovery ($h_r - h_t$) and the maximum height of protrusive bumps ($h_b - h_0$) in the temporary and recovered state were determined (Fig. 2.3).

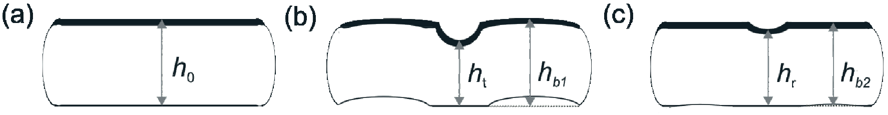

Fig. 2.3: Side view of a schematic cross-section through the permanent (a), the temporarily fixed (b, as characterized by one indentation surrounded by a protrusive bump) and recovered shape (c) of a PEU sample.

Accordingly, we defined the indentation depth-related ratios of shape fixity R_f and shape recoverability R_r in eqs. 2.2 and 2.3:

$$R_f = \frac{h_0 - h_t}{h_p} \cdot 100 \tag{2.2}$$

$$R_r = \frac{h_r - h_t}{h_0 - h_t} \cdot 100 \tag{2.3}$$

3. Results and Discussion

First of all, the PEU surface was colored with the three-component black dye solution, consisting of two triarylmethane dyes (*Victoria Blue B* and *Basic Green 1*) and the hemicyanine dye *Basic Red 28*. As verified by cryomicrotome sections (not shown herein), the black-coloring of the PEU resulted in homogenous dye diffusion depths of around (95±5) µm. The amount of dye inside the polymer surface was (0.13±3) wt%.

To elucidate the indentation-related shape memory properties of the black surface-dyed PEU, a cryomicrotome section was microscopically investigated in the steel ball indented, temporarily fixed state and after the almost complete return of the polymer into the permanent shape due to triggering the shape memory effect. When using a one steel ball type indenter, the functionalized state was characterized by one spherical indentation with a depth $(h_0 - h_t) = (1.50 \pm 0.02)$ mm (Fig. 3.1), which was close to the steel ball penetration depth of (1.67±0.05) mm. Accordingly, the shape fixity ratio R_f was (90±3)%.

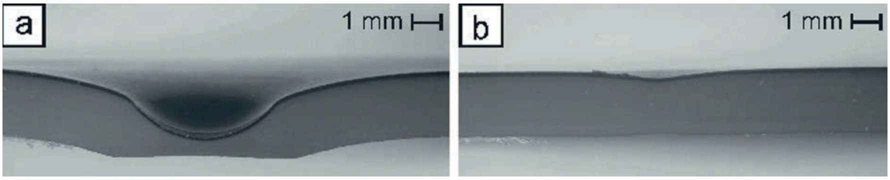

Fig. 3.1: Microscopic image of a cryomicrotome section of black surface-dyed PEU, showing the polymer in the temporary shape (a, functionalized via the one steel ball type indenter) and recovered shape (b).

In parallel, a homogenous circular protrusive bump formed around the indentation with a maximum height $(h_{b1} - h_0) = 0.5$ mm. The indentation-related phenomenon of protrusive bump formation is fairly well known from shape memory polymers like styrene-based block copolymer.[12-14] The triggering of the shape memory effect mostly led to the recovery of the indentation together with the almost complete disappearance of the protrusive bump as evidenced by a negligible residue of $(h_{b2} - h_0) = (0.01 \pm 0.02)$ mm. Beyond that, an R_r ratio of (79±2)% could be detected. Latter is in accordance with the tensile-related shape memory properties of the PEU ($R_r = 77\%$[6]). In agreement with the findings obtained from the one steel ball type indenter, using five steel balls instead at a fivefold compressive force gave similar indentation geometries (Fig 3.2). The averaged data per indentation included a depth $(h_0 - h_t) = (1.50 \pm 0.03)$ mm and an R_f ratio of (89±3)%. Upon triggering the shape memory effect, the protrusive bumps also disappeared almost completely, giving small averaged residues of $(h_{b2} - h_0) = (0.01 \pm 0.02)$ mm and an R_r value of (71±2)%.

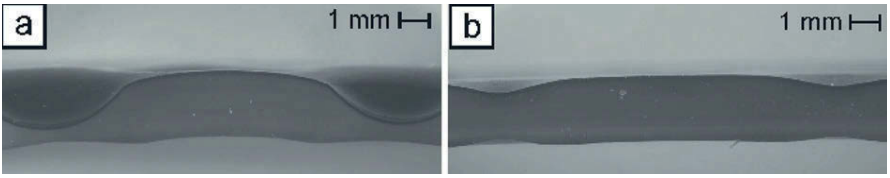

Fig. 3.2: Microscopic image of a cryomicrotome section of black surface-dyed PEU, showing the polymer in the temporary shape (a, functionalized via the five steel ball type indenter) and recovered shape (b).

One further finding included that functionalizations with the freely configurable steel ball type indenter resulted in puncture, when the applied compressive force exceeded a crucial value of 200 N per indentation. For instance, transferring 1000 N via the five steel ball type indenter onto the PEU favored the formation of five holes equal in diameter (1.1 mm) and located in the non-dyed backside of the polymer sample. Once heated to 80 °C, a distinctive shape recovering of the PEU took place, which was accompanied by the shrinkage of the voids to an averaged diameter of 0.4 mm (not shown herein).

The above presented results undoubtfully document the distinct shape memory properties of PEU and imply that the material is an appropriate candidate for discrete surface modifications. Therefore we functionalized switchable information carriers (tags) via the freely configurable steel ball type indenter. The employed 2D codes included in each case two QR and Data Matrix codes of different versions (Fig. 3.3).

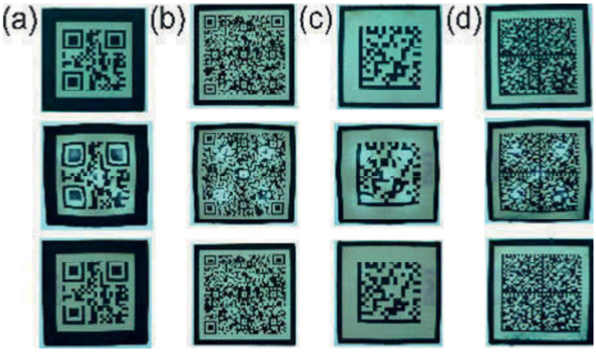

Fig. 3.3: Smart tags with QR (a and b) and Data Matrix codes (c and d). The respective 2D codes include version 1 (a), 7 (b), 4 (c) and 12 (d). Each of the tags is exhibited in the original (top), temporarily fixed (center) and recovered state (bottom).

At first, the tags were programmed with the one steel ball type indenter as described above for the solely surface-colored PEU. We found that in case of QR codes, the exact position of indentation played a major role. Here, the QR codes could be rendered temporarily non-readable through the deformation of one of the three position detection patterns, which had a dimensioning of 5.0×5.0 mm^2 (QR code version 1) and constituted distortion-sensitive areas. In all other scenarios, arbitrary deformations were applied with the one steel ball type indenter and fixed, but the QR codes remained decipherable.

By contrast, the position detection pattern in Data Matrix codes is composed of two so-called “search lines”, which could not be strongly enough distorted by the one steel ball type indenter. Thus, Data Matrix codes remained decipherable, independent of which code area was indented. Neglecting the presence of protrusive bumps atop, the overall deformed code areas were within the high error tolerance of the different 2D code versions (Table. 3.1).

Table 3.1: Error tolerance of QR and Data Matrix codes towards real code distortion (the data were taken from Ref.[9, 10]) and relative deformation of the code areas through the employed one and five steel ball type indenter.

Code type	Code version	Code area in the permanent shape [mm^2]	Error tolerance [%]	Overall code deformation by one indentation [%]	Overall code deformation by five indentations [%]
QR-M	1	15 × 15	15	9	44
QR-M	7	20 × 20	15	5	25
Data Matrix	5	15 × 15	43.8	9	44
Data Matrix	12	18 × 18	29.6	6	30

Finally, we investigated the programming efficiency of our five steel ball type indenter. As a result of functionalization, every single code turned non-readable even though the position detection patterns of QR code version 7 were only slightly distorted. Both in case of QR and Data Matrix codes, the distorted area exceeded the error tolerance values of the employed codes (Table 3.1). Finally, the shape memory effect was triggered, which coincided with the restoration of the 2D code machine-readability.

4. Conclusions

The freely configurable steel ball type indenter turned out to be an appropriate tool to obtain selectively modified temporary shapes in information carries based on poly(ester urethane) as shape memory polymer. In particular, the deformation of the QR code position detection pattern in code version 1 and 7 as simply achievable with a one steel ball type indenter and the more general approach of exceeding the deformation-compensable barrier in both QR and Data matrix codes gave notched, room temperature (23 °C) stable, temporary shapes with non-readable 2D codes. In parallel, the formation of protrusive bumps may have additionally contributed to render the 2D codes temporarily non-readable. Once functionalized *via* the five steel ball type indenter, the information carriers could reliably be switched from non-readable to readable, independent of the investigated code type and version. The use of SMP Tagnologies$^{\text{TM}}$ in manifold ways illustrates the huge potential for product and brand protection applications.

5. Acknowledgments

The authors gratefully acknowledge financial support from the German Federal Ministry of Education and Research (BMBF, project funding reference number 16V0043). Mr. Miteshkumar Patel is acknowledged for programming and recovering the information carriers. The authors thank Bayer MaterialScience AG for kindly providing the PEUs.

6. References

1 Leng J, Lu H, Liu Y, Huang WM, Du S (2009) Shape-Memory Polymers - A Class of Novel Smart Materials. MRS Bull 34:848-855.

2 Huang WM, Ding Z, Wang CC, Wei J, Zhao Y, Purnawali H (2010) Shape Memory Materials. materialstoday 13:54-61.

3 Pretsch T (2010) Review on the Functional Determinants and Durability of Shape Memory Polymers. Polymers 2 (3):120-158.

4 Behl M, Zotzmann J, Lendlein A (2010) Shape-Memory Polymers and Shape-Changing Polymers. Adv Polym Sci:1-40.

5 Pretsch T (2008) Degradation, functional stability and protection of a shape memory polymer. WMRIF Workshop for young scientists. Tsukuba (Japan). ISBN: 978-4-9900563-3-9.:XXX-1 - 11.

6 Pretsch T, Jakob I, Müller W (2009) Hydrolytic Degradation and Functional Stability of a segmented Shape Memory Poly(ester urethane). Polym Degrad Stab 94 (1):61-73.

7 Müller W, Pretsch T (2010) Hydrolytic aging of crystallizable shape memory poly(ester urethane): Effects on the thermo-mechanical properties and visco-elastic modeling. Eur Polym J 46 (8):1745-1758.

8 Pretsch T, Ecker M, Schildhauer M, Maskos M (2012) Switchable information carriers based on shape memory polymer. J Mater Chem 22 (16):7757-7766.

9 Information technology — Automatic identification and data capture techniques — Bar code symbology — QR Code (2000). ISO copyright office, Switzerland.

10 Information technology — Automatic identification and data capture techniques — Data Matrix bar code symbology specification (2006). ISO copyright office, Switzerland.

11 BAM - Shape Memory Polymers (2012) http://www.bam.de/en/kompetenzen/fachabteilungen/abteilung_6/fg65/fb65_formgedaechtnispolymere.htm.

12 Liu N, Huang WM, Phee SJ, Fan H, Chew KL (2007) A generic approach for producing various protrusive shapes on different size scales using shape-memory polymer. Smart Mater Struct 16:N47-N50.

13 Liu N, Xie Q, Huang WM, Phee SJ, Guo NQ (2008) Formation of micro protrusion arrays atop shape memory polymer. J Micromech Microeng 18:art. no. 027001.

14 Liu N, Huang WM, Phee SJ, Tong TH (2008) The formation of micro-protrusions atop a thermo-responsive shape memory polymer. Smart Mater Struct 17:art. no. 057001.

MEMS-based microsensors using piezoelectric thin films as sensors and actuators

Takeshi Kobayashi[1], Hironao Okada[1], Natsumi Makimoto[1], Syoji Oyama[2], Hiroshi Funakubo[3], Tohishiro Itoh[1], and Ryutaro Maeda[1]

[1] *National Institute of Advanced Industrial Science and Technology (AIST), 1-2-1 Namiki Tsukuba, Ibaraki, 305-8564, Japan*

[2] *Hirose Electric Co., 2-6-3 Nakagawa Chuo, Tuzuki, Yokohama, Kanagawa 224-8540, Japan*

[3] *Tokyo Institute of Technology, 4259 Nagatsuda-cho, Midori-ku, Yokohama, Kanagawa 226-8502, Japan*

Abstract

$Pb(Zr,Ti)O_3$ (PZT) thin films are attractive for the application to MEMS-based microsensors. PZT thin films can act as sensors and actuators through direct and indirect piezoelectric effect. Moreover, it is possible to integrate the piezoelectric thin films for sensor and actuator.

The present study describes MEMS-based electrostatic field sensors using PZT thin films as displacement sensors and vibration actuators. The self-sensitive piezoelectric microcantilevers have $Pb(Zr,Ti)O_3$ (PZT) thin films for sensor and actuator. The MEMS-EFS were fabricated through sol-gel deposition of PZT thin films and MEMS microfabrication process. An output voltage of the PZT thin films for sensor was found to be proportional to the displacement of the microcantilevers. Self-excited vibration of the microcantilevers has been achieved by amplifying and forwarding the output voltage of the PZT thin films for sensor with a band-pass filter circuit. The developed MEMS-EFS can evaluate an electrotatic field of -3 to 3 kV with good linearity.

Keywords: *piezoelectric, PZT, MEMS, electrostatic field sensor*

1. Introduction

$Pb(Zr,Ti)O_3$ (PZT) thin films are attractive for the application to MEMS-based microsensors. PZT thin films can act as sensors and actuators through direct and indirect piezoelectric effect. Moreover, it is possible to integrate the piezoelectric thin films for sensor and actuator. The present study describes MEMS-based elec-

W. Udomkichdecha et al. (eds.), *Materials Challenges and Testing for Manufacturing, Mobility, Biomedical Applications and Climate*,
DOI 10.1007/978-3-319-11340-1_4

trostatic field sensors using PZT thin films as displacement sensors and vibration actuators.

Electrostatic field sensors (EFS) are mainly applied for monitoring the electrostatic field on the exposure drum of copy machines and on the semiconductor wafers and flat panels processed in clean rooms. Miniaturization of EFS through MEMS technology can realize arrayed EFS, which enables 2D-mapping of electrostatic field. MEMS-EFS also realize integration with temperature, humidity and particle sensors, which are capable of multi-sensing wireless sensor nodes for monitoring clean rooms. Although MEMS-EFS based on thermal or electrostatic actuation have been developed [1,2], thermal noise and high voltage derived from such actuation interfere precise measurement of an electrostatic filed. Thus, MEMS-EFS should be based on piezoelectric actuation as well as commercially available ones.

EFS have probes to detect electrostatic field. The relation between the voltage of electrified bodies V_s, the surface of the probes S and the charges induced on the probe Q_s is expressed as

$$Q_s = \varepsilon_{air}\varepsilon_0 \frac{S}{L} V_s , \tag{1}$$

where $\varepsilon_{\mathrm{air}}$ and ε_0 are permittivity of air and vacuum, L is the distance between the probes and electrified bodies. Since it is difficult to measure Q_s under DC condition, EFS measure V_s by modulating S or L. Commercially available EFS modulate S by the shutter driven by $Pb(Zr,Ti)O_3$ (PZT) ceramics.

In the previous study, we reported MEMS-EFS, which integrate the probes to detect electrostatic field and PZT thin films for actuator into microcantilever [3]. Using the developed MEMS-EFS, we demonstrated the measurement of electrostatic field by modulating L with vibration of the microcantilevers driven at their resonant frequency. Since the resonant frequency can be varied by the intensity of electrostatic filed and environmental conditions such as temperature and humidity, the microcantilevers should be operated by self-excited vibration [4] so that the microcantilevers follow the variation in resonant frequency.

We have already developed self-sensitive piezoelectric microcantilevers, which have PZT thin films for sensor and actuator (sensor PZT and actuator PZT) [5,6]. Then, we have developed MEMS-EFS composed of the probes to detect electrostatic field and the self-sensitive piezoelectric microcantilevers. We have also developed the electronic circuit for self-excited vibration using a band-pass filter. We have successfully demonstrated the measurement of the electrostatic field of -3 to 3 kV with the developed MEMS-EFS operated by self-excited vibration of the self-sensitive piezoelectric microcantilevers.

2. Design and working principle

Figure 1 illustrates the design of the MEMS-EFS developed in the present study. The MEMS-EFS consist of the probes to detect electrostatic field (EFS-probe) and the self-sensitive piezoelectric microcantilevers. The microcantilevers have sensor and actuator PZT. The surfaces of the EFS-probe are located toward electrified bodies as shown in figure 2. When the distance L is varied at the amplitude of l and frequency of f by the actuator PZT, the charges generated on the EFS-probe Q_m are also varied as

$$Q_m = \varepsilon_{air}\varepsilon_0 \frac{S}{L + l\sin 2\pi ft} V_s \quad . \tag{2}$$

Assuming $L>>l$, equation (2) can be approximated as

$$Q_m = q\sin 2\pi ft + Q_s \quad . \tag{3}$$

This equation means that the charges on the MEMS-EFS are modulated at the amplitude of q. Assuming $q = rQ_s$, eq. (3) is expressed as

$$Q_m = rQ_s \sin 2\pi ft + Q_s \quad . \tag{4}$$

Thus, the amplified output voltage of MEMS-EFS V_{EFS} is expressed as

$$V_{EFS} = \frac{ArQ_s \sin 2\pi ft}{C_{total}} + \frac{AQ_s}{C_{total}} \quad , \tag{5}$$

where A is an amplifier gain and C_{total} is the total capacitance of all of the components. The amplitude of eq. (5), $V_{EFS,pp}$ is given as

$$V_{EFS,pp} = \frac{ArQ_s}{C_{total}} \quad . \tag{6}$$

Using eq. (1), eq. (6) is rewritten as

$$V_{EFS,pp} = Ar\frac{\varepsilon_{air}\varepsilon_0 S/L}{C_{total}} V_s \quad . \tag{7}$$

Equation (7) clearly represents that the amplitude of the AC output voltage obtained by amplifying the charge on the EFS-probe is proportional to the voltage of electrified bodies. Thus, the voltage of electrified bodies can be evaluated by measuring the amplitude of V_{EFS}.

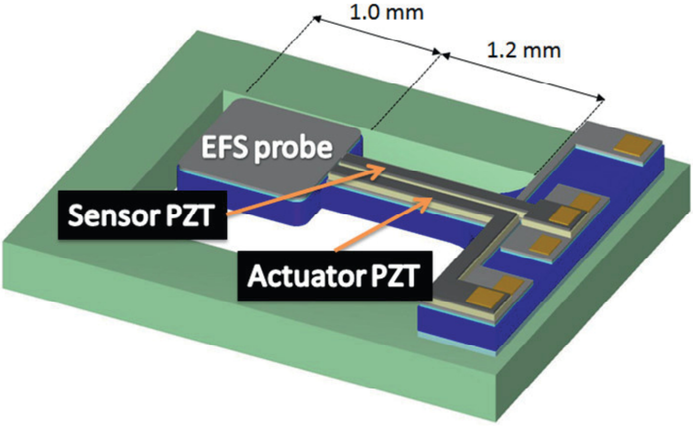

Figure 1. *Design of the MEMS-EFS developed in the present study., which integrate sensor PZT, actuator PZT and probes to detect electrostatic field into microcantilevers. EFS probes are 1 mm-square and cantilever is 1.2 mm-long.*

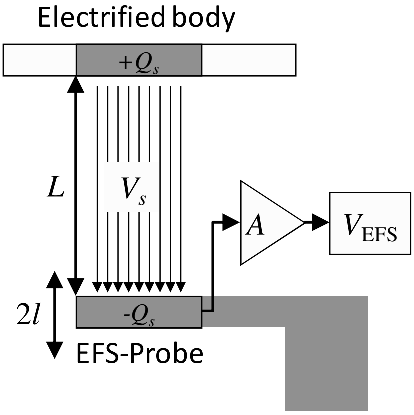

Figure 2. *Schematic of the arrangement of the MEMS-EFS and electrified bodies. The surfaces of the EFS-probe are located toward electrified bodies*

As described above, MEMS-EFS should be operated by self-excited vibration so that the microcantilevers follow the variation in the resonant frequency due to change in the intensity of electrostatic filed and environmental conditions such as temperature and humidity. Figure 3 illustrates the block diagram of the MEMS-

EFS and electronic circuits for self-excited vibration. In self-excited vibration, the output voltage from the sensor PZT, which is amplified and forwarded by the band pass filter, is applied to the actuator PZT. The displacement of the microcantilevers is determined by the source voltage of the band pass filter (5 V at present study). By synchronous detection of the output voltage from the sensor PZT modulated by the band-pass filter and the voltage derived from electric charges induced on the probes, the MEMS-EFS give the output voltage (EFS output) proportional to the intensity of the electrostatic field. The EFS output is calibrated so that the indicator shows the practical voltage of electrified bodies.

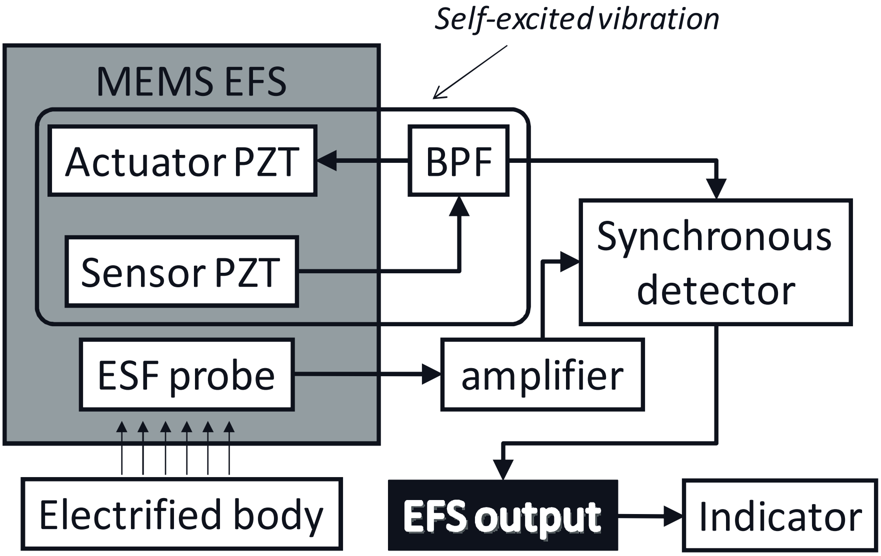

Figure 3. Block diagram of the MEMS-EFS and electronic circuits for self-excited vibration.

3. Device fabrication

Figure 4 shows the schematic cross-section of the fabrication process. The designed MEMS-EFS were fabricated from the multilayers of Pt/Ti/PZT/Pt/Ti/SiO_2 deposited on SOI wafers (structural Si: 10 μm, buried SiO_2: 1 μm, substrate Si: 400 μm) through MEMS microfabrication process [7]. The deposition of the multilayers started from thermal oxidation of the SOI wafers followed by Pt/Ti bottom electrodes sputtering. Then, 1.1 μm thick (100)/(001)-oriented $Pb(Zr_{0.52},Ti_{0.48})O_3$ thin films were deposited by sol-gel process [8]. Finally, Pt/Ti top electrodes were sputtered.

After multilayer deposition, Pt/Ti and PZT thin films were etched by Ar-ion etching (Pt/Ti) and wet etching (PZT) through mask 1-3. Next, thermal SiO_2, structural Si and BOX were etched by RIE with CHF_3 gas (SiO_2) and SF_6 gas (Si) through mask 4. Finally, substrate Si and BOX were etched from backside to release the micro cantilevers and EFS probes. Figure 5(a) shows SEM image of the fabricated MEMS-EFS.

The fabricated MEMS-EFS and amplifiers were mounted on printed circuit boards, which were covered by metal shield caps with an open hole for the probe for electrostatic field detection as shown in figure 5(b). The packaged MEMS-EFS, electronic circuits, and indicators were integrated into plastic cases with dry batteries as shown in figure 5(c). The indicators display measured electrostatic field.

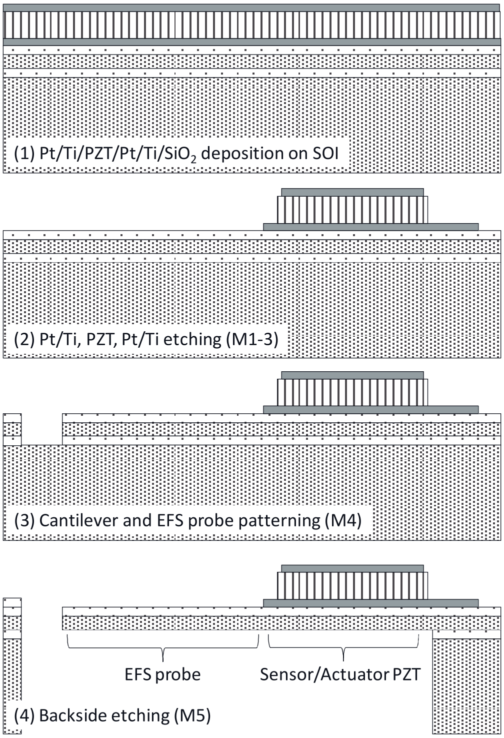

Figure 4. *MEMS microfabrication process for MEMS-EFS. (1)Pt/Ti/PZT/Pt/Ti/SiO_2 deposition on SOI wafer, (2)Pt/Ti, PZT, Pt/Ti etching (Mask 1-3), (3)Cantilever and EFS probe patterning (Mask 4), (4) Backside etching (Mask 5).*

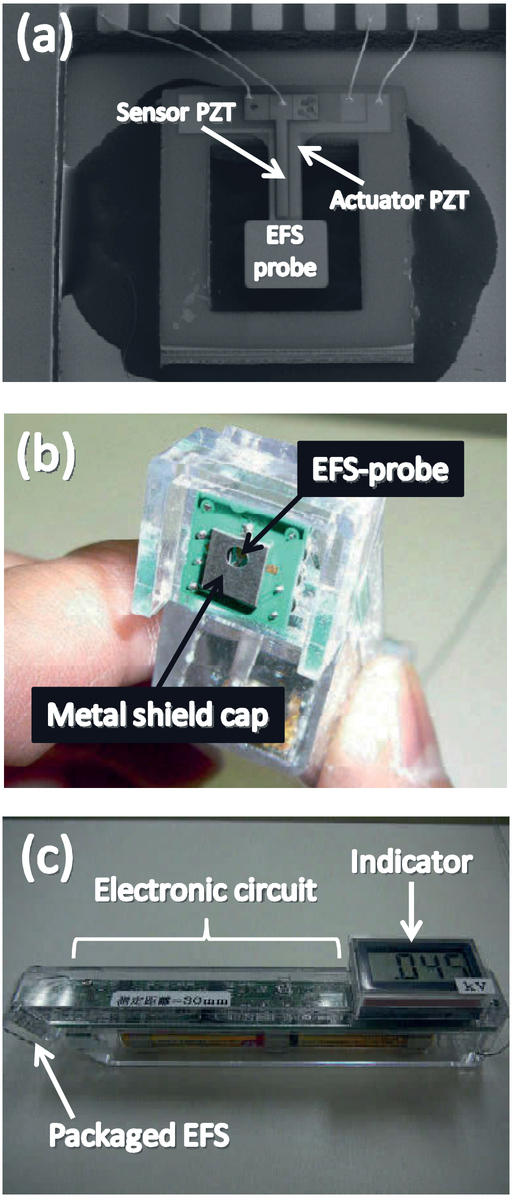

Figure 5. *(a) SEM image of fabricated MEMS-EFS. (b) MEMS-EFS packaged by printed circuit board and metal shield cap. (c)Overview of pencil-type device. EFS is mounted on the top of pencil and electronic circuit is packaged in plastic case. Indicator displays measured electrostatic field.*

4. Test and results

In order to achieve self-excited vibration, the output voltage of the sensor PZT should be proportional to the displacement of the microcantilevers. Thus, we investigated the relation between displacement of the microcantilevers and the output voltage of the sensor PZT by using the similar setup reported in our previous study [5].

AC voltages of 2-10 V_{pp} with 2.5 V of DC bias were applied to the actuator PZT by using a function generator (Tektronix AFG3022, USA). The tip displacement of the vibrating microcantilevers was measured by a laser displacement meter (Graphtec AT1100, Japan). The output voltage of the sensor PZT was directly measured by a digital oscilloscope (Tektronix TDS2004B, USA) by using the AC voltages applied to the actuator PZT as a trigger. The waveforms of the microcantilever displacement and the output voltage of the sensor PZT were simultaneously recorded by the digital oscilloscope.

As shown in figures 6(a) and (b), the output voltage of the sensor was found to be proportional to the microcantilever displacement under both non-resonant (1450 Hz) and resonant conditions (1875 Hz). We have also characterized the relation between the output voltage of the actuator PZT and sensor PZT. Figure 7 shows the output voltage of the sensor PZT, in case the actuator PZT is vibrated under resonant condition (1875 Hz) at 5 V_{pp} by the function generator. The output voltage of the sensor PZT is 0.12 V_{pp} and delays 90 degree compared to the actuation voltage. Figure 8 shows the output voltage of the sensor PZT and that modulated by the band pass filter. The result shows that the output voltage from the sensor PZT is forwarded 90 deg. and amplified to 10 V_{pp}, which indicates the achievement of self-excited vibration.

We have measured an electrified body by using the pencil-type device shown in figure 5 (c). The amplifier shown in figure 3 is tuned so that the indicator shows accurate voltage of the electrified body, where the distance between the MEMEFS and the electrified body should be 30 mm. Figure 9 shows the measurement results. The output of the electrostatic field sensor (EFS output) displayed on the indicator has shown good linearity to the electrostatic field of -3 to 3 kV as we can see in figure 9.

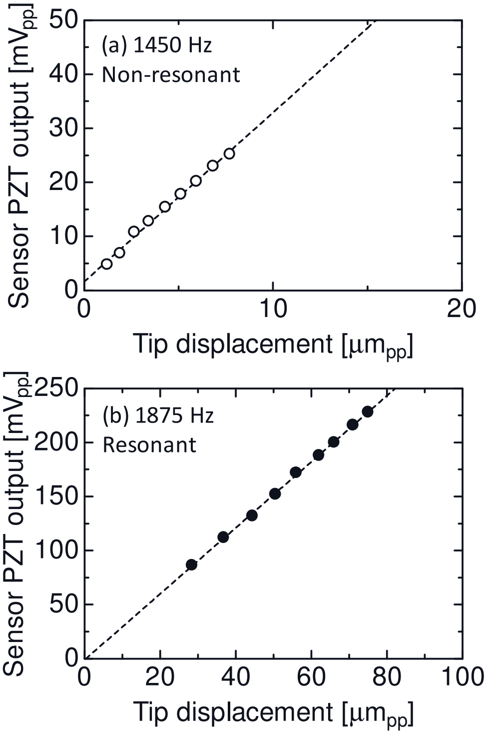

Figure 6. *Relation between the microcantilever displacement and output voltage of the sensor PZT under (a) non-resonant and (b) resonant conditions.*

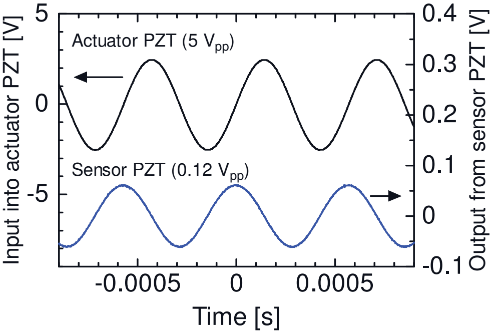

Figure 7. *(top) Input voltage into the actuator PZT from function generator and (bottom) output voltage of the sensor PZT.*

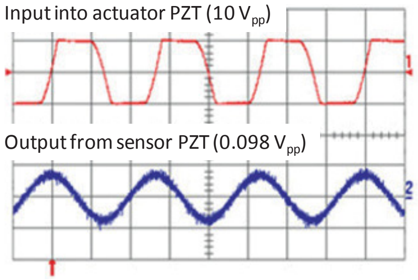

Figure 8. *Input voltage into the actuator PZT obtained by amplifying and forwarding output voltage of the sensor PZT by band pass filter and output voltage of the sensor PZT (0.098 V_{pp}). The result indicates that the microcantilever is under self-excited vibration.*

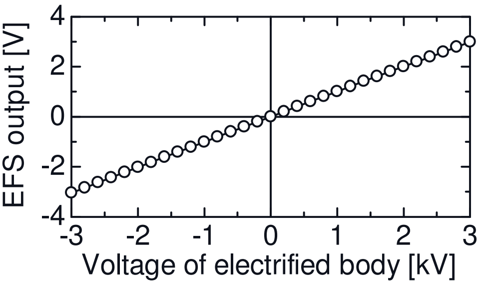

Figure 9. *Output of the electrostatic field sensor (EFS output) as a function of the voltage of electrified body.*

5. Conclusion

We have developed MEMS-based electrostatic field sensors composed of the probes to detect electrostatic field and the microcantilevers with PZT thin films for sensor and actuator. The MEMS-EFS were fabricated through sol-gel deposition of PZT thin films and MEMS microfabrication process. We have also developed electronic circuit using the band pass filter for self-excited vibration of the micro cantilevers. Self-excited vibration of the micro cantilevers has been achieved by amplifying and forwarding the output voltage from the sensor PZT with a band pass filter. By synchronous detection of the output voltage from the sensor PZT modulated by the band-pass filter and the voltage derived from electric charges induced on the probes, the MEMS-EFS give the output voltage proportional to the intensity of the electrostatic field of -3 to 3 kV with good linearity.

Acknowledgement

This research is granted by the Japan Society for the Promotion of Science (JSPS) through the "Funding Program for World-Leading Innovative R&D on Science and Technology (FIRST Program)," initiated by the Council for Science and Technology Policy (CSTP).

References

1. Bahreyni B, Wijeweera G, Shafai C, and Rajapakse A (2008) J Microelectromech Syst 17: 31-36
2. Peng C, Yang P, Zhang H, Guo X, and Xia S (2010) Proc of IEEE sensors 2010 conference: 1183-1186
3. Kobayashi T, Tsaur J, and Maeda R (2008) Jpn J Appl Phys 47: 7533-7536
4. Yabuno H, Kaneko H, Kuroda M, and Kobayashi T (2008) Nonlinear Dynamics 54: 137-149
5. Kobayashi T, Maeda R, and Itoh T (2008) J Micromech Microeng 18: 035025
6. Kobayashi T, Maeda R, and Itoh T (2008) J Micromech Microeng 18: 115007
7. Kobayashi T, Okada H, Masuda T, Maeda R, and Itoh T (2011) Smart Mater Struct 20: 065017
8. Kobayashi T, Ichiki M, Tsaur J, and Maeda R (2005) Thin Solid Films 489: 74-78

Industrial Single-Structure Separation of Single-Wall Carbon Nanotubes by Multicolumn Gel Chromatography

Huaping Liu[1, 2], Takeshi Tanaka[1] and Hiromichi Kataura[1, 2]*

[1]Nanosystem Research Institute, National Institute of Advanced Industrial Science and Technology (AIST), Tsukuba, Ibaraki 305-8562, Japan
[2]Japan Science and Technology Agency, CREST, Kawaguchi, Saitama 330-0012, Japan

**Corresponding Author: Tel. +81-29-861-2551, Fax. +81-29-861-2786, E-mail: h-kataura@aist.go.jp*

Abstract

Single-structure single-wall carbon nanotubes (SWCNTs) with the same electronic types and band gaps are essential for their applications in the fields of electronics and optoelectronics. SWCNTs are usually grown in the mixture of various structures with diverse properties, hindering their practical application. To achieve single-structure SWCNTs, post-growth separation is an important route. Here we report a landmark separation method - multicolumn gel chromatography to separate single-structure SWCNTs (that is, single chirality) on a large scale. In this method, high-purity electronically different semiconducting SWCNTs can be well sorted across different columns by simply pouring excess amount of SWCNT-dispersion aqueous solution into a series of vertically connected gel columns. Metallic SWCNTs are collected as the unadsorbed species. With this technique, we successfully isolated 13 (*n, m*) single-chirality semiconducting species from HiPco-SWCNTs.

Keywords: *Carbon nanotubes; Separation; Single structure; Multicolumn gel chromatography*

1. Introduction

Single-wall carbon nanotubes (SWCNTs) are one-dimensional seamless graphene cylinders with extremely high carrier mobility and structure-tunable optical properties [1]. Depending on the arrangement of carbon atoms, SWCNTs can

W. Udomkichdecha et al. (eds.), *Materials Challenges and Testing for Manufacturing, Mobility, Biomedical Applications and Climate*,
DOI 10.1007/978-3-319-11340-1_5

be semiconductors or metals. The energy bandgap of semiconductor is inversely proportional to the nanotube diameter [2]. These amazing features make SWCNTs have great potentials as next generation electronic materials for fabricating electronic and optoelectronic devices [3]. Current synthesis methods usually produce a heterogeneous mixture of SWCNTs with diverse electronic properties. The fabricated devices lack reliable and reproducible performances. Industrial separation of as-grown SWCNTs into populations of single-structure species is an extremely critical step to promote SWCNTs into electronic applications. Recently, density gradient ultracentrifugation [4] and DNA wrapping chromatography [5] methods have made a breakthrough in the sorting of SWCNTs, realizing isolation of single-chirality carbon nanotubes. However, these methods still suffer from high-cost problems, hindering the separation of SWCNTs into commercial application. The search for a simple, efficient and low-cost separation method is highly desirable.

Tanaka et al. found that semiconducting SWCNTs could be selectively adsorbed in agarose gel [6] and developed agarose gel chromatography for the large-scale separation of semiconducting (S-) and metallic (M-) SWCNTs by simply pouring SWCNT dispersion into an agaorse gel column [7, 8]. This separation technique permits high-efficiency M/S separation of SWCNTs with extremely low cost, because the gel column can be reused. However, single-chirality separation of SWCNTs is unavailable [8] due to the weak selectivity in the interaction of S-SWCNT with agarose gel.

Recently, we report sodium dodecyl sulfate (SDS)-wrapped SWCNTs have chirality-dependent interaction strength with the allyl dextran-based gel [10] that was firstly used as the medium of gel columns for the M/S separation of SWCNTs [9]. On the basis of this finding, we developed multicolumn gel chromatography utilizing a series of vertically connected gel columns [10]. Electronically different semiconducting SWCNTs could be easily sorted across different gel columns by simply pouring excess amount of SWCNT/SDS dispersion into the multistage gel columns, which is similar to the M/S separation process by agarose gel chromatography. Metallic SWCNTs were collected as the unadsorbed SWCNTs because of their weakest interaction with the allyl dextran-based gel. With this technique, we successfully separated 13 (*n, m*) single-species from HiPco-SWCNTs [11].

2. Experimental procedures

HiPco SWCNTs (RØ500, 1.0±0.3 nm, Carbon Nanotechnologies Inc.) were dispersed in 2 wt% SDS (99%, Sigma-Aldrich) aqueous solution with a concentration of 1 mg/ml and sonicated for 20 h using an ultrasonic homogenizer with a power density of 20 W cm^{-2}. To prevent heating during sonication, the bottle containing the sample solution was immersed in a bath of cold water. To remove the residue of catalytic metal particles, nanotube bundles and impurities, the dispersed sample solution was centrifuged at 289,000g for 15 min with an angle rotor (S58A, Hitachi Koki). The upper 90 % of the supernatant was collected for the chirality separation.

Medical plastic syringes (10 ml; 8 cm in length and 1.5 cm in inner diameter) were used as the columns. Allyl dextran-based gel (Sephacryl gel, S-200 HR, GE Healthcare) was used as the medium. Gel columns were prepared by filling 1.4 ml of allyl dextran-based gel beads into syringes. Before filling with gel beads, the outlet of each syringe was plugged with cotton.

Single-chirality separation was performed using a multicolumn gel chromatography method (Fig 2a). In this method, several as-prepared gel columns were vertically connected. After the gel columns were equilibrated with a 2 wt % SDS solution, an excess amount of HiPco-SWCNT dispersion (>5 ml) was loaded. The SWCNT dispersion flowed from one column to another by gravity. The unadsorbed metallic nanotubes were finally collected from the bottom column. The adsorbed semiconducting nanotubes were desorbed and collected from each column by disconnecting the gel column series and injecting a 5 wt % SDS aqueous solution to each of them.

The separated SWCNTs were characterized using optical absorption spectroscopy and photoluminescence (PL) spectroscopy. Optical absorption spectra were recorded using a UV-vis-NIR spectrophotometer (SolidSpec-3700DUV, Shimadzu). PL spectra were measured using a spectrofluorometer (Nanolog, Horiba).

3. Results and discussion

When Sephacryl gel chromatography was used for the separation of SWCNTs, we found the loading amount of HiPco/2%SDS aqueous dispersion had a great in fluence on the chirality distribution of the adsorbed semiconducting nanotubes. As shown in Figure 1a, we loaded the same two gel columns with 1- and 8- ml of HiPco-SWCNT dispersion, respectively. The collected semiconducting SWCNTs were characterized by optical absorption spectra. Results clearly show that, for the 1-ml SWCNT dispersion, the adsorbed semiconducting SWCNTs contain several chiralities and have a wide chirality distribution (Fig 1b); while, for the 8-ml SWCNT dispersion, the adsorbed semiconducting nanotubes exhibit much narrower chirality distribution and are highly enriched with (6, 5) nanotubes. Increasing the loading amount of SWCNT dispersion dramatically enhances the selective adsorption of semiconducting SWCNTs with a specific chirality to the gel. These results indicate that the semiconducting SWCNTs with various structures undergo different interaction with the gel and competitively adsorb to the gel.

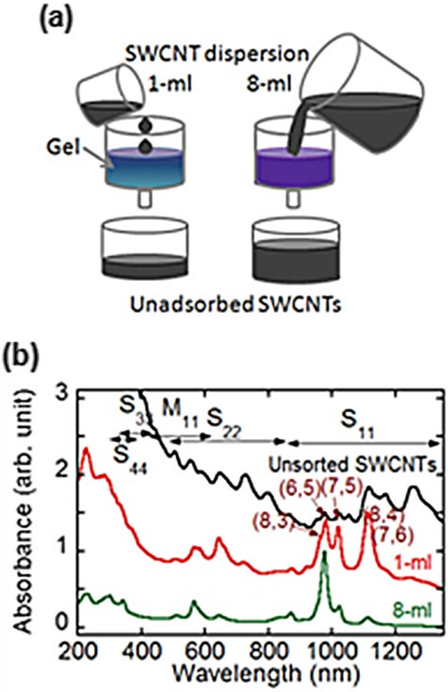

Figure 1. *(a) Schematic diagram of SWCNT separation by loading different amount of SWCNT dispersion to the same two gel columns. (b) Optical absorption spectra of the adsorbed semiconducting SWCNTs.*

As the loading amount of SWCNT dispersion is increased, the nanotubes exhibiting the strongest interaction with the gel replace the other nanotubes and occupy all the adsorption sites in the gel column. A population of nanotubes with identical structure is produced.

On the basis of this finding, we proposed multicolumn gel chromatography (Fig 2a). In this method, several gel columns were vertically connected. As loading an excess amount of the SWCNT dispersion to the multi-stage gel columns (that is, overloading), the nanotubes with the strongest interaction with the gel replace the other nanotubes and adsorb in the first gel column. The unadsorbed nanotubes flow into the second gel column. In this stage, the semiconducting SWCNTs with the second strongest interaction with the gel replace the other nanotubes and adsorb in the second gel column. The same story repeatedly occurs in the following gel columns. In this manner, electronically different semiconducting SWCNTs will be easily sorted across different columns. The metallic nanotubes are finally collected as the unadsorbed nanotubes because they exhibit the weakest interaction with the gel.

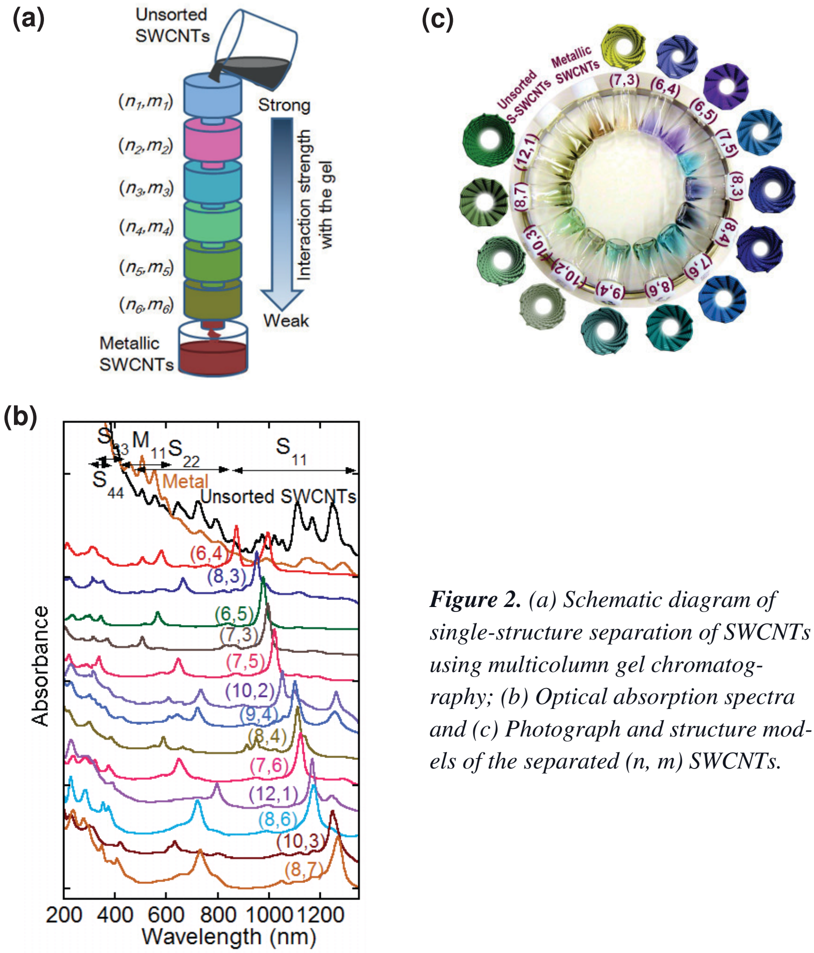

Figure 2. *(a) Schematic diagram of single-structure separation of SWCNTs using multicolumn gel chromatography; (b) Optical absorption spectra and (c) Photograph and structure models of the separated (n, m) SWCNTs.*

Fig 2b shows the optical absorption spectra of the sorted semiconducting SWCNTs by applying multicolumn gel chromatography method to repeatedly separate HiPco-SWCNTs. The spectrum of the finally unadsorbed metallic nanotubes and that of the unsorted HiPco-SWCNT are also presented as references. Each of the sorted semiconducting SWCNTs exhibits a main or single S_{11}, S_{22}, S_{33}, and even S_{44} peak, suggesting that high purity semiconducting SWCNTs fractions with a single chirality were isolated. Totally we successfully separated 13 major (*n, m*) single species from HiPco-SWCNTs. Fig 2c presents the photographs of the isolated (*n, m*) single-chiralities, the separated metallic nanotubes and also the unsorted semiconducting SWCNTs. The colors of these nanotube solutions are well consistent with their optical absorption wavelengths, further confirming the successful separation of single chirality carbon nanotubes. To easily understand the separated (*n, m*) carbon nanotubes, we also present their structure models.

Table 1. *The purity of each (n, m) enriched species*

(*n, m*)	Purity (%)	(*n, m*)	Purity (%)
(7, 3)	89	(8, 6)	89
(6, 4)	46	(9, 4)	46
(6, 5)	93	(10, 2)	39
(7, 5)	88	(10, 3)	69
(8, 3)	56	(8, 7)	68
(8, 4)	63	(12,1)	71
(7, 6)	94	–	–

The purity of the sorted (n, m) SWCNTs is very important in electronic applications. Here, we evaluate the purity of the (n, m) fractions using the method described in Ref. 6; the results are given in Table 1. The highest purity of the sorted (n, m) fractions can be higher than 90%, sufficiently confirming this novel separation technique is highly effective.

Multicolumn gel chromatography technique is based on the structure-dependent interaction strength of the SDS-wrapped SWCNTs with an allyl dextran-based gel. On the basis of the separation index of the (n, m) single species, we can easily conclude that the interaction strength of the SDS-wrapped (n, m) SWCNTs with the gel gradually decreases as the following order: (7, 3), (6, 4), (6, 5), (7, 5), (8, 3), (8, 4), (7, 6), (8, 6), (9, 4), (10, 2), (10, 3), (8, 7) and (12, 1). To clarify the separation mechanism of single-structure SWCNTs, we analyzed the relationships between the interaction strength of (n, m) nanotubes and their chiral angle, diameters and smallest bond curvature radius [12]. As presented in Fig 3, the relationship between the smallest bond curvature radii of the (n, m) nanotubes and the interaction strength exhibit a relatively smooth increasing tendency compared with the relaltionships between interaction strength and chiral angle or diameter, indicating that the nanotubes that interact more strongly with the gel basically have smaller bond curvature radii. Note that the adsorbed semiconducting SWCNTs could be desorbed by injecting 5 wt% SDS aqueous solution. This result suggests that a higher-coverage SDS coating on the nanotubes minimizes their interactions with the gel. The different degrees of SDS coating coverage on the nanotube surfaces scales the interaction strength of each (n, m) single-chirality nanotube with the gel. According to these results, we proposed that differences in the surface π-electron states of the various S-SWCNTs resulting from differing bond curvatures affect the interaction between S-SWCNTs and SDS and cause the variation in the SDS coating coverage, which make the various semiconducting nanotubes have different interaction strength with the gel, inducing the single-chirality separation of SWCNTs.

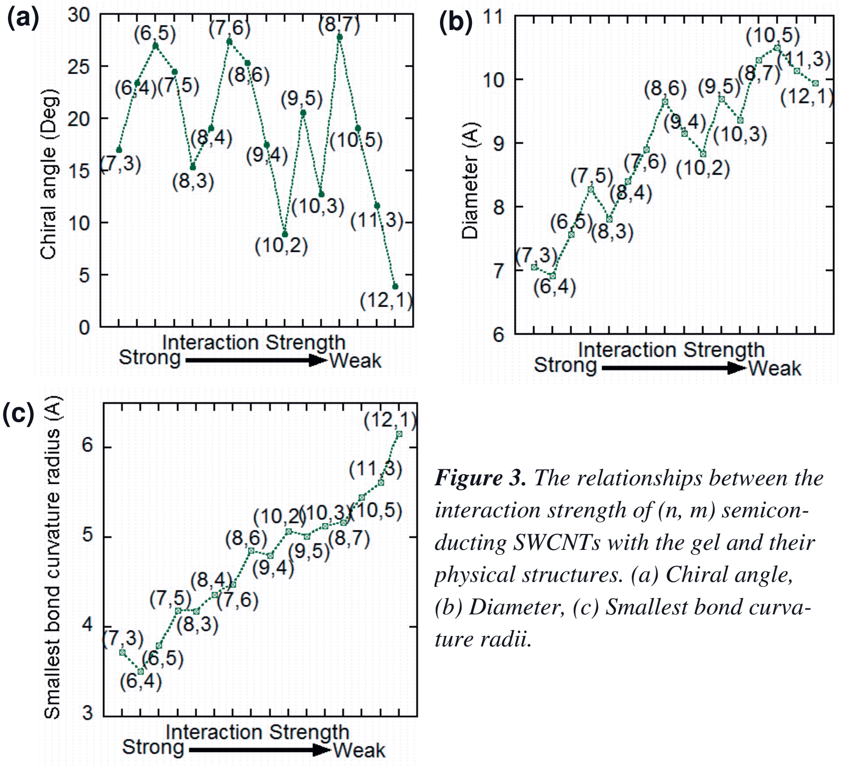

Figure 3. *The relationships between the interaction strength of (n, m) semiconducting SWCNTs with the gel and their physical structures. (a) Chiral angle, (b) Diameter, (c) Smallest bond curvature radii.*

4. Conclusions

We developed a highly effective multicolumn gel chromatography method for single-structure separation of SWCNTs. In the separation method, inexpensive sodium dodecyl sulphate is used as both the dispersant and the eluent of the adsorbed semiconducting SWCNTs. Commercially available allyl dextran-based gel is employed as the medium of columns which can be reused. This novel separation technique permits high-efficiency, lost-cost and industrial separation of single-structure SWCNTs, which will significantly contribute to carbon nanotube industry in future.

References

1. Dresselhaus MS, Dresselhaus G, Avouris P (2001) Carbon Nanotubes Synthesis, Structure, Properties, and Applications. Springer, Berlin
2. Kataura H et al (1999) Optical properties of single-wall carbon nanotubes. Synth Met 103: 2555–2558
3. Avouris P, Martel R (2010) Progress in carbon nanotube electronics and photonics. MRS Bulletin 35: 306–313
4. Arnold MS, Green AA, Hulvat JF et al (2006) Sorting carbon nanotubes by electronic structure using density differentiation. Nat Nanotech 1: 60–65
5. Tu X, Manohr S, Jagota A et al (2009) DNA sequence motifs for structure specific recognition and separation of carbon nanotubes Nature 460: 250–253
6. Tanaka T, Jin H, Miyata Y et al (2009) Simple and scalable gel-based separation of metallic and semiconducting carbon nanotubes. Nano Lett 9: 1497– 1500
7. Tanaka T, Urabe Y, Nishide D et al (2009) Continuous separation of metallic and semiconducting carbon nanotubes using agarose gel. Appl Phys Exp 2: 125002
8. Liu H, Feng Y, Tanaka T et al Diameter-selective metal/ semiconductor separation of single-wall carbon nanotubes by agarose gel. J. Phys. Chem. C 114: 9270–9276
9. Moshammer K, Hennrich F, Kappes MM (2009) Selective suspension in aqueous sodium dodecyl sulfate according to electronic structure type allows simple separation of metallic from semiconducting single-walled carbon nanotubes. Nano Res 2: 599–606
10. Liu H, Nishide D, Tanaka T et al (2011) Large-scale single-chirality separation of single-wall carbon nanotubes by simple gel chromatography. Nat Commun 2: 309
11. Nikolaev P, Bronikowski MJ, Bradley RK et al (1999) Gas-phase catalytic growth of single-walled carbon nanotubes from carbon monoxide. Chem Phys Lett 313: 91-97
12. Li JQ, Jia GX, Zhang YF et al (2006) Bond-curvature effect of sidewall [2+1] cycloadditions of single-walled carbon nanotubes: a new criterion to the adduct structures. Chem Mater 18: 3579-3584

Material Challenges in the Manufacturing of Tailored Structures with Direct Write Technologies

Sini Metsä-Kortelainen, Helena Ronkainen, Tommi Varis, Kimmo Ruusuvuori, Robert Roozeman, Tapio Vehmas, Virpi Kupiainen, Tiina Ahlroos, Juha Lagerbom, and Tomi Suhonen

VTT Technical Research Centre of Finland, P.O. Box 1000, FI-02044 VTT, Finland

Abstract

Two different direct write technologies, Direct Write Paste (DWP) and Direct Write Thermal Spray (DWTS), and the general material challenges related to these technologies are described in this paper. These new technologies open new routes to produce highly functional products that can be tailored and customised according to the demands of the applications. The DWP process is based on dispensing paste-like materials through a tip onto a substrate. Depending on the paste material, either 2 or 3 dimensional structures can be printed. The DWTS technique is based on thermal spraying, which is a spray process where the powder material is accelerated in molten form and impinged onto a surface. Products made using DWTS are especially targeted at harsh environment solutions. Results related to development of printable materials and printed products are presented.

Keywords: *Direct write; Dispensing; Additive manufacturing; Thermal spray.*

1. Introduction

Different Direct Write (DW) technologies have been developed to produce high performance solutions with added value in many kinds of applications. The definition of DW technologies refers to additive manufacturing which can deposit two- or three-dimensional functional structures directly onto flat or conformal surfaces in complex shapes, without any tooling or masks. The products can be tailored and customised according to the demands of the applications and in addition the multi-functionality of the products can be increased. DW technologies enable the integration of multiple manufacturing steps and miniaturisation of the components. Manufacturing with new DW technologies faces challenges that can be overcome by developing and tailoring the materials used in manufacturing to produce reliable and low-cost products with high functionality. This study concentrates on general material challenges related to two different DW technologies, namely Direct Write Paste (DWP) and Direct Write Thermal Spray (DWTS).

W. Udomkichdecha et al. (eds.), *Materials Challenges and Testing for Manufacturing, Mobility, Biomedical Applications and Climate*,
DOI 10.1007/978-3-319-11340-1_6

2. Direct write paste (DWP)

The DWP process is based on dispensing paste-like materials through a tip onto a substrate and it can be used to print antennae, resistors, thermo couples, adhesives, micro-lenses, porous chemical sensors, biological scaffolds and other components and structures. Printing is controlled with a three axis motion system, which utilises CAD approach. The accuracy and repeatability of the XYZ positioning of the dispensing nozzles has a resolution of within a few microns and the system is equipped with a laser scanning system that enables a constant working distance from the surface of the substrate.

The valve technology of the deposition pump generates very precise starts and stops of the printed lines or structures and very fine features starting from 20µm. The functionality of the printed structure comes from the composition of the paste material and its interaction and bonding with the substrate material. The curing of the paste material also affects the properties of the printed structure. Usually the selection of the curing process (e.g. thermal, UV or laser technology) depends on the used paste material, which might also set some limitations for the possible substrate materials.

The properties of the paste material affect the selection of the nozzle (material, shape, size). The inner diameters of the nozzles are between 12.5 µm and a few millimetres. The printing result also depends on several printing parameters, such as speed, pressure, valve opening and printing height.

2.1 Materials for DWP dispensing

The DWP system allows the use of a large variation of dispensable paste materials with a large viscosity scale (1-1,000,000 cps). The materials available include conductive metals, semiconductor and dielectric polymers, ceramics, piezoelectric, ferrites useful to magnetic elements, gels containing living cells and other material types. The paste materials can be deposited onto almost all kinds of substrate materials including metal, plastic, glass, ceramic, paper and even fabrics.

The common requirement for the paste material to be deposited is that the pastes should exhibit a well-controlled viscoelastic response so that they flow through the deposition nozzle and then set immediately in order for them to retain the deposited features. In addition, they must contain a high colloid volume fraction to minimise shrinkage due to drying and to be able to resist compressive stresses arising from capillary tensions (Lewis 2006).

Most of the commercial screen printing paste materials are suitable for DWP printing, but other paste materials can also be developed and tailored. The general requirements for the paste materials are that particles are not very much agglomerated, especially regarding micro particles, and they should be distributed evenly in the paste material. It is highly desirable for the printed paste materials to maintain a constant and controllable cross-section, or to form a predictable and stable 3-D deposition shape.

2.2 DWP experiments and results

The DWP technique is suitable for printing lines or droplets onto flat or 3D surfaces, but building 3D structures by printing is also possible. In this study, different kinds of paste materials were developed and 3D scaffold structures were printed. In addition, the effects of different commercial conductive paste materials and sintering temperatures on the conductivity of printed lines were examined.

2.2.1 Printed scaffolds

New advanced printing technologies open novel routes to building two- or three-dimensional structures and scaffolds for polymeric, ceramic and cementitious materials. In tissue engineering, one of the strong emerging technologies, scaffolds are used to construct artificial organs in vitro before implanting them in vivo. These 3D scaffolds mimic nature's organic components in directing the migration and orientation of the cells in the construct. The same concept of printing 3D scaffolds was used in this work.

Biodegradable polymer pastes were prepared by dissolving poly-caprolactone (PCL) in chloroform. Pastes were sonicated in a water bath and de-aerated before dispensing. Highly volatile solvents like chloroform have the advantage that directly after printing, the solvent on the surface evaporates, leaving a solid polymer skin. This means that the flow of the paste is minimised and the printed structures well retain the printed dimensions. Scaffolds with a constant pore size and gradient architecture were printed at a relatively low printing speed to ensure the evaporation of the solvent of the PCL paste before printing the next layer on the top of the previous one (Figure 1). Scaffolds were ready directly after the printing and natural evaporation of the solvents. PCL paste was quite easy to print, mainly because there were no particles in the paste matrix.

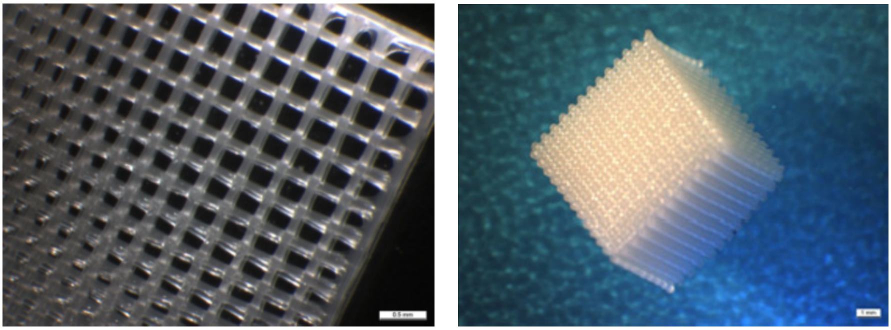

Figure 1. *PCL scaffolds (side length ~5 mm). Gradient structure (left) and 180 layers high with conformal pore size (right).*

Titanium dioxide (TiO_2) pastes were prepared by modifying a formulation for titanium hydride (Ahn et al. 2010). In brief, TiO_2 powder was mixed with a mixture of dichloromethane (DCM), 2-butoxyethanol and dibutyl phthalate and sonicated in a water bath. A polymer solution (poly-acrylate block-polymer in DCM) was then added and the suspension was homogenised and concentrated using a sonicating probe. The printing of ceramic scaffolds was more demanding that polymeric ones because the paste clogged little by little into the printing tip. However, it was possible to produce scaffolds with a few tens of layers (Figure 2). The next step will be the sintering of the ceramic scaffolds to generate solid structures. This will be a two-fold objective: first the polymer is pyrolised and a pure TiO_2 structure is generated. At higher temperatures (~ 1000°C) the individual ceramic particles are merged into a continuous ceramic structure.

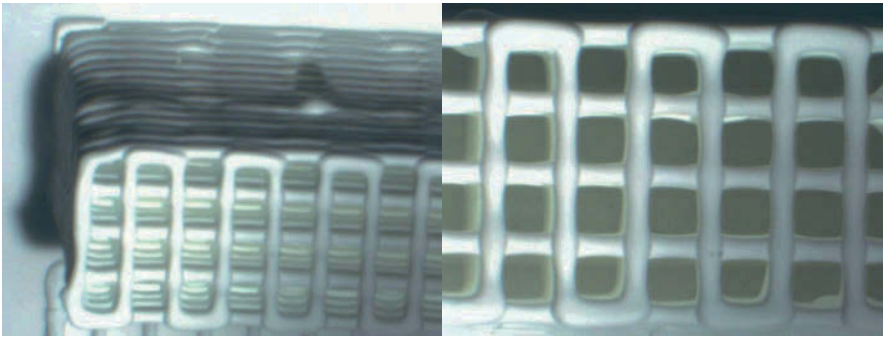

Figure 2. *TiO_2 scaffolds. Pore size ~1 mm x 1 mm.*

Mineral hydration materials can also be used for printable 3D structures. Mineral hydration is an inorganic chemical reaction where water is added to the mineral crystal structure through the dissolution – precipitation process (Bullard et al. 2011). The reaction product is called a hydrate. Ordinary Portland Cement (OPC) hydration is a well-known mineral hydration material used in the construction industry. The main component of OPC, impure tricalciumsilicate, reacts with water producing calcium-silicate-hydrates. Calcium phosphate cement (CPC) is another mineral hydration material which can be used for repairing bones, for example (Liu and Shen 1997). The final product of CPC hydration is hydroxyapatite.

Mineral hydration materials are self-hardening, so there is no need for additional hardening treatment as ceramics, for example need sintering. The hardening process of mineral hydration material is also auto-acceleratory. At the beginning of hydration reaction, the reaction rate is low. When hydration proceeds, the reaction rate increases. This type of behaviour causes a relatively long dormant period at the beginning, where hydrating paste is printable. Because of hydration's auto-acceleratory nature, hardened structures can be attained within 24 hours. The reaction rate of hydration reaction can be easily manipulated with appropriate admixtures (Thomas et al. 2009).

Mineral hydration materials also exhibit limited hardening shrinkage. At the beginning, mineral powder and water have an almost equal volume to that in the final hardened structure. A small amount of hardening shrinkage enables accurate 3D structures.

The biggest problems in mineral hydration materials were encountered in actual printing. Mineral hydration pastes have a natural tendency to segregate. In 3D structures, mineral hydration pastes must have a certain yield stress, but the paste must remain printable. It was found that minimising particle size, optimal dispersion and increased viscosity of liquid phase enabled printable 3D structures with mineral hydration pastes.

With OPC paste optimised according to presented principles, preliminary 3D structures were printed. These structures had a 30MPa compression strength and a total porosity of 30%.

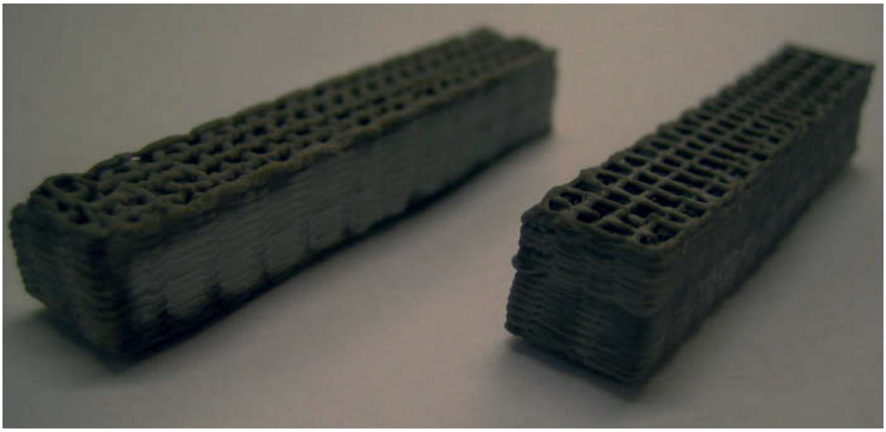

Figure 3. *Printed OPC paste 3D structures (pore size ~2mm x 2mm).*

2.2.2 Conductive lines

The aim of the conductivity measurements was to compare the properties of three silver-based commercial conductive paste materials (DuPont 5028, ANP DGP, Spraylat XCSD-006N) and to study the effect of the curing temperature on the conductivity values. Generally, all three paste materials were suitable for DWP dispensing and the profiles of the printed lines were controllable. Alumina (Al_2O_3) plates were used as substrate materials.

Several parallel lines with each silver paste material were dispensed on the alumina plates. The samples were cured at three different temperatures: 120°C, 300°C and 750°C. The direct current (DC) conductivity was measured using the 4 –point probe method. The cross-sections of the cured lines were determined with a 2D-profilometry.

The results of the DC conductivity measured from 2-4 parallel lines are presented in Figure 4. The conductivity of printed lines is presented as a percentage of the conductivity of the bulk copper. The curing temperature had an effect on the conductivity, since the higher the temperature was, the better the conductivity was. There were also significant differences between different paste materials. The conductivity of XCSD-006N paste was highest after curing at 120°C. When curing at 300°C, ANP DGP nano silver had the highest conductivity values, but conductivity of XCSD-006N dropped significantly. However, at 750°C very good conductivity (>75%) was reached with both 5028 and XCSD-006N. Nano silver paste reached 45% DC conductivity of bulk copper at 750°C.

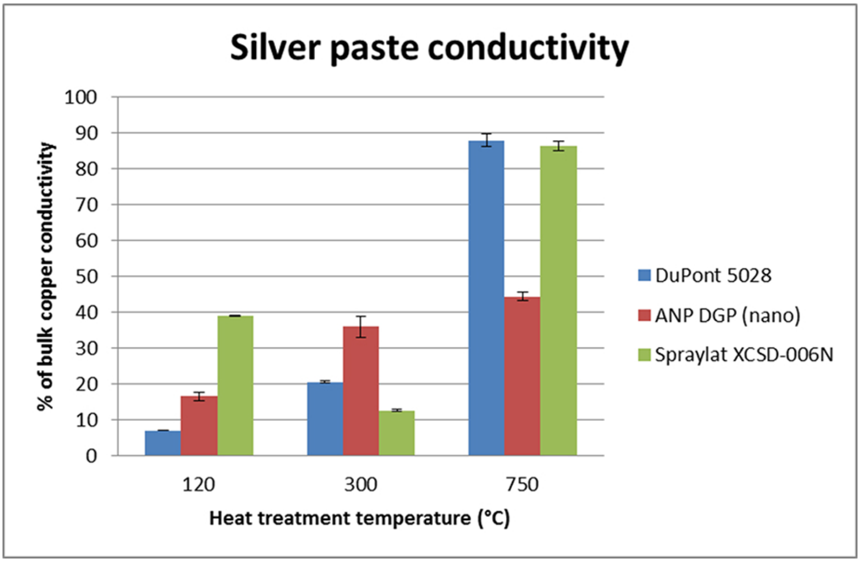

Figure 4. *DC conductivity average values and standard deviations of three silver pastes after three different heat treatment temperatures.*

The material structures of the printed lines were also changed with the higher curing temperatures. The polymeric binder materials were sintered away from the paste and only metallic components were left after sintering at high temperatures (Figure 5). This might have an effect on the functionality of the paste materials in certain applications.

	120°C	**300°C**	**750°C**
ANP DGP			
Spraylat XCSD-006N	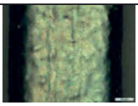	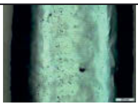	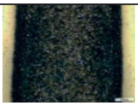

Figure 5. *Microscopic images of conductive lines (width ~200µm) printed with two different pastes materials and cured at 120°C, 300°C and 750°C.*

3. Direct write thermal spray (DWTS)

The DWTS technique is based on thermal spraying, which is a spray process where powder material is accelerated in molten form and impinged onto a surface. A dense and strongly adhered deposit of material is formed by rapid solidification on the substrate surface (Sampath et al. 2002). In DWTS, the material is injected in the powder into a thermal plasma flame, which imparts thermal and kinetic energy to the particles. The deposit is built up by successive impingements of droplets, which are flattened, solidified platelets, or splats. The microstructure and mechanical properties of the deposits are dependent on the process parameters.

DWTS uses a miniature spray gun and an aperture assembly to create fine feature spray depositions (United States Patent, US 6,576,861 B2, 2003). The technique has the ability to spray in a computer-aided pattering way both dielectric and conductive materials directly to the component surface to form conductors, sensors, antenna structures and electromagnetic surfaces, for example. The typical line widths and feature sizes achievable routinely with DWTS are 300 μm; smaller dimensions have also been demonstrated (Sampath 2010). The DWTS deposition process is controlled by a six-axis articulated robot that enables deposition of patterns and features onto non-conformal 3D surfaces.

3.1 Materials for DWTS

By controlling the spray process, a wide range powder of materials can be deposited with DWTS, covering metals, ceramics, polymers, semiconductors and their combinations. The requirement for the powders is that the particle size is very fine, normally between 10-30 μm, to ensure through melting and enable finely detailed structures to be sprayed. These kinds of powders can be manufactured by high pressure inert gas atomisation (metals) and spray drying with high speed rotary nozzle. The DWTS materials undergo a melting and solidification process during deposition and can be used in an as-deposited state without post-treatments. Several dielectric materials can be sprayed for electrical insulation with differing dielectric properties. Typical dielectrics, such as Al_2O_3 and $MgAl_2O_4$, can also be used as protective coatings on layered structures. Typical metals used for electrical components are e.g. copper for conductors and e.g. NiCr and Ni-5%Al for sensor materials (Sampath 2010).

There are several challenges for material development as well as for manufacturing technology that is used to fabricate the desired material. In order to successfully embed the electric circuits on or into the structures, certain prerequisites needs to be met. For example, the electronic structures need to be electrically insulated from the conductive materials of the component. In a similar way, it is viable to cover the electronic structure with a protective layer. The insulating dielectrics need to have high resistivity, high permittivity (close to bulk value) and low dielectric losses. When the electronic structures are fabricated on mechanical components, the insulating layers must also have sufficient mechanical strength. The material properties of the electronic structures need to meet the functional requirements. Conductor material, for example, needs to have high conductivity to e.g. minimize power losses. For wireless communication the radio-frequency (RF) conductivity also has to be sufficiently high to meet the functionality requirements. The functionality requirements are mainly set by the desired application and the manufacturing process and therefore the multi-material structures need to meet the desired lifetime expectations.

The material development and the manufacturing technique are closely related to each other. In order to achieve good material properties, both of them need to be developed and tuned.

3.2 DWTS experiments and results

In thermal spraying, metallic materials are melted or heated and some oxidation will take place during the flight onto substrate and on the substrate. There is a strong need to find a solution to produce metal wiring from cheaper materials, such as copper, without oxidation. In this study, the approach was to compare commercially available copper for DWTS and further develop these powders to achieve better conductivity values. Conductive lines were sprayed with DWTS using three different commercial copper powder materials (Table 1, Figure 6). The DC conductivity of the lines was measured, and it was noted that several parameters influenced the printed structure made using DWTS. One of those is the number of sprayed layers, as thermal spray coatings are normally made by several passes over the surface area. The cross-sections of the printed structures were dependent on the number of sprayed layers, and the powder-feeding parameters also influenced the coating. From the powder side the powder type, morphology and size distribution had the greatest influence on the spray parameters and are thus powder-dependent variables.

Table 1. *DWTS sprayed copper materials.*

Powder	Composition	Structure	Particle size (µm)	Oxide content (w%)
Cu	Cu	spherical	8–15	0,51
Cu(H)	Cu (High purity)	spherical	7–21	0,18
Cu(H2)	Cu heat treated in H2	spherical, contain agglomerates	9–36	0,36

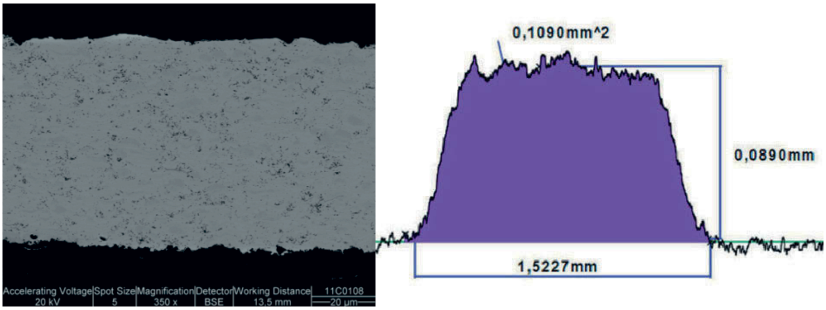

Figure 6. *SEM microstructure of typical DWTS sprayed Cu conductor (left) and a typical Cu line profile cross section (right). Note the magnification x50 and y500.*

The conductivity of sprayed structures is presented as a percentage (%) IACS (International Annealed Copper Standard) of bulk copper conductivity (Figure 7). In general, the increment of the cross-section area from 0,020 to 0,060 mm^2 increased the conductivity of all materials. Above 0,060 mm^2 the effect of the cross-section on the conductivity was not significant. The conductivity of high purity copper with the smallest particle size and oxygen content was highest, while the normal copper reached the lowest values. As summarised, both the powder material and its oxygen content had an effect on the conductivity.

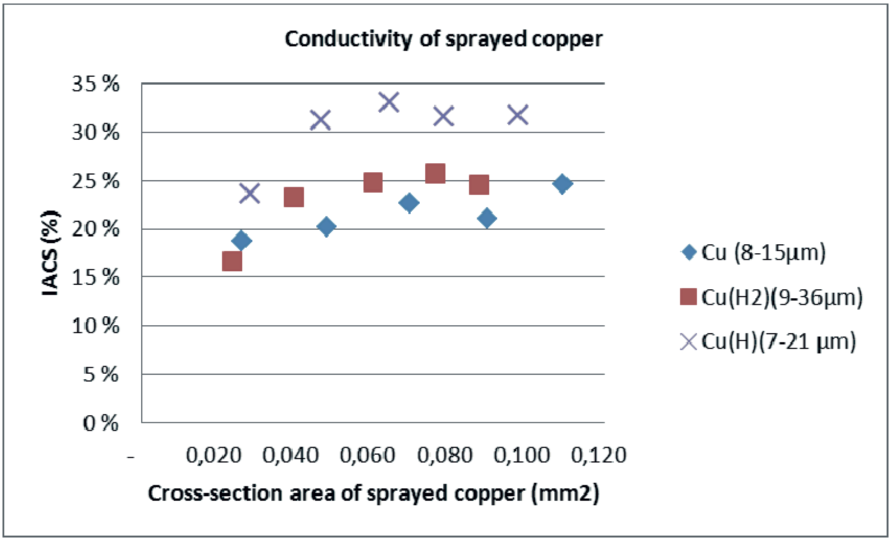

Figure 7. *The effect of the cross-section area of the sprayed material on conductivity (IACS value). Maximum standard deviation (STD) is 1,97 % for the IASC values and 5,76 % for the cross-section values.*

4. Conclusions

Material challenges related to DWP and DWTS technologies differentiate from each other. DWP technology is based on dispensing paste-like materials and DWTS technology is based on thermal spraying, which is a spray process where powder material is accelerated in molten form and impinged onto a surface. Different kinds of paste materials were developed and 3D fine structures were printed with DWP. In addition, the printing of commercial conductive pastes was tested and significant differences between the conductivity values of different paste materials were detected. The sintering temperature also had a remarkable effect on the conductivity. Three different commercial copper materials were sprayed with DWTS and the conductivity of the printed structures was determined. The amount of sprayed layers and the composition of the powder material had a significant effect on conductivity values.

References

1. Ahn BY, Shoji D, Hansen C, Hong E, DunandDC Lewis JA (2010) Printed Origami Structures.Adv Mater 1-4
2. Bullard JW, Jennings HM, Livingston RA, Nonat A, Scherer GW, Schweitzer JS, Scrivener KL, Thomas JJ (2011) Mechanisms of cement hydration. Cem. Concr. Res 41(12): 1208-1223
3. Lewis JA(2006)Direct ink writing of 3D functional materials. AdvFunct Mater 16: 2193–2204
4. Liu C, Shen W (1997) Effect of crystal seeding on the hydration of calcium phosphate cement. J. Mater. Sci. Mater. Med. 8 (12): 803-807
5. Sampath S, Longtin J, Gambino R, Herman H, Greenlaw R Tormey E(2002) Direct-write thermal spray of multilayer electronics and sensor structures. In: Pique A, Chrisey DB Direct-Write Technologies for Rapid Prototyping Applications: Sensors, Electronics, and Integrated Power Sources. Academic Press, USA 261-302
6. Sampath S (2010) Thermal Spray Applications in Electronics and Sensors: Past, Present, and Future. J. Therm. Spray Technol.19(5): 921–949
7. Thomas JJ, Jennings HM, Chen JJ (2009) Influence of Nucleation Seeding on the Hydration Mechanisms of Tricalcium Silicate and Cement. J. Phys. Chem. C. 113 (11): 4327-4334
8. United States Patent, US 6,576,861 B2 (2003) Method and apparatus for fine feature stray deposition. 20p

Fabrication of Three-Dimensional Nanostructured Materials by Interference Lithography and Inversion Process

Sung-Gyu Park, Dong-Ho Kim [1], Kee-Seok Nam [1], Yongsoo Jeong [1], and Paul V. Braun[2]

[1]*Korea Institute of Materials Science, 797 Changwondaero, Seongsangu, Changwon, Gyeongnam, 642-831, Korea*
sgpark@kims.re.kr
[2]*Department of Materials Science and Engineering, Frederick Seitz Materials Research Laboratory, Beckman Institute, University of Illinois at Urbana-Champaign, Urbana, IL 61801, USA*

Abstract

Interference lithography has great potential for simple and rapid production of defect-free, large-area periodic nanostructures. In interference lithography, multi-beam interference produces multi-dimensional intensity profile of light in space. The interference-induced intensity profile can be transferred to photosensitive materials in very short exposure times, typically less than 1 sec. More importantly, interference lithography allows for precise control of the feature size and a variety of lattice symmetries through a proper arrangement of laser beams. In this paper, the fabrication of various polymer nanostructures is demonstrated. Also, 2D gold nanohole array is formed by using interference lithography and Ar ion milling process. Finally, 3D titania inverse structures are generated by sol-gel chemistry reaction, which is very attractive for the simplicity and ease of fabrication. We believe that facile and reliable methods for generating metal or semiconductor nanostructured materials can be applied to photonic sensors and optoelectronic devices.

Keywords: *Interference lithography; 3D nanostructured materials; Optoelectronic devices; Inversion process; Titania*

1. Introduction

Various periodic nanostructures made of semiconductor materials or metals have been studied extensively due to their potential characteristics for high efficiency optoelectronic, photonic, and energy applications. These periodic nanostructures have been developed using various lithographic techniques, including

W. Udomkichdecha et al. (eds.), *Materials Challenges and Testing for Manufacturing, Mobility, Biomedical Applications and Climate*,
DOI 10.1007/978-3-319-11340-1_7

electron-beam lithography, nano-imprint lithography, nanosphere lithography, and soft lithography, which normally allow for only 1D and 2D nanostructures. Recently, 3D nanostructures made of semiconductor materials have been utilized for photonic and optoelectronic devices due to large interfacial area [1]. Therefore, it is essential to make various periodic nanostructures for different applications.

Meanwhile, interference lithography (IL) uses the optical interference of coherent light beams, i.e., laser beams to fabricate defect-free periodic nanostructures in a simple and rapid manner. For example, interference between the two laser beams produces a sinusoidal intensity distribution that can be used to form grating patterns in a photosensitive film. The period of the grating (*P*) is determined by following equation [2]:

$$P = \lambda / 2n\sin\theta \tag{1}$$

where λ is the vacuum wavelength of the exposing laser beam, θ is the angle of intersection of the beams, and n is the refractive index of the photoresist (PR) film in which the interference takes places. In order to make 2D pattern, three laser beams are needed to produce 2D spatial intensity profile. Finally, 3D nanostructures can be made by interference of more than four laser beams. The holographic intensity profile I can be expressed by the general interference equation [3]:

$$I = \sum_{i} \vec{E}_i^{\,2} + \sum_{i<j} \vec{E}_i \bullet \vec{E}_j \cos\left[(\vec{k}_i - \vec{k}_j) \bullet \vec{r} + (\varphi_i - \varphi_j) \right] \tag{2}$$

Therefore, the intensity profile I of the resulting interference pattern can be determined by the electric fields $\boldsymbol{E}_i$, wave-vectors k_i and phase shifts φ_i.

In this paper, the fabrication of various 1D, 2D, and 3D polymer nanostructures via IL is demonstrated. Also, 2D gold nanohole array is formed using dual-beam multiple exposure and Ar ion milling process. Finally, 3D titania inverse structures are generated by sol-gel chemistry reaction, which is very attractive for the simplicity and ease of fabrication. We believe that these facile and reliable methods for generating metal and semiconductor nanostructured materials can be applied to photonic sensors and optoelectronic devices.

2. Experimental

2.1 Materials and experimental procedures

The materials used in IL were epoxy-based resin (EPON SU-8, Miller-Stephenson), cationic photoinitiator (PI, triarylsulfonium hexafluorophosphate salts, Sigma-Aldrich), and solvent (gamma-butyrolactone (GBL), Sigma-Aldrich). The PR film of 400 nm ~ 5 μm in thickness was obtained by spin casting the solution on a substrate and subsequent softbaking at 95 °C to evaporate the solvent. Then, laser was exposed to the PR for 0.1~1 sec. Proper exposure condition was determined by PI concentration and thickness of the PR. After the post-exposure baking process, unexposed regions were removed by PGMEA (propylene glycol methyl ether acetate, Sigma-Aldrich). Rinsing with 2-propanol left behind highly polymerized regions by UV exposure.

In order to make 3D titania inverse structures, we followed the sol-gel chemistry-based infiltration, developed by Bartl [4]. High stability and hydrophobicity of titania precursor enabled planar titania inverse structures. More specifically, the titania sol-gel precursor solution was prepared by adding 2 mL (Aldrich) of titania ethoxide to a mixture of 1.6 mL of trifluoroacetic acid (99%, Aldrich) and 0.4 mL of hydrochloric acid (12 M, Aldrich) while vigorously stirring. After 20 min, 2 mL ethanol and 2 mL ethylene glycol was added to the titania precursor to adjust the viscosity of the solution. In order to prevent overcoat on the 3D template, a thin coverslip was affixed on top of the 3D polymer template and the titania sol-gel precursor was allowed to infiltrate the template via capillary force between the substrate and coverslip. Then, the infiltrated polymer template/titania composite was allowed to dry overnight. After drying, top coverslip was removed. The sample was then calcined in air by raising the temperature slowly (1 °C/min) to 450 °C and keeping it there for 0.5 h. After calcinations process, the crystalline anatase-phase titania inverse structures were formed.

2.2 Generation of various polymer nanostructures

An optical setup for two-beam interference was used to generate 1D grating pattern. The single laser beam (He-Cd laser, 325 nm, 50 mW, Kimmon) with 1 mm diameter is expanded by 10 times through the beam expander, split by beam splitter and recombined on the PR surface. A PR grating pattern was realized by single exposure of the two-beam interference pattern. A 2D square nanohole array was realized by doubly exposing the same interference pattern with sample rotated by 0° and 90°. Likewise, a hexagonal nanohole array was generated by triple exposure with sample rotated by 0°, -60° and 60°.

In order to make 3D polymer nanostructures, we used a specially-designed top-cut fused silica prism whose refractive index is 1.48 at the wavelength of 325 nm. The geometric feature of the prism can be found in previous reports [5-7]. Specifically, three beams designated by wave vectors, k_1, k_2, and k_3 are generated by refraction from three side surfaces of the prism and another beam of wave vector k_0 travels through the top surface of the prism. The four split beams are recombined at the bottom surface of the prism, which sits on top of an SU-8 PR coated substrate.

3. Results

3.1 Generation of one-dimensional polymer grating pattern

Figure 1 shows the top and cross-sectional scanning electron microscopy (SEM) views of 1D SU-8 grating pattern. Highly uniform 1D grating pattern was successfully generated by using simple optical setup. From equation (1), the grating period highly depends on the wavelength of laser (λ = 325 nm), refractive index of SU-8 (n = 1.70 at 325 nm), and the angle (θ) of intersection of two beams. Once the laser wavelength and PR materials are chosen, the grating period can be tuned by the intersection angle of two beams. The grating pattern with period of 770 nm was formed at the intersection angle of 7°. From the high magnification image (Figure 1c), we observed the small ripples on the sidewall. These ripple patterns arise from the interference between incident and reflected laser beams from the reflective silicon substrate. The ripple patterns can be removed by coating an anti-reflection layer on top of silicon substrate or using transparent glass substrate.

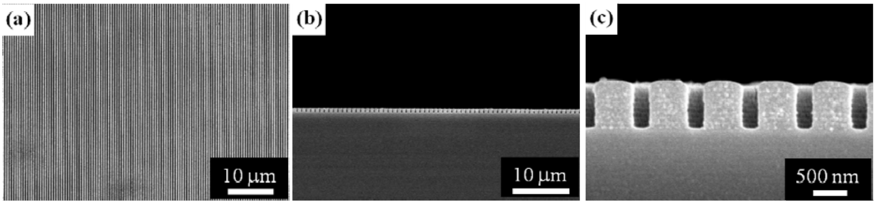

Figure 1. *(a) Top and (b), (c) cross-sectional scanning electron microscopy (SEM) views of 1D SU-8 grating pattern. The grating pattern with period of 770 nm was formed at the intersection angle of 7°.*

3.2 Generation of two-dimensional polymer nanohole array

2D nanostructures can be realized by using the same optical setup for two-beam IL. At this time, the sample should be rotated accordingly for the desired lattice symmetry. For example, a square nanohole array was realized by dual-beam double exposure with sample rotated by 0° and 90° (Figure 2). The square nanohole array with period of 770 nm was formed at the intersection angle of 7°, while nanohole diameter was tuned from 350 nm to 225 nm by exposure dose. The diameter decreases with increasing exposure time for negative PR.

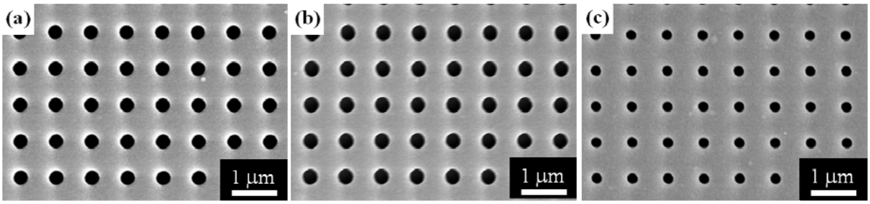

Figure 2. *2D square nanohole array generated by dual-beam double exposure with sample rotated by 0° and 90°. The pitch between nanoholes is 770 nm and the diameters are (a) 350, (b) 300, (c) 225 nm, respectively.*

A hexagonal nanohole array was generated by dual-beam triple exposure with sample rotated by 0°, -60° and 60° (Figure 3). Highly uniform hexagonal SU-8 nanohole array was formed by dual-beam triple exposure. At this time, a hexagonal nanohole array with pitch 450 nm was formed at the intersection angle of 12°. The nanohole diameters were also tuned from 250 nm to 200 nm.

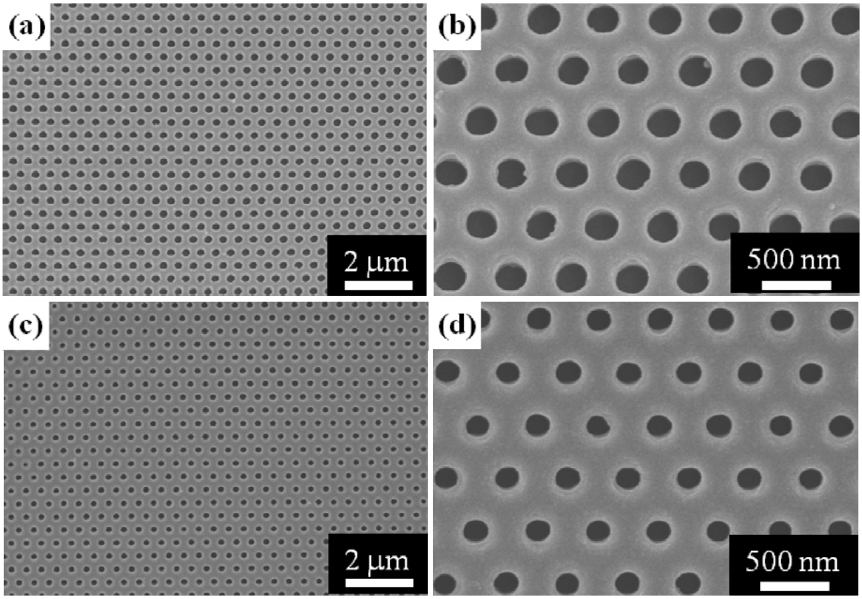

Figure 3. *A hexagonal nanohole array was generated by dual-beam triple exposure with sample rotated by 0°, -60° and 60°. The nanohole diameters are (a), (b) 250, and (c), (d) 200 nm, respectively.*

In order to further utilize dual-beam multiple exposure, Yang group made 3D polymer nanostructures with diamond symmetry via dual-beam quadruple exposure [8]. However, in this case, high accuracy of alignments is needed to make 3D nanostructures. Instead using complicated dual-beam quadruple exposure system or single exposure of four laser beams [9-10], we used a simple optical element (specially-designed top cut prism) to generate 3D polymer nanostructures, as we'll explain shortly.

3.3 Fabrication of gold nanohole array by IL and Ar ion milling *process*

Metallic nanohole array has been extensively utilized for plasmonic sensing applications. Except for bottom-up approaches, electron-beam, focused-ion beam and nano-imprint lithography were used to generate nanohole array [11-15]. However, electron-beam and focused-ion beam lithography are limited to a small area and nano-imprint lithography also requires nano-patterning process. Here, we demonstrate the fabrication of gold nanohole array combining IL and Ar ion milling process. First, 200 nm gold thin film was evaporated onto glass substrate and then SU-8 PR was spincoated on the gold film (Figure 4a).

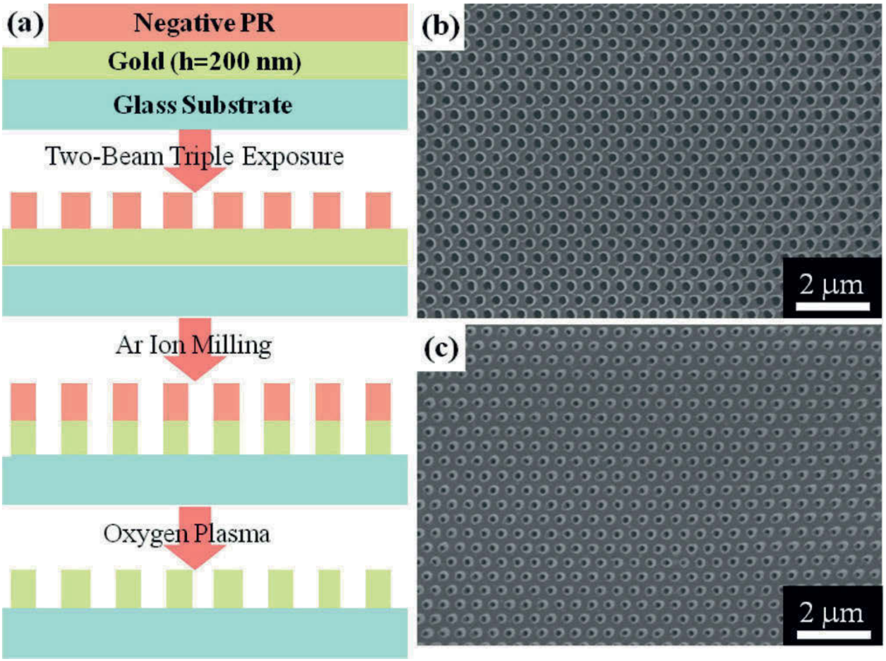

Figure 4. *2D hexagonal gold nanohole array by dual-beam triple exposure and Ar ion milling process. (a) Schematic diagram of process procedure for realizing gold nanohole array. Hexagonally-patterned gold nanohole array with diameter of (b) 250 nm and (c) 200 nm.*

After soft-baking the PR, dual-beam triple exposure of UV laser was performed to make a hexagonal nanohole array. Then, after developing process, Ar ion milling (18W and 6 sccm) was performed to remove the deposited gold for 5 min [16]. Finally, hexagonally-ordered gold nanohole array was formed after removing residual SU-8 by O_2 reactive ion etching (Figure 4b and 4c).

Highly uniform gold nanohole array was formed by simple dual-beam multiple exposure and Ar ion milling process.

3.4 Fabrication of three-dimensional semiconductornanostructures by IL and inversion process

In order to realize 3D nanostructures by IL, one laser beam should be split into four or more interfering beams and the split beams should be also recombined on a PR coated substrate [9-10]. Therefore, the optical setup is bulky and complicated [2, 9-10]. In order to prevent the complexity of optical setup and difficulty of beam alignments, a specially-designed prism was used to generate 3D interference pattern. The geometries of the prism and optical setup can be found in previous reports [5-7]. The tilted SEM image of the polymer template reveals that the unit atom of face-centered cubic (FCC) lattices is elongated to the [111] direction and its interlayer distance is about 0.75 μm (Figure 5a). The polymer template was infiltrated with a hydrophobic and air/moisture stable titania precursor. More specifically, solubilizing titanium-ethoxide in organic/inorganic acid mixtures results in a highly air and moisture stable sol-gel precursor solution and slowing down the condensation kinetics, which enables a very uniform and complete infiltration of titania precursor into SU-8 polymer network. After calcination process, crystalline anatase-phase titania inverse structures with completely open surface and uniform thickness were formed, without the use of additional processing steps such as reactive ion etching and ion milling (Figure 5b). Unlike conformal coating methods such as chemical vapor deposition or atomic layer deposition, this solution-based method provide a simple and easy fabrication process for complete filling of high refractive-index materials into 3D porous template.

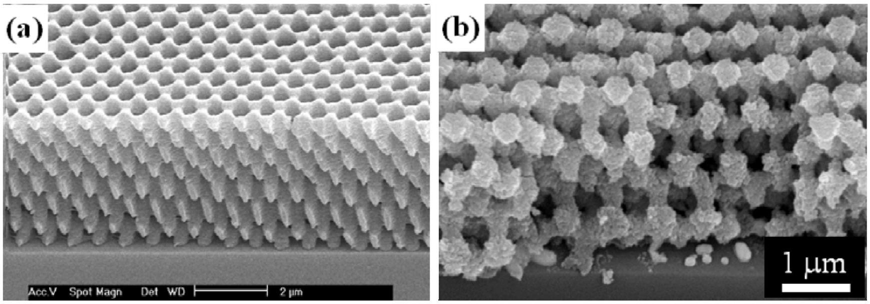

Figure 5. *Tilted SEM image of (a) 3D polymer template with face-centered cubic (FCC) symmetry and (b) 3D titania inverse structures.*

Conclusion

We have demonstrated the versatility of IL for generating various polymer nanostructures. 1D grating pattern was formed by single exposure of the two-beam interference pattern and 2D nanohole array was generated by dual-beam multiple exposure. 2D polymer nanohole array was used as an etch mask for Ar ion milling and uniform gold nanohole array was formed by using IL and Ar ion milling process. Finally, highly uniform 3D polymer nanostructures were fabricated via prism IL and the 3D polymer template was converted into 3D titania inverse structures by sol-gel method. Hydrophobic and air/moisture stable titania precursor was completely infiltrated into hydrophobic SU-8 polymer network. We believe that facile and reliable methods for generating metal or semiconductor nanostructured materials can be applied to photonic sensors and optoelectronic devices.

Acknowledgement

The present research was supported by the research fund (2012-PNK2860) of the Korea Institute of Materials Science, a subsidiary branch of the Korea Institute of Machinery and Materials.

References

1. Jang JH, Ullal CK, Maldovan M, Gorishny T, Kooi S, Koh, CY, Thomas EL (2007) 3D Micro- and nanostructures via interference lithography. Adv Funct Mater 17: 3027–3041
2. Moon JH, Ford J, Yang S, (2006) Fabricating three-dimensional polymeric photonic structures by multi-beam interference lithography. Polym Adv Technol 17: 83–93
3. Lee SK, Park SG, Moon JH, Yang SM (2008) Holographic fabrication of photonic nanostructures for optofluidic integration. Lab Chip 8: 388–391
4. Galusha JW, Tsung CK, Stucky GD, Bartl MH (2008) Optimizing sol−gel infiltration and processing methods for the fabrication of high-quality planar titania inverse opals. Chem Mater 20:4925–4930
5. Park SG, Lee SK, Moon JH, Yang SM (2009) Holographic fabrication of three-dimensional nanostructures for microfluidic passive mixing. Lab Chip 9: 3144–3150

6. Park SG, Moon JH, Lee SK, Shim JW, Yang SM (2010) Bioinspired holographically featured superhydrophobic and supersticky nanostructured materials. Langmuir 26: 1468–1472
7. Park SG, Miyake M, Yang SM, Braun PV (2011) Cu_2O inverse woodpile photonic crystals by prism holographic lithography and electrodeposition. Adv Mater *23*: 2749–2752
8. Liang G, Zhu X, Xu Y, Yang S (2010) Holographic design and fabrication of diamond symmetry photonic crystals via dual-beam quadruple exposure. Adv Mater 22: 4524–4529
9. Campbell M, Sharp DN, Harrison MT, Denning RG, Turberfield AJ (2000) Fabrication of photonic crystals for the visible spectrum by holographic lithography. Nature 404: 53–56
10. Miyake M, Chen YC, Braun PV, Wiltzius P (2009) Fabrication of three-dimensional photonic crystal using multi-beam interference lithography and electrodeposition. Adv Mater 21: 3012–3015
11. Brolo AG, Arctander E, Gordon R, Leathem B, Kavanagh KL (2004) Nanohole-enhanced Raman scattering. Nano Letter 4: 2015–2018
12. Gordon R, Hughes M, Leathem B, Kavanagh KL, Brolo AG, (2005) Basis and lattice polarization mechanisms for light transmission through nanohole arrays in a metal film. Nano Letter 5: 1243–1247
13. Brolo AG, Kwok SG, Moffitt MG, Gordon R, Riordon J, Kavanagh KL (2005) Enhanced fluorescence from arrays of nanoholes in a gold film. J AM CHEM SOC 127: 14936–14941
14. Leebeeck AD, Kumar LK, Lange VD, Sinton D, Gordon R, Brolo AG (2007) On-chip surface-based detection with nanohole arrays. Anal Chem 79:4094–4100
15. Gordon R, Sinton D, Kavanagh KL, Brolo AG, (2008) A new generation of sensors based on extraordinary optical transmission. Acc Chem Res 8: 1049–1057
16. Heo CJ, Kim SH, Jang SG, Lee SY, Yang SM (2009) Gold nanograils with tunable dipolar multiple plasmon resonances. Adv Mater 21: 1726–1731

Effect of Phase architecture on mechanical properties of interpenetrating metal/ceramic composites

Siddhartha Roy[1], Jens Gibmeier[1], Kay André Weidenmann[1], Alwin Nagel[2], Alexander Wanner[1]

[1] Institute for Applied Materials, Karlsruhe Institute of Technology, Kaiserstr. 12, 76131 Karlsruhe, Germany
[2] Aalen University, Beethovenstr. 1, 73430 Aalen, Germany

Abstract

The aim of this article is to compare the influence of the phase architecture on the mechanical properties of two interpenetrating MMCs with same metallic and ceramic phases and similar phase contents. One of the composites was fabricated by infiltrating freeze-cast alumina preforms, while the other composite was fabricated by infiltrating open porous alumina foam. Tests were carried out to determine the three longitudinal elastic constants, elastic-plastic flow behavior under compression and mechanism of internal load transfer under compression. Results show that phase morphology has a significant influence on the composite mechanical properties. Highest stiffness and compressive strengths are observed along the freezing direction in the freeze-cast MMC and this result from the significantly higher fraction of load carried by the alumina phase in this MMC type. Foam based MMC shows more isotropic behavior and its properties lie between the longitudinal and transverse properties for freeze-cast MMC.

Keywords: *Interpenetrating MMC; Freeze-casting; Anisotropy; Load transfer*

1. Introduction

Metal matrix composites (MMC) with a ceramic reinforcement offer good combination of strength, stiffness, creep-, fatigue- and wear resistance at significantly reduced density [1]. These make MMCs attractive in weight critical applications such as in aircraft and automobile industries. Phase architecture is known to have strong influence on the mechanical properties of MMCs. While particle reinforced composites display near isotropic behavior, they show only marginal im-

W. Udomkichdecha et al. (eds.), *Materials Challenges and Testing for Manufacturing, Mobility, Biomedical Applications and Climate*,
DOI 10.1007/978-3-319-11340-1_8

provement in strength and stiffness over the matrix phase. Highest strength and stiffness are observed in continuous fiber reinforced MMCs along fiber direction. However, these composites typically display a pronounced anisotropy, with significantly reduced properties transverse to the fiber direction [2].

In an interpenetrating (IPC) MMC both metallic and ceramic phases are percolating in 3D. These composites, apart from being mostly isotropic, display good combination of strength, stiffness and toughness [3]. In spite of these, IPCs are less studied in comparison to particle and fiber reinforced MMCs. This is mainly due to their complex phase architecture, which makes understanding the mechanics of these composites a challenging task.

This work is aimed at comparing the influence of phase architecture on the mechanical properties of two interpenetrating MMCs with very different microstructures. Both composites were fabricated by infiltrating AlSi12 alloy in open porous alumina preforms. One of the preform types was fabricated by freeze-casting and it had a porous lamellar structure. The other preform type was fabricated by cold isostatic pressing and sintering of a mixture of alumina powder and cellulose fiber and it had an open porous foam structure.

In several recent research papers the authors studied the mechanical properties of these two IPCs separately [4-7]. These studies, although yield valuable information about the mechanics of individual composite materials, this combined study allows directly comparing the influence of phase architecture on the composite mechanical properties. Results are reported from analyses of elastic properties, elastic-plastic flow behavior as well as the mechanism of internal load transfer when loaded externally.

2. Experimental procedure

2.1 Specimen material

Thorough descriptions of the processing route of the studied MMCs have been provided in earlier publications [4, 7]. Microstructures of the two MMC types are shown in Fig. 1 and a very brief description is provided here in order to make it easier for the reader to follow the difference between the two MMCs.

The MMC based on freeze-cast preforms (hereafter named as MMC Type A) consists of a lamellar domain structure in the plane orthogonal to the freezing direction. Within each domain alternating ceramic and metallic lamellae lie parallel to each other. Sizes of the lamellae and the spacings between them strongly depend on the freeze-casting parameters like freezing temperature, ceramic content etc. Numerous ceramic bridges are present between the adjacent lying ceramic lamellae. They enhance the structural stability of the preforms and make them self-supporting. Parallel to the freeze-casting direction the lamellae lie predominantly parallel to the freeze-casting direction. Microstructures of different faces of MMC Type A are shown in [4].

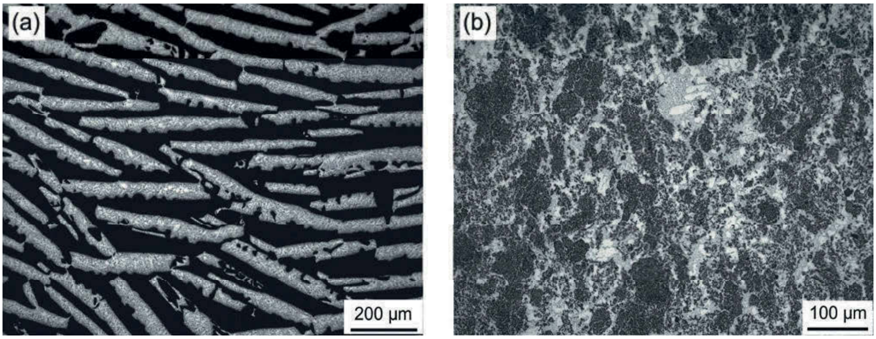

Figure 1. *Optical microstructures of the two MMC types: (a) MMC Type A and (b) MMC Type B*

The MMC based on ceramic foam (hereafter named as MMC Type B) consists of clusters of both alumina and aluminum based alloy AlSi12. The alumina clusters in the uninfiltrated preform had numerous micropores remaining after sintering. These micropores were also filled by the metallic alloy during infiltration. During preform fabrication the mixture of alumina powder and pore former was first uni-axially pressed under 100 MPa pressure. As a result the MMC had different microstructures on different faces. While the plane orthogonal to the press direction has a more random structure; the phases are aligned normal to the press direction in the planes parallel to it. Microstructures of different faces of MMC Type B are shown in [7].

2.2 Elastic analysis

Elastic analysis of the MMC samples was carried out using ultrasound phase spectroscopy (UPS). Thorough description of the technique is given in [8, 9].

Results obtained from measurement of only the three longitudinal elastic constants in several MMC samples of two types are reported here. The samples had rectangular parallelepiped shape with nominal side lengths in the range of 6-9 mm. Measurements were carried out using an electronic network-analyzer R3754A from Advantest, Tokyo, Japan and two identical longitudinal wave transducers of type V122 (central frequency 7.5 MHz and nominal diameter 12.7 mm).

2.3 Analysis of elastic-plastic flow behavior and internal load transfer

Analysis of the elastic-plastic flow behavior of the MMC samples was carried out under external compression using a universal mechanical testing machine from Zwick GmbH & Co. KG, Ulm, Germany at a nominal strain rate of 10^{-3}/s using a load cell with a maximum capacity of 500 kN. Samples for the compression test were rectangular parallelepiped in shape and had nominal dimensions in the range of 7-9 mm.

Mechanism of internal load transfer was studied in-situ under external compression using energy dispersive synchrotron X-ray diffraction (EDXRD). The diffraction experiments were carried out at the materials science beamline EDDI at BESSY, Berlin, Germany. Samples for compression were rectangular parallelepiped in shape with nominal dimensions in the range of 2.5-3 mm. Compression tests were carried out using a miniature mechanical testing device from Kammrath & Weiss GmbH, Dortmund, Germany. 20 µm thick aluminum foil was used between the sample and the hardened steel punches applying external compression to minimize the effects of friction. Tests were carried out at a constant velocity of 2 µm/s, corresponding to a nominal strain rate of 10^{-3}/s. Tests were stopped at different points and the complete diffraction spectrum was acquired by tilting the testing device along with the sample between ψ = 0-89.9°. Lattice strain in all crystalline phases of the MMC samples was measured from the shift of the diffraction peaks and using the peak positions obtained from the sample under only the pre-load before compression test [6, 11].

3. Results and discussions

Fig. 2 shows the plot of longitudinal elastic constants along three orthogonal directions in several MMC samples of the two MMC types as a function of the ceramic content in each sample. In this plot the square symbols correspond to the MMC Type A while the circular symbols correspond to the MMC Type B. C_{xx} (x = 1-3) is the longitudinal elastic constant along direction x. Data points within individual rectangles correspond to same MMC sample. In MMC Type A the direction 1 is the direction of freeze-casting, while in MMC Type b the direction 1 is the direction of uni-axial pressing of the preform prior to sintering. Infiltration of both MMC types was carried out along direction 1.

The figure shows that for similar ceramic content the architecture of the ceramic phase has a strong influence on the longitudinal elastic constants of the MMC. Highest stiffness is observed in MMC Type A along the freezing direction. This results from the mostly continuous ceramic lamellae along the freezing direction in this MMC type. However, this MMC type displays rather strong anisotropy, with significantly reduced elastic constants along directions transverse to the freezing direction (directions 2 and 3). Stiffness along directions 2 and 3 in MMC Type A depend upon the orientation of individual domains and the randomness in their distribution [4]. Although the highest stiffness in MMC Type B is less than that in MMC Type A, the samples are more isotropic. In MMC Type B the lowest stiffness is observed along the direction of preform pressing prior to sintering. This results from the orientation of the ceramic rich clusters orthogonal to this direction. As a result the MMC behaves as transverse isotropic, with stiffness being similar along the two directions transverse to the uni-axial press direction (directions 2 and 3).

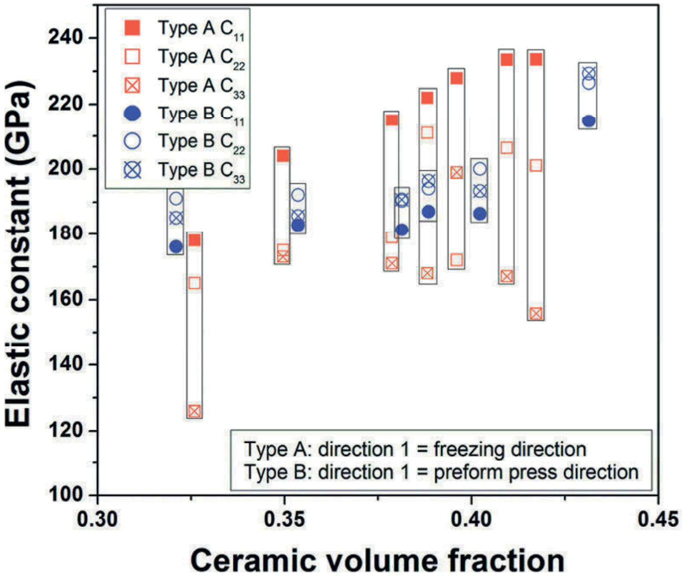

Figure 2. *Effect of reinforcement architecture on the longitudinal elastic constants of the two MMC types*

Fig. 3 shows typical compressive stress-strain plots for the two MMC types. The samples had ceramic content in the range of 35-40 vol.%. For MMC Type A compression tests were carried out both along freezing direction (= longitudinal direction) and transverse to this direction. For MMC Type B compression tests were carried out only along the direction of preform pressing prior to sintering. Typical compression stress-strain plot for unreinforced AlSi12 is also shown in Fig. 3 for reference purpose. The plot shows that the MMC Type A displays pronounced anisotropy. While very high compressive strength (approx. 900 MPa) and limited ductility is observed along the freezing direction, along transverse direction the behavior is more metallic alloy controlled; displaying significant plastic deformation. The compressive stress-strain plot for MMC Type B lies intermediate to the plots for MMC Type A along longitudinal and transverse directions.

Compressive strength of the sample is about 600 MPa and it shows a total strain to compressive failure of about 10%.

Mechanism of progressive compressive damage evolution in the two MMC types was studied in our earlier studies using in-situ compression tests inside scanning electron microscope. When compressed along freezing direction, the principle mode of damage propagation in MMC Type A is longitudinal crushing of the ceramic lamellae. When compressed along transverse direction, damage propagation strongly depends upon the orientation of the ceramic lamellae with respect to the direction of stress application. At orientations in the range of 0-15° the behavior is ceramic controlled, while at orientations between 30-90° the behavior is metallic alloy controlled. Within 15-30° orientation range a transition from ceramic controlled to metallic alloy controlled behavior is observed with increasing lamellae orientation [5]. In MMC Type B compressive damage propagates in the form of shear cracks through the ceramic rich regions and oriented at approximately 45° to the loading direction. The mechanism is similar to that observed within particle clusters in particle reinforced MMCs [11].

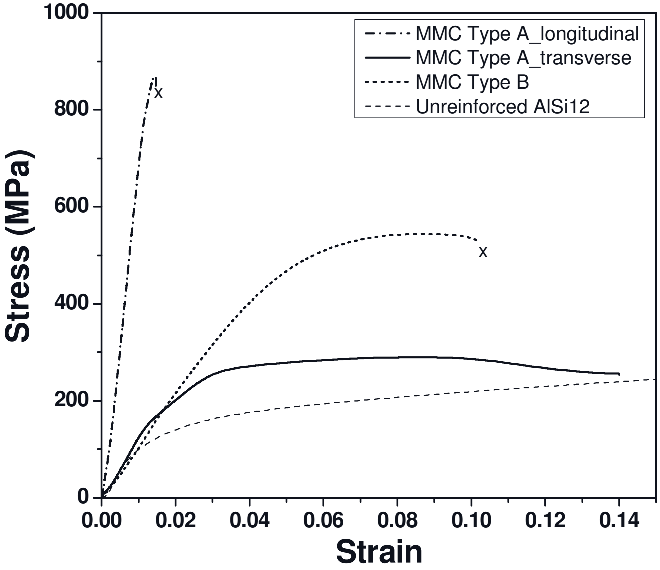

Figure 3. Compressive stress-strain plots for the two MMC types. Plot for unreinforced AlSi12 is shown for reference purpose

Evolution of lattice microstrain in alumina and aluminum solid solution phases of the two MMC types as a function of the applied stress is shown in Fig. 4. The ceramic content of the samples used in this study differed significantly. While, the sample of MMC Type A had 42 vol% alumina, the ceramic content was 31 vol% in the MMC Type B sample. The figure shows that upto an applied compressive stress of 100 MPa, microstrain in both alumina and aluminum solid solution phases in both MMC types increase almost linearly with increase in applied stress. This suggests that upto this point both phases behave elastically. However, at higher applied stresses, in both MMC types the aluminum solid solution lines show an increase in slope, suggesting reduction in load carrying capacity resulting from initiation of plastic deformation in this phase. At all applied stresses the microstrain within the aluminum solid solution phase in MMC Type B is significantly higher than the aluminum solid solution phase in MMC Type A. Correspondingly, the microstrain in the alumina phase in MMC Type A is higher than the alumina phase in MMC Type B. For the same applied stress, the higher the microstrain within a phase, the higher is its load carrying capacity. Hence, these results suggest that in comparison to alumina phase in MMC Type B, alumina phase in MMC Type A carries higher amount of load.

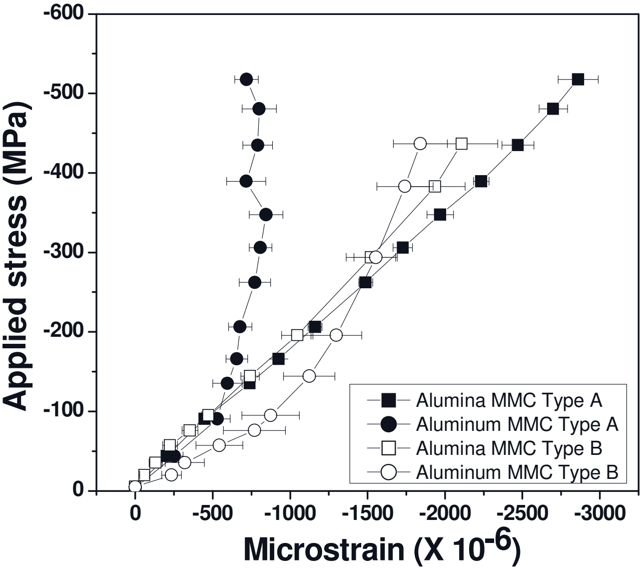

Figure 4. *Microstrain evolution in alumina and aluminum solid solution phases of the two MMC types a s a function of applied stress*

Although the above analysis based on microstrain in each phase is helpful for a qualitative discussion of the internal load transfer, stress in each phase needs to be calculated for a more direct evaluation. For MMC Type A sample the stress in each phase along the loading direction was calculated assuming generalized Hooke's law and ideal laminate theory [10]. For MMC Type B the phase stress along the loading direction was calculated according to elastic stress-strain relations for three-dimensional state of stress and assuming no coupling between normal stress-strain and shear stress-strain [6]. The diffraction elastic constants of each indexed plane were used for stress calculation. To cancel out the effect of different ceramic contents in the two MMC types, further discussion about load carried by the different phases is carried out in terms of load fractions. According to Wanner and Dunand [12] load fraction within a phase can be estimated following the expression

$$l_f = V_f \cdot \frac{\sigma_1}{\sigma_a} \tag{1}$$

where l_f is the load fraction in a phase, V_f is the volume fraction of the phase present within the composite, σ_l is the calculated phase stress along the loading direction and σ_a is the applied stress.

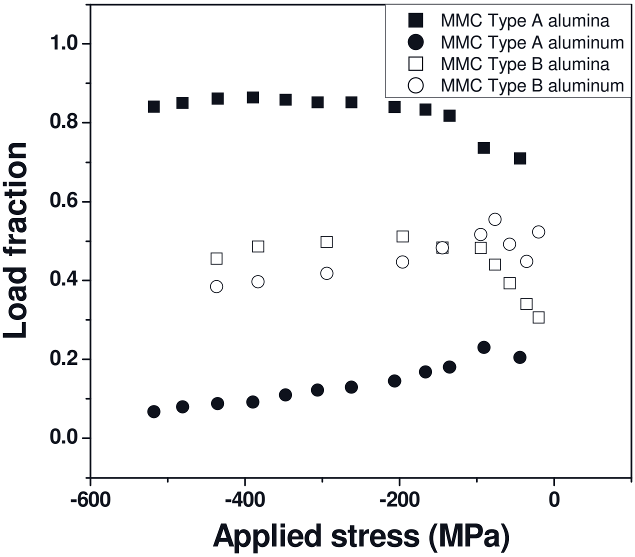

Figure 5. *Calculated load fraction in alumina and aluminum solid solution phases of the two MMC types plotted against the applied stress*

Fig. 5 plots the calculated load fraction in alumina and aluminum solid solution phases of the two MMC types plotted against the applied stress. It is observed that the two MMC types behave very differently. When MMC Type A is loaded along freezing direction, most of the load is carried by the stiffer and stronger alumina phase. Load fraction within this phase reaches about 90% of the applied stress, while the compliant and softer aluminum solid solution phase carries only a minor fraction of load. In contrast, when MMC Type B is loaded along the direction of preform pressing prior to sintering, both alumina and aluminum solid solution phases carry roughly similar fraction of the applied stress. Considering that the ceramic content in MMC Type B was 31 vol%, it still shows that load transfer takes place within MMC Type B from the more compliant aluminum solid solution phase to the alumina phase.

Behavior of a composite under external load depends upon the extent of load transfer from the softer phase to the stiffer load bearing phase. Composite design philosophy for load bearing applications aims for a highest possible load transfer to the stiffer phase through the interface without introducing any damage. The significantly higher fraction of load carried by the alumina phase in MMC Type A along the freezing direction thus explains its higher stiffness and compressive strength in comparison to MMC Type B.

4. Conclusions

Two alumina/AlSi12 interpenetrating composites with similar ceramic contents but different phase architectures were studied in this work. It is observed that phase architecture strongly influences the composite mechanical properties. Highest stiffness and compressive strength are obtained along the freezing direction in the MMC fabricated from freeze-cast preforms. These composites are rather anisotropic, being compliant and softer along transverse direction. The MMC based upon foam preform, although more isotropic, displays reduced stiffness and compressive strength than the freeze-cast MMC. The significantly higher mechanical properties along the freezing direction in the freeze-cast MMC can be explained by the higher fraction of load carried by the alumina phase in this MMC. Load transfer analysis shows that the load fraction within alumina in this composite reaches approximately 90% of the applied stress, while this is only about 50% in the foam based MMC.

Processing of MMCs with varying phase morphologies and analysis of their thermo-mechanical properties will be reported in our future publications.

Acknowledgements

The authors thank T. Waschkies, R. Oberacker and M. J. Hoffmann at IAM-KM, Karlsruhe Institute of Technology for fabricating the freeze-cast preforms. Financial support from German Research Foundation (DFG) under grant number RO 4164/1-1 is thankfully acknowledged.

References

1. Chawla N, Chawla KK (2006) Metal matrix composites. Springer, New York
2. Clyne TW, Withers PJ (1993) An introduction to metal matrix composites. Cambridge university Press, Cambridge
3. Prielipp H, Knechtel M, Clausen N et al (1995) Strength and fracture toughness of aluminum/alumina composites with interpenetrating networks. Mater Sci Eng A 197: 19-30
4. Roy S, Wanner A (2008) Metal/ceramic composites from freeze-cast ceramic preforms: domain structure and elastic properties. Compos Sci Technol 68: 1136–1143
5. Roy S, Butz B, Wanner A (2010) Damage evolution and domain-level anisotropy in metal/ceramic composites exhibiting lamellar microstructures. Acta Mater 58: 2300-2312
6. Roy S, Gibmeier J, Kostov V, Weidenmann KA, Nagel A, Wanner A (2011) Internal load transfer in a metal matrix composite with a three dimensional interpenetrating structure. Acta Mater 59: 1424-1435
7. Roy S, Stoll O, Weidenmann KA, Nagel A, Wanner A (2011) Analysis of the elastic properties of an interpenetrating AlSi12-Al2O3 composite using ultrasound phase spectroscopy. Compos Sci Technol 71: 962-968
8. Wanner A (1998) Elastic modulus measurements of extremely porous ceramic materials by ultrasonic phase spectroscopy. Mater Sci Eng A248: 35-43
9. Roy S, Gebert J-M, Stasiuk G, Piat R, Weidenmann KA, Wanner A (2011) Complete determination of elastic moduli of interpenetrating metal/ceramic composites using ultrasonic techniques and micromechanical modelling. Mater Sci Eng A528: 8226-8235
10. Roy S, Gibmeier J, Wanner A (2009) In situ study of internal load transfer in a novel metal/ceramic composite exhibiting lamellar microstructure using energy dispersive synchrotron X-ray diffraction. Adv Eng mater 11: 471-477
11. Roy S, Gibmeier J, Kostov V, Weidenmann KA, Nagel A, Wanner A (2012) Internal load transfer and damage evolution in a 3d interpenetrating metal/ceramic composite. Mater Sci Eng A551: 272-279
12. Wanner A, Dunand DC (2000) Synchrotron X-ray study of bulk lattice strains in externally loaded Cu-Mo composites. Met Mater Trans 31A: 2949-2960

Mechanical properties of HfB_2 reinforced B_4C matrix ceramics processed by insitu reaction of B_4C, HfO_2 and CNT

K. Sairam, T.S.R.Ch. Murthy, J.K. Sonber, C. Subramanian, R.C. Hubli and A.K. Suri

Materials Group, Bhabha Atomic Research Centre, India 400085

Abstract

Boron carbide and its composites find a wide range of applications such as armour material, p-type semiconductor in electronic industries, as a neutron detectors and absorbers in nuclear industry and as a thermo-electric device for space applications, due to their unique physical, thermal and thermo-electric properties. This work discusses about the development of B_4C-HfB_2 ceramic-ceramic composites. Nearly full dense B_4C-HfB_2 ceramic composites were fabricated by in-situ processing using B_4C, HfO_2 and CNT, as starting materials. The effect of HfO_2 and CNT content on microstructure and mechanical properties of B_4C composite has been investigated. Additions of 2.5 – 30 wt.% HfO_2 and 0.2 – 2.5 wt.% CNT resulted in improvement in density and fracture toughness of the material. On increasing the additive contents, the fracture toughness of the composite increased more than twice that of monolithic B_4C, whereas hardness decreased by about 12%. Elastic Modulus of the composites was measured to be in the range of 570-625 GPa. Crack deflection observed in the composites was found to be the major toughening mechanism due to the existence of residual thermal stress. The maximum value of hardness, fracture toughness and elastic modulus were 36 GPa, 6.6 MPa $m^{1/2}$, and 625 GPa, respectively.

Keywords: *B_4C; CNT; HfB_2; Composite; Mechanical Properties;*

1. Introduction

Monolithic Boron Carbide (B_4C) is a promising candidate material for many high performance applications due to its attractive properties. Conversely, its widespread application in real life is limited due to extreme brittleness and low self-diffusion coefficient [1]. Strong covalent bonding between boron and carbon in B_4C necessitates high temperatures, close to its melting point, for achieving full density. Moreover, rapid grain growth and entrapped residual porosity were observed in the end product at temperatures above 2000°C [2-5].

W. Udomkichdecha et al. (eds.), *Materials Challenges and Testing for Manufacturing, Mobility, Biomedical Applications and Climate*,
DOI 10.1007/978-3-319-11340-1_9

Most of the research activities on B_4C have focused on improving the sintering behaviour and mechanical properties by the addition of different sintering aids. Addition of 1 wt.% CNT to B_4C was found to increase the fracture toughness to 4 $MPa.m^{1/2}$ which is about 1.6 times that of monolithic B_4C [6]. It has been shown that the in-situ reaction of B_4C with MeO (Me= Ti, Zr, Cr, V, Y and Hf) yielded high dense B_4C-MeB_2 composite at lower sintering temperatures with improved mechanical properties compared to monolithic B_4C ceramic [7-16]. B_4C composites containing in situ formed 24 vol.% ZrB_2 have been reported to exhibit a relative density of 98 %TD, as compared to the composites fabricated with pre synthesized ZrB_2 which could reach only 94%TD [15]. Reaction hot pressing of B_4C, TiO_2 and carbon black mixtures yielded a full dense B_4C-15 vol.% TiB_2 composite at 2000°C under 50 MPa pressure for 1 h [17]. In our earlier study, a high fracture toughness value of 7.07 $MPa.m^{1/2}$ was achieved for B_4C-8.9 vol.% HfB_2 composite fabricated by reaction hot pressing of B_4C and HfO_2 for 1 h at 1900°C under a pressure of 40 MPa [16]. In situ synthesis of B_4C-HfC mixture favored the formation of B_4C-10% HfB_2 composite that exhibit a fracture toughness of 5.24 $MPa.m^{1/2}$[18]. Fabrication of B_4C-HfB_2 composite by the reaction between Hf and B_4C have been reported to exhibit improved thermo mechanical properties as compared to monolithic B_4C [19]. In-situ formation of TiB_2 upon addition of TiO_2 to B_4C was found to be more effective than Ti addition because of the formation of substoichiometric compound in the former case [8].

In the present study, B_4C-HfB_2 composites were fabricated by reaction hot pressing a mixture of B_4C, HfO_2 and CNT. The effect of additive content on mechanical properties was examined and compared with the monolithic B_4C.

2. Experimental Procedure

B_4C-HfB_2 composites were fabricated by in situ reaction of boron carbide (B_4C, Purity 96%, particle size D_{50} = 3.7 µm, specific surface area = 3.31 m^2/g), Hafnium oxide (HfO_2, Purity 99%, particle size D_{50} = 5.1 µm, specific surface area = 3.61 m^2/g) and carbon nano tube (CNT, Purity 95%). The starting powder compositions were chosen for the formation of B_4C ceramics containing 0-8.9 vol.% HfB_2 and milled together in a high energy impact mill (MXL 005, Insmart systems, India) for 1 h using WC milling balls (Φ = 6 mm, Insmart systems, India). The following possible reaction was considered for the formation of HfB_2 phase.

$$HfO_2 + (1/2)\ B_4C + (3/2)\ C \rightarrow HfB_2 + 2\ CO \qquad (1)$$

Under standard state conditions, this reaction is thermodynamically feasible at temperatures above 1550°C and their change in free energy is expressed as : $\Delta G = 520.34 - 0.34\ T$ (kJ) [20]. The powder mixture was weighed and loaded into a high density graphite die with a cavity of 17 mm inner diameter and 50 mm height. The die cavity was coated with hexagonal boron nitride (h-BN, ESK Ceramics, Germany) in order to avoid carbon diffusion from the graphite material. Reaction hot pressing was conducted in a high temperature graphite resistance furnace at 1900°C for 1 h with a load of 40 MPa under 10^{-4} mbar pressure. Density of sintered compacts was measured using Archimedes principle. The dense compacts were polished to mirror finish using series of diamond suspensions ranging from 15 µm - 0.5 µm grades (Struers, Denmark). X-ray diffraction (XRD; XRG 3000, Inel, France) was performed with Cu-Kα radiation to identify the crystalline phases and also to determine the lattice parameters of the boron carbide phase. Fracture surface was observed using scanning electron microscopy (SEM; MB 2300 CT/100, CAMSCAN, UK). Vickers hardness and fracture toughness were measured by indentation technique with a load of 1.961 N and 9.807 N respectively and dwell time of 15 s. Anstis methodology [21] was adopted for indentation fracture toughness calculation. Elastic modulus was determined using ultrasonic wave velocity technique (UT 340 pulser receiver system, UTEX Scientific Instrument Inc., Canada). 15 MHz normal beam ultrasonic probe with a sampling rate of 1000 MHz was employed for velocity measurements; $(v_L/v_T) = (2T_{LT}/T_{LL}) - 1$, $E = \rho v_L^2$, where E, ρ, v_L, v_T, T_{LL}, and T_{LT} are elastic modulus (GPa), density (g/cm^3), longitudinal velocity (m/s), transverse velocity (m/s), time of flight of L-L wave (µs) and time of flight of L-T wave (µs) respectively. All the reported data points represent the average of five measured values.

3. Results and discussion

Table 1. *Density and mechanical properties of reaction hot pressed B_4C ceramic upon addition of HfO_2 and CNT at 1900°C under 40 MPa*

Wt.% (CNT + HfO_2)	Measured density (g/cm^3)	Relative density (%)	Hardness H (GPa)	Fracture toughness K_{IC} (MPa.m$^{1/2}$)	Elastic Modulus E (GPa)
0	2.42	96.1	36.80 ± 1.5	2.42 ± 0.2	460 ± 5
(0.21 + 2.5)	2.56	100	35.73 ± 0.4	3.96 ± 0.4	574 ± 12
(0.43 + 5)	2.61	100	34.46 ± 0.8	4.84 ± 0.4	614 ± 3
(0.85 + 10)	2.70	100	34.05 ± 1.2	5.35 ± 0.5	625 ± 5
(1.68 + 20)	2.90	100	33.52 ± 1.3	5.91 ± 0.5	615 ± 10
(2.5 + 30)	3.13	100	32.07 ± 1.1	6.60 ± 0.5	573 ± 15

Table 1 show the density and mechanical properties of reaction hot pressed B_4C ceramic with the addition of HfO_2 and CNT. The minimum addition of 2.5

wt.% HfO_2 along with 0.21 wt.% CNT was sufficient in achieving a nearly full dense B_4C-HfB_2 composite. Similar behavior on relative density was observed when only HfO_2 was added to B_4C. The principle governing the sinterability of B_4C ceramics upon addition of HfO_2 was reported in our earlier work [16]. At high temperatures, the chemical reactivity of B_4C with HfO_2 explains the formation of in-situ HfB_2. The oxygen atom from HfO_2 could react with carbon atoms of B_4C and/or CNT which causes deviations from its stoichiometric conditions. This deviation establishes increased structural vacancies and enhances the diffusion mobility of the constituent atoms and causing lattice distortion. The distortion in lattice in turn enhances the mass transport sintering mechanism which is considered beneficial for sintering and resulted in near theoretical dense B_4C-HfB_2 composites [8,22]. Also, in order to reduce free energy, boron atoms may diffuse into the defect sites available at CNT and that can result in the formation of boron carbide nano rods as reported [23]. CNT that was not consumed in the reduction reaction is left unreacted in the composite as excess carbon [24]. Benefits of nano reinforcements could be realized while measuring the mechanical properties of the sintered composites.

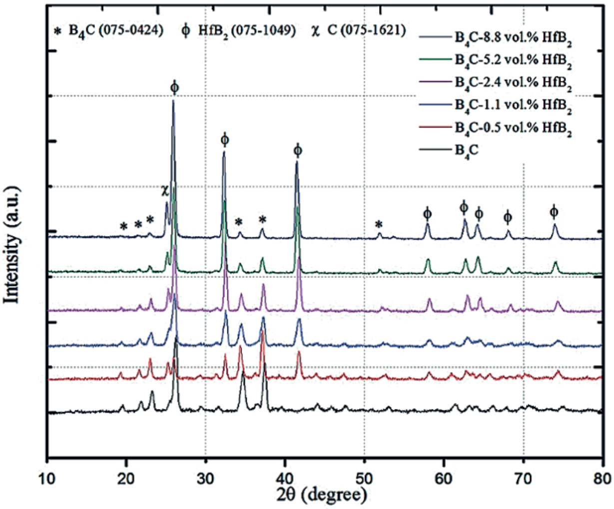

Figure 1. *X-ray diffraction patterns of B_4C matrix ceramics with varying concentration of HfB_2*

Phase identification of monolithic B_4C ceramic show the presence of carbon peak at $2\Theta = 26.25°$ that confirms the existence of free carbon in composite (Fig1). X-ray diffraction pattern reveal the major phases as B_4C and HfB_2 along with residual carbon peak in the resultant B_4C-HfB_2 composites. Moreover, XRD result ensures the completion of reaction (1) by confirming the absence of HfO_2 in the product phase. No net change in lattice parameters of B_4C phase was observed with respect to increasing both HfO_2 and CNT contents. Increase in lattice parameter of B_4C phase was reported when B_4C was added with HfO_2 only, that indicated the depletion of carbon content in B_4C as it was taking part in the reduction reaction [16]. Whereas in the present study, the external addition of carbon in the form of CNT compensates for depletion of carbon in carbide phase and therefore it does not show any effect on lattice parameters (Fig2). It is reported that the carbon addition to B_4C prevented the formation of residual porosities by inhibiting coarsening effects [25] and thereby helps in achieving nearly full density [26]. Addition of only carbon black of 20 nm size to B_4C was reported to exhibit a density of 97.7 %TD by sintering at 2250°C for 2 h [27]. From the above discussion it is clear that the carbon required for reduction reaction (1) can either be CNT, or free carbon available with B_4C or carbon originating from B_4C phase.

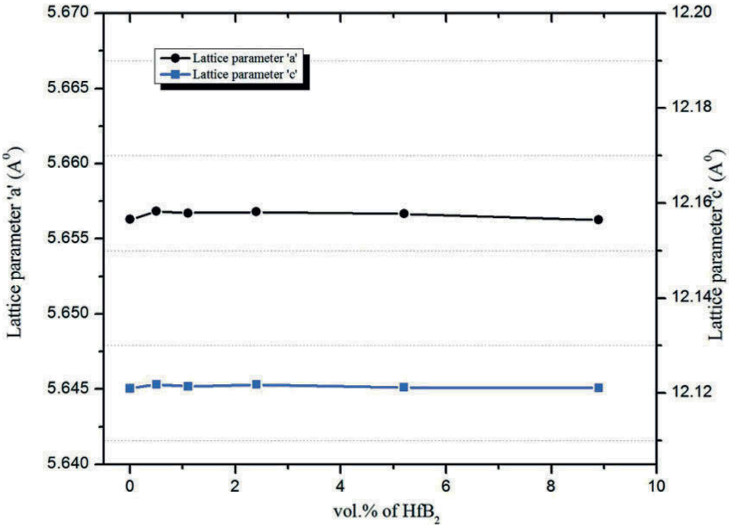

Figure 2. *Variation of lattice parameters of B_4C with respect to HfB_2 content*

Fig3 show the hardness and fracture toughness variations of B_4C matrix ceramics with respect to increasing HfB_2 content. It is observed that the Vickers hardness of B_4C matrix ceramics decreased with increasing the amount of HfO_2 and CNT. Hardness of the composite corresponding to 2.5-30 wt.% HfO_2 and 0.2-2.5 wt.% CNT addition was measured to be in the range of 35.8-32 GPa. This decrease in hardness was due to addition of soft phase (HfB_2) to the hard matrix (B_4C). The magnitude decrease in hardness for currently prepared composite is relatively lower compared to composite obtained from B_4C and HfO_2 [16]. This difference could be attributed due to the presence of residual CNT's in the composite that offers resistance while indentation.

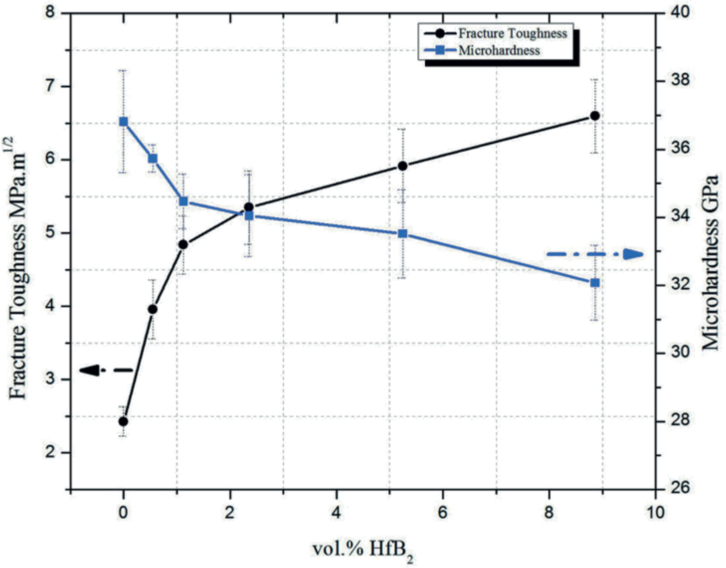

Figure 3. *Variation of hardness and fracture toughness of B_4C matrix ceramics with repect to HfB2 content*

It can be seen that the fracture toughness of the B_4C ceramic increases with increasing addition of both HfO_2 and CNT (Fig3). Similar trend in fracture toughness was observed with reaction hot pressed B_4C-HfB_2 composites fabricated from B_4C and HfO_2 [16]. The highest fracture toughness of 6.6 MPa.m$^{1/2}$ was achieved for the B_4C-HfB_2 composite that are fabricated with 30 wt.% HfO_2 and 2.5 wt.% CNT. The observed increase in fracture toughness is due to the crack tip interaction with thermal residual stress that arises from mismatch in thermal expansion coefficients [28] between B_4C and HfB_2 particles. The crack propagation pattern observed for B_4C-HfB_2 composite reveals crack deflection and crack bridging as the major toughening phenomena (Fig 4a and 4b). The crack deflects as it encounters the region of residual strain or weak interface and takes a longer propagation path that contributes for improving the fracture toughness [16,29]. The bridging effect improves the fracture toughness by lowering tension stress from crack tip and hindering its further propagation [30]. Figure 4a and 4b indicates the distribution of bubble like structures in the B_4C-HfB_2 composites which requires higher resolution microscopic analysis for detailed investigation. Compared to B_4C-8.9 vol.% HfB_2 composite fabricated from B_4C and HfO_2 [16], a slight decrease in fracture toughness from 7.07 MPa.m$^{1/2}$ [16] to 6.6 MPa.m$^{1/2}$ was observed for currently investigated B_4C- 8.9 vol.% HfB_2 composite which is about 6%. The decrease in fracture toughness could be explained based on the dominance of elastic modulus [6] due to presence of unreacted of CNT in the composite.

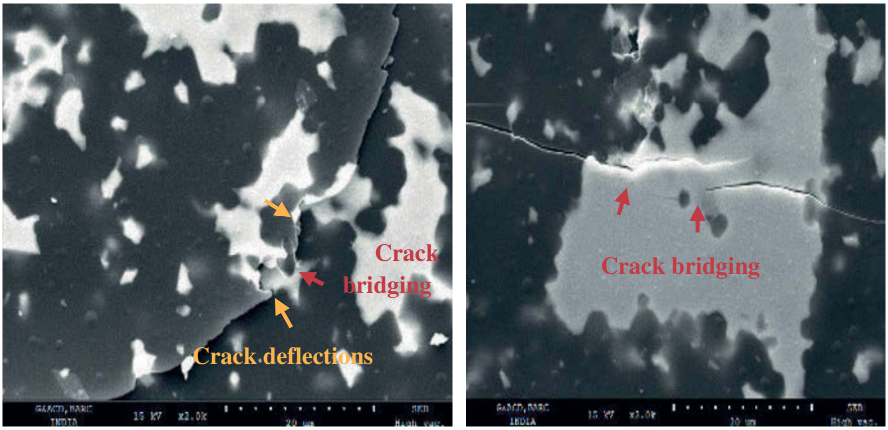

(a) (b)

Figure 4(a) and 4(b). *Scanning electron micrographs of B_4C-8.9 vol.% HfB_2 composite. (a) Crack deflection. (b) Crack bridging.*

The elastic modulus of B_4C and B_4C-1.1 vol.% HfB_2 was measured as 460 GPa and 575 GPa respectively and increased to 625 GPa with increasing HfB_2 content to 2.4 vol.%. Significant difference in modulus of monolithic B_4C and B_4C-HfB_2 composite arise due to the intrinsic elastic modulus of both HfB_2 and CNT. Further increase of additive content decreases the elastic modulus of the composites (Fig5). Similar behavior was reported for the B_4C matrix ceramic with only HfO_2 addition [16].

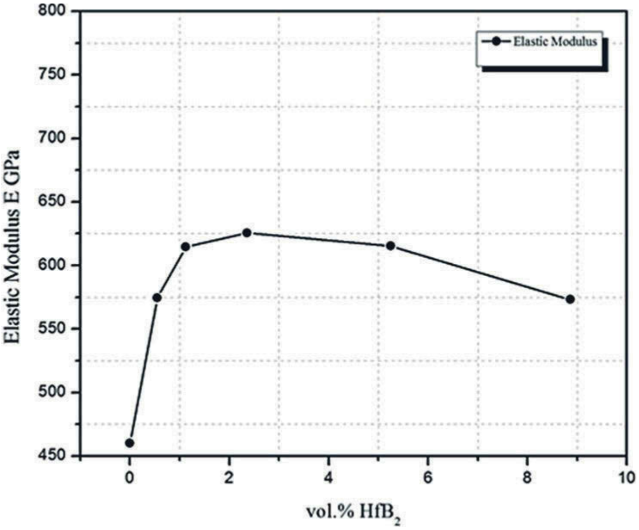

Figure 5. *Effect of HfB_2 addition on elastic modulus of B_4C matrix ceramics measured by ultrasonic pulse-echo technique.*

4. Conclusion

In this study, full dense B_4C-HfB_2 composites were fabricated by insitu processing a mixture of B_4C, HfO_2 and CNT at 1900°C under a load of 40 MPa. The major findings of this study are summarized as follows.

1. No significant effect on lattice parameter of B_4C was observed with respect to addition of varying concentration of HfO_2 and CNT.
2. Hardness of B_4C matrix ceramics decreases from 36-32 GPa upon increasing addition of HfO_2 and CNT. This decrease in hardness was due to the generation of soft phase HfB_2 in the hard matrix B_4C.
3. Fracture toughness of B_4C-HfB_2 composite increases with increasing volume fraction of HfB_2 and exhibits a maximum of 6.6 $MPa.m^{1/2}$ corresponding to 8.9 vol.% HfB_2.
4. Pronounced toughening effect in B_4C-HfB_2 composite can be attributed to the crack tip interaction with residual stress that arise from the mismatch in thermal expansion coefficients of B_4C and HfB_2. Microstructural observation reveals the crack deflection and crack bridging as the toughening phenomena in B_4C-HfB_2 composite.
5. High elastic modulus of 625 GPa was measured for the B_4C-HfB_2 composite fabricated with 10 wt.% HfO_2 and 0.8 wt.% CNT additions.

References

1. Thevenot F (1990) Boron carbide – a comprehensive review. J Eur Ceram Soc 6: 202-225
2. Suri AK, Subramanian C, Sonber JK, Murthy TSRCh (2010) Synthesis and consolidation of boron carbide: a review. Int Mater Rev 55[1]: 4-38
3. Angers R, Beauvy M (1983) Hot-Pressing of Boron Carbide. Ceram Int 10[2]: 49-55
4. Kuzenkova MA, Kislyi PS, Grabchuk BL, Bodnaruk NI (1979) The structure and properties of sintered boron carbide. J Less Comm Met 67[1]: 217-223
5. Dole SL, Prochazka S, Doremus RH (1989) Microstructural coarsening during sintering of boron carbide. J Am Ceram Soc 72[6]: 958-966
6. Zhang F, Fu Z, Zhang J, Wang H, Wang W, Wang Y (2009) Reinforcement of B_4C Ceramics with Multi-walled Carbon Nanotubes. Adv Mater Res 66: 41-44
7. Kim HW, Koh YH, Kim HE (2000) Reaction sintering and mechanical properties of B_4C with addition of ZrO_2. J Mater Res 15[11]: 2431-2436
8. Levin L, Frage N, Dariel MP (1999) The Effect of Ti and TiO_2 Additions on the Pressureless Sintering of B_4C. Met Mater Trans A 30A: 3201-3210

9. Goldstein A, Geffen Y, Goldenberg A (2000) Boron Carbide-Zirconium Boride In Situ Composites by the Reactive Pressureless Sintering of Boron Carbide-Zirconia Mixtures. J Am Ceram Soc 84[3]: 642-644
10. Huang SG, Vanmeensel K, Van der Biest O, Vleugels J (2011) In situ synthesis and densification of submicrometer-grained B_4C-TiB_2 composites by pulsed electric current sintering. J Eur Ceram Soc 31: 637-644
11. Skorokhod V, Krstic VD (2000) High strength-high toughness B_4C-TiB_2 composites. J Mater Sci Lett 19: 237-239
12. Yue XY, Zhao SM, Lu P, Chang Q, Ru HQ (2010) Synthesis and properties of hot pressed B_4C-TiB_2 ceramic composite. Mat Sci Eng A A527: 7215-7219
13. Grigor'ev ON, Koval'chuk VV, Zaporozhets OI, Bega ND, Galanov BA, Prilutskii ÉV, Kotenko VA, Kutran' TN, Dordienko NA (2006) Synthesis and physicomechanical properties of B_4C-VB_2 composites. Powder Mett Metal Ceram 45[1-2]: 47-58
14. Subramanian C, Roy TK, Murthy TSRCh, Sengupta P, Kale GB, Krishnaiah MV, Suri AK (2008) Effect of zirconia addition on Pressureless sintering of boron carbide. Ceram Int 34: 1543-1549
15. Goldstein A, Yeshurun Y, Goldenberg A (2007) B_4C/metal boride composites derived from B_4C/metal oxide mixtures. J Eur Ceram Soc 27[2-3]: 695-700
16. Sairam K, Sonber JK, Murthy TSRCh, Subramanian C, Hubli RC, Suri AK (2012) Development of B_4C-HfB_2 composites by reaction hot pressing. Int J Refr Met Hard Mater 35: 32-40
17. Yamaha S, Hirao K, Yamauchi Y, Kanzaki S (2003) High strength B_4C–TiB_2 composites fabricated by reaction hot-pressing. J Eur Ceram Soc 23: 1123-1130
18. Radev D (2010) Pressureless Sintering of Boron Carbide-based Superhard Materials. Sol State Phenom 159: 145-148
19. Gosset D, Provot D (2001) Boron carbide as a potential inert matrix: an evaluation. Prog Nucl Energy 38[3-4]: 263-266
20. Barin I (1995) Thermochemical Data of Pure Substances. 3rd edition, Wiley-VCH., Weinheim
21. Antis GR, Chantikul P, Lawn BR, Marshall DB (1981) A Critical Evaluation of Indentation Techniques for Measuring Fracture Toughness: I, Direct Crack Measurements. J Am Ceram Soc 64: 533-538
22. Telle R, Petzow G (1988) Strengthening and toughening of boride and carbide hard material composites. Mater Sci Eng A 105/106: 97–104
23. Wie J, Jiang B, Li Y, Xu C, Wu D, Wei B (2002) Straight boron carbide nanorods prepared from carbon nanotubes. J Mater Chem 12: 3121-3124
24. Lee H, Speyer RF (2003) Pressureless Sintering of Boron Carbide. J Am Ceram Soc 86[9] 1468-1473
25. Sigl SL (1998) Processing and Mechanical Properties of Boron Carbide Sintered with TiC. J Eur Ceram Soc 18: 1521-1529

26. Yin BY, Wang LS (2003) Studies on activated sintering of jet milled B_4C powders. Atom Energy Sci Technol 37 (Suppl.): 70-72, 76
27. Zorzi JE, Perottoni CA, da Jornada JAH (2005) Hardness and wear resistance of B_4C ceramics prepared with several additives. Mater Lett 59: 2931-2935
28. Taya M, Hayashi S, Kobayashi AS, Yoon HS (1990) Toughening of a Particulate-Reinforced Ceramic-Matrix Composite by Thermal Residual Stress. J Am Ceram Soc 73[5]: 1382-1391
29. Weiderhorn SM (1984) Brittle fracture and toughening mechanisms in ceramics. Ann Rev Mater Sci 14: 373-403
30. Zhou JP, Gong QM, Yuan KY, Wu JJ, Chen YF, Li CS, Lian Ji (2009) The effects of multiwalled carbon nanotubes on the hot-pressed 3 mol% yttria stabilized zirconia ceramics. Mater Sci Engg A 520: 153-157

Recent progresses in R&D of methods to fabricate inch-sized diamond wafers

Hideaki Yamada, Akiyoshi Chayahara, Yoshiaki Mokuno,

Nobuteru Tsubouchi, and Shin-ichi Shikata

Diamond Research Laboratory, National Institute of Advanced Industrial Science and Technology (AIST), 1-8-31 Midoriga-oka, Ikeda, Osaka 5638577, Japan.

Abstract

To realize industrial use of excellent characteristics of single-crystal diamond, we have developed techniques to fabricate the wafers with inch-size area. Artificial growth of the bulk crystals and a lift-off process to synthesize the freestanding wafers from the seed wafers can be successfully conducted. In this paper, motive forces of our research as well as presented status of related techniques are briefly summarized, as well as our recent progresses.

Keywords: *Single crystal diamond; wide band gap materials; microwave plasma; inch size wafer; lift-off process with ion implantation.*

1. Introduction

Development of alternative energy resources and improvement of power efficiency are common issues all over the world. In the case of the former issues, the renewable energies, such as the solar power, wind power, biomasses and so on are expected to be important candidates, which may reduce use of fossil fuel and limit emissions of carbon dioxide [1]. On the other hand, reduction of the frictional force is one of the common strategies to solve the later issue, because most of all of those energy resources and consumption utilize sliding of wheels and the bearing friction of them directly affect on the power efficiency. As another method to improve the power efficiencies, reductions of power losses which are attributed to performance of electronic devices have been studied. Actually, we have to cool down any electronic devices to avoid thermal runaway, which means certain amount of power is wasted as heat. In addition, we may need additional power for the cooling down, such as power for rotation of fans and circulation of cooling water.

W. Udomkichdecha et al. (eds.), *Materials Challenges and Testing for Manufacturing, Mobility, Biomedical Applications and Climate*,
DOI 10.1007/978-3-319-11340-1_10

Material constants, of which those devices are made, are reflected on the performance of those devices. For example, one may pay attention to the band gap and the mobilities of the carriers of those materials. Breakdown electric filed strength of devices, which is made of a material with low band gap, e.g. Si, is low. Therefore, thickness of the drift layer of those devices must be thick sufficiently for withstanding high voltage. This makes the resistance of those devices high, and makes the power efficiency low. In this point of view, wide-band-gap (WBG) materials, such as SiC and GaN are considered to be important material to realize improvement of the power efficiency [2]. Among such WBG materials, single crystal diamond (SCD) has characteristics superior to those of others [3]; in addition to wider band gap and higher carrier mobilities, thermal conductivity of SCD is also much higher than those of Si, SiC and GaN. Parts of its excellent characteristics were clearly shown recently such as rapid response and stable performance at relatively high temperature [4, 5]. Owing to its extreme material constants, in addition to the use for the power devices, several applications, such as electron sources [6] and X-ray windows [7], have been studied. Realization of industrial use of such applications, it is indispensable to establish techniques to fabricate inch size wafers of SCD artificially. At present, commercialized wafer sizes of Si and SiC are 12 inches (=300mm) and 6 inches (=150mm) in diameter. On the other hand, commercially available size of SCD is only several mm in edge length [8-10].

Actually, at present, most common use of the diamond is the mechanical applications, such as cutting, grinding, polishing, and so on, owing to its mechanical hardness. For this purpose, nowadays, synthetic diamond is produced by several countries and has taken place of natural diamond [11]. Most of those are synthesized by using high-pressure-high-temperature (HPHT) method [8, 12]. This method is well established and can synthesize quite high quality crystal [12]. Because the apparatus is typically quite huge, however, this method is considered to be impractical to fabricate inch sized wafer.

Chemical vapor deposition (CVD) is another way to synthesize diamond artificially. Compared with HPHT method, growth area of chemical vapor depositions can be easily enlarged. Flame deposition may be the most well known CVD method, which can synthesize diamond with relatively high growth rate and quality [13]. To synthesize poly-crystal diamond tools, hot filament CVD is widely used [14]. Number of filaments which are set to be very close to the substrate is heated up which is caused by the Joule heating of those filament. The source gases, typically, plenty of hydrogen with small amount of methane, are dissociated into the radicals due to the heat of the filaments, followed by deposition of them onto the substrate. One of the big advantages of this method is that one may easily enlarge deposition area by increasing the number of the filaments. However, impurities from and carbon materials on the filament, which are generated during the operation, cause certain amount of contamination in the deposited layer. From this reason, this method is considered to be not appropriate for synthesis of the semiconductor grade SCD. In stead of the hot-filament, plasma can be an excitation source of the reactive source gases. One of the simplest ways of plasma CVD is the direct-current (DC) plasma CVD. DC plasma is generated between electrodes and dissociates the source gases. By choosing appropriate condition, one can enlarge deposition area up to 8 inches [15]. However, because this method requires the electrodes which must be close to the substrate in principle, one may afraid the contamination of the CVD layer in this method too. Compared with above methods, diamond can be grown with relatively high growth rate and crystal quality in stable manner by using microwave (MW) plasma CVD [16]. This method does not require electrodes close to the substrate, and therefore, contamination-free deposition is expected. Depending on the frequency of MW, deposition area can be enlarged to approximately ≤2inch (=50mm) and ≤6inch (=150mm) in diameter, when 2.45GHz and 915MHz of MW frequencies are utilized, respectively [17].

Main reason why we do not have large size wafer of SCD is in difficulty to enlarge the seed crystal. Areas of the top surfaces of the seed crystals of Si and SiC can be enlarged during the growth of their bulk crystals. In the case of the SCD, this mode of the growth requires strict control of the growth condition. One may call this method as "α-parameter control", where α is defined as a ratio of the growth rates of [100] direction to that of [111] direction [18]. In Fig. 1(a), arrangement of carbon atoms in SCD is depicted.

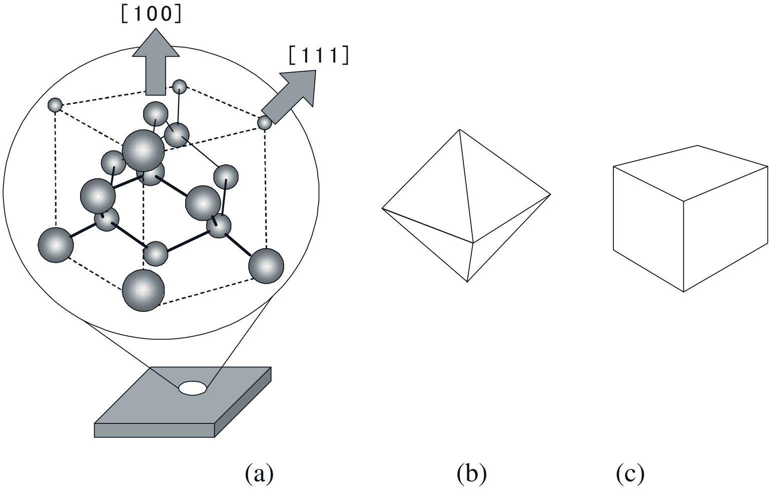

(a) (b) (c)

Figure 1. *(a) We usually use [100] oriented substrate, where carbon atoms are arranged as schematically drawn in the figure. α is defined as a ratio of the growth rate in [100] direction to that in [111] direction. (b) Therefore, if one grows the diamond under condition which gives large α, the area of the top surface shrinks and the crystal become pyramidal shape. (c) To maintain or enlarge the area of the top surface, we have to choose growth condition which gives small α.*

We usually utilize [100] oriented top surface of the SCD seed crystal. Therefore, for the condition which is followed by large α, resultant shape of the crystal is pyramidal as shown in Fig. 1(b) [18, 19]. To enlarge the top surface, we have to choose condition which is followed by low α [18], which maintain or enlarge the area [Fig. 1 (c)]. However, it is known that this condition [20] usually requires extremely low growth rate. This means that extremely long time period of the growth is required to enlarge centimeter size seed crystals into inch size ones. This motivates Mokuno et al., to conduct “3-dimensional growth”, which is described in the following sections, and succeeded in fabricating the half-inch size SCD seed crystal [19]. Furthermore, we have studied “a method to connect SCD substrates” smoothly [21] as described in the following sections too. By using this method, one may be able to enlarge the wafer size efficiently.

Growth of SCD by using MW plasma CVD is affected by many parameters, such as the source gas pressure, imposed MW power, component of the source gas species, and so on. Even the shape of the substrate holder affect the distribution of the plasma, i.e. electron number density, followed by changes of the fluxes of the several radicals which react with the substrate top surface. In practical, it is not easy to optimize such growth condition experimentally due to difficulty to measure plasma parameters. Aiming at understanding mechanism and predicting improved conditions of the growth, we have studied MW plasma numerically [22]. Our progresses in this field are also described in the following sections too. Difficulty is in above mentioned variety of parameters as well as chemistry among the species, where highly reactive hydrocarbon system is taken into account. Furthermore, in principle, atomic scale interactions as well as dynamics of bulk plasma is required to be taken into account. In addition to the chemistry, this “stiff” problem is not easy to treat generally. We have developed an original model to prescribe such MW plasma CVD, and conducted simulation under conditions which are similar to those of actual experiments.

2. Experiments

2.1 Growth and lifting-off

To grow SCD, we use AX-6500 or AX-5200 type MW plasma CVD apparatuses [17]. Source gas pressure and MW power are set to 20kPa and 10kW, respectively. The source gas mixture consists of plenty of H_2 and small amount of CH_4, whose mass flow rates are typically set to 1slm and0.1slm, respectively. In addition, quite small amount of N_2 and O_2 are also introduced. We use [100] oriented seed substrates. The SCD substrate is mounted on the water cooled substrate stage, where the substrate temperature is maintained approximately 10^3 degrees in Celsius during the growth. Usually, ball shape plasma is ignited just above the substrate top surface. Typical growth rate, which is obtained under such condition, is ≲100 μm/hr.

As mentioned in the preceding section, “3-dimensional growth” is conducted, which is schematically drawn in Fig. 2 [19]. After a growth in a [100] direction, a side surface of the substrate is cut and polished so that the side surface is (010) surface [Fig. 2 (a)]. Then, another growth is conducted onto this surface again [Fig. 2 (b)]. After repeating these processes several times, one may have larger area than that of the initial seed substrate [Fig. 2 (c)].

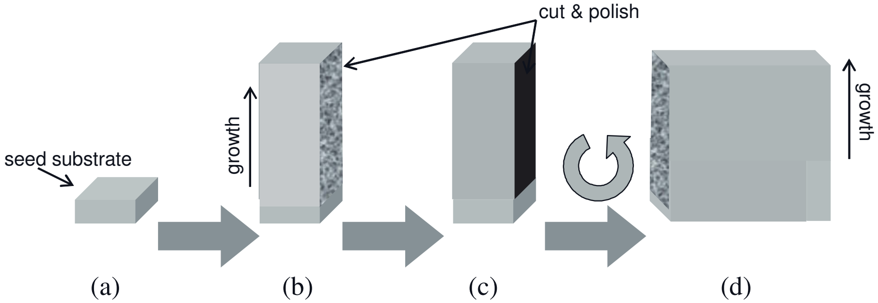

Figure 2. *Procedure to grow a crystal 3-dimensionally (a) initial seed substrate; (b) the crystal after growth in a [100] direction; (c) side surfaces are cut and polished; (d) the crystal after growth in a [010] direction.*

Freestanding wafers are fabricated from such enlarged seed crystal by using high energy ion beam [19]. Ion beam with several MeV of incident energy is irradiated onto the top surface of the substrates, which is followed by generation of graphitic layer beneath the top surface. After growing SCD layer onto this surface, this graphitic layer is removed by selective etching. Then, the SCD is separated from the seed substrate as a freestanding wafer.

2.2 Clones and Tiled-clones

Even by using the 3-dimensional growth, it is still not easy to fabricate inch size wafers from a seed crystal with several mm in edge length in practice; even with 100 μm/hr. of growth rate, it takes more than 500 hours to grow 20mm in three directions. This motivated us to study other way to fabricate inch size wafers efficiently. One of the options is the mosaic wafer. In previous works, which were reported by other groups [23, 24], before our trial, several SCD substrates with relatively small sizes were put together [Fig. 3 (a)]. Then, diamond layers were deposited onto those substartes [Fig .3 (b)]. After that, the small substrates under the deposited layer were removed. However, it is not easy to achieve smooth connection due to mismatching of, for example, crystallographic orientations of the constituent substrates. Furthermore, one may remember that the SCD is not easy to process. Advantage of our approach is in the use of “clone” substrates, which are synthesized from one identical seed crystal [21]. By using the lift-off process with the ion implantation, we can synthesize several freestanding wafers from one identical seed substrate, which have similar characteristics with each other. Therefore, these are expected to be connected smoothly. We shall call such mosaic wafer as “tiled-clones”.

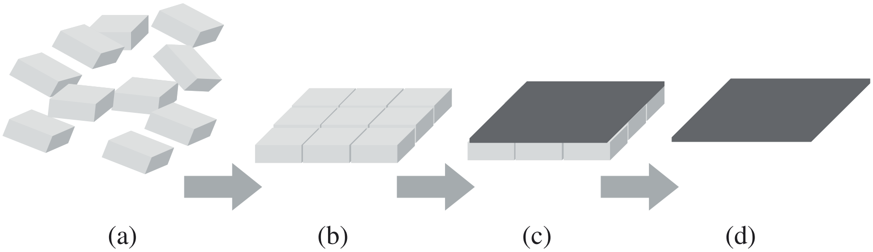

Figure 3. *Procedure to make a mosaic wafer (a), (b), (c). In the case of the “tiled-clones”, all constituent substrates as shown in (a) are “clone” substrates [21].*

We apply the lift-off process with ion implantations on such tiled-clones so that we do not have to remove the seed tiled-clones by polishing or cutting as in the previous works [23, 24]. Therefore, by connecting large sized tiled-clones, we may have several large size freestanding wafers with the same size.

3. Simulations

To understand mechanism of the MW plasma CVD of SCD and find optimized conditions for this, we have studied MW plasma numerically. Difficulty to conduct calculation is in the variety of independent parameters; electromagnetic fields, electron number density, electron temperature, gas temperature, concentration of each atomic/molecular species, flow patterns, and so on. In principle, this means that many governing equations for those parameters must be solved consistently to prescribe bulk plasma. In addition, we have to take into account chemical reactions not only for bulk plasma but also for the surface reactions, whose time scales are much different from that of the dynamics of the bulk plasma. Therefore, it is practically hard to conduct such stiff simulation. To avoid such complexity, we have developed an original model to predict such MW plasma, where the governing equations are reduced into simplified ones under the condition which we are interested in [22]. By using this model, we have conducted simulation under configurations similar to the actual apparatus in 2- or 3-dimensional system and conditions corresponding to the experiments.

4. Results and Discussion

Figure 4 shows fabricated substrates by processes which are described in §2. Substrates with larger than 10 mm in edge length shown in Fig. 4 (a) are freestanding substrates, which are lifted-off from half-inch size seed substrates. From such substrates, clones with 10mm square of area are cut out. Tiled clones made of four clones are shown in Fig. 4 (b). Furthermore, two of these tiled clones are connected into one tiled-clone. Freestanding tiled-clones of SCD with $20 \times 40\text{mm}^2$ of area is shown in Fig. 4 (c). Full-width-half-maxima of X-ray rocking curve spectra and Raman spectra [25, 26] saturate into a certain level in region where is further than 200 μm from the boundaries. Optical transparency was also confirmed where such tiled clones are transparent for wavelength larger than the band-edge [25].

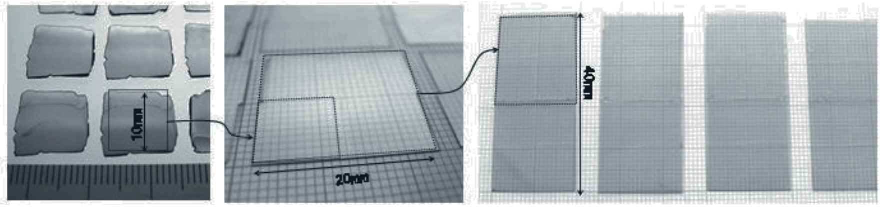

(a) (b) (c)

Figure 4. *(a) half-inch size substrates; they are not tiled-clones (b) 20 mm size and (c) 40mm size tiled-clones.*

Figure 5 shows some results of numerical calculations. Figure 5 (a) shows dependences of the power density as well as the growth rate (experiments) on diameter of the substrate holder, where contours of the calculated power density are shown in the inset. Because the concentration of the plasma is enhanced for small sized holder, the both of them are inverse proportion to the holder size. Therefore, for larger wafer, it is not easy to keep the growth rate higher. Estimated gas temperature is approximately 3000 degrees in maximum just above the top surface of the substrate as shown in Fig. 5 (b). The substrate temperature is 1000 degrees and, there is steep temperature gradient in the distance approximately 10mm. Because of such high gas temperature and relatively high gas pressure as plasma CVD, ≈ 10kPa, thermal reactions are dominant dissociation paths to generate radicals rather than those caused by electron impacts Figs. 5 (b) and (c) show H and

CH_3 distributions which are similar to and much different from that of the gas temperature, respectively. Because in the central region of the plasma, atomic hydrogen is generated, which react with CH_3 to generate CH_4. Therefore, concentration of CH_3 is relatively low in that region and shell like structure. This means that CH_3 is abundant in periphery of the substrate compared with the central region. Sometimes we have high (low) growth rate in central (periphery) region. These results suggest that, in addition to CH_3 which is an important precursor to determine the growth rate, there must be other important factors, such as substrate temperature and concentration of H. Dependences of the growth rate on the contributions of such parameters are left for future work, which requires comparison with experimental results more in detail.

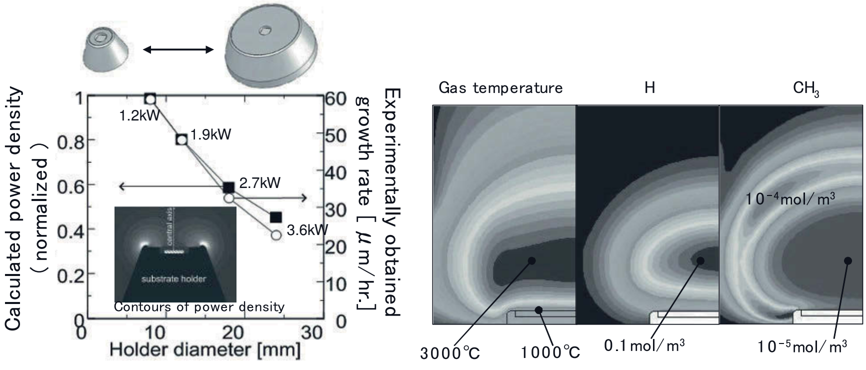

Figure 5. *Numerical results; (a) dependences of the power density on the holder diameter. That of the growth rate, which is obtained by corresponding experiments, are also given; contours of (b) gas temperature, (c) H, and (d)* CH_3*.*

5. Summary

We have developed techniques to fabricate inch size SCD wafers and studied MW plasma CVD of SCD. In addition to the 3-dimensional growth and the lift-off process with ion implantation, use of the tiled-clones accelerates speed to enlarge the wafer size. For fabrication of wafers, however, other important processes such as cutting and polishing must be developed for such a hard material. On the other hand, an improvement of crystal quality is also important. Specification and reduction of the killer dislocations are left for future work. While we recently obtained some distributions of radicals and fundamental comparison with experiments, understanding of MW plasma CVD is not easy. Detailed analyses of the chemistry and specifying dominant paths are left for future work, which may give some important prediction of improved growth conditions.

References

1. IPCC, 2011: IPCC Special Report on Renewable Energy Sources and Climate Change Mitigation, prepared by Working Group III of the Intergovernmental Panel on Climate Change, O Edenhofer, R Pichs-Madruga, Y Sokona, K Seyboth, P Matschoss, S Kadner, T Zwickel, P Eickemeier, G Hansen, S Schlömer, C von Stechow (eds), Cambridge University Press, Cambridge, United Kingdom and New York, NY, USA, 1075 pp
2. Technology of Semiconductor SiC and Its Application, ed. H Matsunami (Nikkan Kogyo Shinbun, Tokyo, 2003) [in Japanese] Chap. 8.
3. S Koizumi, C Nebel, and M Nesladek: Physics and Applications of CVD Diamond (Wiley-VCH, Weinheim, 2008) Chap. 3
4. H Umezawa, Y Mokuno, H Yamada, A Chayahara, and S Shikata (2010) Diamond Relat Mater 19: 208-212
5. T Funaki, K Kodama, H Umezawa and S Shikata (2011) Materials Science Forum 679-680: 820-823
6. T Yamada, P R Vinod, D H Hwang, H Yoshikawa, S Shikata and N Fujimori (2005) Diamond Relat Mater 14: 2047-2050
7. S Shikata, A Chayahara, H Yamada, and H Umezawa (2012) presented at NDNC2012, May 21, USA
8. Sumitomo Electric Industries Ltd. http://www.sumitomoelectricusa.com/products/heatsinks/sumicrystal.html. Accessed 12 July 2012
9. Element Six. http://www.e6cvd.com/cvd/page.jsp?pageid=100&lang=en. Accessed 12 July 2012
10. EDP Corp. http://www.d-edp.jp/index_en.html. Accessed 12 July 2012
11. US Geological Survey. http://www.usgs.gov/. Accessed 12 July 2012
12. H Sumiya and S Satoh (1996) Diamond Relat Mater 5: 1359-1365
13. Y Hirose, S Amanuma, K Komaki (1990) J Appl Phys 68: 6401-6405
14. sp3 diamond technologies Inc. http://sp3diamondtech.com/index.asp . Accessed 12 July 2012
15. K-W Chaeb, Y-J Baika, J-K Parka, W-S Le (2010) Diamond and Related Materials 19: 1168–1171
16. M Kamo, Y Sato, S Matsumoto, and N Setaka (1983) J Cryst Growth 62: 642-644.
17. E Sevillano and B Williams (1998) Diamond Films Technol 8: 73-91
18. C Wild, P Koidl, W Müller-Sebert, H Walcher, R Kohl, N Herres, R Locher, R Samlenski, and R Brenn (1993) Diamond Relat Mater 2: 158-168
19. Y Mokuno, A Chayahara, H Yamada, and N Tsubouchi (2009) Diamond Relat Mater 18: 1258-1261.
20. A Gicquel, F Silva, K Hassouni (2000) J Electrochem Soc 147: 2218-2226
21. H Yamada, A Chahahara, Y Mokuno, H Umezawa, S Shikata, and N Fujimori (2010) Appl Phys Express 3: 051301 (3 pages)

22. H Yamada, A Chahahara, and Y Mokuno (2007) J Appl Phys 101: 063302 (6 pages).
23. M W Geis, H I Smith, A Argoitia, J.Angus, G-H M Ma, J T Glass, J Butler, C J Robinson, and R Pryor (1991) Appl. Phys. Lett. 58: 2485-2487.
24. K Meguro, Y Nishibayashi, and T Imai (2003) SEI Technical Review 163: 53-59 [in Japanese]
25. H Yamada, A Chayahara, Y Mokuno, N Tsubouchi, S Shikata, N Fujimori (2011) Diamond and Related Materials 20: 616-619
26. H Yamada, A Chayahara, H Umezawa, N Tsubouchi, Y Mokuno and S Shikata (2012) Diamond Relat Mater 24: 29-33

Anodic TiO_2 Nanotube Arrays: Effect of Electrolyte Properties on Self Ordering of Pore Cells

Sorachon Yoriya

National Metal and Materials Technology Center, 114 Thailand Science Park, Pahonyothin Road, Klong 1, Klong Luang, Pathumthani 12120, Thailand

Abstract

The formation of self-organized, highly ordered TiO_2 nanotube arrays have been widely studied with an aim to enable precise control of nanotube morphologies and properties. Electrochemical anodization process has attracted considerable attention due to its simplicity, low cost, and reliable fabrication technique for the arrayed nanotubular films. This work presents a facile pathway to achieve the uniform anodic TiO_2 nanotube arrays with open pores through systematically manipulating the synthesis parameters and properly incorporating the solvent additives. Using diethylene glycol containing hydrofluoric acid as the electrolyte model, the conductivity-titanium concentration relation has been investigated, and thus the self ordering regimes in terms of construction architecture of nanopores have been established. The porous structure could be obtained only in the critical range of low electrolyte conductivity of approximately < 100 μS cm^{-1}, while the electrolyte with higher conductivity was found to yield the well ordered nanotube arrays. Formation of the pore cell structures is strongly dependent upon the combination effect of anodization voltage, electrolyte properties and composition.

Keywords: *TiO_2 nanotube arrays; Electrochemical anodization; Electrolyte properties; Self-ordering regimes*

1. Introduction

Vertically oriented TiO_2 nanotube arrays have demonstrated utility in applications including room-temperature hydrogen gas sensing, photocatalysis, generation of hydrogen by water photoelectrolysis, and heterojunction solar cells. [1,2] The

W. Udomkichdecha et al. (eds.), *Materials Challenges and Testing for Manufacturing, Mobility, Biomedical Applications and Climate*,
DOI 10.1007/978-3-319-11340-1_11

performance of such devices is to a large extent determined by the geometrical parameters of the nanotube arrays including wall thickness, pore size, and nanotube length. To a large degree control of the nanotube-array architecture enables control of the functional properties, for example by determining the internal surface area that in turn controls light absorption properties. Due to the great properties in biocompatiblility and hemocompatibility, the titania nanotubes have also attracted considerable attention for use in many biomedical implantable devices, drug delivery, blood clotting, tissue engineering scaffolds, and platforms for bone cell. [3]

The self-organized titania nanotube array films are synthesized by electrochemical anodization of titanium foil generally in fluoride ion containing electrolytes. Over the past decade, the anodization of titanium has grown rapidly through several electrolyte systems ranging from aqueous to non-aqueous electrolytes. [4-10] Tube geometry can vary considerably with the electrolyte chemistry in which the tubes are formed. A proper variation of anodization parameters and fabrication techniques allow achievements to fabricate the titania nanotube array films with superior control over nanotube dimensions; as the ability to precisely control morphology, orientation architecture, and uniformity of nanotubes is necessary to further enhance device performance and application. While there have been many reports on attempts to cover parameter significance, [5,11-13] the driving force for nanotube formation in terms of pore cell orientation have yet to be elucidated. Therefore, this work examines evolution of pore cell architectures, porous towards tubular structure of the titania films using diethylene glycol as a model electrolyte, particularly elucidating details how solvent additives and anodizing parameters affect electrolyte properties, pore/tube cell morphologies and arrangements. This work also presents a reliable manufacturing, facile pathway to achieve the uniform anodic TiO_2 nanotube arrays with a systematic manipulation of anodization parameters.

2. Experimental Procedures

Titanium foils (0.25 mm thick, Sigma-Aldrich 99.7%) were cleaned with acetone, soap, and iso-propanol prior to anodization. Potentiostatic anodization of titanium foils was performed in a two-electrode electrochemical cell using a platinum foil as a counter electrode under room temperature of ~23 °C. The anodization electrolytes were prepared by mixing diethylene glycol (DEG, 99%) with 2% hydrofluoric acid (HF, 48% aqueous solution) and different solvent additives, including formamide (FA, 99.5%), *N*-methylformamide (NMF), hexamethylphophoramide (HMPA, 99%), dimethyl sulfoxide (DMSO, 99.9%), acetyl acetone (Acac, 99%), acetonitrile (AN, 99.8%), formic acid (HCOOH, 96%), acetic acid (HOAc), tetrahydrofuran (THF, 99%), propylene carbonate (PC, 99.7%), methyl acetate (MA, 99%), ethanol (EtOH), and de-ionized water. Relative permittivity (ε) values of these solvent additives are shown in Figure 1. After anodization, the anodized electrolytes were subjected to characterization in terms of electrolyte conductivity and titanium concentration. Electrolyte conductivity was measured by a conductivity meter (YSI 3200, Cole-Parmer). Titanium concentration of the anodized electrolytes were examined by inductively coupled plasma atomic emission spectrometry (ICP-AES, Perkin-Elmer Optima 5300 ICP). Morphologies of nanotubes were examined by a field emission scanning electron microscope (FESEM, Leo 1530 and JEOL JSM-6301F).

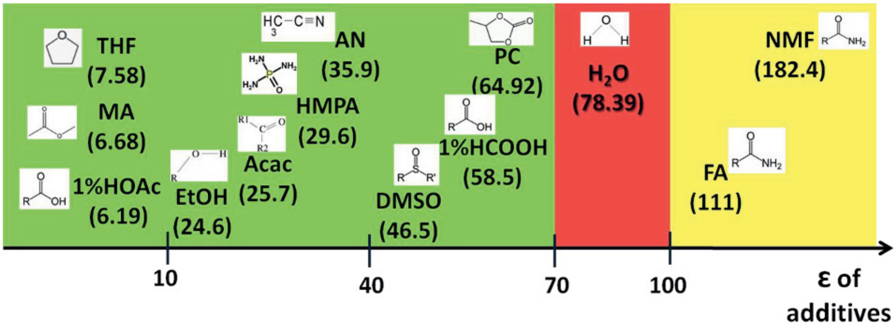

Figure 1. *Solvent additives with their relative permittivity* [14] *shown in the bracket ( ), in this work, are classified into three groups: Group 1 (green)— other solvent additives, Group 2 (red)—Water additive, and Group 3 (yellow)—Formamide additive.*

3. Results and Discussion

Figure 2 shows linear conductivity-titanium concentration relations observed under a variety of anodization conditions, confirming the close relationship between these two parameters. The increased conductivity is due to the increased titanium concentration or the number of predominating titanium ions, including titanium-complex anions (TiF_6^{2-}) in the electrolyte; see Equation (1), and Ti^{4+} migrating from the field-assisted dissolution and the chemical dissolution (oxide etching) of TiO_2 wall. [1-3]

$$TiO_2 + 4H^+ + 6F^- \rightarrow TiF_6^{2-} + 2H_2O \qquad (1)$$

For Group 1, where the low polar solvents were added, the relative permittivity showed no significant effect on the increased conductivity. This could be attributed to the formation of ion pairs occurring in these low conductivity electrolytes. However, it is apparent that the conductivity is directly dependent upon the increased titanium concentration. The similar linear relationship is also seen in Group 2, where the higher relative permittivity solvent like water was added with different contents. With larger water contents, more dissociating ions are available in the electrolyte leading to higher conductivity. Due to the high permittivity and moderate acidity and basicity of water, the force between the opposite charged ions—the cation-anion interaction in electrolyte is overcome, dissociating to separated solvated ions. [4] The higher conductivity due to the greater supply of free ions in the electrolyte in turn induces more charges to be formed on the oxide layer, thus improving extraction of Ti^{4+} ions. Considering H^+ concentration in the tubes in Figure 3, the effect of proton-enhanced dissolution driven by the high water concentration could occur preferentially at the inner oxide wall and consequently lead to the more cell wall etching; [5] the fast pore growth and uniform cell pore alignment are obtained.

The idea of ion dissociation depending upon relative permittivity could also be applied to Group 3, when the high relative permittivity of FA was added into the electrolyte. Addition of FA should allow more free ions forming in the electrolyte that leads to the increased conductivity; however, the dependence of conductivity on the titanium concentration is uncommon for Group 3 compared to those seen in Group 1 and 2. The reflecting high conductivity, independent on the titanium concentration, is probably due to the enhanced effect of ionophore dissociation. The ionophores in the ionic forms arranged in crystalline state may dissociate almost completely into free ions resulting in such high conductivity of electrolyte.

In Figure 2, the self ordering regimes were also established and classified upon the construction of nanopores. From morphological study, the electrolyte conductivity is found to have a significant effect on the degree of nanotube self ordering. For Group 1, the alumina-like nanoporous structure and disordered nanotube arrays were commonly observed in the conductivity range of $< 100\ \mu S\ cm^{-1}$. For Group 2 and Group 3, the relatively high electrolyte conductivities resulted in more uniformly aligned pore cells and well separated nanotube arrays. Due to the high conductivity effect, the pore growth speed is sufficiently high, over each nanotube, to allow homogeneous pore deepening at the metal oxide interface with uniform expansion of the oxide walls. While in low conductivity electrolyte, the oxide growth is limited by ionic movement into the oxide layer, leading to the inconsistent oxide growth and hence irregular pore formation. In other words, the limitation of interface kinetics of oxide growth has a significant effect on individual pore cell enlargement; the disordered pore arrays are obtained.

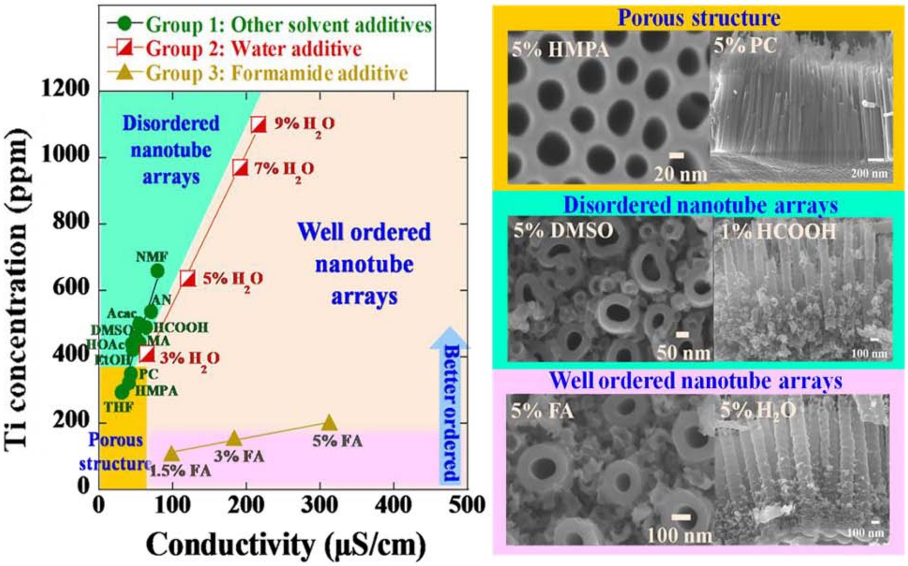

Figure 2. *(Left) Relationship between electrolyte conductivity and titanium concentration of the DEG+2%HF electrolytes mixed with different solvent additives, anodized at 60 V for 24 h. The green solid circle line represents the data of 5% THF, HMPA, PC, EtOH, MA, DMSO, Acac, AN, NMF, and 1% HCOOH and 1% HOAc. The red half-filled square line represents the data of 3-9%* H_2O*. The filled triangle line represents the data of 1.5-5% FA. This figure has been published by the author in J.Mat.Chem.*[15] *(Right) FESEM images showing top/cross-sectional views of titania films obtained from DEG+2%HF electrolytes containing 5% HMPA/5% PC, 5% DMSO/1% HCOOH, and 5% FA/5%*H_2O*, anodized at 60 V for 24 h.*

In addition, x-ray diffraction pattern of the titania nanotube array films has also investigated; the as-anodized films were found amorphous, while the high-temperature annealed films were identified as the crystallized phases, including a predominant anatase (101) and some trace of rutile (110). The annealing conditions used are at 530 °C for 3 h in air ambient and the optimized ramping rate of 1 °C min^{-1}.[16]

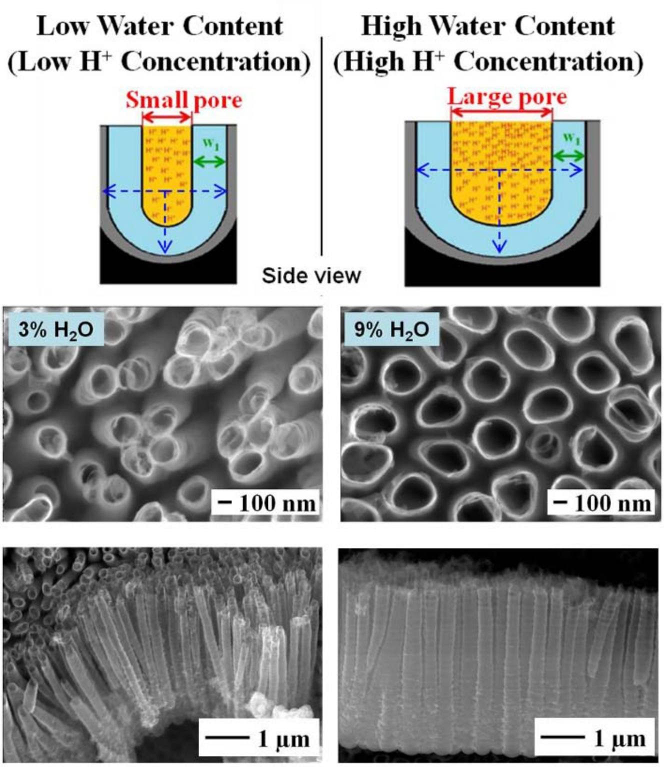

Figure 3. *(Top) Schematic drawings illustrating the effect of water content in terms of* H^+ *concentration on pore cell expansion and (Bottom) FESEM images of titania nanotube array films obtained from the electrolytes containing 3% and 9%* H_2O.

4. Conclusion

Using DEG as model electrolyte, this work has presented a systematic, facile pathway to fabricate the uniform TiO_2 nanotube arrays *via* a reliable manufacturing process of electrochemical anodization. Over a wide range of pore growth architectures, the self ordering regimes have been established covering the formation of porous towards nanotubular structures, clarifying the effect of highly polar solvent additives on the cell wall separation. The work also provides needed insights to the driving force for pore cell arrangement of anodic titania films, elucidating that the cell orientation has a strong relation to the electrolyte properties. With well manipulating the synthesis parameters, it is anticipated that the achieved electrolyte property-nanotube structure relationship will be applicable to the titanium anodization in other non-aqueous electrolytes.

Acknowledgement

The author acknowledges the National Metal and Materials Technology Center (MTEC) for providing facilities and research funding through the Ceramics Technology Research Unit. Partial support of this work through the Material Research Institute, the Pennsylvania State University USA, is also gratefully acknowledged.

References

1. Mor GK, Varghese OK, Paulose M, Shankar K and Grimes CA, (2006) A Review on Highly ordered, Vertically Oriented TiO2 Nanotube Arrays: Fabrication, Material Properties, and Solar Energy Applications. Sol Energ Mat Sol Cells 90:2011-2075.
2. Mor GK, Varghese OK, Paulose M, Mukherjee N, Grimes CA, (2003) Fabrication of Tapered, Conical-Shaped Titania Nanotubes. J Mat Res 18:2588-2593.
3. Grimes CA, Mor GK (2009) TiO2 nanotube arrays: synthesis, properties, and applications. Springer, New York
4. Gong D, Grimes CA, Varghese OK, Hu WC, Singh RS, Chen Z, Dickey EC, (2001) Titanium Oxide Nanotube Arrays Prepared by Anodic Oxidation. J Mat Res 16:3331-3334.
5. Bauer S, Kleber S, Schmuki P, (2006) TiO2 nanotubes: Tailoring the geometry in H3PO4/HF electrolytes. Electrochem Comm 8:1321-1325.
6. Habazaki H, Fushimi K, Shimizu K, Skeldon P, Thompson GE, (2007) Fast Migration of Fluoride Ions in Growing Anodic Titanium Oxide. Electrochem Comm 9:1222–1227.
7. Ruan CM, Paulose M, Varghese OK, Mor GK, Grimes CA, (2005) Fabrication of Highly Ordered TiO2 Nanotube Arrays using an Organic Electrolyte. J Phys Chem B 109:15754-15759.

8. Paulose M, Shankar K, Yoriya S, Prakasam HE, Varghese OK, Mor GK, Latempa TA, Fitzgerald A, Grimes CA, (2006) Anodic Growth of Highly Ordered TiO2 Nanotube Arrays to 134 um in Length. J Phys Chem B 110:16179-16184.
9. Yoriya S, Prakasam HE, Varghese OK, Shankar K, Paulose M, Mor GK, Latempa TJ, Grimes CA, (2006) Initial Studies on the Hydrogen Gas Sensing Properties of Highly-Ordered High Aspect Ratio TiO2 Nanotube-Arrays 20 um to 222 um in Length. Sens Lett 4:334-339.
10. Paulose, M., H. E. Prakasam, O. K. Varghese, L. Peng, K. C. Popat, G. K. Mor, T. A. Desai and C. A. Grimes, (2007) TiO2 Nanotube Arrays of 1000 um Length by Anodization of Titanium Foil: Phenol Red Diffusion. J Phys Chem C 111:14992-14997.
11. Paulose M, Prakasam HE, Varghese OK, Peng L, Popat KC, Mor GK, Desai TA, Grimes CA, (2007) TiO2 Nanotube Arrays of 1000 um Length by Anodization of Titanium Foil: Phenol Red Diffusion. Journal of Physical Chemistry C 111:14992.
12. Ghicov A, Tsuchiya H, Macak JM, Schmuki P, (2005) Titanium oxide nanotubes prepared in phosphate electrolytes. Electrochem Comm 7:505-509.
13. Macak JM, Tsuchiya H, Schmuki P, (2005) High-Aspect-Ratio TiO2 Nanotubes by Anodization of Titanium. Angewandte Chemie-International Edition 44:2100-2102.
14. Tsuchiya, H., J. M. Macak, L. Taveira, E. Balaur, A. Ghicov, K. Sirotna and P. Schmuki, (2005) Self-Organized TiO2 Nanotubes Prepared in Ammonium Fluoride Containing Acetic Acid Electrolytes. Electrochemistry Communications 7:576-580.
15. Izutsu, K., (2002) Electrochemistry in Nonaqueous Solutions Wiley-VCH, New York.
16. Yoriya, S. and C. A. Grimes, (2011) Self-Assembled Anodic TiO2 Nanotube Arrays: Electrolyte Properties and their Effect on Resulting Morphologies. Journal of Materials Chemistry 21:102-108.

Part II
Material Challenges for Mobility Systems

Multiscale Multiphysics Simulations for Development of High Temperature Alloys in Jet Engines

Tomonori Kitashima

National Institute for Materials Science, Ibaraki 305-0047, Japan

Abstract

High temperature materials such as nickel-base superalloys and titanium alloys are used in the compressor and/or the turbine of a jet engine. Multiscale multiphysics simulations to be used for development of such high temperature alloys, which combine theoretical and empirical methods, are described in this paper. In addition, a new phase-field method coupling with the CALPHAD method to simulate gamma-prime precipitation of multicomponent Ni-base superalloys in two dimensions is proposed as part of the multiscale multiphysics simulations. This phase-field method demonstrates both diffusion-controlled precipitate growth under local equilibrium at phase interfaces and precipitation interaction such as coalescence.

Keywords: *Alloy Development, Multicomponent, Multiscale Multiphysics, Jet Engine.*

1. Introduction

High temperature materials such as nickel-base superalloys and near-alpha titanium alloys are used in the compressor and/or the turbine of a jet engine. These alloys are exposed to the severe environment in an engine under the condition of high temperature and high stress. Increasing the temperature capability of these alloys leads to an improvement in the thermal efficiency of the jet engine, which results in a reduction of CO_2 gas emission and fuel consumption. Therefore, the development of materials with high temperature capabilities is sought by engine makers and airlines.

In order to design and develop new alloys which meet the requirement of engine makers and airlines, it's necessary to consider several properties such as creep, yield strength, oxidation, low-cycle fatigue, etc. However, it is complicated

W. Udomkichdecha et al. (eds.), *Materials Challenges and Testing for Manufacturing, Mobility, Biomedical Applications and Climate*,
DOI 10.1007/978-3-319-11340-1_12

and time-consuming to develop these alloys for practical use because they are multicomponent systems which contain six to ten elements. To my knowledge, the microstructures and mechanical properties of these alloys have been predicted mainly using empirical formulae. To develop the alloys more logically and to improve properties further, multiscale multiphysics simulation methods have been developed.

I have carried out modeling and development of nickel-base superalloys and titanium alloys. The present article describes how such high temperature materials can be developed using multiscale multiphysics simulations. One of the difficulties of developing these simulation methods is to understand the effects of element interactions on the microstructure and the properties in multicomponent systems. As for gamma prime precipitation in Ni-base superalloys, there have been few reports on its simulation in multicomponent systems because of complexity associated with deriving the Gibbs free energy surface for multicomponent systems. In this paper, a new phase-field method coupling with the CALPHAD method for the gamma-prime precipitation is proposed using a single function formalism of gamma and gamma prime phases. In addition, there have been few modeling of elastic energy in a multicomponent system. For the elastic energy, an empirical formula using the published data of lattice misfits between gamma and gamma-prime phases is combined with Khachaturyan's theory [1]. The temporal evolution of element compositions during the growth and coalescence of gamma-prime precipitates is also discussed.

2. Multiscale Multiphysics Simulations

My notable goal is to predict the lifetime of engine components such as a turbine blade and compressor blade from an alloy composition and a service condition. As an example, a turbine blade in service is exposed to inhomogeneous temperature and stress distributions because of centrifugal force, internal cooling and the blade's characteristic shape. These temperature and stress distributions can be simulated using the finite element method. Using the boundary condition of temperature and stress, the local deformation strain of the blade is estimated based on the microstructure morphology and dislocation motions. Also environmental properties such as an oxidation resistance can be predicted from microstructure change near the surface and interaction with coatings. Development of simulation methods of multicomponent systems is one of key targets in my work. I have been developing simulation methods for oxidation process, microstructure evolution and dislocation motions in multicomponent systems. A schematic of the multiscale and multiphysics modeling for a high temperature blade is shown in Fig. 1 [2]. Among them, a new phase-field method to predict the microstructure morphology of multicomponent Ni-base superalloys is described in the next section.

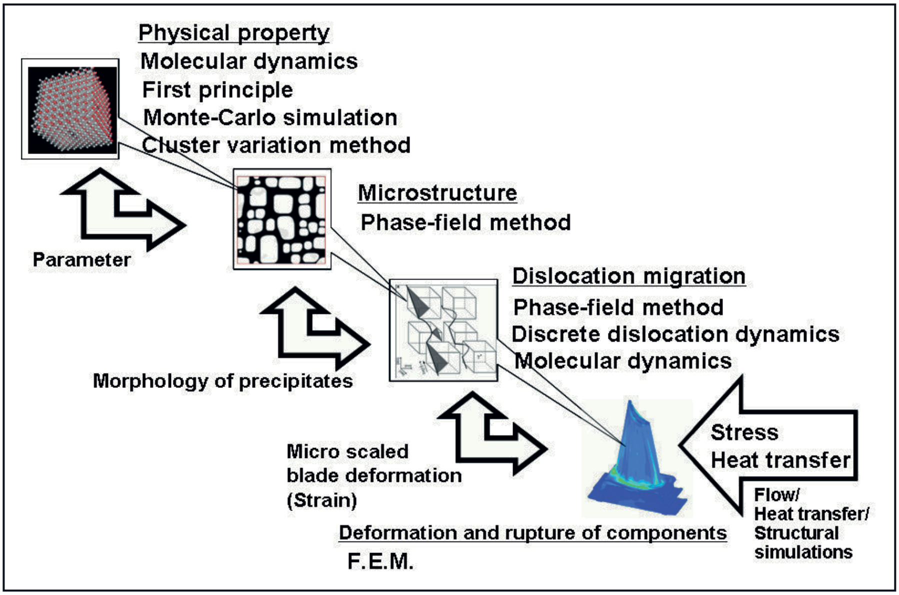

Figure1. *Schematic of the calculation procedure for a high temperature blade in a jet engine [2].*

3. A New Phase-Field Method for Simulating Gamma-Prime Precipitation in a Multicomponent Ni-base Superalloy

The Ni-base superalloys are composed of the gamma matrix (fcc structure) and gamma-prime precipitates ($L1_2$ structure). The morphology of the precipitates affects the turbine blade's mechanical properties. The phase-field method has been a powerful means to simulate the microstructure morphology. However, previously reported simulations were focused on binary and ternary systems even though commercial Ni-base superalloys incorporate as many as ten elements. This is partly due to the complexity of Gibbs free energy surface in a multicomponent system, and due to the difficulty of modeling elastic energy in a multicomponent system. In this section, a new phase-field model for multicomponent Ni-base superalloys is described.

3.1 Gibbs energy [3,4]

The molar Gibbs energy is expressed using a single function formalism of the gamma and gamma-prime phases in the CALPHAD method with a four sublattice model. These sublattices can be an origin of the $L1_2$ structure. The site fraction of each element i on the sth sublattice is denoted as $y_i^{(s)}$. The Gibbs energy of the gamma-prime phase was described by separating it into disordered and ordered contributions in a single function as follows [5]:

$$G\left(c_i, y_i^{(s)}\right) = G^{fcc}(c_i) - \Delta G^{ord}\left(y_i^{(s)}\right) \tag{1}$$

where $\Delta G^{\mathrm{ord}}\left(y_i^{(s)}\right) = \Delta G^{\mathrm{L1_2}}\left(y_i^{(s)}\right) - \Delta G^{\mathrm{L1_2}}\left(y_i^{(s)} = c_i\right)$, i can be Al, Co, Cr, Mo, Re, Ta, W and Ni. c_i is a mole-fraction of element i. The first term of Eq. (1) corresponds to the Gibbs energy of the disordered gamma phase; $\Delta G^{ord}\left(y_i^{(s)}\right)$ is the ordering energy of the gamma-prime phase as a function of the site fractions. All thermodynamic parameters for Eq. (1) were obtained from the NIST thermodynamic database [6].

The order parameters and the composition for each element are defined as:

$$\phi_i^1 = \left(-y_i^{(1)} - y_i^{(2)} + y_i^{(3)} + y_i^{(4)}\right)/4c_i \ , \tag{2a}$$
$$\phi_i^2 = \left(-y_i^{(1)} + y_i^{(2)} - y_i^{(3)} + y_i^{(4)}\right)/4c_i \ , \tag{2b}$$
$$\phi_i^3 = \left(y_i^{(1)} - y_i^{(2)} - y_i^{(3)} + y_i^{(4)}\right)/4c_i \ , \tag{2c}$$
$$c_i = \left(y_i^{(1)} + y_i^{(2)} + y_i^{(3)} + y_i^{(4)}\right)/4, \tag{2d}$$

where i= Al, Co, Cr, Mo, Re, Ta, W. As for Ni:

$$c_{Ni} = 1 - \sum_i c_i \ , \tag{3a}$$
$$y_{Ni}^{(s)} = 1 - \sum_i y_i^{(s)} \ . \tag{3b}$$

By combining Eqs. (1)-(3), the molar Gibbs energy of the gamma and gamma-prime phases for the multicomponent system can be described using the variables of order parameter and composition fields.

3.2 Elastic energy

The elastic energy for a multicomponent system was calculated based on Khachaturyan's theory [1]. The actual elastic strain in materials is expressed as follows:

$$\varepsilon_{ij}^{el}(\mathbf{r}) = \varepsilon_{ij}(\mathbf{r}) - \varepsilon_{ij}^{0}(\mathbf{r}) \tag{4}$$

where $\varepsilon_{ij}(\mathbf{r})$ is the total strain in the material, $\varepsilon_{ij}^{0}(\mathbf{r})$ is the eigen strain. Based on the Vegard's law, the eigen strain for a binary phase, e.g., Ni-Al, is

$$\varepsilon_{ij}^{0}(\mathbf{r}) = \frac{a(\mathbf{r}) - a_0}{a_0} = \frac{1}{a_0}\frac{da}{dc_{Al}}\left\{c_{Al}(\mathbf{r}) - c_{Al}^{0}\right\}\delta_{ij} \tag{5}$$

where a_0 is the lattice parameter of gamma matrix at composition c_{Al}^{0} . δ_{ij} is the Kronecker delta function. Eq. (5) is extended to a multicomponent system as follows:

$$\varepsilon_{ij}^{0}(\mathbf{r}) = \frac{1}{a_0}\sum_{k}\frac{da}{dc_k}\left\{c_k(\mathbf{r}) - c_k^{0}\right\}\delta_{ij} \cdot \tag{6}$$

The parameters of da/dc_k in Eq. (6) were determined from experimental data of lattice misfits between gamma and gamma-prime phases. The elastic energy density is given as $\varepsilon_{el} = \lambda_{ijkl}\varepsilon_{ij}^{el}\varepsilon_{kl}^{el}/2$ [7]. The elastic constants of TMS-75 were used [8].

3.3 Phase-Field Model

The total chemical free energy in the multicomponent system includes the local free energy, the interface energy and the elastic energy, given as

$$F \equiv \frac{1}{V_m}\int_V\left(G + \frac{\alpha}{2}\sum_j(\nabla c_j)^2 + \frac{\beta}{2}\sum_j\sum_{i=1}^{3}(\nabla\phi_j^i)^2\right)dV + \int_V e_{el}dV \tag{7}$$

where V_m is the molar volume, which was assumed to be constant, $V_m = 7.0\times10^{-6} m^3/mol$. α , β are the gradient energy coefficients, $\alpha = 1.56\times10^{-14} Jm^2/mol$, $\beta = 2.50\times\ 10^{-16} Jm^2/mol$.

The temporal evolution of the element compositions and order parameters are obtained by solving the following equations:

$$\frac{\partial c_i}{\partial t} = \sum_j \nabla \cdot \left(\tilde{M}_{ij} \nabla \frac{\delta F}{\delta c_j} \right), \tag{8}$$

$i = j = Al,$ Co, Cr, Mo, Re, Ta, W,

$$\frac{\partial \phi_i^j}{\partial t} = -L \frac{\delta F}{\delta \phi_i^j}, \tag{9}$$

$i = Al,$ Co, Cr, Mo, Re, Ta, W, $j = 1,2,3$,
where $\tilde{M}_{ij}$ is the chemical mobility with Ni as the dependent species and L is the structural relaxation coefficient. $\tilde{M}_{ij}$ is obtainable from a mobility database [9]. Parameter L was determined from $\tilde{M}_{AlAl} = La_0/16$ with the lattice parameter $a_0 = 3.35 \times 10^{-10} m$.

3.3 Results and discussion

This paper focuses on an eight element superalloy, TMS-75; i.e. Ni-13.7Al-12.6Co-3.6Cr-1.3Mo-1.7Re-2.1Ta-2.0W (at%). The Gibbs energy surfaces of gamma and gamma-prime phases in eight element systems, which are obtained using Eqs. (1)-(3) under the condition of $\partial G / \partial \phi_i^j = 0$ (i =Al, Co, Cr, Mo, Re, Ta, W, j = 1, 2, 3), are shown in Fig. 2 [3]. To validate the accuracy of this new method to describe the Gibbs free energy in a multicomponent system, the results were compared with the calculated results from Thermo-Calc software. Both results are in good agreement, which indicates that the free energy surface in the multicomponent system is successfully derived by linkage to the CALPHAD method.

One of the characteristics of this Gibbs energy function is that order parameters have a physical meaning, i.e., long-range ordering. Fig. 3 shows equilibrium profiles of order parameters between gamma and gamma-prime phases [3]. According to the definitions of order parameters, i.e., Eq. (2), the closer the value is to 1 or -1, the more the element substitutes for an Al site or a Ni site, respectively. The order parameter of Ta in the gamma-prime phase is close to 1 in Fig. 3, which means Ta strongly occupies Al site in the gamma-prime phase. In addition, this strong partitioning is found even in the gamma phase adjacent to the gamma/gamma-prime interface. On the other hand, the site partitioning tendency of Re in the gamma-prime phase is not significant. Co prefers to occupy Ni sites in the gamma-prime phase. The ordering tendency is thus dependent on the elements. In the microstructure of TMS-75, Al and Ta are rich in the gamma-prime phases, whereas Re, Co, Cr, Mo, Ta, W are rich in the gamma phase. The equilibrium compositions of gamma and gamma-prime phases were compared with an experimental data obtained by Yokokawa et al. using an electron probe x-ray microanalyzer [10]. As a result, both the calculated and measured compositions and element partitioning behaviors showed good agreement.

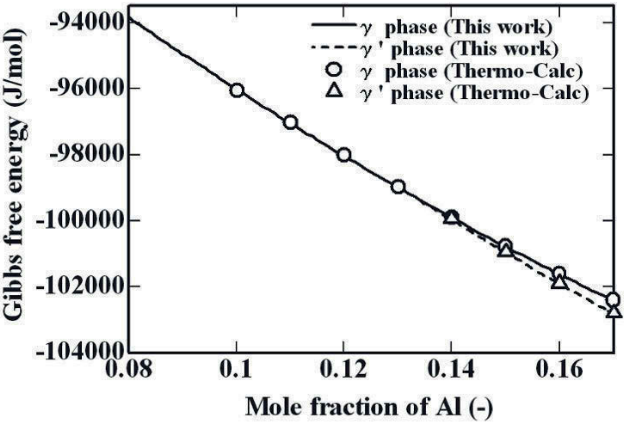

Figure 2. *Comparison of the Gibbs energy obtained in this work with the calculated results using Thermo-Calc software [3].*

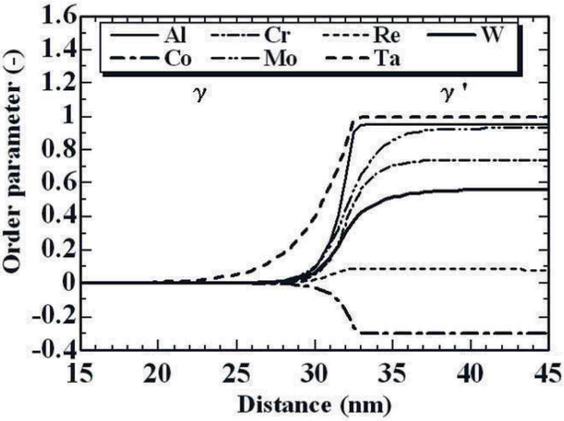

Figure 3. *Equilibrium order parameter profiles at the gamma/gamma-prime interface [3].*

Fig.4 shows snapshots of simulated temporal evolution of compositions of Al and Re in TMS-75 at 1100°C. Re concentration is more inhomogeneous compared to Al because of its small diffusivity. After nucleation of the precipitates, they grow, merge, and coarsen. In addition, the local equilibriums of elements at the gamma/gamma-prime interface are confirmed. In this study, four different domains in L12 structure can be distinguished by the order parameters because they have a physical meaning of long range ordering. Therefore, the different domain precipitates do not merge because of high anti-phase boundary energy. During the coalescence of the precipitates which have the same domain, Re and W supersaturated in the gamma phase.

There have been few reports on the modeling of such gamma-prime precipitation in an eight element system at the practical level. Therefore, it can be concluded that the present modeling is very useful to design and develop new alloys coupling with multiscale multiphysics simulations. The present article focused on a single crystal Ni-base turbine blade. However, polycrystalline materials are used for low pressure turbine blades and compressor blades. For those materials, parameters affecting the evolution of grain boundaries, e.g., grain boundary character distribution, the formation of carbides and TCP phases, are important. The incorporation of these parameters into the current simulation is our future work.

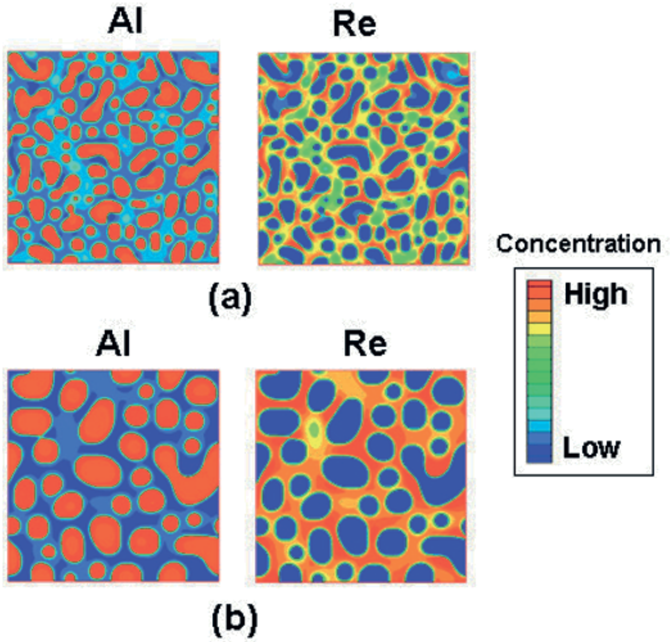

Figure 4. Concentration distributions of Al and Re in TMS-75 at dimensionless times (a) t=200, (b) t*=1756.*

4. Summary

In this paper, multiscale multiphysics simulations for development of high temperature materials were described. In addition, a new phase-field model for gamma-prime precipitation in multicomponent systems was also shown. New methods to describe Gibbs energy and elastic energy in multicomponent systems were proposed in this study. This model would be useful to design and develop new alloys coupling with other multiscale mutiphysics simulations.

References

1. Khachaturyan AG (1983) Theory of Structural Transformations in Solids. Wiley, New York
2. Kitashima T, Wang J, Harada H, Sakamoto M, Yokokawa T, Fukuda M (2007) Development of a virtual jet engine integrating material and system simulations. Proceedings of International Gas Turbine Congress 2007, Gas Turbine Society of Japan, 220-224
3. Kitashima T, and Harada H (2009) A new phase-field method for simulating gamma-prime precipitation in multicomponent nickel-base superalloys. Acta Mater 57: 2020-2028
4. Kitashima T (2008) Coupling of the phase-field and CALPHAD methods for predicting multicomponent, solid-state phase transformations. Philos Mag 88: 1615-1637
5. Ansara I, Dupin N, Lukas HL and Sundman B (1997) Thermodynamic assessment of the Al-Ni system. J Alloys Compd 247: 20-30
6. Kattner UR (2002) Construction of a thermodynamic database for Ni-base superalloys: A case study. CALPHAD and Alloy Thermodynamics, TMS (The Mineral, Metals & Materials Society), 147-164
7. Hu SY, and Chen LQ (2001) A phase-field model for evolving microstructures with strong elastic inhomogeneity. Acta Mater 49: 1879-1890
8. Osawa M, Shiraishi H, Yokokawa T, Harada H, and Kobayashi T (2004) 3D-FEM calculations of rafting in Ni-base superalloys based on high temperature elastic and lattice parameters. Proceedings of Superalloys 2004, TMS (The Mineral, Metals & Materials Society), 977-985
9. Campbell CE, Boettinger WJ, and Kattner UR (2002) Development of a diffusion mobility database for Ni-base superalloys. Acta Mater 50: 775-792
10. Yokokawa T, Osawa M, Nishida K, Kobayashi T, Koizumi Y, and Harada H (2003) Partitioning behavior of platinum group metals on the gamma and gamma-prime phases of Ni-base superalloys at high temperatures. Scripta Mater 49: 1041-1046

Low friction slip-rolling contacts – Influences of alternative steels, high performance thin film coatings and lubricants

Christian Scholz[1, 2] **and Mathias Woydt**[1]

[1] *BAM Federal Institute for Materials Research and Testing, Berlin 12200, Germany*

[2] *KYB Corp., 1-12-1 Asamizodai, Minami-ku, Sagamihara 252-0328, Japan*

Abstract

Original equipment manufacturers perceive diamond-like carbon (DLC) coatings as part of a strategy for low frictional tribosystems. Especially the automotive industry anticipates a benefit in applying such coatings in association with the lightweight construction of mechanical parts, for instance in gears and engines. Further improvements in creating low-friction contacts were achieved in the present work using alternative, available steel metallurgies as substrates for thin film coatings. Additional factors, such as tribological influences of the lubrication on the surface chemistry (additives and base oils) were investigated.

Keywords: *slip-rolling; DLC; low friction; high toughness steel; additives*

1. Introduction

Due to the growing environmental awareness worldwide, containment provisions for CO_2 emissions in mobility systems and increasing performance requirements the demands on mechanical systems and their materials continuously rise. These high demands require the implementation of new technical approaches, for example of light-weight strategies in automotive powertrains, and directly raise questions about the suitability of the most promising technical solution.

In addition to light-weight strategies a reduction in friction and an increase of the fatigue lifetime are two other major development directions to strive the mentioned targets. It is clear, that any kind of solution must show an equal application profile, preferably an improvement, compared to the state-of-the-art solutions. For tribological systems, the following paths may offer lower friction and higher load carrying capabilities:

W. Udomkichdecha et al. (eds.), *Materials Challenges and Testing for Manufacturing, Mobility, Biomedical Applications and Climate*,
DOI 10.1007/978-3-319-11340-1_13

1. Alternative base oils and additives (such as esters, polyglycols),
2. Thin film coatings (e.g. DLC)
   and/or
3. Novel but already existing steel metallurgies.

Alternative lubricant formulations may reduce the coefficient of friction under mixed/boundary lubrication, enhance fatigue life and increase extreme pressure behavior (anti-galling) of uncoated and thin-film-coated-steels. Being 'chemicals', these lubricants are subjected to many regulations in view of their environmental impact (REACh, European Preparations Directives[1]). In consequence, the number of high performance additives available will be limited or restricted. Alternative base oils (esters, polyglycols) meet bio-no-tox criteria (low toxicity) and offer an attractive tribological profile. Although it is not imperative to respect these regulations at all times, keeping them in mind early in the product development cycle is both a corporate responsibility and good business practice. This is in line with the current vision of business solutions based on the philosophy referred to as 'Zeronize' [1] [2]. Zeronize symbolizes the efforts for the minimization of negative and adverse effects of energy conversion and mobility environment.

Recently, the load carrying capacity and slip-rolling resistance of some of the DLC, a-C and ta-C thin film coatings were significantly improved. Although thin film coatings have thus pushed the tribological barriers to new heights, they still do not comply with the quality demands (batch-to-batch) in mass production and functional needs in highly solicited tribosystems. In view of this, there is still room for improvements. Additionally, two major issues have to be considered for using coatings on carbon steel substrates. Firstly, especially carbon containing coatings need to match the constitutional behavior of the carbon steels. Secondly, the annealing temperature of these steels is generally not high enough to sustain the higher deposition temperature and time required for improved adhesion of such thin films.

Often, the influence is underestimated of the steel substrate on the adhesion of thin film coatings and the mechanical properties of the tribological system. Previous investigations conducted at BAM showed that by using nowadays common tempered steels, positive aspects of thin film coatings were ruined due to structural changes of the steel substrate during the coating process [3] [4] [5]. Due to a decrease in the hardness values of the steel substrate during deposition process, the metallurgy of steels needs to be optimized to higher annealing temperatures (above 300°C). Novel, but already existing steel grades can withstand sufficiently high deposition temperature for a necessary adhesion (metallurgical diffusion bonding) of modern thin films [6].

---

[1] REACh – Regulation, Evaluation, Authorization and Restriction of Chemicals, European Commission Environment, 2007

In previous investigations on the slip-rolling resistance (endurance test up to 10 million load cycles) of thin film coatings (a-C, ta-C, Zr(C,N)) at contact pressures of up to $P_{max} = 2.9$ GPa ($F_N = 2{,}000$ N), the substrates were mainly made of the bearing steels 100Cr6H and Cronidur 30. The aim of the present work is to illuminate the influences of lubricants (engine oil BMW SAE 0W-30 VP1 and polybutylene glycol B20), high performance thin film coatings and alternative steel solutions in highly stressed slip-rolling contacts at oil temperatures of 120°C. In using new steel metallurgies, high toughness and high strength steels, in combination with thin film coatings, even if they compete in the uncoated state, the Hertzian contact pressures could be increased up to $P_{max} = 4.2$ GPa ($F_N = 5{,}000$ N) without any failures of coating or substrate after 10 million load cycles. It was shown that selected thin film coatings can minimize the wear rates down to nearly zero-wear in highly stressed contacts.

2. Experimental procedure

2.1 Materials

In previous investigations [3] [4] on slip-rolling resistance of thin film coatings, the substrates were mainly made of the quenched and tempered steels 100Cr6H and Cronidur 30 (nitrogen alloyed). Both have very low inclusion populations. Most suppliers offer these steel grades with hardness values in the range of 63 – 64 HRC (Rockwell hardness C) for the 100Cr6H steel and 59 – 60 in the case of the Cronidur 30. These steels are typically used in bearings and serve as a reference for the investigations of DLC-coated and uncoated, alternative steel grades.

Table 1. *Mechanical properties of steel substrates used*

Material	100Cr6H AISI 52100	Cronidur 30 AMS 5898	V300 1.8062	NC310YW 40SiNiCrMo10	CSS-42L AMS 5932
ρ [g/cm³]	7.8	7.67	7.8	7.66	7.93
E [GPa]	210	213	198	202	211
Strain [%]	-	< 5	~ 10	~ 9	< 18
HRC	63	60	51.1	56.8	62.5
K_{IC} [MPa·m$^{1/2}$]	~ 16.5	~ 21	80	~ 52	> 120
KV [J]	-	-	10	30	-
R_m [MPa]	~ 2300	~ 2300	~ 1600	~ 2150	~ 1840
T_a [°C]	150	475	410	300	552

Good slip-rolling resistance is fine for rolling bearings, but high toughness and fatigue strength properties are essential for the load carrying capability on teeth roots of gears. In consideration of this increased demand on substrate properties, two high toughness steels and an aerospace steel of ultra-high toughness were selected for this investigation. The novel and already available steel grade CSS-42L combines properties such as high surface hardness (63 – 64 HRC), hot hardness for usage up to 427°C and high fracture toughness. The high toughness steels V300 and NC310YW have also low inclusion contents. All steel grades have maximum annealing temperatures above 300°C (see Table 1). If these steel grades are used as substrates for coatings, the substrate temperature required by the deposition process of the coatings will stay below the annealing temperature of this type of steels.

Furthermore, friction results conducted by use of aforementioned steels are compared with DLC coatings supplied by BMW Group (Munich). The coatings deposited by PECVD (Plasma-enhanced chemical vapor deposition) process, referred as BMW 4, 11, 13 and 14, consist of different adhesion layers and a functional layer. A SIMS (Secondary ion mass spectroscopy) measurement [7], shown in Figure 1 reveals different chemical compositions and structural positions of the layers. Starting with a chromium-based adhesive layer and a W-C:H interlayer the functional layer is a hydrogenated amorphous carbon coating doped in some configurations with nitrogen or silicon (a-C:H, a-C:H:-N, a-C:H-Si). The hardness of coatings ranges from 12 to 25 GPa, whereas the Young's Modulus has been indented between 135 to 214 GPa. During the development process of the coatings, some process parameters, i.e. the interlayer and film thickness, were modified by BMW in order to get the best coating in practice. That is why several coatings from this supplier can be found. Furthermore, roughness properties of the coatings were determined by a HOMMEL-ETAMIC roughness and contour measurement system. In case of the investigated BMW coatings roughness R_a ranges from 0.015 to 0.023 whereas R_z values lie between 0.0116 and 0.169. It has to be noted that BMW 4 coating exhibited the roughest surface of coatings analyzed in the present study. The results obtained by use of thin film coatings are considered in chapter 3.3.

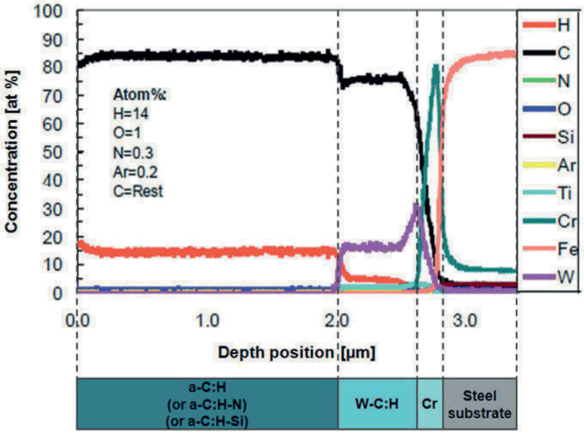

__Figure 1.__ SIMS measurement of a used a-C:H type DLC coating (BMW 4) [7]

2.2 Test parameters

The slip-rolling tribological tests were carried out in an Amsler-type twin disc tribometers and in a newly designed Optimol 2Disk tribometer [8]. Both used two discs with the same outer diameter rolling against each other on their cylindrical surface (cf. ***Table 2***).

They are described in detail by reference [9]. The lower, cylindrical, commonly coated discs run at a rotating speed of 390 rpm with a slip of 10% to the upper, spherical discs (cf. ***Figure 2***). The target is 10 millions of cycles or approximately 18 days without showing any surface failures. With 430 hours at 120°C, this includes a kind of 'oxidation aging' for the engine oil.

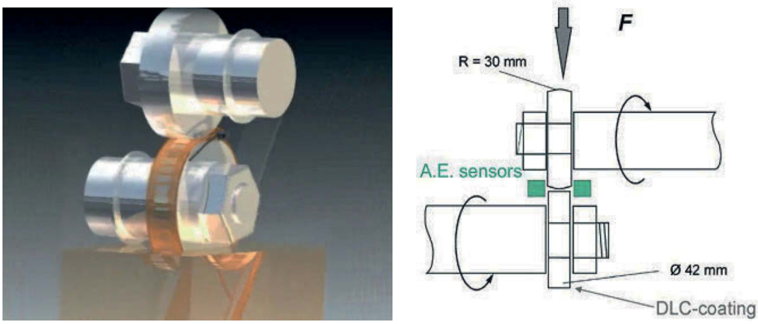

Figure 2. *Sample arrangement in the Amsler type tribometer*

In the newly designed twin disc test rig, it is possible to test thin film coatings under mixed/ boundary conditions up to an average Hertzian contact pressure of $P_{mean} = 2.62$ GPa ($F_N = 5{,}000$ N or $P_{max} = 3.92$ GPa).

Table 2. *Experimental Setup*

Conditions	**Parameter**
Dimensions of the discs	Diameter: 42 mm; Width: 10 mm
Contact	Grinded and polished curved disc (radius of curvature: 21 mm) against uncoated/coated super polished cylindrical disc
Substrate	100Cr6H, Cronidur 30, V300, NC310YW, CSS-42L
Type of motion	Rolling with a slip rate of 10%
Initial average Hertzian pressure P_{mean}	1.5 GPa ($F_N = 930$ N)
Rotation at speed	390 – 354 rpm
Sliding speed V_{diff}	0.08 m/s
Load cycles n_{tot}	Up to 107 or rupture (damaged surface area of > 1 mm^2)
Effective sliding distance	Up to 132 km
Ambient temperature	120 °C oil bath temperature
Lubricants	BMW FF SAE 0W-30 'VP1', Polybutylene Glycol 'B20'

The calculated value of minimal oil thickness h_{min} of SAE FF 0W-30 (HTHS = 3.0 mPas, ACEA A3/B4) at T = 120°C and F_N = 2,000 N is 0.0252 µm. The roughness values of uncoated V300 steel ($R_{a\,cyl.} = 0.0048$ µm, $R_{a\,sph.} = 0.17$ µm) result in a parameter of Tallian of $\lambda \sim 0.077$ to 0.068, which denotes the regime of mixed/boundary lubrication [4]. At 120°C, the calculated oil film thicknesses are $\approx$ 1/10 of those at RT. The Hertzian contact stresses are at 120°C likely transmitted through the micro-asperities and not by hydrostatic pressure generated from a hydrodynamic oil film.

3. Test results

3.1 Tribological influences of alternative steels and lubricants

Considering the evolution of the coefficient of friction as function of the test duration (10 million load cycles) in endurance tests conducted in the present work, the tribological benefit of the alternative steels becomes clearly visible (see **Figure 3**). As test parameter, a contact pressure of P_{mean} = 1.5 GPa at 120°C lubricant temperature was chosen. In comparison to conventional bearing steel, such as 100Cr6H and Cronidur 30, the steel grade V300 could reduce the friction values by approximately 25 %.

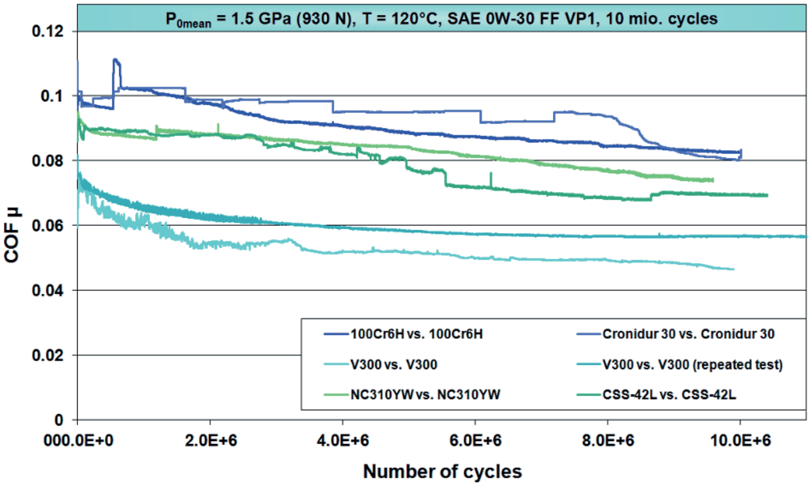

Figure 3. Evolution of the coefficient of friction over the test period of 10 million load cycles at P_{mean} = 1.5 GPa and T = 120°C in SAE 0W-30 VP1 oil

In order to confirm the test results of V300 the test was repeated under the same conditions. Consequently, the low friction values of V300 down to 0.05

could be reproduced. In the light of this comparison it may be concluded that a reduction of friction by an optimal choice of interacting materials could be achieved. With regard to different varying degrees of material interactions revealed the tribo-system could made more effective, compatible and consistent. Another interesting aspect in this view is that NC310YW compared with the conventional steels also offered a friction reduction, but not to the same degree as V300, although it has nearly an identically chemical composition.

Compared to the other steels V300 leads to a remarkable reduction in friction, which might be explained in two ways. The first possibility is the formation of tribo-reactive thin films due to the contact pressure and presence of reactive oil additives. It would be conceivable that V300 offers a greater chemical affinity for the formation of reactive thin films on the steel surface than the other steel grades. The second possibility for explaining this test results is the formation of a nanocrystalline structure within the stressed area of V300. In industrial applications self-nanocrystallization is used to achieve increased mechanical properties of metallic surfaces [9]. Structural and chemical analysis of the steel surface after tribological tests by means of SEM/EDX, AES and XPS confirmed the first assumption of a Ca-based tribo-reactive film formation during running-in phase. The most likely scenario of the tribofilm formation is the interaction of the steel surface with overbased sulfonate structures. The reaction of calcium carbonate, widely used as detergent in lubricants, forms together with the steel surface a boundary film composed of CaO and $CaCO_3$. The formation of such films can lead to friction reduction after 100,000 to 500,000 load cycles running-in time (see Figure 4 V300 steel). Detailed structural analysis results are described in Ref. [10].

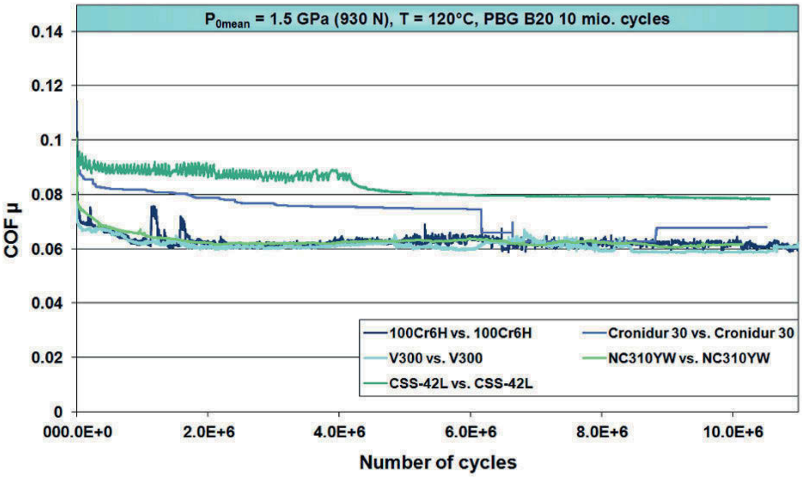

Figure 4. *Evolution of the coefficient of friction over the test period of 10 million load cycles at P_{mean} = 1.5 GPa and T = 120°C in PBG B20 oil*

Comparing the test results obtained with SAE 0W-30 VP1 to those of polybutylene glycol PBG B20, an indication is evident for the formation of tribo-reactive thin film on V300. In ***Figure 4*** the friction values are plotted of five steels, each tested with the aforementioned PBG B20 oil over the test duration of 10 million load cycles. In this case, the friction coefficients of 100Cr6H, V300, NC310YW and even Cronidur 30 are nearly in the same range of 0.06 and also comparable to the results of V300 lubricated with VP1. This result implies furthermore that PBG B20 offers a greater potential to decrease friction values independent from the steel choice, in contrast to VP1.

3.2 Tribological influence of lubricant additives

In this work, the frictional benefit of distinct DLC coatings was established. ***Figure 5*** reveals another step in frictional optimization of tribological systems due to the interaction of DLC-coatings with special additives. The tests were conducted for 500,000 load cycles at 1.5 GPa using self-mated BMW DLC-coating and a modified version of the lubricant VP 1 containing no EP/AW additives. One percentage of the following additives was added to the lubricant, which are mainly used as EP/AW additives or antioxidants:

- 2-ethylhexyl-MoDTP (CAS number[2]: 72030-25-2)
- Molybdenum di-n-butyldithiocarbamate (68412-26-0)
- 5,5'-dithiobis-(1,3,4-thiadiazole-2(3H)-thione) (71342-89-7)
- Dibenzyl disulfide (150-60-7)
- Triethanolamine (102-71-6)

In contrast to the general expectation of additivated lubricants not reacting with DLC coatings, a friction reducing effect of some additives became visible. Especially, the molybdenum containing complex as well as dibenzyl disulfide and triethanolamine revealed lower friction values down to 0.03. This fact is astonishing since the reduction of friction values due to DLC coatings is already known. The interaction of lubricant and coating represents a new perception of such tribosystems and are still not fully understood.

These test results are a selection of 25 different additives tested in combination with uncoated steel surface as well as DLC coatings. Hence, it has been shown that by optimizing the lubricant in terms of additives interacting with rather chemical inert surfaces the friction values could be remarkably reduced.

---

[2] CAS Registry Numbers are unique numerical identifiers assigned by the Chemical Abstracts Service to every chemical described in the open scientific literature [11]

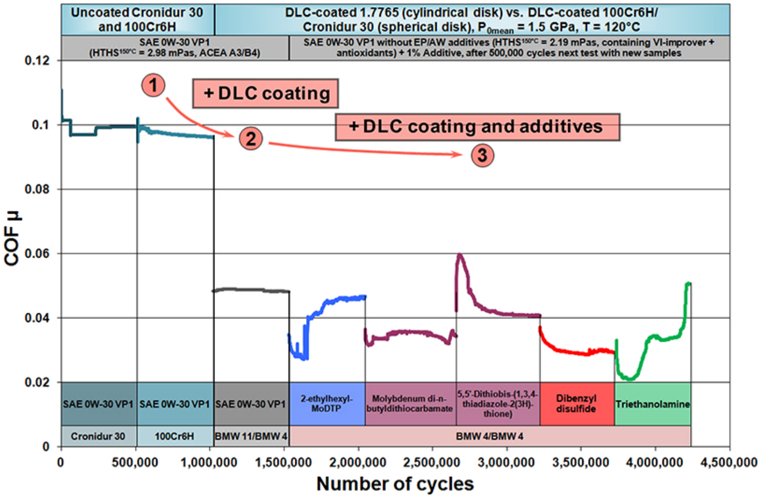

Figure 5. *Frictional behavior of combining uncoated steel samples with DLC coatings and modified lubricant compositions in slip-rolling tests at* P_{mean} *= 1.5 GPa and T = 120°C*

3.3 Tribological influence of high performance thin film coatings

The frictional profile of tribological systems can be optimized by a suitable material choice for example the steel grade V300. Similar results can be obtained by applying a highly wear resistant and low friction DLC coating. Therefore, an endurance test series, with different a-C:H thin film coatings of the BMW Group was conducted in order to show the frictional potential of these coating types. The test series was separated into two parts. The first part included the material pairing uncoated steel (spherical) vs. DLC-coated steel (cylindrical). After finishing these tests, the second part followed comprising the DLC-coated steel (spherical) vs. DLC-coated steel (cylindrical). The test results are presented in ***Figure 6***, including one endurance test of uncoated Cronidur 30 vs. uncoated 100Cr6H as reference (red curve) and the best in practice steel pairing, uncoated V300 vs. uncoated V300 (yellow curve). The diagram plotted reveled three areas.

Area one represents uncoated steel pairings with average coefficients of friction of 0.07 at test end. The application of a DLC-coating on the cylindrical test sample could remarkably reduce the friction values, shown by the green curves in ***Figure 6***. Considering the course of the yellow curve it is remarkable that suitable steels could offer the same potential to reduce friction as a DLC coating. The blue curves represented by DLC vs. DLC pairings showed the most promising results to reduce friction. In comparison to uncoated systems the combination of DLC coatings in the contact is at the moment an optimum.

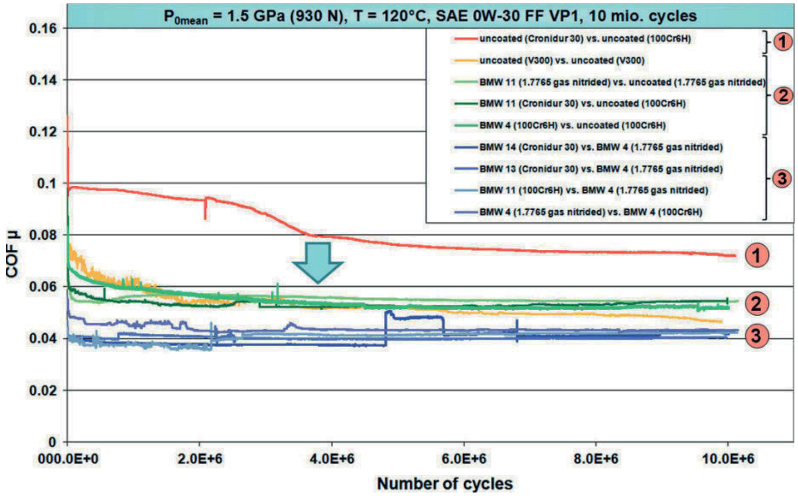

Figure 6. *Comparison of friction coefficients of test pairings without any DLC coatings, single coated samples and pairings with DLC coatings applied on both samples tested at P_{mean} = 1.5 GPa and T = 120°C in SAE 0W-30 VP1 oil*

4. Summary and Conclusion

The objective target of the present work was to show the potential of different optimization paths to realize a low friction and low wear system under slip-rolling motion. Therefore, the development paths were tribologically considered in order to create and environmental friendly tribo-system with low friction properties:

- Alternative steels with high fatigue strength and fracture toughness properties
- Thin film coating (DLC)
- and
- Eco-no-tox lubricants including additives

Figure *7* summarizes the global impact of thin films and alternative, uncoated steels on friction and additional the wear rates r mixed/boundary conditions for slip-rolling motion lubricated by SAE FF 0W-30 VP1 oil at 120°C. It is clearly visible at a glance that the friction values of completely uncoated systems offered considerably higher friction coefficients at test beginning than systems were both DLC coated surfaces are mated.

The majority of uncoated steels presented coefficients of friction between 0.06 – 0.09, but selected iron based steel metallurgies, such as the high toughness steel

V300, can also achieve low values of ~ 0.04 in the same range as self-mated DLC-type thin films (40% reduction in friction compared to commonly used steels). From this point of view, it can be said that the application of thin film coatings on steel surfaces with their difficult deposition and quality assurance can be avoided, if alternative steels are used.

Thin films reduce wear rates by factors of 2 – 5, rather than by orders of magnitude. Some iron based steel metallurgies, especially in the case of V300 steel, can compete as uncoated triboelements with specific thin films. Some thin films enabled to reach the resolution limit of tactile technique used to quantify wear of these tests.

In any case, low friction and “zero wear” requires a new metallurgy, either through thin films or alternative steels. Due to alternative steels, higher stresses can be withstood by showing good fatigue strength properties and fracture toughness values in the frictional contact .

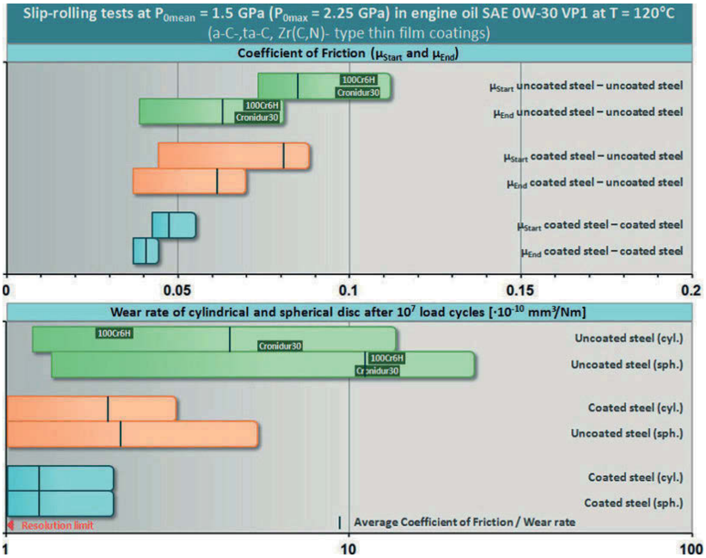

Figure 7. *Comparison of friction and wear behavior of uncoated steel pairings, single coated pairings and pairings with two coated tribo-elements*

It has been shown that the global functional profile of tribological systems could be optimized by the application of suitable steel and coating combinations. With regard to the potential of CO_2 emission reduction in internal combustion engines it became visible that still existing and optimized technologies offers certain capabilities for new improvements. In the future, the load carrying capacity of the steels should be increased further with regard to the light weight design of mechanical systems. Therefore, new steel production processes need to be used in order to create steel solutions with micro-structural benefits and improved mechanical properties with strength values reaching 5,000 MPa. The interaction of tribological stressed surfaces and lubricants/additives will be part of furture works.

References

1. Toyoda S (2007) All Toyota tribological innovation to realize “Zeronize” and “Maximize” society. Tribol Int 2: 19-22
2. Renault SA (2002) Sustainable development – “ELLYPSE” – radically designed. Das Magazin für Forschung und Entwicklung 26, ISSN: 1289-009x
3. Manier C-A (2010) Slip-rolling resistance of novel Zr(C,N) thin film coatings under high Hertzian contact pressures. BAM PhD series, Vol. 60, Berlin
4. Manier C-A, Theiler G, Spaltmann D et al (2010) Benchmark of thin film coatings for lubricated slip-rolling contacts. Wear 268: 1442-1454
5. Woydt M, Manier C-A, Brückner A et al (2010) Wälzbeständigkeit von ta-C Dünnschichten unter hohen Hertzschen Beanspruchungen bis zu 3000 MPa. Tribol. Schmierungstech. 57: 30-36
6. Scholz C, Spaltmann D, Woydt M (2011) Slip-rolling resistance of thin films and high toughness steel substrates under high Hertzian contact pressures. Wear 270: 506-514
7. Seitz, J, Schnagl, J (2011) Investigation of the wear behaviour of DLC-coated cam followers in an automotive engine. DGM Friction, Wear and Wear Protection confer-ence, Karslruhe, 26. – 28.10.2011
8. Effner U, Woydt M (2003) Slip-rolling and machining of fine ceramics. BAM research report 259, ISBN 3-89701-976-0
9. Li G, Chen J, Guan D (2010) Friction and wear behaviors of nanocrystalline surface layer of medium carbon steel. Tribol Int 43: 2216-2221
10. Scholz, C (2013) Low friction slip-rolling contacts – Influences of alternative steels, high performance thin film coatings and lubricants. BAM PhD series, Vol. 96, Berlin
11. http://www.cas.org/expertise/cascontent/registry/regsys.html, 15.06.2012

Part III
Material Challenges for Biomedical Applications

Characterization of Randomly Branched Polymers Utilizing Liquid Chromatography and Mass Spectrometry

Jessica N. Hoskins, Jana Falkenhagen, and Steffen M. Weidner

BAM- Federal Institute for Materials Research and Testing, 12489 Berlin

Abstract

Branching in polymers is an important way to modify the materials properties, however the characterization of random branching in polymeric materials is a challenge in polymer analysis. In this work, liquid adsorption chromatography methods are developed for a commercially available hyperbranched polyester (Boltorn^{TM}). This chromatographic techniques was then coupled to offline MALDI-TOF MS analysis, a first in the analysis of randomly branched polymers. The coupling of these two techniques provides superior MALDI-TOF spectra, enabling the easy identification of structural subdistributons based on theoretical molecular weight. Detailed analysis of the MALDI-TOF spectra shows that these chromatographic conditions separate cyclic Boltorn polymers (with no core molecule) from non-cyclic polymers (with core molecule), and these are the only two architectures observed. MALDI MS also confirms that the chromatographic separation mode is adsorption, but further analysis is needed to determine if there is a separation by degree of branching.

Keywords: *hyperbranched polyesters, polymer mass spectrometry, polymer chromatography, liquid adsorption chromatography, MALDI-TOF MS*

1. Introduction

The incorporation of branching into linear polymers is recognized to significantly alter their materials properties. Specifically, increased branching lowers the crystallinity and rigidity of polymeric materials, as illustrated by the wide range of polyethylene applications which result from statistically varying the amount of branching. Furthermore, as branching increases, the amorphous regions and the number of end groups also increase. These two properties are important to consider for the biomedical application of polymers, as increasing the amorphous regions

W. Udomkichdecha et al. (eds.), *Materials Challenges and Testing for Manufacturing, Mobility, Biomedical Applications and Climate*,
DOI 10.1007/978-3-319-11340-1_14

and the number of end groups has been shown to lead to an increase in the degradation rate of polyesters.[1] Branched polymers can be divided into two main categories: regularly branched polymers (stars, dendrimers, combs, etc.) and randomly branched polymers (hyperbranched polymers, polyethylene, polyacrylates, etc.). The main difference between these two categories is that randomly branched polymers (RBPs) contain a distribution in the number and/or size of branches, whereas regularly branched polymers do not. Additionally, in RBPs geometrical isomers can be formed, with identical molar mass and amount of branching.[2] Thus, RBPs present a greater challenge for polymer analysis, as precise characterization of both the amount and arrangement of branching (i.e. degree of branching (DB)) is difficult.

The most widely utilized characterization method to determine the DB of RBPs is NMR spectroscopy (^{1}H, ^{13}C, and/or ^{1}H COSY), with peak assignment generally aided by the synthesis of model compounds corresponding to each type of structural unit of the RBP (i.e. terminal, branched, or partially branched monomer units).[3] While this technique is relatively effective, it is both time consuming and potentially limited by the fact that the signal of the polymer backbone can quickly overwhelm that of the branching points, if only small degrees of branching are incorporated. This is an important consideration as only small degrees of branching are required to dramatically alter materials properties.

Another commonly utilized characterization technique is size-exclusion chromatography (SEC), which separates polymer chains according to hydrodynamic volume. When coupled to a multiangle laser light scattering detector (MALLS) and/or a viscosity detector, it is possible to obtain information about the number average molecular weight (M_n) or weight average molecular weight (M_w) during the elution chromatogram.[4-7] However, this does not overcome the fundamental problem of SEC for RBPs- namely, co-elution of different molecular species due to the heterogeneity of both molecular weight and structural topology of RBPs- and thus molar mass and size information again only represent averaged values at any time point during the elution.[7]

Mass spectrometry, specifically matrix-assisted laser desorption ionization time-of-flight mass spectrometry (MALDI-TOF MS), can provide complementary information for polymer analysis, including accurate measurement of the degree of polymerization (DP), detailed end group analysis, and fragmentation to enable structural characterization,[8] however its utility for RBPs is largely unrealized to this point, as RPBs are typically polydisperse, and often high in molecular weight, and both of these factors can complicate MS analysis. Wolf and Frey report that it is possible to distinguish subdistributions in the MALDI-TOF spectra of hyperbranched poly(lactide) copolymer, with each subdistribution corresponding to a different number of incorporated branching units. For their samples this required fractionation by SEC prior to MALDI-TOF MS acquisition, due to the broad molecular weight distribution, and not all fractions yielded acceptable MALDI signal intensity.[9]

Chromatography techniques alternative to SEC, such as liquid adsorption chromatography (LAC) or liquid adsorption chromatography at the critical conditions (LACCC), have proven useful for the separation of complex polymers according to their chemical composition rather than their hydrodynamic volume.[10-12] LACCC and gradient chromatography were recently reported to separate aromatic hyperbranched polyesters with a correlation between degree of branching and elution volume.[13] However, these non-SEC chromatographic techniques have yet to be coupled to MS for the analysis of RBPs.

Therefore, the goal of this work is to develop non-SEC chromatographic methods for the structural resolution of hyperbranched RPBs, and couple this chromatographic separation to MALDI-TOF MS analysis, in order to enable detailed structural characterization. Commercially available aliphatic hyperbranched polyesters prepared from the polycondensation of 2,2-bis(hydroxymethyl)propionic acid (bis-MPA) with an ethoxylated pentaerythritol core (PP50) (marketed as Boltorn^{TM} polymers) were chosen for these initial studies.[14] These polymers are biomedically relevant, as they are biocompatible, biodegradable, nontoxic, and highly soluble, and have been investigated for applications such as encapsulation, controlled release, gene delivery, and the formation of unimolecular micelles.[2]

2. Experimental Procedures and Methods

High performance liquid chromatography (HPLC) was performed on an Agilent system (Agilent Technologies GmbH, Boeblingen, Germany) consisting of a 1200 series degasser (G1322A), 1100 series quaternary pump (G1311A), 1200 series autosampler (G1329A), 1100 series column oven (G1316A), and 1100 series variable wavelength detector (G1314A). The HPLC system was coupled to an evaporative light scattering detector (PL-ELS 1000, Polymer Laboratories), with a nitrogen flow rate of 1.0 SLM, nebulizer temperature of 40°C, and evaporator temperature of 80°C. Data collection and processing was performed with Agilent Chemstation for LC 3D systems (Rev.B.04.01). Chromatography was performed on a single Nucleosil column (5 µm, 100 Å, 4.6 mm ID, Macherey-Nagel, Düren, Germany). For chromatographic conditions, the injection volume was 25 µL, sample concentrations were 2-10 mg/mL, the column temperature was 45°C, and the flow rate was 0.5 mL/min. Acetone (Merck, Darmstadt, Germany) and n-hexane (Carl Roth, Karlsruhe, Germany) were HPLC grade and used as received.

MALDI-TOF MS was performed on a Bruker Autoflex III (Bruker Daltonik GmbH, Bremen, Germany) equipped with a Smartbeam^{TM} laser (356 nm, frequency 200 Hz). Polymer samples were prepared at approximately 2 mg/mL, the matrix (dithranol) was prepared at 10 mg/mL, and sodium trifluoroacetate (3 mg/mL) was used for ionization, with all solutions prepared in tetrahydrofuran. The polymer (20 µL), matrix (50 µL), and counterion (3 µL) solutions were mixed, and 3 µL was spotted on the MALDI target using the dried droplet technique. MALDI spectra were calibrated with an external PEG standard. The instrument was operated in reflector mode with the following parameters: IS1 19.00 V, IS2 16.60 V, Lens 8.60 V, R1 21.00 V, R2 9.70 V, and extraction delay 0 ns. The laser power was generally set to 25-30%, and each spectrum was a total of at least 10000 laser shots. The data was acquired in FlexControl (Version 3.0), and the data processed with FlexAnalysis (Version 3.0) (Bruker Daltonik GmbH, Bremen, Germany).

Boltorn™ hyperbranched polyesters (H20. H30, and H40 premium grade) (see Figure 1) were obtained from Polymer Factory Sweden AB, Stockholm, Sweden. The numbers (20, 30, or 40) represent the "pseudo-generation" of the polymer, and the average number of hydroxyl groups is 16, 32, and 64, respectively.

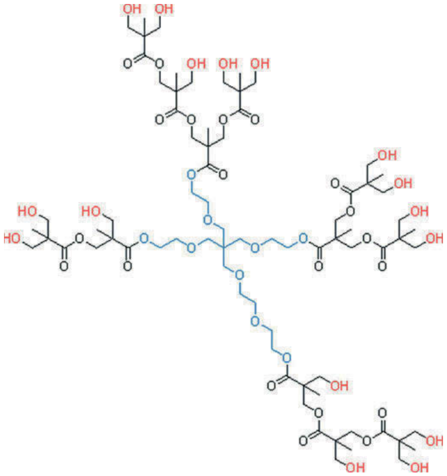

Figure 1. Representative structure of Boltorn H20. This particular structure represents the average number of hydroxyl groups (16) and the average number of ethylene oxide groups (5) present on the PP50 core molecule, however many structural isomers are possible even with this particular (average) chemical formula.

3. Results and discussion

3.1 Liquid Chromatography

After initial investigations into reverse phase and gradient chromatographic conditions for Boltorn™ polymers (not presented), a LAC chromatographic system was chosen instead. In LAC, enthalphic interactions between the analyte and the stationary phase govern retention, and analytes are typically eluted from low molecular weigh to high molecular weight (i.e. opposite the order of elution in SEC separations). Similarly to work reported for LACCC of poly(lactide),[12] the hydroxyl groups of the Boltorn samples were expected to have strong adsorptive interactions with the stationary phase. Thus, a polar silica column was chosen as the stationary phase, and a moderately polar solvent (acetone) was selected as the mobile phase, with the polarity modified as necessary with small amounts of n-hexane. Figure 2 displays the chromatograms of all three Boltorn samples under these LAC conditions.

As seen in Figure 2, all three samples elute as relatively broad peaks with the same general retention time. The sharp peaks within the overall distribution, particularly observed between 5 and 10 min retention time, were consistent between runs for each sample and indicated the possibility of some sort of structural resolution, perhaps by DB, DP, or architecture.

In order to further investigate this effect, fractions were collected from the chromatographic runs. Initial chromatographic experiments were performed with a 2 mg/mL sample concentration for all Boltorn polymers. However, further investigations indicated that it was possible to increase the sample concentration to 6 mg/mL for Boltorn H30 and 10 mg/mL for Boltorn H40 with no loss of resolution in the resulting chromatogram (with these concentrations largely determined by the solubility of the each polymer in acetone). Thus, these higher sample concentrations were utilized for the fraction collection in order to minimize the number of runs needed to obtain sufficient material for MALDI-TOF MS analysis. Fractions were collected every 2 minutes, beginning from 6 min and ending at the end of the elution for each sample. For H20, H30, and H40 the number of HPLC runs performed was 20, 10, and 5, respectively, with the solvent removed by evaporation prior to re-solvation in 40 μL of THF for MALDI-TOF MS.

3.2 Mass Spectrometry

While, as mentioned previously, MALDI-TOF MS analysis of RBPs can be complicated by high molecular weight and polydispersity (PDI), all three Boltorn samples have relatively low PDIs (<1.4) and low molecular weights (<10 kDa theoretical). Thus, the total MALDI-TOF spectra of each sample are easily obtained with dithranol as the matrix and sodium trifluoroacetate to assist in ionization. However, as is shown in the example spectrum for Boltorn H30 (Figure 3), the spectra are quite complicated and contain numerous (>15) subdistributions. All of the subdistributions (each marked with a different color in the Figure 3 inset) are separated by a mass of ~116 Da (corresponding to the molecular weight of the bis-MPA monomer), but are offset from one another, indicating a possible difference in chemical structure. Ionization studies indicate that all species are singly charged $[M+Na]^+$ adducts, and thus these numerous subdistributions do not seem to result from ionization with different cations (e.g. H^+ of K^+) or the presence of multiply charged species.

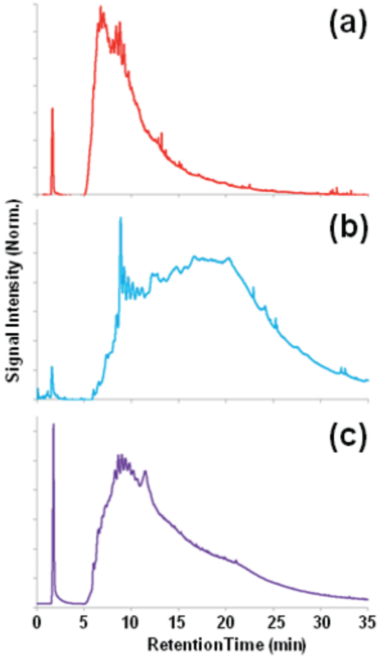

__Figure 2.__ LAC chromatograms for (a) Boltorn H20 (b) Boltorn H30 and (c) Boltorn H40. For (a) and (b) the mobile phase was 99% acetone/1% n-hexane (v/v), and for (c) the mobile phase was 100% acetone. The sharp peaks within the overall broad distribution (especially between 5 and 15 min in all samples) were consistent between runs and indicated the possibility of structural resolution.

The complexity of the total MS of these polymer samples stems from the complexity of the samples themselves. Of course, as for all polymers with polydispersity, a Gaussian distribution of signals is expected for each distribution, which results directly from the number of monomers on each molecule (i.e. DP). Additionally, however, the PP50 core used in the polycondensation is itself a polydisperse molecule. Thus, while the PP50 core has an average of 5 ethylene oxide units, variations of this number in either direction are possible, so that a normal Boltorn molecule with a DP=10, for example, will result in multiple signals due to the presence of multiple core species. Furthermore, Boltorn polyesters are known to form cycles through intramolecular esterification or etherification, either with or without a core molecule. Additionally, intermolecular esterification or etherification can occur, which can result in two core species on one molecule. Finally, it is also reported in the literature that the bis-MPA molecules can self-condense with no core molecule at all.[15]

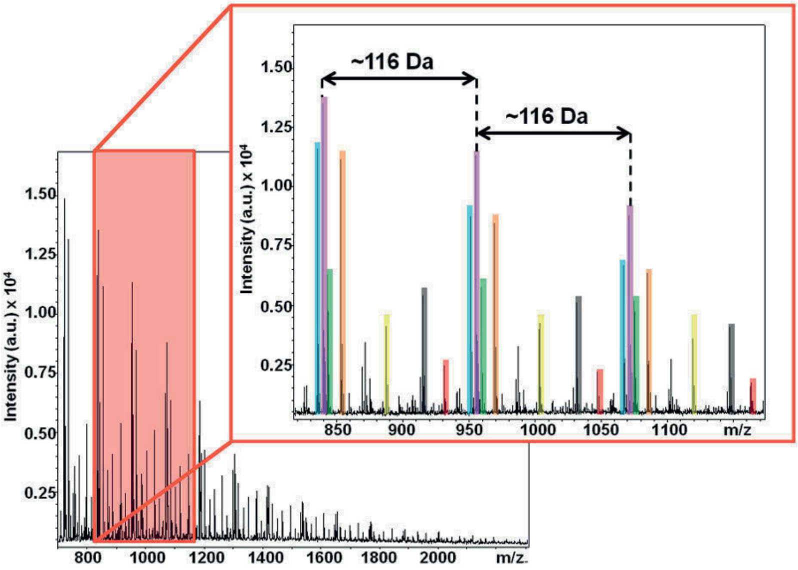

Figure 3. *MALDI-TOF MS spectra for Boltorn H30. On the left is the total spectrum of the sample, from m/z 800 to 2200. The box on the left highlights the region which is expanded in the inset on the right (from m/z 850 to 1150). In the inset, the different shaded boxes each correspond to a different subdistribution, separated by ~116 Da. Only seven major distributions are highlighted to enhance clarity, but eight more are easily visible, for a total of at least 15 different structures in this one sample.*

The MALDI data for the Boltorn H30 fractions, as a representative example, is displayed in Figure 4. Confirming that the separation mechanism was indeed adsorption, for any given subdistribution the molecular weight increases with retention time. This effect can be clearly observed by examining the signals marked by an asterisk (*) in the first four fractions in Figure 4. With careful MALDI-TOF calibration, the observed *m/z* values can be accurately compared to theoretical (calculated) values for the possible Boltorn structures discussed previously. For example, the calculated monoisotopic mass $[M+Na]^+$ for an intramolecularly cyclized Boltorn molecule (DP=10) with no core is 1183.46 Da. This corresponds closely to the observed peak in the (*) distribution at 1183.55 Da, indicating that cyclized Boltorn elutes first. The next distribution, marked by triangles, appears in fraction 2, offset from the first distribution by +4 Da. It is probable that this is also a molecule without a core, as there is only one such distribution and not several, as would be expected if the PP50 molecule was incorporated. However, it could not be conclusively identified as one of the structures known to exist in Boltorn samples, and thus perhaps is the result of an unknown starting material impurity in the bis-MPA monomer or core molecule.

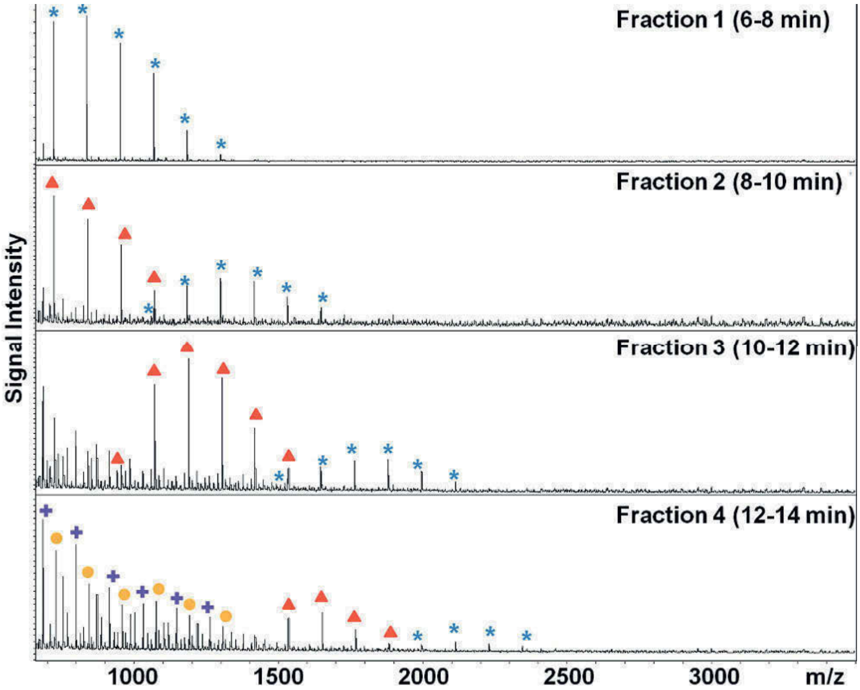

__Figure 4.__ MALDI-TOF MS spectra for the first 4 fractions collected for Boltorn H30. Each symbol corresponds to a different structure, or subdistribution. The asterisk distribution is a cyclized Boltorn with no core molecule, while the circle and cross distributions are hyperbranched Boltorn with PP50 core molecule. The triangle distribution could not be identified.

Beginning in fraction 3 (Figure 4), the lower molecular weight region of the spectrum becomes much more complicated. This is the start of the elution of the "normal" hyperbranched Boltorn with a PP50 core molecule (that is, variations of the non-cyclic structure in Figure 1). In fraction 4, two of these distributions are marked. The distribution marked with the circles corresponds to the Boltorn with the PP50 core molecule as drawn (with 5 ethylene oxide groups), while the cross distribution corresponds to Boltorn with the PP50 core molecule with only 4 ethylene oxide groups. The other two main distributions in fraction 4 (not marked) correspond to Boltorn with a PP50 core molecule with either 6 or 3 ethylene oxide groups. Boltorn with the PP50 core with 3 through 6 ethylene oxide groups remain the primary distributions for fractions 5-8 (14-22 min retention time), with the additional appearance of a PP50 core with 7 ethylene oxide units beginning in fraction 6. As observed for the early eluting cyclic distribution, the Boltorn with PP50 core distributions likewise increase in molecular weight with increasing elution time. There was no evidence of intermolecular dimerization or cyclic molecules containing a core in any of the mass spectra. These same general trends were observed in the fractions collected for Boltorn H20 and H40.

4. Conclusion

LAC conditions have been established which allow the separation of Boltorn hyperbranched polyesters based on architecture (cyclic versus non-cyclic). Furthermore, this LAC separation enables better MALDI-TOF MS analysis, as the fractionation increases signal intensity for each subdistribution relative to the total mass spectrum. As the same Boltorn structure (non-cyclic) is eluted in the latter half of each spectrum, it is possible that this broad elution is governed by degree of branching, however further investigations are needed. Only cyclic Boltorn with no core and non-cyclic Boltorn with a PP50 core were observed in the mass spectra.

Acknowledgement

Bianka Manger (HPLC) and Rosemarie Laging (MALDI-TOF MS) are thanked for their assistance in data acquisition. This work was partially funded by an Adolf Martens Postdoctoral Fellowship from BAM (to J.N.H.).

References

1. Numata K, Srivastava RK, Finne-Wistrand A, Albertsson A-C, Doi Y, Abe H (2007) Branched Poly(lactide) Synthesized by Enzymatic Polymerization: Effects of Molecular Branches and Stereochemistry on Enzymatic Degradation and Alkaline Hydrolysis. Biomacromolecules 8 (10):3115-3125.
2. Žagar E, Žigon M (2011) Aliphatic hyperbranched polyesters based on 2,2-bis(methylol)propionic acid—Determination of structure, solution and bulk properties. Prog Polym Sci 36 (1):53-88.
3. Hawker CJ, Lee R, Frechet JMJ (1991) One-step synthesis of hyperbranched dendritic polyesters. J Am Chem Soc 113 (12):4583-4588.
4. Wyatt PJ (1993) Light scattering and the absolute characterization of macromolecules. Anal Chim Acta 272 (1):1-40.
5. Podzimek S (1994) The use of GPC coupled with a multiangle laser light scattering photometer for the characterization of polymers. On the determination of molecular weight, size and branching. J Appl Polym Sci 54 (1):91-103.
6. Simon PFW, Müller AHE, Pakula T (2001) Characterization of Highly Branched Poly(methyl methacrylate) by Solution Viscosity and Viscoelastic Spectroscopy. Macromolecules 34 (6):1677-1684.

7. Gaborieau M, Nicolas J, Save M, Charleux B, Vairon J-P, Gilbert RG, Castignolles P (2008) Separation of complex branched polymers by size-exclusion chromatography probed with multiple detection. Journal of Chromatography A 1190 (1–2):215-223.
8. Weidner SM, Trimpin S (2010) Mass Spectrometry of Synthetic Polymers. Anal Chem 82 (12):4811-4829.
9. Wolf FK, Frey H (2009) Inimer-Promoted Synthesis of Branched and Hyperbranched Polylactide Copolymers. Macromolecules 42 (24):9443-9456.
10. Weidner SM, Falkenhagen J, Knop K, Thünemann A (2009) Structure and end-group analysis of complex hexanediol-neopentylglycol-adipic acid copolyesters by matrix-assisted laser desorption/ionization collision-induced dissociation tandem mass spectrometry. Rapid Commun Mass Spectrom 23 (17):2768-2774.
11. Falkenhagen J, Weidner SM (2005) Detection limits of matrix-assisted laser desorption/ionisation mass spectrometry coupled to chromatography – a new application of solvent-free sample preparation. Rapid Commun Mass Spectrom 19 (24):3724-3730.
12. Biela T, Duda A, Rode K, Pasch H (2003) Characterization of star-shaped poly(l-lactide)s by liquid chromatography at critical conditions. Polymer 44 (6):1851-1860.
13. Al Samman M, Radke W, Khalyavina A, Lederer A (2010) Retention Behavior of Linear, Branched, and Hyperbranched Polyesters in Interaction Liquid Chromatography. Macromolecules 43 (7):3215-3220.
14. Malmström E, Hult A (1996) Kinetics of Formation of Hyperbranched Polyesters Based on 2,2-Bis(methylol)propionic Acid. Macromolecules 29 (4):1222-1228.
15. Žagar E, Žigon M (2002) Characterization of a Commercial Hyperbranched Aliphatic Polyester Based on 2,2-Bis(methylol)propionic Acid. Macromolecules 35 (27):9913-9925.

Quantitative Online NMR Spectroscopy of Technical Mixtures: On the Fly Quantification of Fluids

Michael Neugebauer, Nicolai Zientek, and Michael Maiwald

BAM Federal Institute for Materials Research and Testing, Richard-Willstaetter-Str. 11, D-12489 Berlin, Germany, michael.neugebauer@bam.de

Abstract

In this paper quantitative NMR spectroscopy is demonstrated as a tool for process analytical technology (PAT) in order to obtain real time information from dynamic processes. Different methods for quantification are presented and as a result the limit of detection for NMR measurement could be determined to 3.3 mg kg^{-1} (ethanol in water). As model processes esterification reactions and dissolution of pharmaceutical formulations are presented and important process parameters are extracted. Furthermore it is demonstrated that not only ^{1}H-NMR spectroscopy can be used for process monitoring but also ^{13}C-NMR for technical mixtures.

Keywords: *NMR; Quantification; Online; Process Analytical Technology.*

1. Introduction

Reliable manufacturing and process analytical technology (PAT) go together. The conventional way of monitoring processes is the measurement of pressure, temperature, mass flow and physicochemical properties. Nowadays an increasing number of spectroscopic methods are involved in PAT. Most often, NIR and UV/VIS spectroscopy are used to get more specific information out of the process. Those methods in general do not give detailed chemical information, however, from nuclear magnetic resonance spectroscopy (NMR) such chemical information can be retrieved.

NMR spectroscopy is one of the most important analytical methods in science and medicine. NMR spectra provide a lot of information on physico-chemical properties of the analyte as well as, e.g. on its configuration and conformation. Usually NMR spectroscopy is applied for structure determination. Spectra are recorded at stationary conditions and the analyte is prepared in deuterated solvents. In addition, NMR spectroscopy is a useful tool for quantification [1] because the peak area is directly proportional to the number of nuclei. Furthermore, NMR

W. Udomkichdecha et al. (eds.), *Materials Challenges and Testing for Manufacturing, Mobility, Biomedical Applications and Climate*,
DOI 10.1007/978-3-319-11340-1_15

spectroscopy can also be performed at flow conditions, for example as a detector for HPLC [2].

Here we present a combination of the two techniques, flow NMR and quantitative NMR spectroscopy (qNMR), which allows online monitoring of chemical reactions. Therefore technical mixtures, i.e. pure analytes or reaction mixtures, are pumped out of the reactor directly through the spectrometer without further preparation. Under flow conditions, monitoring of dynamic changes of composition in reactions and processes can be carried out simultaneously to structure verification. Even intermediates can be detected and quantified. Another advantage of flow NMR spectroscopy over the static method is the ability for real-time manipulations on the system under investigation.

2. Methods

The experimental setup is shown in figure 1 [3]. The vessel **C1** is equipped with a stirrer **M1**. A dosing pump **P1** (HPD Multitherm 200, Bischoff Chromatography, Leonberg, Germany, 0.1–20 ml min^{-1} flow rate, thermostated hastelloy pump head) is used to transport the reaction mixture from the vessel to the T-split. Filters **F1**, **F2** are equipped to the PEEK tubing to prevent blocking caused by particles. **V**alve **4** regulates the T-split. The 500 MHz NMR spectrometer DDR2 (Agilent Technologies, Santa Clara, CA, United States) is equipped with a flow probe (95 µl active volume). The length of the tubing between vessel and NMR is about 5 m.

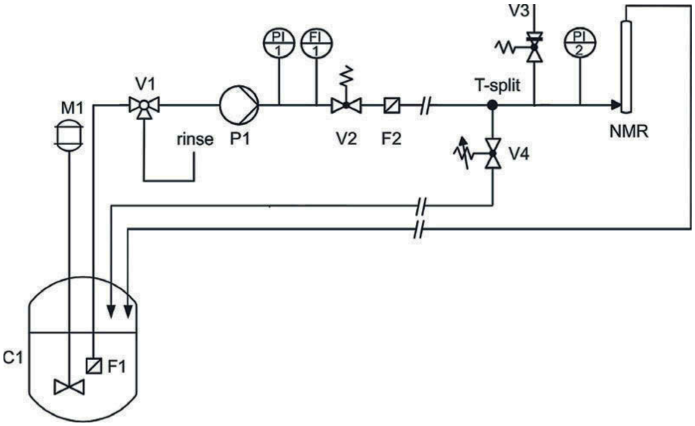

Figure 1. *Experimental setup, PI pressure indicator, FI flow indicator, V valves [3].*

For experiments on methanol in biodiesel, the NMR spectrometer was equipped with an OneNMR probe for 5 mm tubes.

3. Results and discussion

3.1 LoD & LoQ — ethanol in water

Quantification of organic substances at low concentrations in water is a common task. Therefore, the limit of detection (LoD) was determined for a straightforward NMR spectroscopic method. Solutions of ethanol in water were available from calibration series for the certified reference materials (CRM) BAM–K001 … BAM–K007 used for the calibration of breath alcohol analyzers. These solutions were further diluted gravimetrically to obtain the concentrations used here.

A series of NMR spectra with different ethanol concentrations was recorded in stopped flow mode. Figure 2 shows a spectrum of a highly diluted solution containing only 0.6 mmol L^{-1} ethanol corresponding to approximately 10.7 ppm (*n*/*n*). At first glance only the intense water peak can be seen in the spectrum. Nevertheless, at a closer look to 1.16 ppm (chemical shift) one can still identify the triplet of the methyl group of ethanol.

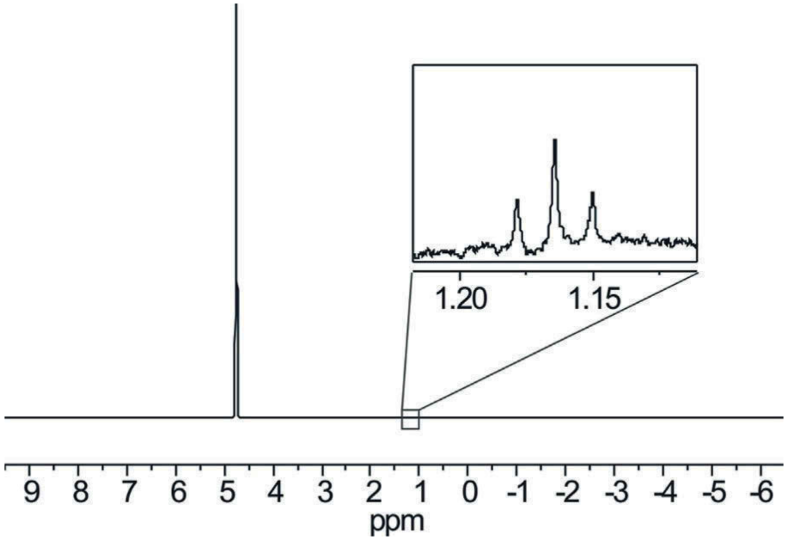

Figure 2. *^{1}H-NMR-spectrum of ethanol in water (27 mg kg^{-1}, 1 scan, no solvent suppression) full spectrum and expansion*

According to ISO 6143 the limit of detection (LoD) for NMR measurement was determined to 3.3 mg kg^{-1}, using only a single NMR pulse and no solvent suppression techniques. The limit of quantification (LoQ) was determined to 10.9 mg kg^{-1}. One can anticipate that these values can still be improved by increasing the number of scans and by solvent suppression techniques (work in progress).

Quantification in NMR spectroscopy is generally performed by referencing to an internal standard, which is added to the sample [1]. For the monitoring of processes this is not desirable since an additional compound can influence the reaction or is affected, e.g., by decomposition. An alternative option is virtual referencing, e.g., using the ERETIC technique (electronic reference to access in vivo concentrations), where electronically generated signals serve as standard by simultaneous acquisition with the sample signals [4]. Due to the stability of present NMR components, the method is obsolete.

As mentioned, due to the extreme linearity of modern NMR equipments, absolute quantifications in liquids became possible after calibrating the spectrometer in a preliminary step. At present, temperature, sample volume, and electrical regulation of the console have to be reproduced reliably. However, a systematic evaluation of sources of uncertainties is still in progress. It turns out that the accuracy of temperature regulation of the probe and the spectrometer electronics are important parameters.

Concentrations of ethanol in water were determined by direct integration method using the absolute quantification method described above. Table 1 shows that the detected ethanol concentrations are in general higher than the estimated values (roughly +3.5%). This may be caused for example by setting of different integration limits between calibration and determination. As integration limits are a crucial step in quantification, peak deconvolution as used for methanol in biofuels (see next section) is recommended, since that method is very robust, as even overlapping peaks may be separated by this deconvolution.

Table 1. *Reference values and experimentally determined concentrations of ethanol in water*

concentration (*m*/*m*)/ g kg^{-1}	estimated concentration/ mmol L^{-1}	found concentrations/ mmol L^{-1}
3.401	≈ 73.8	76.4 ± 0.3
1.139	≈ 24.7	25.7 ± 0.3
0.859	≈ 18.7	19.3 ± 0.2
0.239	≈ 5.2	5.3 ± 0.2
0.027	≈ 0.6	0.6 ± 0.3

3.2 Methanol in biofuels

Determination of methanol concentrations in biofuels is an analytical task, since there is a concentration limit of methanol in biodiesel of 0.2 wt% according to EN 14214 (ASTM D6751). For calibration, a series of NMR spectra in the range of 0.0–0.3 wt% were recorded. Figure 3 shows a ^{1}H-NMR spectrum with

0.15 wt% methanol. Peak areas were determined by spectral deconvolution using Voigt profiles (mixed Lorentz Gauss curves) and calculating the integrals thereof.

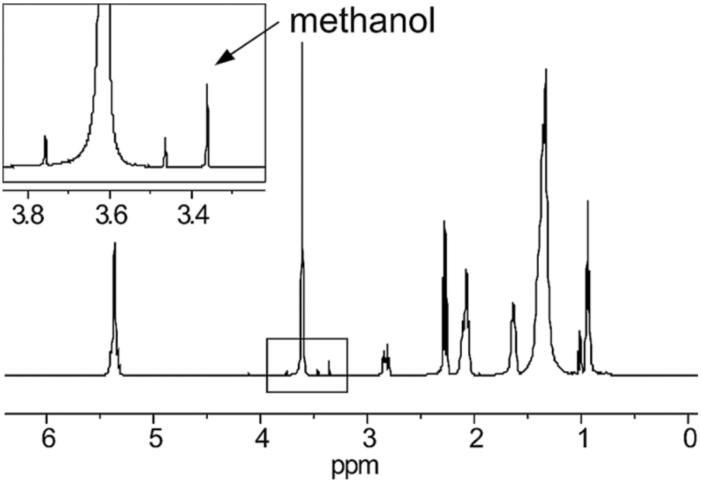

Figure 3. *^{1}H NMR spectrum of rapeseed biodiesel with 0.154 % MeOH. Full spectrum and detail (box). Acquisition: 8 scans, no solvent suppression. The arrow indicates the methanol peak.*

These data were also used for Mandel tests, which gave as result a linear connection between concentration and peak area. These Mandel tests also indicate that integrals of different spectra from the same spectrometer can be compared to each other, as done in the direct integration method. As can be seen in table 2, the NMR results are in good agreement with the gravimetrically determined values.

Table 2. *Mass fractions of methanol in biodiesel determined by NMR spectroscopy and weighing*

feedstock	methanol mass fractions/%wt	
	gravimetrical	NMR
rapeseed based BD	0.154 ± 0.002	0.150 ± 0.003
soy bean based BD	0.154 ± 0.002	0.149 ± 0.004

3.3 Quantification with internal standards

In this chapter precision of quantification by NMR spectroscopy is described using an internal standard. The esterification of acetic acid with methanol to methyl acetate (MeOAc) is used as an example. To monitor the esterification of methanol and acetic acid a reaction mixture according to table 3 was prepared and the reaction monitored by NMR spectroscopy in stopped flow mode. The product was quantified compared to dimethyl sulfoxide (DMSO), which is not taking part in the reaction and can therefore be used as an internal standard. In figure 4 the formation of the product MeOAc is displayed as an increasing signal, with a precision far below 100 ppm. Furthermore, the rate constant of this bimolecular reaction was determined to $k = (1.12 \pm 0.03)\ 10^{-6}\ \mathrm{L\ mol^{-1}\ s^{-1}}$ at $T = 353$ K.

Table 3. *Mole fractions of the initial reaction mixture*

x(water)/ % (*n*/*n*)	*x*(DMSO)/ % (*n*/*n*)	*x*(methanol)/ % (*n*/*n*)	*x*(acetic acid)/ % (*n*/*n*)
69.965	0.096	14.947	14.992

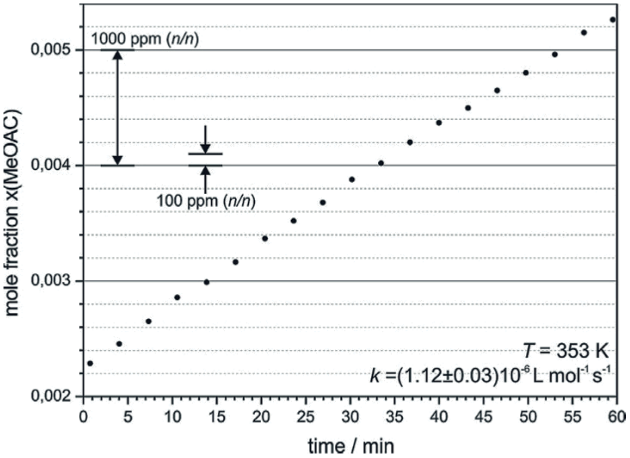

Figure 4. *Formation of MeOAc. Increasing mole fraction of product methyl acetate vs. internal standard DMSO (T = 353 K). NMR spectroscopy short time precisions are below 100 ppm for such experiments.*

3.4 Reaction monitoring

Flow NMR spectroscopy has several advantages in comparison to common NMR spectroscopy. Due to the experimental setup with the flow probe in a thermostated bypass, manipulations on the reaction conditions can be performed at any time without stopping the measurement, which is not possible when conventional NMR tubes are used. Since the technical mixture is not diluted during sample preparation, it is possible to use just a small number of scans in ^{13}C-NMR spectroscopy. It should be pointed out that the sensitivity for ^{13}C is approximately

5700 times lower than that of ^{1}H [5]. However, for the first time, an array of ^{13}C NMR spectra is presented in figure 5 following the course of the reaction with only a single ($^!$) ^{13}C NMR acquisition for each time step. Butanol and acetic acid undergo an esterification forming butyl acetate. The reactor was filled with the reactants and the mixture was cycled through the spectrometer. Addition of oleum (H_2SO_4) after 30 min, which acts as a catalyst, considerably accelerated the reaction (cf. Figure 6).

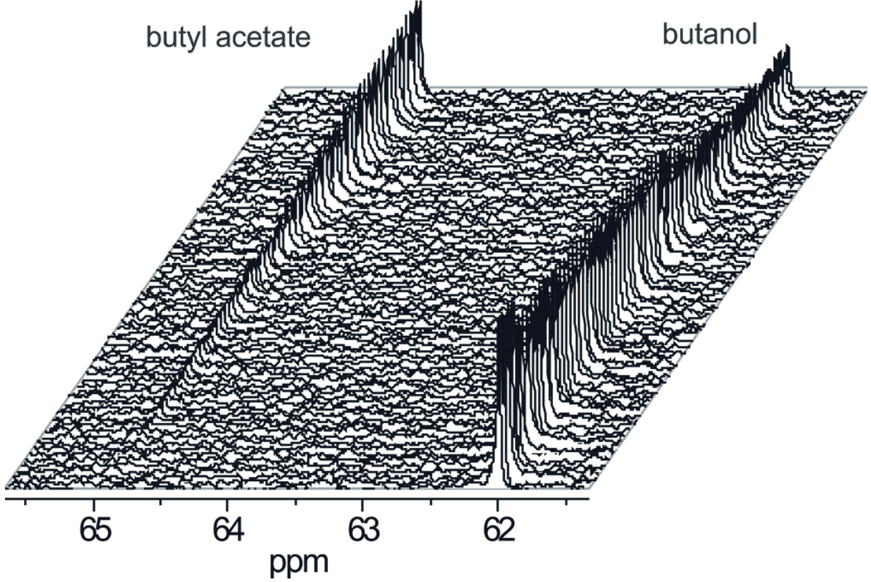

Figure 5. Detail of arrayed ^{13}C NMR spectra (single scan) used for reaction monitoring (signals of –C–O of the n-butyl / 1-butanol)

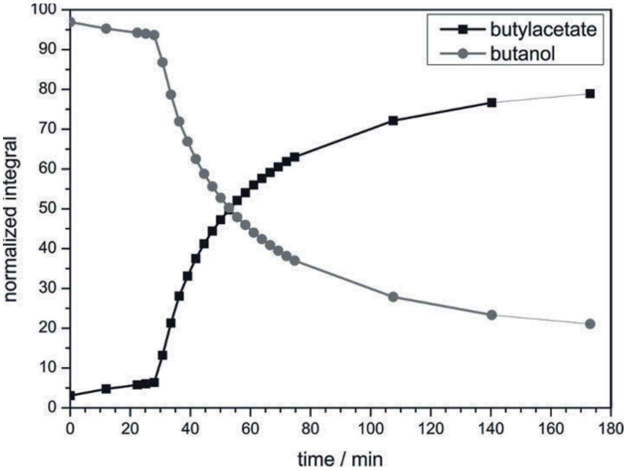

Figure 6. Time dependent normalized integral intensities of butanol and butyl acetate from ^{1}H-NMR spectra.

3.5 Dissolution of pharmaceutical formulations

Dissolution tests of pharmaceutical solid dosages are routinely performed in standard apparatuses during pharmaceutical formulation development. Normally chromatographic methods or UV/VIS spectroscopy are used as detection methods [6]. Here we present an alternative NMR method, which advantageously can be used to detect the time behaviour of individual components in such formulations. The dissolution of paracetamol in water was studied as an example.

Therefore, an online NMR setup was used as described above. The bypass was closed at valve V4 and water (~450 ml) was cycled through the spectrometer with a flow rate of 1 ml min^{-1}. The vessel was stirred with 700 rpm and methanol was added. After five minutes, a paracetamol tablet (acetaminophen, 500 mg drug, tablet 650 mg) was added in a cage to prevent additional crushing by the stirrer [6]. The increasing signals are fitted by ascending sigmoidal Boltzmann curves using equation 1 and are depicted in figure 7 [7]. In addition, step traces experiments were carried out in order to study transport delays from the stirring vessel to the NMR spectrometer.

$$y = b + \frac{a-b}{1+\exp\left(\frac{x-c}{d}\right)} \qquad \Leftrightarrow \qquad x = c + d \cdot \ln\left(\frac{a-b}{y-b} - 1\right) \tag{1}$$

a = start value of integrals, *b* = end value of integrals, *c* = inflexion point/min, *d* = time constant/min

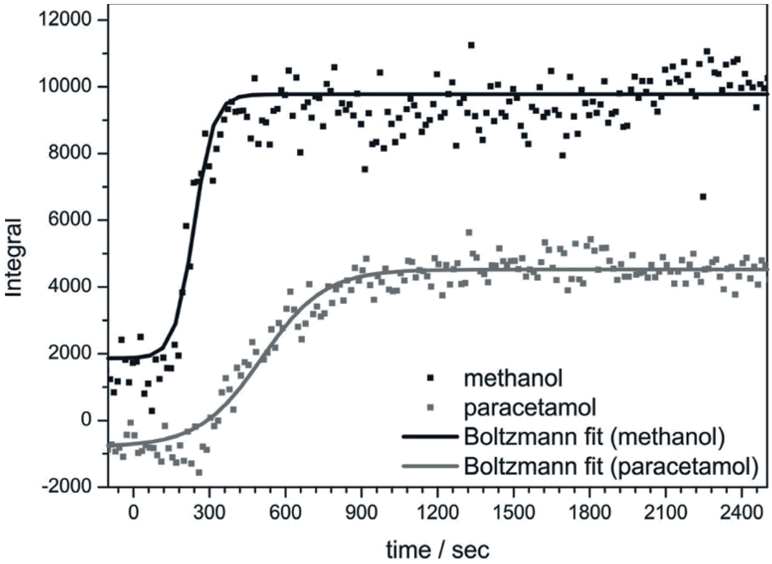

Figure 7. *Black: methanol, grey: Me (acetaminophen); squares: peak integrals, lines: fitted sigmoid Boltzmann curves*

Assuming instantaneous distribution of methanol over the whole vessel after addition, the black curve in figure 7 of methanol peak areas describes the residence time behaviour of the setup. The grey curve in addition includes the dissolving process of the tablet. In order to illustrate these processes, inflexion point *c* and time constant *d* deduced from the sigmoid fit shown in figure 7 are provided in table 4. Parameters *a* and *b* represent only numbers of the integrals, but inflexion point *c* defining the position in the time scale and time constant *d* defining how fast the curve ascends are the essential parameters of the fit.

Table 4. *Essential parameters inflexion point c and time constant d deduced from the sigmoidal fits*

	methanol	paracetamol
c / min	236 ± 6	509 ± 10
d / min	37 ± 5	123 ± 8

4. Conclusion

Online NMR Spectroscopy provides quantitative information on the chemical composition and also facilitates structure elucidation at the same time. Measurement of batch processes in flow mode with a bypass setup enables to acquire process information in real-time. This, taken together, induces the high potential of high resolution online NMR spectroscopy as a tool for PAT. Based on selected exemplary processes some applications of quantitative flow NMR spectroscopy are demonstrated.

Regarding quantitative examination, different kinds of quantification techniques, e.g., using an internal standard, spectral deconvolution, direct integration, as well as the internal referencing tool were successfully applied. Spectral deconvolution is useful if peaks are overlapping and direct integration, however, is not applicable. The same applies to the use of the internal referencing method, which is superior to internal standards if signal overlapping occurs or interference with the process cannot be ruled out. However, each method provides reliable information. For a modern 500 MHz NMR spectrometer, limits of detection of 10 mg kg^{-1} for methanol in water were found with a straightforward method. This could be further improved by control of the environmental conditions of the NMR probe or the console. Therefore, qNMR spectroscopy becomes interesting for the pharmaceutical development, e.g., for purity assessments of active pharmaceutical ingredients or studies of real-time release of pharmaceuticals.

Acknowledgement

The authors kindly thank Bastian Bräuer for sample preparation (methanol in biodiesel), Hugo Ent (VSL) for the kind supply of biodiesel and Andrea Paul for proof reading. We also thank DFG for financial support.

References

1 Malz F, Jancke H (2005) Validation of quantitative NMR. J Pharm Biomed Anal 38: 813–823
2 Bayer E, Albert K, Nieder M, Gromm E, Keller T (1979) On-line coupling of high-performance liquid chromatography and nuclear magnetic resonance. J Chromatogr 186: 497–507
3 Maiwald M, Fischer HH, Kim Y-K, Albert K, Hasse H (2004) quantitative High-resolution on-line NMR spectroscopy in reaction and process monitoring. J of Magnet Reson 166: 135–146
4 Akoka S, Barantin L, Trierweiler M (1999) Anal Chem 71:2554–2557
5 Harris RK (1976) N.m.r. and the periodic table. Chem Soc Rev 5: 1–22
6 Klein S (2012) Anwendung und Vergleich unterschiedlicher Dissolutionsmethoden. TechnoPharm 2: 54–61
7 Costa P, Sousa Lobo JM (2001) Modelling and comparison of dissolution profiles. Eur J Pharma Sci 13:123–133

Aspect-ratio-controlled Au Nanorods: Preparation and Dispersion toward Applications

Yoshiko Takenaka[1]

[1] *National Institute of Advanced Industrial Science and Technology, Tsukuba, Ibaraki, 305-8565, Japan*

Abstract

The synthesis of aspect-ratio-controlled gold nanorods is introduced. Gold nanorods are usually synthesized in a liquid-state surfactant solution. In this paper, we present that their synthesis in a gel-state surfactant solution is useful to control their diameter and length in wide range. The diameter is controlled from ~ 10 to 80 nm. According to the previous study, it is reported that a decrease in the curvature of the surfactant bilayer neighboring the gold surface affects the increase in the nanorod diameter. In this paper, we synthesize the nanorods with different kinds of surfactants and confirm that the mechanism is appropriate. We also introduce a method to control the long-axis length of gold nanorods in a gel-state surfactant solution from several tens of nm to 1 μm. The dispersion method of high-aspect-ratio gold nanorods is also presented.

Keywords: *Gold nanorods, Surfactant self-assembly, Size control.*

1. Introduction

Gold nanorods, which are expected to be used in many applications[1], are one-dimensional crystals of gold. Some of the applications use the plasmon absorption whose wavelength depends on the aspect-ratio (AR) of gold nanorods. Low-AR gold nanorods (AR < 10) have the absorption wavelength in the region from visible-light to near infra-red and are studied extensively for the medical probes which can kill the cancer cells [2] through the irradiation from outside the body. While, high-AR gold nanorods (AR > 20) are expected for the application to electrodes [3], nano-gap electrodes [4,5], and so on. Thus, the control of the diameter and length of the nanorods is important.

W. Udomkichdecha et al. (eds.), *Materials Challenges and Testing for Manufacturing, Mobility, Biomedical Applications and Climate*,
DOI 10.1007/978-3-319-11340-1_16

There are many reports of high-yield synthesis of gold nanorods [6-11]. It is well known that the gold nanorods grow spontaneously in a cationic surfactant solution. In previous works, HNO_3 [7], nitrate [8] or NaOH [10] were often added to a surfactant growth solution to control the size of gold nanorods. In such case, the possible control range of the diameter and the length of gold nanorods were from ~10 to 30 nm and from ~ 10 to 500 nm, respectively.

Recently we reported that the gelation of a surfactant growth solution, i.e. structural change in self-assembly of surfactant molecules, affects the morphology of gold nanorods [11,12]. Here we will present the methods how we can use the gelation to control the diameter and the length of gold nanorods. At the last section, we will also discuss the dispersion of high-aspect-ratio gold nanorods (AR ~ 50).

2. Control of the nanorod diameter

Following to the previous study [12], we synthesized gold nanorods in octadecyltrimethylammonium bromide (OTAB: $C_{18}H_{37}N(CH_3)_3Br$, Wako Pure Chemical Industries) solution. As shown in Fig. 1, when the growth temperature was 35 °C, the growth solution was in a liquid-state and the average diameter of gold nanorods was ~ 20 nm (Fig. 1a). On the other hand, when the growth temperature was 15 °C, the growth solution was in a gel-state and the average diameter of gold nanorods was ~ 80 nm (Fig. 1b). From the observation of small-angle X-ray scattering (SAXS), we revealed that the micellar structure appears in a liquid-state solution, while the lamellar structure with interdigitation appears in a gel-state solution. As a result, we presented a model that the decrease in the curvature of the surfactant membrane neighboring the gold surface affects the increase in the diameter of gold nanorods [12]. It is commonly known that gold nanorods are covered with surfactant bilayer in a growth solution. Thus we considered that structural transition of the self-assembly of surfactant molecules should affect the diameter of gold nanorods.

To confirm the above model, we synthesize gold nanorods with different surfactants and compared their diameter. We use 200 mM hexadecyltrimethylammonium bromide (HTAB: $C_{16}H_{33}N(CH_3)_3Br$, Tokyo Chemical Industry) solution and 200 mM mixed solution of HTAB and OTAB with the ratio of 1:1. The length of the hydrophobic part of HTAB is shorter than that of OTAB. Assuming that HTAB and OTAB are mixed homogeneously, the curvature of the membrane made of HTAB is larger than that of the mixed surfactants. It menas that the diameter of gold nanorods grown in the HTAB solution will be smaller than that grown in the mixed solution.

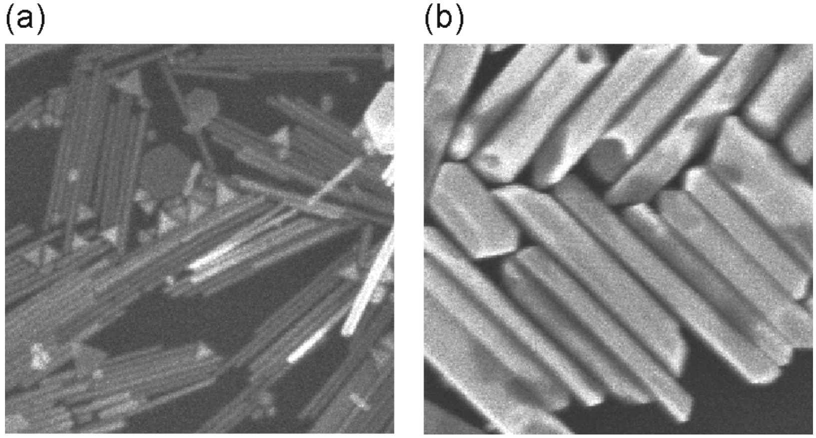

Figure 1. *SEM images of gold nanorods. Growth temperatures are (a) 35 °C and (b) 15 °C. Scale bar is 1 μm.*

By the seeding method, we synthesize gold nanorods at 15 °C. The procedures for the synthesis are the same as the case of OTAB expect for surfactants [12]. Figure 2 shows the SEM images of gold nanorods grown in the HTAB solution and in the mixed solution. When we used the HTAB solution, the diameter of the gold nanorods is 15.0 ± 2.5 nm. On the other hand, the diameter is 24.7 ± 4.1 nm for the mixed solution. As we expected above, the diameter of gold nanorods grown in the HTAB solution is smaller than that grown in the mixed solution. Therefore we can conclude that the model is appropriate.

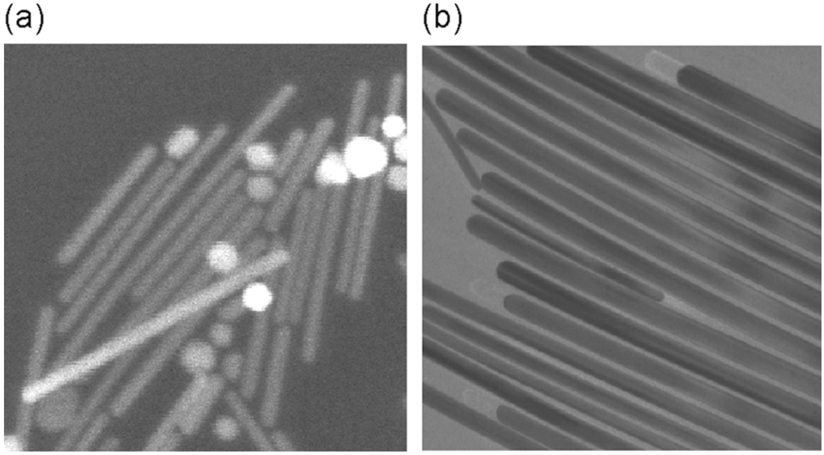

Figure 2. *SEM images of gold nanorods. The surfactants of the growth solution are (a) 200 mM HTAB and (b) 200 mM mixed solution of HTAB and OTAB with the ratio of 1:1, respectively. Growth temperature is 15 °C in both cases. Scale bar is 100 nm.*

3. Control of the nanorod length

The synthesis of gold nanorods in a gel-state surfactant solution is also useful to control the long-axis length of gold nanorods. When the mixed surfactant of HTAB and OTAB with the ratio of 1:1 was used, the gold nanorods with the length of around 1 μm can grow at 15 °C [11]. The technique to stop the growth at any instant by the addition of the dodecanethiol [13] allows us to obtain the nanorods with favorite length from ~ 10 nm to 1 μm. The mechanism how the gelation affects the nanorod length is now investigated.

4. Dispersion of high-aspect-ratio gold nanorods

Toward applications, the dispersion of gold nanorods in an aqueous solution is important. Gold nanorods usually grow in a surfactant solution whose concentration is much higher than its critical micelle concentration (CMC), thus the centrifugation after the synthesis is important to wash out the excess surfactants. We can easily disperse the low-AR gold nanorods in an aqueous solution. For the high-AR gold nanorods, however, they do aggregate during the centrifugation process (Fig. 3a). To avoid the aggregation, we modified the surfaces of the gold nanorods by mercaptosuccinic acid ($C_4H_6O_4S$, Tokyo Chemical Industry). Mercaptosuccinic acid has negative charge attributed to the carboxyl group, thus the gold nanorods become repulsive each other and they disperse well (Fig. 3b).

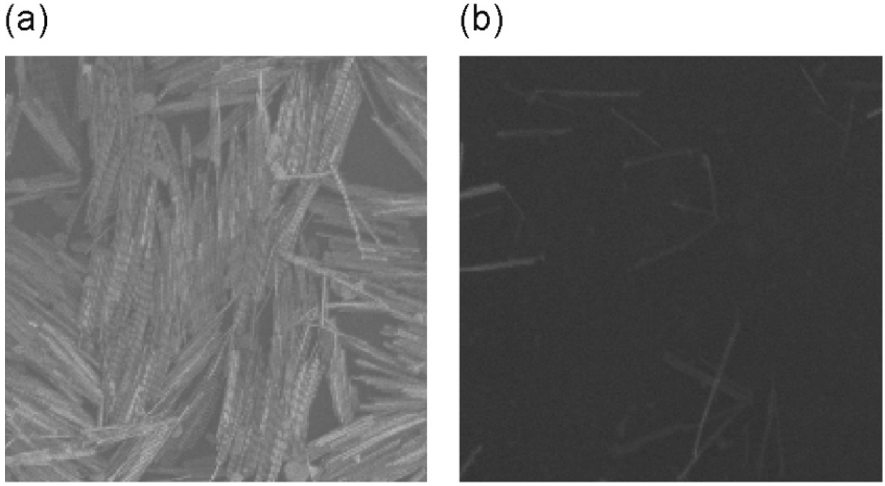

Figure 3. SEM images of gold nanorods. (a) Without and (b) with the surface modification by using the mercaptosuccinic acid. Scale bar is 5 μm.

5. Conclusion

The synthesis of gold nanorods in a gel-state surfactant solution is useful to control their diameter and length in wide range. The diameter and the length are controlled from ~ 10 to 80 nm and from ~ 10 nm to 1 μm, respectively. Toward applications, the dispersion method of high-aspect-ratio gold nanorods is also presented. These results are useful for further applications of the high-aspect-ratio gold nanorods.

References

1. Grzelczak M, Mezzasalma S A, Ni W, Herasimenka Y, Feruglio L, Montoni T, Perez-Juste J, Fornasiero P, Prato M, LizMarzan L M, (2012) Langmuir 28: 8826.
2. Pissuwan D, Niidome T, Cortie M B, (2011) J. Contr. Release 149: 65.
3. Mieszawska A , Jalilian R, Sumanasekera G U, Zamborini F P, (2005) J. Am. Chem. Soc. 127: 10822.
4. Tnag Q, Tong Y, Jain T, Hassenkam T, Wan Q, Moth-Poulsen K, Bjornholm T, (2009) Nanotechnology 20: 245205.
5. Jain T, Westerlund F, Johnson E, Moth-Poulsen K, Bjornholm T, (2009) ACS Nano 3: 828.
6. Murphy C J, Thompson L B, Chernak D J, Yang J A, Sivapalan S T, Boulos S P, Hung J, Alkilany A M, Sisco P N, (2011) Curr. Op. Colloid Interface Sci. 16: 128.
7. Sau T K, Murphy C J, (2004) Langmuir 20: 6414.
8. Wu H -Y, Huang W -L, Huang M H, (2007) Cryst. growth & Des. 7: 831.
9. Seo D, Park J H, Jung J, Park S M, Ryu S, Kwak J, Song H, (2009) J. Phys. Chem. C 113: 3449.
10. Park W M, Huh Y S, Hong W H, (2009) Curr. Appl. Phys. 9: e140.
11. Takenaka Y, Kitahata H, (2009) Chem. Phys. Lett. 467: 327.
12. Takenaka Y, Kitahata H, Yamada L N, Seto H, Hara M, (2011) J. Colloid Interface Sci. 356: 111.
13. Takenaka Y, Kitahata H, (2009) Phys. Rev. E 80: 020601(R).

Study of The Cytotoxicity of The Nitinol Surface with The Anodic Treatment

S.Y. Chen[1], W.C. Wang[1], Y.N. Chen[1,2], W.J. Shih[*]

[1] *Combination Medical Device Technology Section, Metal Industries Research & Development Centre, Kaohsiung 82059, Taiwan.*
[2] *Department of Biomedical Engineering, National Cheng Kung University, No.1 University road, Tainan 701, Taiwan.*

Abstract

Nitinol, the nickel-titanium alloy, is equipped with good physical and mechanical properties and has been used in various medical devices. However, the releasing of the nickel ions causes the immunological problems in the human body that should be seriously considered. This article aims to study the effect of anodic treatment with various voltages on the cytotoxicity of the nitinol surface. The response index used for estimating the cytotoxicity shows high voltage anodic treatment to produce thick oxide layer that prevents the nickel ion from releasing, and greatly reduces the nitinol cytotoxicity.

Keywords: *Cytotoxicity, Nitinol, Anodic treatment.*

1. Introduction

Nitinol, the shape memory and superelastic NiTi alloy, becomes an extensively used material in several medical devices, such as self-expanding stents for good corrosion resistance and biocompatibility [1-3]. However, recent studies indicate that some nitinol implants can be corroded in vivo and release high nickel content [4,5]. Nickel is an essential element to human body, but when daily digestion exceeds 200-300g [6], nickel will cause severe immunological problems. Although the amount of Ni recovered in biological studies in vitro may be either very low from the beginning or decreases to undetectable levels after a brief exposure to biological environment [7,8], the occurrence of "nickel case" is continuing. Thus, the recent results obtained from commercial ready-to-use orthodontic wires show that the Ni release varied in a wide range from 0.2 to 7μg cm^{-2}[9].

The surface property of an implant plays a critical role in determining its biocompatibility and ultimately its integration, due to its direct contact with blood and host tissues. However surface treatment, such as electro-polishing[7], thermal treatment[10], passivation in nitric acid[11] and combination of H_2O_2 and NaOH

W. Udomkichdecha et al. (eds.), *Materials Challenges and Testing for Manufacturing, Mobility, Biomedical Applications and Climate*,
DOI 10.1007/978-3-319-11340-1_17

treatment[12], has indicated to significantly improve the Nitinol corrosion resistance. Surface modification is an easy and economical way to improve the surface characteristics and to enhance the biocompatibility of biomedical materials [13-17]. However, the rate of nickel released from such treatments can be increased undesirably [18].

The electrochemistry of Nitinol is gradually developed recently that papers are published on the subject of electro-polishing processes in various electrolytes [19-22], and anodizing in various solutions and voltage regimes[22,23]. The first evaluation is the anodizing process in nitinol indicates that it is different from that of pure Ti[22,23]. Although anodizing is employed to generate thicker oxide films and to modify surface topography, no thick films could be obtained on NiTi in acetic acid electrolyte, and in 0.1M sulfuric acid, as well as in alkaline solutions [20]. Unfortunately, the anodizing[23] does not reduce the Ni surface content, and the surface obtained by using an optimized anodizing regime is heavily cracked.

This study aims to compare different surface condition of untreated, chemical polished and anodized nitinol rod and to evaluate their suitability by cytotoxicity test.

2. Experimental method

2.1 Preparation

The medical grade nitinol rods of ø=3mm and 5cm in length are rinsed by acetone, alcohol and D.I. water respectively for 10 minutes continually. After chemical polishing by TB-100(Poligrat, German) for 60 minutes at RT, the rods are rinsed in D.I. water for 10 minutes in the ultrasonic bath for 3 times. The well rinsed nitinol rods are fixed on anode in 250ml 1M $H_3PO_{4(aq)}$, and treated with different voltage of 5V, 10V, 15V, 20V, 170V and 300V separately for 10 minutes. The anodizing treated rods are rinsed in D.I. water for 10 minutes in the ultrasonic bath for 3 times again and are dried at 60 ^{o}C for further cytotoxicity test.

2.2 Cytotoxicity test

The cytotoxicity test is carried out with L929 cell (mouse fibroblasts) to conform to ISO 10993-5. (ISO 10993-5 describes test methods to assess the in vitro cytotoxicity of medical devices. The method specifies the incubation of cultured cells in contact with a device and/or extracts of a device either directly or through diffusion to determine the biological response of mammalian cells in vitro by using appropriate biological parameters.) After immersing treated nitinol rods in culturing media with a 0.55ml/cm ratio in the laminar flow, nitinol rods are kept at 37°C, 95% humidity for 72 hours in the 5% CO_2 incubator. The extracted media of each specimen is drawn for 100μl and is mixed with 100μl media with L929 cells(1*105/ml) in the 96 culturing well for co-culturing for 24, 72 and 120 hours separately (at 37°C, 95% humidity in the 5% CO_2 incubator). Then the number of cells is counted to observe the living organism by hemocytometer with microscope morphologies (BX51, Olympus, Japan). The fresh media is used as the control group for comparison.

Table 1. *Descriptions of cell reactions for (a) zone description index and (b) lysis description index.*

(a)

Zone Description Index	Zone Description
0	No zone is detected near or under the specimen
1	*Zone is restricted under area of the specimen*
2	Zone is larger than the specimen but less than 0.5 cm
3	Zone is larger than the specimen for 0.5 to 1.0 cm
4	Zone is larger than the specimen for more than 1.0 cm but does not occur within the entire disk
5	Zone is occurred in the entire disk

(b)

Lysis Description Index	Lysis Description
0	No cytotoxicity is observed
1	Affected zone is less than 20%
2	20% to 39% of zone is affected
3	20% to 59% of zone is affected
4	20% ~ 80% zone is affected
5	More than 80% of the zone is affected

The cytotoxicity is estimated with the Zone Description Index (ZI) and Lysis Description Index (LI). ZI (0~5) indicates that the number of cells cannot be clearly colored in the toxicity zone, and LI (0~5) shows that the number of cells exhibits a certain effect in the toxicity zone. The indexes display in Table 1 with the relative descriptions. Any visual malformation, degeneration, sloughing, lysis or reducing density of cell layer of a cultured cell under a microscope, can be regarded as a toxic reaction. The Response Index (RI) of each specimen will be determined via the fractions, the numerator of ZI, and the denominator of LI (RI = ZI/LI). If a group of specimens is observed as cytotoxic in the negative control specimen, or no cytotoxic is existed in the positive control specimen, such a group is regarded as invalid.

3. Results and Discussion

3.1 Surface morphology

Fig.1 shows surface morphologies of untreated and treated specimens by the optical microscope. The commercial untreated nitonol is often produced by drawing into rod shape at low temperature annealing for short time to release the residue stress and induces some carbon ions, as the scratches (along the long axis) and dark clusters show in Fig.1(a).

After chemical-polishing (containing HF), some scratches, oxide, nickel and carbon containing are removed with part of the residue stress. The removing of Ni ions may reduce the toxicity and forms more TiO_2. Owing to an increase of total energy caused by the differences in the enthalpy of formation of Ti and Ni oxides [19], the preferential oxidation of Ti on nitinol surface always occurs. The bare nitinol surfaces are therefore built from Ti oxides, while Ni concentrations are from ~2 to 7%, depending on the employed regimes. Nitinol inclusions tend to be uniformly distributed in the bulk of the material, their removal during chemical etching leaves a structural surface that may be beneficial for cell attachment and locomotion.

For the surface of 5V anodizing specimen (Fig.1(b)), the dense TiO_2 thin layer is built as smooth and clean surface with shallow scratches. However, the anodizing process in nitinol doesn't generate thicker oxide films, and doesn't reduce the Ni surface content [20]. When anodizing voltage is increasing to 20V, the rough surface in Fig.1(c) reveals that the oxide thickness may not increase but forms porous TiO_2 layer. Moreover, the 300V anodized nitinol surface shows larger roughness and surface defect in Fig.1 (d).

3.2 Cytotoxicity test result

The previous cytotoxicity tests indicate that each different method have different standard for grading toxicity. The determination of the cell toxicity classification is basically according to the following description about the cell variation levels:

(1) Cell death
(2) Loss of cell membrane integrity
(3) Reduction of cell adhesion
(4) Change of cellular morphology
(5) Decrease of cell proliferation
(6) Reduction of biosynthetic activity

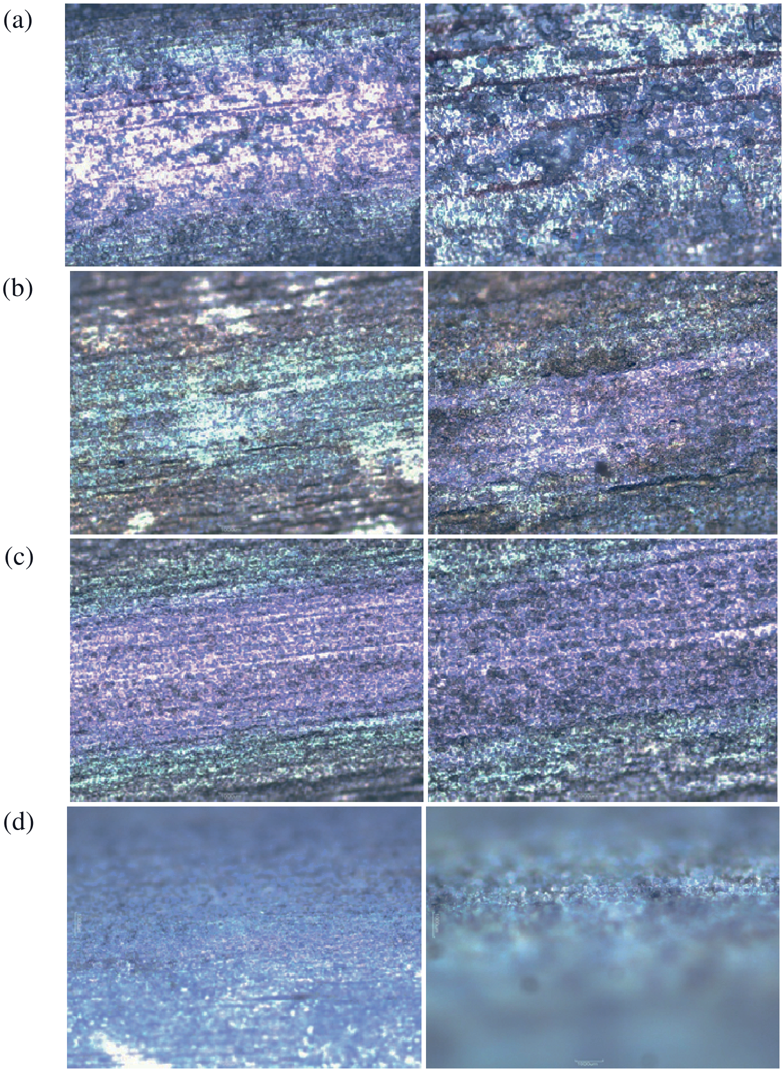

Figure 1. *50 and 100X surface morphologies of untreated and anodic treated specimens, for (a) untreated, (b) 5V anodized, (c) 20V anodized, and (d) 300V anodized.*

The cell culture results of the specimens are counted as Fig. 2. The negative control group shows normal cell activity and increases along with culture duration, but the positive control (adding 10% dimethy sulfoxide, DMSO) shows cell toxicity and decreases along with time All the specimens with various surface treatments have the same trend and similar counted cells as the negative control. Although the dyeing of the trypan blue only shows the living cells, it cannot separate the healthy cells from the mutation cells. So this result shows that all nitinol specimens have no cytotoxicity on L929 cells, but may cause the mitosis.

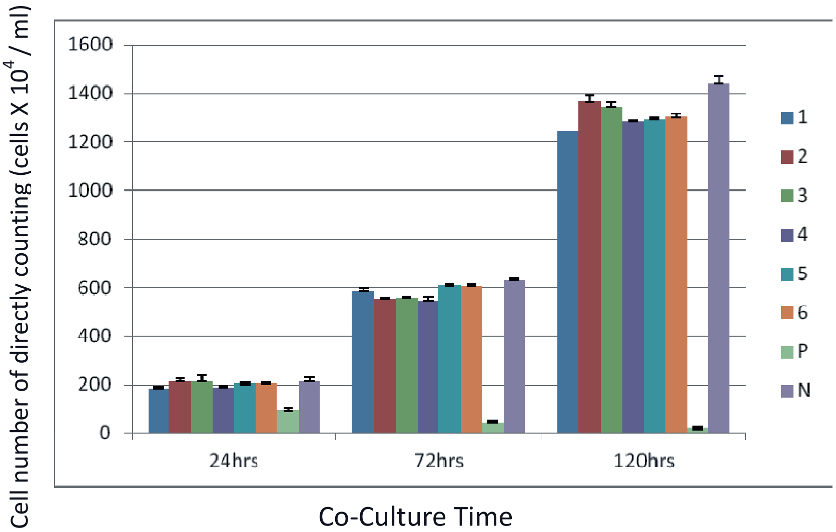

Figure 2. *L929 cell culture counting for various culture duration of the extract media of untreated and anodic treated specimens, for 1: untreated, 2: chemical-polished, 3: 5V anodized, 4: 20V anodized, 5: 170V anodized, 6: 300V anodized, p: positive control, and n: negative control.*

The 100X optical microscope image of cell culturing of untreated nitinol specimen shows a lot of living cells but poor cell extension and differentiation in Fig. 3(a). After chemical polishing, the nitinol culturing indicates a significant malformation shown in Fig. 3(b), which is similar as Fig. 3(c) of 5V anodized specimen, showing that the surface treatment induces mild biological reaction. Furthermore, the increasing anodizing voltage reduces the surface defect and nickel content, so the 20V anodized specimen in Fig. 3(d) shows the normal spindle cell morphology revealing. When the anodizing voltage is increasing from 170V to 300V (Fig. 3(e)(f)), the surface roughness increases and the porous TiO_2 indicates lower surface nickel content, and the cells are healthy and well extended.

The observed L929 cells response cultured in various extract media are listed in Table 2. According to Table 1, the control group shows that 20% to 39% of zone is affected and the affected scope falls between 0.5 and 1.0 cm, revealing the tox icity caused by nickel ions. After chemical-polishing, the affected zone is less than 20% and the zone is restricted under area of the specimen. Although less toxicity is observed, the risks are still existed for further medical use

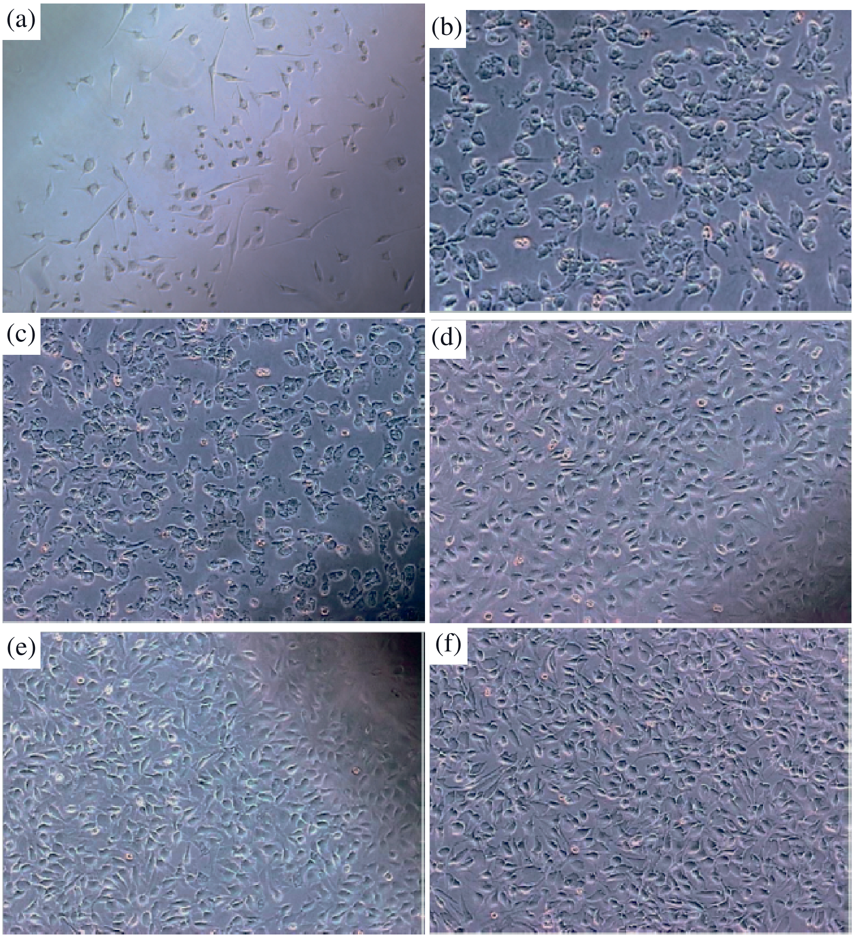

Figure 3. *L929 cell morphology (100X) after culturing for 72 hours of the nitinol rod extract media of (a) untreated, (b) chemical-polished, (c) 5V anodized, (d) 20V anodized, (e) 170V anodized, and (f) 300V anodized.*

The 5V anodized specimen shows the same result as chemical-polished specimen, indicating that thin layer oxide cannot block the releasing of nickel or transforms most of the Ni ion into NiO. However the result of 20V anodizing shows that no cytotoxicity is observed and no zone is detected near or under the specimen. Although 20V anodizing may not cause a much thicker oxide layer, the homogeneous surface condition in Fig.1(c) shows more TiO_2 forming than NiO on the surface, and further eliminates the toxicity releasing. When the voltage is increasing to 170V and 300V respectively, no more cytotoxicity is observed, indicating that 20V anodizing should be good enough. Since the future implant application requires the long term stability, the high voltage anodizing should be considered.

Table 2. *L929 Cell culturing response on various surface conditions*

Nitinol surface	Response Index (Zone Description/ Lysis Description)
Untreated surface	3/2
Chemical-polished	1/1
5V treated	1/1
20V treated	0/0
170V treated	0/0
300V treated	0/0

4. Conclusions

Nitinol is widely applied in the biomedical engineering, but shows a high risk due to the potential toxicity of releasing nickel ions in the in vivo environment. Since the safety of nitinol has been questioned, a number of studies intend to improve the biocompatibility of the nitinol, especially variety of the surface modification methods, including oxidation, coating, passivation, grafting, etc. This study combines the chemical-polishing and anodizing treatment to effectively passivate the nitinol surface and to reduce the toxicity caused by the releasing of nickel ions. The negative result of cytotoxicity test proves that the biocompatibility of anodized surface is existed at low voltage of 20V. And the well grown L929 cells reveal the need of the rough surface at high voltage treatment of 300V, while nickel content is decreased.

References

1. Trépanier C, Tabrizian M, Yahia LH et al (1998) Effect of modification of the oxide layer on NiTi stent corrosion resistance. J Biomed Mat Res A 43:433-440
2. Venugopalan R, Trépanier C (2000) Assessing the corrosion behavior of Nitinol for minimally-invasive devic e design. Invas ther & Allied Technol, 9(2): 67-74
3. Ryhänen J (2000). Biocompatibility of Nitinol. Min Invas Ther Allied Technol 9: 99-106.
4. Riepe G, Heintz C, Kaiser E et al (2002) What can we learn from explanted endovascular devices? Eur J Vasc Endovasc Surg. 24(2):117-122.
5. Gimenez-Arnau A, Riambau V, Serra-Baldrich E, Camarasa JG (2000) Metal-induced generalized pruriginous dermatitis and endovascular surgery. Contact Dermatitis 43(1):35-40.

6. Barrett RD, Bishara SE, Quinn JK (1993) Biodegradation of orthodontic appliances. Part I. Biodegradation of nickel and chromium in vitro. Am J Orthod Dentofacial Orthop 103(1):8-14.
7. Wever D, Velderhuizen A, De Vries J et al (1998) Electrochemical and surface characterization of NiTi alloy. Biomaterials 19:761-769.
8. Cui Z, Man H, Yang X (2005) The corrosion and nickel release behavior of laser surface-melted NiTi shape memory alloys in Hanks solution. Surf Coat Technol 192:347-353.
9. Arndt M, Bruck A, Scully T et al (2005) Nickel ion release from orthodontic NiTi wires under simulation of realistic in-situ conditions. J Mater Sci 40:3659-3667.
10. Gu YW, Tay BY, Lim CS, Yong MS (2005) Characterization of bioactive surface oxidation layer on NiTi alloy. Applied Surf Sci 252(5):2038–2049.
11. O'Brien B, Carroll WM, Kelly MJ (2002) Passivation of nitinol wire for vascular implants - a demonstration of the benefits, Biomaterials 23:1739-1748.
12. Chu CL, Chung CY, Zhou J et al (2005) Fabrication and characteristics of bioactive sodium titanate/titania graded film on NiTi shape memory alloy. J Biomed Mater Res A 75(3):595-602.
13. Cui ZD, Chen MF, Zhang LY et al (2008) Improving the biocompatibility of NiTi alloy by chemical treatments: An in vitro evaluation in 3T3 human fibroblast cell. Mater Sci Eng C 28(7):1117-1122.
14. Plant SD, Grant DM, Leach L (2005) Behaviour of human endothelial cells on surface modified NiTi alloy. Biomaterials 26(26):5359-5367.
15. Shevchenko N, Pham MT, Maitz MF (2004) Studies of surface modified NiTi alloy. App Surf Sci 235(1):2126-2131.
16. Wirth C, Grosgogeat B, Lagneau C et al (2008) Biomaterial surface properties modulate in vitro rat calvaria osteoblasts response: Roughness and or chemistry? Mater Sci Eng C 28 : 990-1001.
17. Yeung KWK, Poon RWY, Liu XM et al (2007) Nitrogen plasma-implanted nickel titanium alloys for orthopedic use. Surf Coat Tech 201(9-11):5607-5612.
18. Waver DJ, Veldhuizen AG, Vereis JD et al (1998) Electrochemical and surface characterization of nickel-titanium alloy. Biomaterials 19:761-769.
19. Pohl M, Hesing C, Frenzel J. (2004) Electrolytic processing of NiTi shape memory alloys. Mater Sci Eng A378:191-199.
20. Barison S, Cattarin S, Daolio S, Musiani M, Tuissi A (2004) Characterization of surface oxidation of nickel-titanium alloy by ion-beam and electrochemical techniques. Electrochem Acta 50:11-18.
21. Fushimi K, Startmann M, Hassel A (2006) Electropolishing of NiTi shape memory alloys in methanolic H_2SO_4. Electrochem Acta 52:1290-1295.
22. Shi P, Cheng F, Man H (2007) Improvement in corrosion resistance of NiTi by anodization in acetic acid. Mater Lett 61:2385-2388.
23. Kawakita J, Startmann M, Hassel W (2007) High voltage pulse anodization of a NiTi shape memory alloy. J Electrochem Soc 154: C294-298.

Part IV
Material Challenges in Mitigation and Adaptation to Climate Change

Hydration – Dehydration Technique: From Low Cost Materials to Highly Active Catalysts for Bio-Diesel Production

Boonyawan Yoosuk, Parncheewa Udomsap and Buppa Shomchoam

Bio-Energy Laboratory, National Metal and Materials Technology Center, Pathumthani 12120, THAILAND

Abstract

An efficient technique for increasing the transesterification activity of low cost natural rocks (calcite and dolomite) was proposed in order to make them highly suitable for use as heterogeneous catalysts for biodiesel. This technique involves water treatment of the oxide phase under mild conditions followed by thermal decomposition at an elevated temperature. The transformation of oxide to hydroxide phase and the reverse occurred simultaneously during the hydration–dehydration step with changes in the chemical and textural properties of the sample. The effectiveness of the hydration interaction appears to be due to a change in pore-size distribution, which is created by particle expansion in the formation of the hydroxide structure and the formation of more porosity and surface area during the dehydration and re-crystallization of oxide structure. Transesterification of palm olein was used to determine the activity of catalysts to show that this technique make catalyst has higher activity than the typical calcinations method. This study provides an understanding regarding how this hydration–dehydration process influences the properties and activity of dolomite.

Keywords: *Biodiesel; Catalyst; Hydration*

1. Introduction

In many areas of Thailand, calcite and dolomite exists in natural abundance and has low toxicity. Its main natural source is calcium carbonate, magnesian calcite with small amounts of silica, alumina, and ferrite. Calcite and dolomite are mainly used in agriculture and cement manufacturing. Their use as a catalyst in many processes such as gasification and reforming has attracted much attention, as it is cheap, has high basicity, and is environmentally friendly. However, there are few

W. Udomkichdecha et al. (eds.), *Materials Challenges and Testing for Manufacturing, Mobility, Biomedical Applications and Climate*,
DOI 10.1007/978-3-319-11340-1_18

studies of its applications in the literature, and a particularly neglected area is that of its role in basic catalyzed chemical synthesis. A few studies [1, 2], however, have reported uses of calcined and/or modified dolomite as a solid catalyst for biodiesel production. Although this reported successful application, dolomite's activity is not high as those of liquid catalysts. In addition, it would cost a higher catalyst weight and longer reaction time. Different methods of increasing its activity such as the addition of alkaline and/or alkaline earth oxide have been proposed. However, because of the chemical complexity and the cost of processes that inhere in these methods, they are not currently regarded as commercially attractive.

Many types of heterogeneous solid base catalysts have been studied intensively as alternative catalysts for biodiesel production and increasing attention is directed towards more effective catalysts capable of carrying the transesterification of oils proficiently under mild reaction conditions in short reaction times, for example, alkaline, alkaline earth and transition metal oxides [3, 4], various alkali metal compounds supported on alumina or zeolite, hydroxides, alkoxides, calcined hydrotalcites [5] and polymer-supported guanidines [6]. The order of activity among alkaline earth oxide catalysts is BaO > SrO > CaO > MgO [5, 7]. For most supported alkaline catalysts, the active ingredients are easily corroded by methanol and they exhibit short catalyst lifetimes. However, in most of the experiments using heterogeneous catalysts, the transesterification reaction proceed at a relatively slow rate compared to those conducted with homogeneous catalysts. The slow reaction rates are due to diffusion problems since these heterogeneous media behave as a three-phase system (oil/methanol/catalyst) [8]. Thus, the development of an active solid basic catalyst to carry transesterification of oils proficiently under mile reaction conditions in short reaction times still remains an intriguing challenge.

In the present work, we propose the technique to improve the activity, basicity, and surface area of calcined natural rocks by using the hydration-dehydration method. A variety of characterization techniques was applied in order to monitoring the structural transformations of the calcite and dolomite during the synthesis process. The transesterification reaction of palm olein was performed with a series of catalysts to systematically explore the relationship between the activity of the catalysts and their properties at each step of the synthesis process.*2. Experimental procedures*

2.1 Catalyst preparation and characterization

Natural rocks (calcite and dolomite) used in the study were from the Saraburi Province of Thailand. The fresh sample was thermally decomposed at 800 °C for 3 h. the obtained solids product from calcite and dolomite were denoted as CaO-S and CaMg-S, respectively. The samples were further modified by hydration-dehydration technique by refluxing in water at 60 °C for 6 h. The sample was filtered and heated at 120 °C over night. The products, referred to as CaO-W and CaMg-W, were activated at 650 °C for 3 h prior to test the catalytic activity for a transesterification reaction. The solid product was denoted as CaO-CH and CaMg-CH. Commercially available CaO (CaO-C) and MgO (MgO-C), as purchased from Ajax Finechem, were used for comparison purposes.

The X-ray diffraction (XRD) was performed by a JEOL JDX-3530 theta-2theta X-Ray diffractometer with Cu Kα emission with 0.02° per step. The diffractograms were analyzed using the standard JCPDS files. The N_2 adsorption and desorption isotherms were measured by a Micromeritics ASAP 2020 instrument.

Hammett indicator experiments were conducted to determine the H_- range of basic sites. The Hammett indicators were bromothymol blue (pKa = 7.2), phenolphthalein (pKa = 9.8), indigo carmine (pKa = 12.2), 2,4-dinitroaniline (pKa = 15.0), and 4-nitroaniline (pKa = 18.4). Although Hammett indicator measurements are usually performed in non-polar solvents, in this case anhydrous methanol was used in order to provide a more realistic assessment of base strength under transesterification conditions. 25 mg of catalyst was mixed with 4 ml of indicator solution and allowed to sit for at least 2 h. The basic strength of the catalyst was taken to be higher than the weakest indicator that underwent a color change and lower than the strongest indicator that did not undergo a color change.

The basicity of catalyst was studied by temperature programmed desorption (TPD) using CO_2 as a probe molecule. Prior to CO_2 adsorption, catalysts (0.3 g) were pretreated under a nitrogen stream at 120 °C for 30 min (10 °C/min and 20 mL/min). Then, the temperature was decreased down to room temperature, and a flow of pure CO_2 (20 mL/min) was subsequently introduced into the reactor for 150 min. The system was flushed with N_2 for 60 min. The TPD of CO_2 was carried out under a helium flow at a flow rate of 20 mL/min. The temperature was ramped from 40 °C to 960 °C and held at this temperature for 60 min with a temperature ramp of 10 °C/min. The CO_2 desorption was monitored by an online gas chromatograph provided with a thermal conductivity detector (TCD).

2.2 Transesterification reaction

The palm olein oil was purchased from Morakot Industries, PCL., Thailand. Its acid value is 1.10 mg. of KOH/g. of oil. Purchased from Fluka, the methanol used in this study was of analytical reagent grade. The transesterification reaction was carried out in a batch reactor. A 200-ml round-bottom flask was equipped with a reflux condenser. The reaction temperature was controlled by a hotplate with temperature sensor, and the magnetic stirring rate of 500 rpm was adjusted (Heidolph).

The synthesized catalyst was mixed methanol at the desired ratio. The mixture was warm at 60 °C. In addition, the 25 ml of palm olein oil also became warm at

60 ºC, after which it was added to the mixture of methanol and catalyst. The mixture's temperature was kept at 60 ºC by an oil bath. After the desired reaction time, the product of reaction was separated from the catalyst by centrifugation, and then the excess methanol was evaporated before the biodiesel yield was analyzed. The yield and compositions of the methyl ester products were determined by a gas chromatograph (GC-2010, Shimadzu) equipped with a capillary column, DB-WAX (30 m. x 0.15 mm.), and a flame ionization detector. The column temperature was programmed from 180 ºC to 230 ºC with the heating rate of 5 ºC /min. Methylheptadecanoate was used as an internal standard for quantification. The percentage of methyl esters was calculated based on the standard method, EN 14103. Duplicate or triplicate experiments were performed and the average of duplicated tests is reported here. The errors for % ME content values were typically within plus/minus 2.0 wt.%.

3. Results and Discussion

3.1 Structural transformation of rocks during the synthesis

The phase present in the samples in each step of synthesis process were characterized in structure terms by using the powder XRD technique as shown in Figure 1 and Figure 2. After the calcination, the reflections arising from the calcite and dolomite were lost, coincident with the appearance of new crystalline phases that can be assigned to highly crystalline CaO and MgO. Following hydration, the reflections arising from the oxide structure were lost, coincident with the appearance of the hydroxide phases of both Ca and Mg. Since diffraction is bulk property, the observation of those hydroxide peaks suggests that the surface hydration proceeded deeply into the bulk. When the samples decomposed at 650 ºC, the transformation of the hydroxide structure to the oxide structure occurred, as shown in Figure 1B and Figure 2B. The first salient finding is that, this technique caused the significant decrease in the peak intensity of both Ca and Mg oxides as compared to that of the CaO-S and CaMg-S. The XRD results show that water treatment has a strong effect on the crystallinity and crystalline size of the catalyst. The very high degree of crystallinity of the starting sample with a large crystalline size significantly decreased during the hydration-dehydration process. When the process was completed, the nano-crystalline oxide was obtained. Natural rocks have a very small surface area and negligible basicity, as shown in Table 1 Calcination at 800 ˚C changes both the structural and chemical properties of calcite, as evidenced by an increased surface area and increased basic strength. This result should be due to the expulsion of CO_2 from carbonate-rich areas that generate higher porous material. An attempt was made to increase the solid surface area by hydration followed by use of the thermal decomposition technique. This technique yielded solid product CaO-CH and CaMg-CH with a surface area twice that of the calcined samples. This is likely associated with the evolution of H_2O, whose expulsion from the lattice during the calcination of hydrated products would be expected to fracture the crystallites, with the concomitant formation of extra base sites in CaO-CH and CaMg-CH.

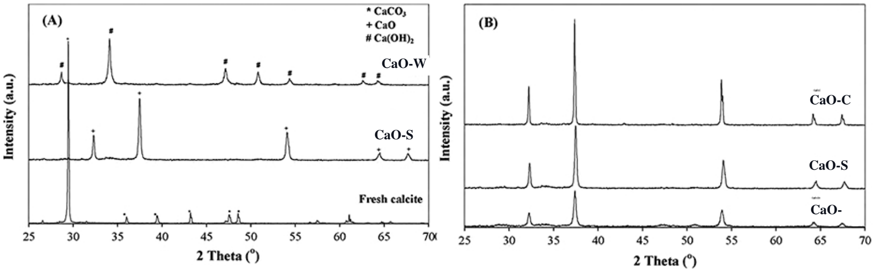

Figure 1. XRD patterns of calcite and its products compared with commercial CaO and MgO. The peak intensity of dolomite was reduced by a factor of 2.5.

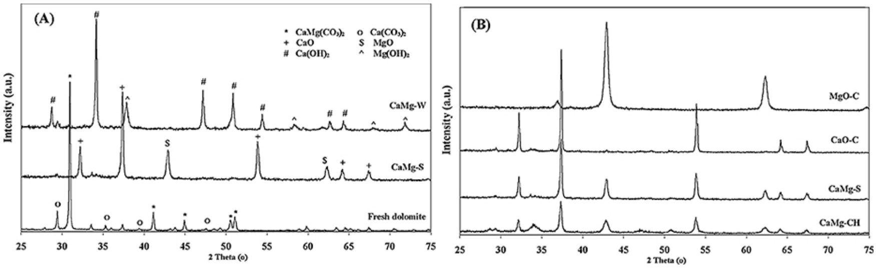

Figure 2. XRD patterns of dolomite and its derived samples compared with commercial CaO and MgO. The peak intensity of dolomite was reduced by a factor of 2.5.

Figure 3 and Figure 4 shows the rate of CO2 desorption, normalized to the sample loading, as a function of the run time and temperature. For calcite derived products (Figure 3), the desorption profiles of all the samples are qualitatively similar and constitute a main desorption peak. Among the three catalysts, CaO-C showed a desorption peak at the lowest temperature, while CaO-CH showed a peak at the highest temperature. From the results, the amount of total basicity varied in the order of CaO-HC > CaO-S > CaO-C.

Table 1. *Properties offresh calcite dolomite and their derived samples compared with commercial CaO and MgO.*

Samples	Surface area (m^2 g^{-1})	Pore vol-ume (cm^3 g^{-1})	Crystalline size (nm)		Basic strength (H_)
			CaO	MgO	
Calcite	0.4	0.01	-	-	(H_) <7.2
CaO-S	12.4	0.19	55.5	-	12.2< (H_) <15.0
CaO-CH	25.0	0.25	42.2	-	12.2< (H_) <15.0
Dolomite	8.0	0.01	-	-	(H_) <7.2
CaMg-S	21.4	0.25	54.1	36.1	15.0< (H_) <18.0
CaMg-W	28.0	0.31	-	-	9.8< (H_) <12.2
CaMg-CH	39.2	0.44	28.4	23.1	15.0< (H_) <18.0
CaO-C[a]	2.1	0.02	>100.0	-	9.8< (H_) <12.2
MgO-C[a]	59.0	0.55	-	22.8	7.2< (H_) <9.8

[a] Commercial available sample

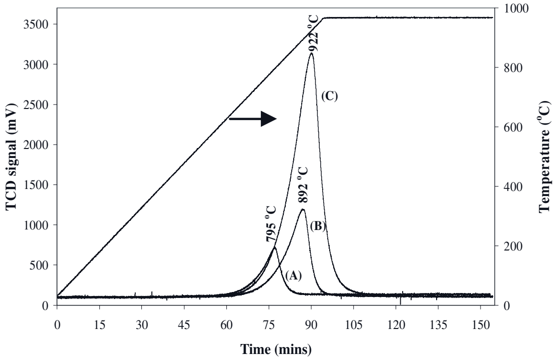

Figure 3. *CO_2-TPD adsorbed on commercial CaO(A), CaO-S(B) and CaO-HC(C).*

In case of dolomite derived products (Figure 4), the TPD results show that the basic sites of the oxide samples before and after water treatment (CaMg-S and CaMg-CH) have same strength. Since the base strength order can be used as an indicator of the chemical nature of these basic sites, as low-coordination oxygen anions > oxygen in Ca2+ / Mg2+ and O2- pairs > hydroxyl groups, it seems that

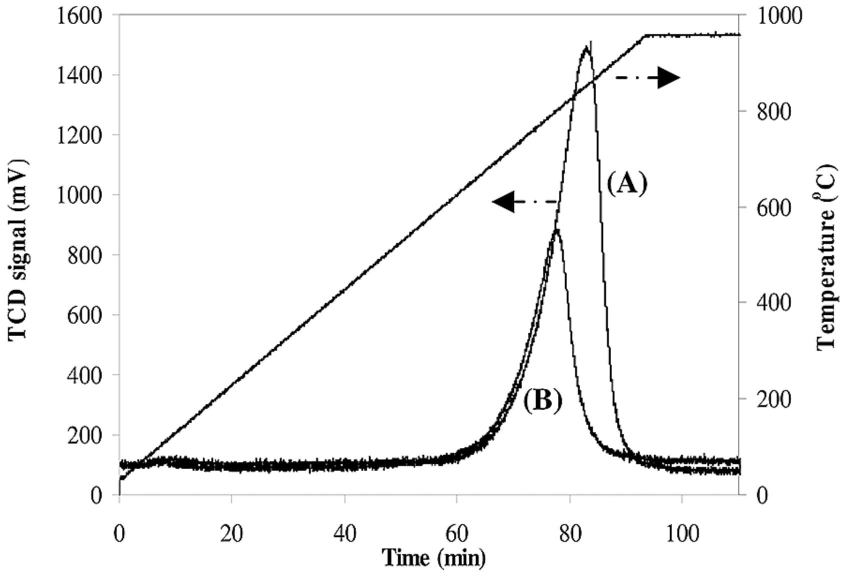

Figure 4. *CO_2-TPD profiles of CaMg-CH (A) and CaMg-S (B)*

the samples have a similar type of basic site. A consideration of the desorped CO_2 amount shows that the water treatment increased the number of basic sites in the oxide sample. According to TPD, it can be concluded that, in the hydration–dehydration step, the number of strong basic sites in the sample significantly increased while the chemical nature of these sites did not change.

3.2 Transesterification activity

The catalytic activities of all samples were subsequently examined by the transesterification of palm olein with methanol. Figure 5 graphically illustrates the evolution of the ME content for a series of fresh calcite and its derived samples compared with commercial CaO. No methyl ester was observed when fresh calcite was used. This suggests that the basicity of the carbonate form of calcium is not high enough to catalyze the transesterification reaction. These activity results are consistent with the order of basic strength, as shown in Table 1: CaO-S > CaO-W > fresh calcite. The greatest catalytic activity was observed for CaO-CH. It is clear that the hydration and subsequent thermal decomposition of the calcined calcite is essential in order to get an active catalyst for this kind of reaction.

In case of dolomite (Figure 6), the activity of the samples follows this sequence: CaMg-CH > CaMg-S > CaMg-W > Fresh dolomite. This trend correlated directly with the measured basic strength of the catalysts. By considering the two oxide samples, the hydration–dehydration technique led to a strong increase in the activity of the calcined dolomite This significant increase in activity could be due to the presence of a greater total number of basic sites of CaMg-CH as reported

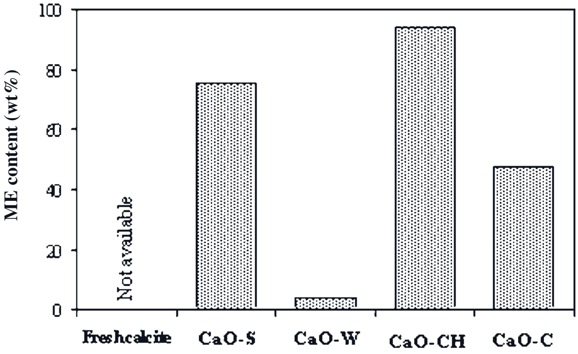

Figure 5. ME content obtained over calcite and its derived samples. Reaction conditions: methanol/oil molar ratio, 15; catalyst weight, 7 wt.%; time 60 min and temperature 60 °C.

.

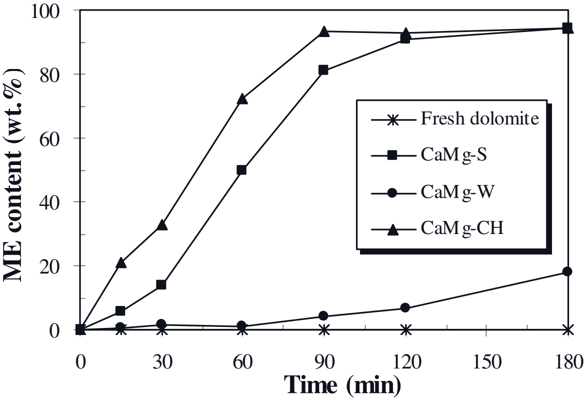

Figure 6. Reaction time dependence of methyl ester content over CaMg-CH catalyst with various catalyst loading amounts. Reaction conditions: methanol/oil molar ratio, 10 and temperature, 60 °C.

by the TPD technique. In addition to the basicity improvement, it seems that the water treatment of the CaMg-S develops more surface area and porosity in the CaMg-CH. As a result, the basic center becomes more accessible to reagents. This is probably another contributor to the enhanced catalytic activity that accrues from this method

Taking into account all the results obtained from the characterization and transesterification reaction, it can be concluded that the structure and activity of our starting material (natural rock) have been changed via the catalyst synthesis process. The hydration–dehydration technique, which is a result of ongoing research, is a simple and sufficient method for generating a new oxide structure with excellent chemical-textural properties and a large number of basic sites.

4. Conclusion

The present study shows that hydration and subsequent thermal decomposition is a sufficient method to increase the activity of natural rocks and contributes to the development of better heterogeneous catalysts for biodiesel production. This technique generates a new calcium oxide with excellent textural properties and a large number of basic sites. The characterization data showed that the calcination changes the non-porous structure of natural rock to the mesoporous structure of which results from the movement of CO_2 from the most internal interface towards the external one. This oxide particle becomes swollen after being exposed to water and transforms to hydroxide structure. The hydroxide structure is reversed back to an oxide one coincident with the release of the H_2O molecules in the thermal dehydration step. This results in solid product with greater porosity and larger pore diameter as compared with oxide sample without water treatment. This technique also generates a new oxide structure with higher surface area and lower crystalline size. The desorption profile exhibited the significant enhancement of strong basic sites in the oxide sample after hydration-dehydration step. The transesterification reaction confirmed this result. The synthesized catalyst achieved an excellent performance of 93.3 wt.% ME content within 90 min compared with 81.1 wt.% ME content obtained from catalyst produced without this technique.

Acknowledgement

The authors gratefully acknowledge the support of National Metal and Materials Technology Center.

References

1. Wilson, K., Hardacre, C., Lee, A.F., Montero, J.M., Shellard, L. (2008) The application of calcined natural dolomitic rock as a solid base catalyst in triglyceride transesterification for biodiesel synthesis. Green Chem. 10:654-659.
2. Ngamcharussrivichai, C., Wiwatnimit, W., Wangnoi, S. (2007) Modified dolomites as catalysts for palm kernel oil transesterification. J. Mol. Catal. A: Chem. 276:24-33.
3. Yoosuk, B., Krasae, P., Puttasawat, B., Udomsap, P., Viriya-empikul, N., Faungnawakij, K. (2010) Magnesia modified with strontium as a solid base catalyst for transesterification of palm olein. Chem. Eng. J. 162:58-66.
4. Cannilla, C., Bonura, G., Rombi, E., Arena, F., Frusteri, F. (2010) MnCeOx catalysts for biodiesel production by transesterification of vegetable oils with methanol. Appl. Catal. A: Gen. 382:158-166.
5. Cantrell, D.G., Gillie, L.J., Lee, A.F., Wilson, K. (2005) Structure-reactivity correlations in MgAl hydrotalcite catalysts for biodiesel synthesis. Appl. Catal. A: Gen. 287:183-190.
6. Sercheli, R., Vargas, R.M., Schuchardt, U. (1999) Alkylguanidine-catalyzed heterogeneous transesterification of soybean oil. J. Am. Oil Chem. Soc. 76: 1207-1210.
7. Seki, T., Kabashima, H., Akutsu, K., Tachikawa, H., Hattori, H. (2001) Mixed Tishchenko Reaction over Solid Base Catalysts. J. Catal. 204:393-401.
8. Xie, W., Peng, H., Chen, L. (2006) Transesterification of soybean oil catalyzed by potassium loaded on alumina as a solid-base catalyst. Appl. Catal. A: Gen. 300:67-74.

In Situ Study of PEMFC Start-up Degradation Using a Novel Through-Plate Reference Electrode Array

Edward Brightman and Gareth Hinds

National Physical Laboratory, Hampton Road, Teddington, Middlesex, TW11 0LW, United Kingdom

Abstract

In order to meet cost and durability targets for polymer electrolyte membrane fuel cells (PEMFCs), there is an urgent need for improved in situ measurement techniques to enhance understanding of degradation mechanisms and to facilitate design optimisation. A highly innovative reference electrode design has recently been developed at NPL that makes use of a standard hydrogen electrode (SHE) connected to the active area of the cell via a fine Nafion tube salt bridge inserted through the end plates of the fuel cell. The ion conducting path through the gas diffusion layer is achieved by Nafion impregnation at the point of contact with the Nafion tubing. Use of an array of such electrodes has for the first time enabled mapping of the spatial distribution of electrode potential in an operating PEMFC while minimising the perturbation of the measurement that occurs with conventional fuel cell reference electrode designs.

Here we demonstrate application of this technique to the investigation of catalyst support corrosion during fuel cell start-up, when fuel is introduced to the cell without a nitrogen purge. In this situation an air/fuel boundary progresses through the anode flow-field causing a transient mixed potential at the cathode of > 1.4 V vs. SHE, which enables carbon oxidation to occur. The NPL reference electrode array allows unprecedented time-resolved measurement of this potential spike as it progresses through the cell. The influence of flow-field design on the potential transient behaviour during start-up is investigated, supported by measurements of CO_2 evolution from corrosion of the carbon catalyst support.

Keywords: *Fuel cells; PEMFC; in situ; reference electrode.*

W. Udomkichdecha et al. (eds.), *Materials Challenges and Testing for Manufacturing, Mobility, Biomedical Applications and Climate*,
DOI 10.1007/978-3-319-11340-1_19

1. Introduction

The polymer electrolyte membrane fuel cell (PEMFC) is a promising electrochemical energy conversion technology that is central to the "hydrogen economy". Currently, large scale commercialization of the technology is hampered by high material and processing costs, lack of a refuelling infrastructure and limited durability [1]. Solving these issues and optimizing performance and durability present a range of problems of particular interest to materials scientists, especially in the fields of electrochemistry and catalysis. With the aim of facilitating deeper understanding of the physical processes that govern fuel cell performance and degradation, it is of particular scientific and engineering importance to develop improved in situ techniques for measurement of critical parameters such as temperature, humidity and electrode potential.

Measurement of electrode potential with respect to a reference electrode is commonly carried out in liquid electrolyte systems by placing a Luggin capillary (or salt bridge) in the ionic current path close to the working electrode. In a thin solid electrolyte system such as is found in a PEMFC, positioning of the reference electrode is less straightforward due to geometrical constraints. Where hydrogen is used as a fuel, electrochemical measurements can be carried out with the fuel cell anode acting as a pseudo-reference, assumed to be at a constant potential due to the higher catalytic performance of state-of-the-art catalysts for the anode hydrogen oxidation reaction (HOR) compared to the cathode oxygen reduction reaction (ORR). This is a reasonable assumption at low current densities where cell potential is dominated by activation losses at the cathode, but in systems where fuel other than hydrogen is used (e.g. methanol), this approach is not an option.

Most previous approaches to incorporating a reference electrode in PEMFCs may be grouped into two categories: (a) internal, or sandwich-type electrodes which involve hot-pressing a reference electrode between two membranes, and (b) external, or edge-type electrodes, which are connected to the edge of the membrane via a salt bridge such as a strip of Nafion membrane. The main drawbacks of the internal type are that both charge and water transport in the membrane are perturbed by the presence of the electrode and associated wires [2]. The external type on the other hand suffers from large potential drop effects due to being located far from both electrodes. Significant errors can also arise from any slight misalignment of the electrodes leading to the measured potential being dominated by the edge of the nearer electrode [3, 4]. However, both external and internal reference electrodes are fundamentally limited by the fact that they do not account for the potential drop in the membrane.

NPL has recently published the successful demonstration of a novel reference electrode that overcomes these major limitations by making contact with the working electrode through the back of the gas diffusion layer (GDL) [5]. A very small diameter Nafion tubing is inserted through the end plates of the fuel cell to act as a salt bridge, and the ionic pathway is extended through the GDL to the electrode by impregnating the GDL with Nafion at the point of contact. By making contact with the working electrode in this way, potential drop effects in the membrane are avoided, and by using an array of such electrodes the spatial distribution of the electrode potential across the active area of the electrode can be measured.

During start-up/shut-down of a PEMFC, a fuel/air boundary progresses through the anode flow-field causing a transient mixed potential in the cathode of > 1.4 V vs. SHE, due to lateral currents in the cell [6, 7]. This causes corrosion of the high surface-area carbon catalyst support material to occur in the cathode, and is a major cause of degradation that is of particular concern for automotive applications where frequent start-up/shut-down cycles are expected. The problem can be avoided by purging with nitrogen before start-up or shut-down; however the additional weight and bulk this would incur is undesirable in an automotive system.

The spatial variation of this high potential transient was accurately measured in situ for the first time using the NPL reference electrode array [5], which showed the effect of the progress of the hydrogen/air front through a serpentine flow-field. In the present study, two different flow-field designs are compared under the same start-up conditions, and the extent of carbon corrosion is compared using a CO_2-probe to measure the amount of CO_2 produced by the transient potential spike in each case. The potential uses of this technique in design optimization are discussed.

2. Experimental

A 7 cm × 7 cm single cell PEMFC was used for all measurements with an MEA supplied by Johnson Matthey Fuel Cells Ltd (UK) consisting of two identical Pt/C electrodes (Pt loading 0.4 mg/cm^2) on a JMFC V3 membrane. The MEA was pre-conditioned at 80 °C and 100% RH at 0.5 A cm^{-2} for 18 h. Experiments were carried out at 24 °C and 100% RH using a Hydrogenics FCATS-G50 test stand. Compression of the cell was achieved using a pressurized gas/piston arrangement with a compression pressure of 7 bar.

The NPL through-plate reference electrode has been described previously [5] and is illustrated in Fig. 1. It consists of a thin Nafion tubing (Perma Pure, NJ, USA) with 0.64 mm ID and 0.84 mm OD enclosed in a PTFE sheath of 1.01 mm ID and 1.27 mm OD (Adtech Engineering Ltd., UK). This acts as a salt bridge which is inserted at one end into a glass vessel containing 0.5 M H_2SO_4 into which was placed a Hydroflex hydrogen reference electrode (Gaskatel GmbH, Germany).

The other end of the Nafion tubing is inserted through a hole in the end plates of the cell, and sealed using an O-ring as illustrated inset in Fig. 1. In order to create an ion-conducting path through the GDL, the GDL was impregnated with Nafion at the point of contact with the salt bridge using a 2 μL pipette to dispense a 50:50 mixture of 10% Nafion dispersion in water (Sigma Aldrich, UK) and 2,2,3,3-tetrafluoro-1-propanol (Sigma Aldrich, UK).

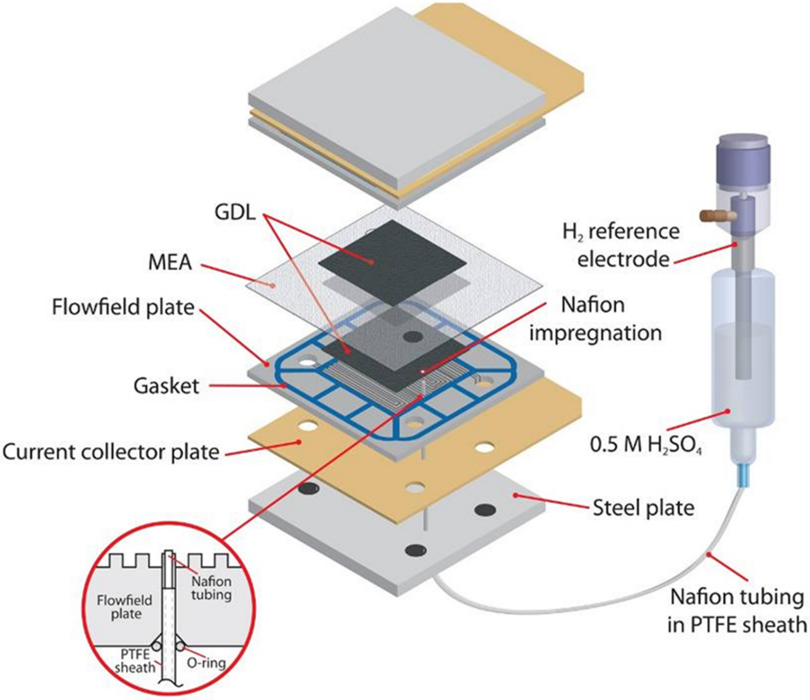

Figure 1. *Schematic diagram of a single NPL through-plate reference electrode. Inset: hole in graphite flow-plate and sealing arrangement.*

The flow-plates used were machined from impregnated graphite with flow channels of approx. 1 mm × 1 mm in cross-section. In order to make a comparison of different flow-field designs in this study, a 6-channel serpentine flow-field and an interdigitated flow-field were used with a 3×3 array of reference electrodes to probe the variation in electrode potential across the active area of the cell. The locations of the reference electrodes with respect to the flow-fields are shown in Fig. 2.

In each case the electrodes are numbered in order of the direction of hydrogen flow. The cell potential and the potential difference between the fuel cell cathode and each of the nine reference electrodes were measured and logged using the in-built voltmeters on an Agilent 34970A data acquisition/data logger switch unit (Agilent Technologies Ltd., UK) connected to a PC.

CO_2 concentration in the cathode exhaust stream was measured using an in-line infra-red GMP343 CO_2 probe (Vaisala Oyj., Finland) connected to a PC.

For the start-up experiments, the cell was held with stagnant air on the anode and an air flow rate of 0.5 sL min^{-1} on the cathode. After approx. 30 s, hydrogen was introduced to the anode at a flow rate of 0.136 sL min^{-1}.

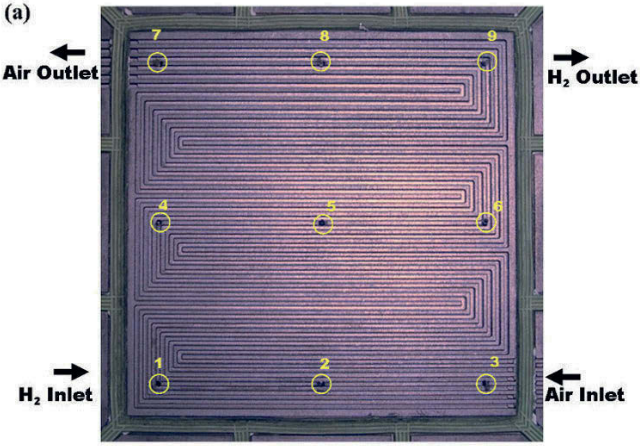

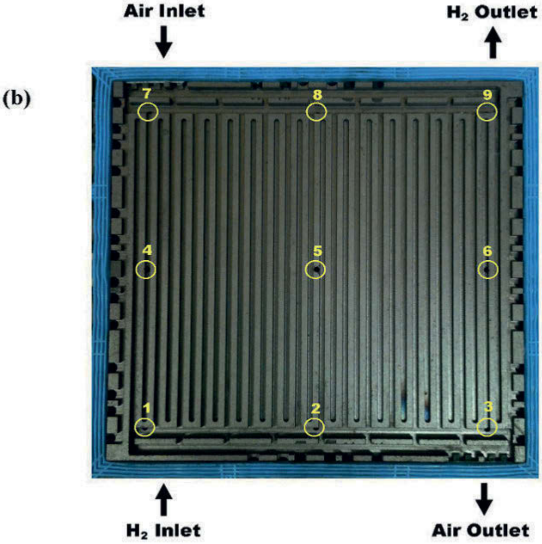

Figure 2. *Location of contact points with reference electrodes in (a) serpentine and (b) interdigitated flow-field plates. The image for Fig. 2(a) has been reoriented to match the layout of Fig. 3(a).*

3. Results and discussion

Fig. 3a shows the potential difference measured with the hydrogen reference electrode array at each of the nine points on the serpentine flow-field versus time. To aid interpretation, three critical points in time are marked across all nine readings. Near the inlet the cathode potential drops when hydrogen enters the cell, whilst the potential across the rest of the cathode rises above 1.4 V, which is sufficient to drive corrosion of the carbon support, and reaches as high as 1.54 V near the outlet. The drop in potential near the inlet provides the cathodic current to support the carbon oxidation reaction. The potential initially rises at the points measured against reference electrodes 2 and 3 along the inlet channel until the H_2 front reaches them, whereupon it drops sharply down to the cathodic level. In total the spike lasts for approx. 5 s.

The serpentine flow-field consists of 6 channels, each of 1 mm^2 cross-section and 490 mm in length, giving a total volume of 2940 mm^3 or 2.94 mL of stagnant air present before startup. At the flow rate of hydrogen used, i.e. 136 mL/min, it should take about 1.3 seconds for the hydrogen to displace all the air in the channels. The observed potential spike is significantly longer than this, because it takes some time for the hydrogen to permeate the GDL and reach the electrode surface.

By comparison, the progress of the hydrogen/air front through the interdigitated flow-field (shown in Fig. 3b) is significantly slower, as indicated by the duration of the potential spike. The maximum potential measured is also higher, at 1.59 V vs. reference electrode 9. A major difference in the two flow-field designs is that, whilst the serpentine flow-field has continuous channels from inlet to outlet, enabling unrestricted gas flow, the interdigitated flow-field consists of dead-end, finger-like channels which force the gas to flow into the GDL before it can reach the outlet channels. Therefore it takes a longer time for the hydrogen to fully displace the air throughout the GDL. The electrode in position 6 experiences the longest period at high potential, suggesting that displacement of air by H_2 is least efficient in this part of the cell.

Fig. 4 shows the results from the CO_2 probe measurements, which were carried out at the same time as the potential measurements. There is a delay of about 10 s in the onset of the CO_2 detection due to the position of the probe down-stream from the fuel cell. Also worth noting is that the end of the CO_2 spike is more spread out than the potential spike, taking around 50–70 s compared to 5–10 s for the potential spike. Again, this is most likely due to diffusion through the GDL, but may also be a sign that the carbon corrosion occurs for longer than can be measured with the reference electrodes, on a microscopic scale for as long as there is air that has not been fully purged from the anode.

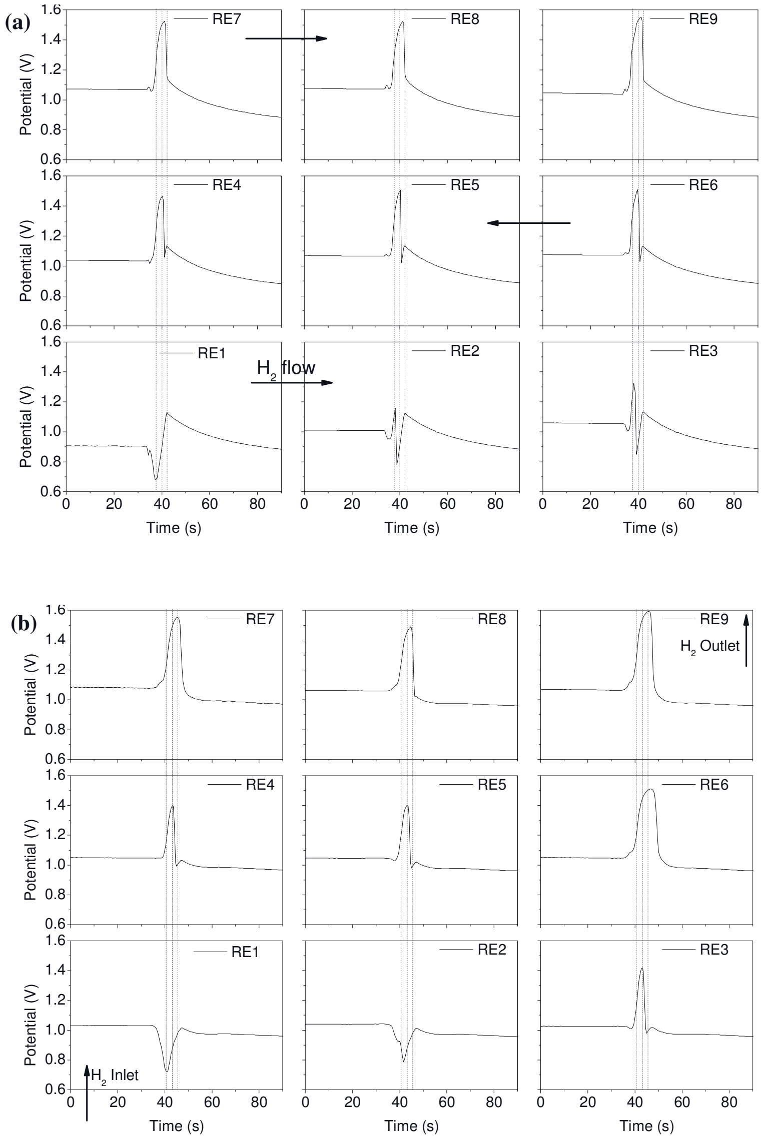

Figure 3. *Cathode potential vs. hydrogen reference electrode measured simultaneously at nine different points during start-up where* H_2 *is introduced to the anode at t = 30s. (a) Serpentine flow-field, (b) interdigitated flow-field.*

The area under the CO_2 peak above the background level has been highlighted in Fig. 4 and gives a relative measurement of the amount of corrosion that has taken place in each case. The corrosion generated during start-up under these conditions is ~80% higher for the interdigitated flow-field than for the serpentine flow-field, which is consistent with the higher magnitude and longer duration of the potential spike measured using the reference electrode array. It is clear that the combination of in situ potential and evolved CO_2 measurement is a powerful tool in the optimisation of fuel cell design to mitigate start-up degradation.

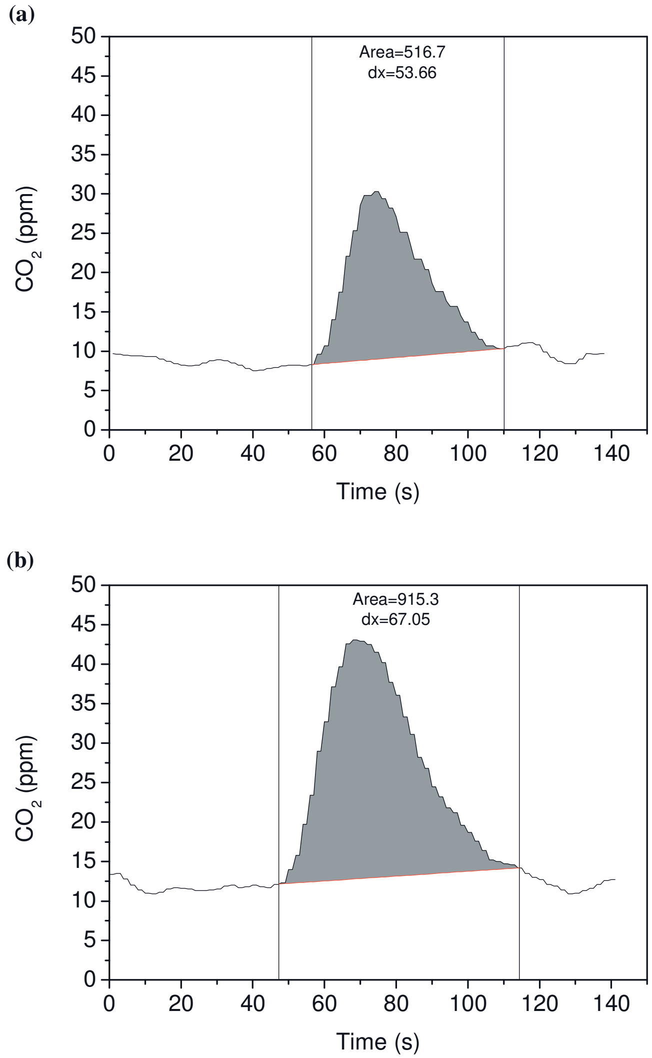

Figure 4. *CO_2 measured in cathode outlet (flow rate = 0.5 sL/min) for start-up experiments, arising from corrosion of the cathode catalyst support. The shaded area under the peak corresponds to the amount of CO_2 produced by start-up-induced corrosion. Results correspond to (a) serpentine and (b) interdigitated flow-fields.*

4. Conclusions

- An innovative through-plate reference electrode design has been developed at NPL to make spatially-resolved measurements of electrode potential in an operating PEMFC.
- The technique has been applied to investigate the transient potential spike that occurs during PEMFC start-up, which is a major cause of degradation and performance loss over time.
- Simultaneous CO_2 measurements at the cathode outlet and in situ potential measurements using an array of NPL reference electrodes have been carried out for the first time, showing that a serpentine flow-field results in less severe corrosion under identical start-up conditions than an interdigitated design.

List of Abbreviations

GDL	gas diffusion layer
ID	internal diameter
JMFC	Johnson Matthey Fuel Cells Ltd.
MEA	membrane electrode assembly
NPL	National Physical Laboratory, UK
OD	outer diameter
PEMFC	polymer electrolyte membrane fuel cell
PTFE	poly(tetrafluoroethylene)
RH	relative humidity
SHE	standard hydrogen electrode

Acknowledgements

This work was supported by the UK National Measurement System and an Industrial Group comprising Acal Energy, AFC Energy, C Tech Innovation, CMR Fuel Cells, Intelligent Energy and Johnson Matthey. The authors are grateful to Johnson Matthey for supply of fuel cell components.

References

1. Borup, R., Meyers, J., Pivovar, et al.: Scientific aspects of polymer electrolyte fuel cell durability and degradation. Chemical Reviews. 107, 3904-51 (2007).

2. Li, G., Pickup, P.G.: Measurement of single electrode potentials and impedances in hydrogen and direct methanol PEM fuel cells. Electrochimica Acta. 49, 4119-4126 (2004).

3. He, W., Nguyen, T.V.: Edge Effects on Reference Electrode Measurements in PEM Fuel Cells. Journal of The Electrochemical Society. 151, A185 (2004).

4. Liu, Z., Wainright, J.S., Huang, W., Savinell, R.F.: Positioning the reference electrode in proton exchange membrane fuel cells: calculations of primary and secondary current distribution. Electrochimica Acta. 49, 923-935 (2004).

5. Hinds, G., Brightman, E.: In situ mapping of electrode potential in a PEM fuel cell. Electrochemistry Communications. 17, 26-29 (2012).

6. Reiser, C. A., Bregoli, L., Patterson, T.W., Yi, J.S., Yang, J.D., Perry, M.L., Jarvi, T.D.: A Reverse-Current Decay Mechanism for Fuel Cells. Electrochemical and Solid-State Letters. 8, A273 (2005).

7. Sidik, R. A.: The maximum potential a PEM fuel cell cathode experiences due to the formation of air/fuel boundary at the anode. Journal of Solid State Electrochemistry. 13, 1123-1126 (2009).

Membranes Made of Hardened Cement Paste for Processing Wood Gas – Influence of Paste Composition on Separation Factors

Gregor J. G. Gluth[1], **Maria Gaggl**[2], **Weiqi Zhang**[2], **Bernd Hillemeier**[3], **Frank Behrendt**[2]

[1] *BAM Federal Institute for Materials Research and Testing, Division 7.4 Technology of Construction Materials, Unter den Eichen 87, 12205 Berlin, Germany*

[2] *Technische Universität Berlin, Institute for Energy Engineering, Fasanenstr. 89, 10623 Berlin, Germany*

[3] *Technische Universität Berlin, Institute for Civil Engineering, Gustav-Meyer-Allee 25, 13355 Berlin, Germany*

Abstract

The efficiency of wood gasification can be improved by applying membrane based gas separation operations in several of its sub-processes. In the present study the use of membranes made of hardened cement pastes for this purpose was investigated to provide a low cost alternative to conventional membrane materials. The pastes were tested for their diffusional properties in a Wicke-Kallenbach cell and analyzed with regard to their pore structure. The use of low water to binder ratios and slag and/or pozzolans led to a finer pore structure and higher separation factors; in particular, an approximately linear dependence of the separation factors on the threshold radii was observed. The results implicated that Knudsen diffusion is the prevailing diffusion mechanism in the membranes. Deviations from the theoretically expected separation factors were found, which may be ascribed to concentration polarization and channeling effects.

Keywords: *Hardened cement paste; Pore structure; Diffusion; Gas separation*

W. Udomkichdecha et al. (eds.), *Materials Challenges and Testing for Manufacturing, Mobility, Biomedical Applications and Climate*,
DOI 10.1007/978-3-319-11340-1_20

1. Introduction

Because of the finite availability of fossil fuels and the necessity to significantly lower the anthropogenic contribution to the greenhouse effect, energy sources other than fossil fuels have to be found. A promising option to produce energy from renewable resources is the gasification of wood [1]. The effectiveness of this operation can be significantly improved by separating certain components from the gas mixtures which are involved in several of its sub-processes. Most notably, the product gas of wood gasification (wood gas) contains significant amounts of carbon dioxide and nitrogen when air is used for partial oxidation, which lowers its fuel value [1, 2]. By removing these components from the product gas, the fuel value of the latter can be significantly raised. Furthermore, by re-feeding the carbon dioxide to the gasification reactor, the chemical equilibria can be shifted and the gasification process made more efficient.

Membrane based separation processes are the most cost-effective procedures to separate components from gas mixtures when the demand for purity is moderate to low [3, 4]. In general, polymeric membranes are used for membrane gas separation. However, their resistance to high temperatures (> ca. 100 °C) and corrosive chemical environments is very limited, thus, inorganic membrane materials such as zeolites and carbon constitute a large area of research [5, 6]. Yet, at present time these materials still suffer from several drawbacks such as low fluxes, brittleness and poor reproducibility, which hampers their commercial application. Moreover, with costs of up to 3000 US$/m^2, modules made from these materials are very cost-intensive [3, 5, 6].

Also in the case of wood gasification, the product gas initially has a temperature of about 500-1000 °C and may contain corrosive components, which excludes the use of polymeric membranes unless the gas is treated before separation. Further, the high expenses for inorganic membrane modules may not be justified for this operation, which is normally carried out in relatively small sized plants. Therefore, in the present work the principal use of membranes made of hardened cement paste (hcp) for gas separation was assessed.

Although numerous studies that are concerned with transport processes in cementitious materials have been published, there are only few that investigated the mechanisms of gas transport in these materials. The more recent ones of these yielded evidence of Knudsen diffusion being an important transport mechanism in hcp, mortars and concrete [7-10], which gives reason to presume the applicability of cement-based materials in gas separation operations. However, no previous studies investigating the separation ability of this type of material exist.

2. Experimental procedures and methods

Membranes were prepared from several cement pastes. The raw materials used were two Portland cements (PC1 and PC2), a blast furnace slag and Portland clinker-based microfine binder (MF), a slag cement (SC), fly ash (FA) and silica fume (SF). All materials are commercially available products with typical chemical compositions (given elsewhere [11]). The mixture compositions of the pastes are shown in Table 1. The pastes were mixed for six minutes and then cast into cubes of 100 x 100 x 100 mm³ and capped. After one day the pastes were demoulded and stored in a water tank at ca. 20 °C for 28 days. On the seventh day of curing, discoidal membranes with a thickness of 5 mm and a diameter of 51 mm were cut from the cubes, cleaned in an ultra sonic water bath and put back into the water tank. After 28 days of curing all samples were dried by oven-drying at 105 °C until their mass loss was less than 0.1% within 24 hours.

Table 1. *Mixture compositions and water to binder ratio (w/b) of the cement pastes*

	Amount in g dm^{-1}						
Component	PC1 (0.25)	PC2 (0.25)	PC2 (0.45)	PC2+SF (0.25)	MF (0.30)	SC+FA (0.20)	SC+FA (0.37)
Cement	1762.2 (PC1)	1762.2 (PC2)	1303.0 (PC2)	1344.8 (PC2)	1556.5 (MF)	1245.1 (SC)	962.3 (SC)
Addition	-	-	-	336.2 (SF)	-	560.3 (FA)	433.1 (FA)
Water	440.6	440.6	586.3	420.3	467.0	367.3	511.0
w/b	0.25	0.25	0.45	0.25	0.30	0.20	0.37

To emulate the temperature rise at the beginning of the diffusion measurements (see below), samples for pore structure analyses were heated to 350 °C for 24 hours in an electro-oven and then allowed to cool down in the closed oven. This heating duration was chosen since the samples were considerably larger than the membranes.

Mercury porosimetry was performed on single samples of ca. 6 cm^3. Conversion from pressure to pore sizes was done by means of the Washburn-Laplace equation, assuming cylindrical pores, a surface tension of the mercury of $\gamma = 0.480$ N m^{-1} and a contact angle mercury/hcp of $\theta = 141.3$ °. The threshold radius, r_{thr}, [12] of the pastes was determined as proposed by Härdtl [13], i.e. as the pore radius at which the slope of the cumulative pore size distribution curve exceeds 0.1 $cm^3\ g^{-1}\ \mu m^{-1}$. This procedure yields virtually the same r_{thr} as the usual, graphical procedure of determination (taking the pore radius at the intersection of the tangents on the steep and the flat part of the cumulative distribution curve as r_{thr}). In the case of paste PC2+SF(0.25) after heat treatment, however, the graphical procedure was used, since for this paste the slope of the cumulative distribution curve was already high for large pore radii.

Nitrogen sorption isotherms were recorded on samples ground and sieved to particle sizes of 800-2000 μm. The volume of micropores (pore size < 2 nm) was determined by means of the *t*-method [14]. The specific surface area, a_s, was determined by the BET method.

Helium pycnometry was performed on the same particles as for nitrogen adsorption. The open porosity, ε, was calculated from the measured apparent density and the bulk density of the unground specimens.

Diffusion measurements were performed in a Wicke-Kallenbach cell. In this cell the gases flow laterally across the two surfaces of the membrane in slits of 2.5 mm width, the gases on either side of the membrane moving in opposite directions. The feed side of the membrane was fed with a mixture of 49.8% H_2 and 50.2% CO_2 by volume and the permeate side was swept with N_2. The gases were fed to the membrane with flow rates adjusted to 30 cm^3 min^{-1}. The total pressures on the two sides of the membrane were kept at $p = (1.050\pm0.005)\bullet10^5$ Pa. Measurements were performed at 350 °C, 200 °C, 100 °C and room temperature (32±5 °C) (in this order). For all temperature steps the compositions of the outflowing gas mixtures on each side of the membrane were determined by gas chromatography; by waiting at least 15 min. before taking the measurement in each step, steady-state diffusion was ensured.

The diffusion cell and all applied experimental procedures have been described in more detail elsewhere [11].

3. Results and discussion

3.1 Pore structure

The pastes showed markedly differing pore structures. As expected, for equal binders a lower water to binder ratio (w/b) led to a smaller open porosity and smaller threshold radius (Table 2). This is due to the fact that at lower w/b there is less water-filled space between the binder particles which has to be filled with hydration products to achieve a dense microstructure. The use of slag containing cements and/or the addition of pozzolans (silica fume, fly ash) caused a further significant decrease of ε and r_{thr} compared to the pure Portland cement pastes. This behavior is generally attributed to the altered morphology of the calcium silicate hydrates (C-S-H), which are the main product of the hydration reactions of the binders. Due to a lower Ca/Si ratio the C-S-H phases in slag or pozzolan containing pastes, their morphology gradually changes to more sheet like instead of fibrous as in neat Portland cement pastes [15-17]. This causes the constrictions in the pore system to become smaller and possibly close. In addition, the proper use of supplementary materials such as silica fume and fly ash improves the particle size distribution of the binder and by this means leads to a finer pore system [18].

Heat treatment of the pastes led to increased open porosities, which was found to be most significant for the slag or pozzolan containing pastes (Table 2). In the temperature range up to 350 °C, the C-S-H phases as well as the calcium aluminate hydrates (AFm, AFt) of the hardened pastes start to lose bound water [16] and shrink or decompose, thus creating new pore space. However, the temperature is not high enough to decompose the calcium hydroxide, the third important reaction product of the cement hydration. The heat treatment caused only a slight increase of the threshold radii of the pastes, a finding which is consistent with the results of others [8]. The mercury porosimetry curves of the heat treated samples can be found in Fig. 1 [19].

Table 2. *Open porosities, threshold radii and separation factors at room temperature (RT) and 350 °C*

	open porosity		threshold radius (nm)		separation factor	
Paste	-	350 °C	-	350 °C	RT	350 °C
PC1(0.25)	21.7%	22.4%	62	78	1.79	1.44
PC2(0.25)	16.1%	18.5%	56	61	2.35	1.67
PC2(0.45)	25.0%	26.0%	92	96	1.61	1.42
PC2+SF(0.25)	7.3%	10.4%	22	20	3.43	1.76
MF(0.30)	7.5%	13.2%	20	28	2.50	1.72
SC+FA(0.20)	8.5%	13.6%	29	38	2.54	1.87
SC+FA(0.37)	19.1%	22.9%	82	103	1.45	1.68

Pore structure parameters: -: non-heat treated specimen; 350 °C: heat treated specimen

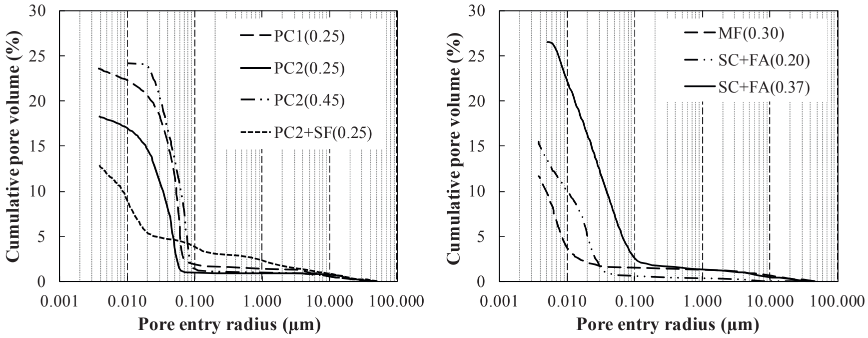

Figure 1. *Mercury porosimetry curves of the heat treated pastes*

The nitrogen sorption isotherms of all samples exhibited H3 hysteresis loops according to IUPAC classification, which confirms the existence of mesopores in the pastes. While the width of the hysteresis loops differed between the pastes, heat treatment led to a widening of the loops in all cases. The BET specific surface areas ranged from 1.2 to 8.9 m^2 g^{-1} for the non-heat treated pastes. Heat treatment led to a moderate increase in surface area in all cases (2.7 to 10.2 m^2 g^{-1}). Micropores were not found in any of the samples, whether heat treated or not.

3.2 Diffusion coefficients

The effective diffusion coefficient, $D_{eff,i}$, of the pastes is given by

$$D_{eff,i} = (J_i \bullet L)/\Delta c_i \qquad (1)$$

where J_i is the flow through the membrane, L is the thickness of the membrane, Δc_i is the concentration gradient and the index i denotes the gas species. To calculate the concentration gradient of each species the concentration on either side of the membrane was taken as the mean of the species' concentration at the inlet and the outlet of the respective side.

The calculated effective diffusion coefficients ranged from 10^{-7} to 10^{-6} m^2 s^{-1}, which is in line with earlier studies [10]. Fig. 2 [19] shows an example of the temperature dependence of the diffusion coefficients. It can be seen that $D_{i,eff}$ for hydrogen and nitrogen depended on the temperature by approximately $T^{0.5}$, which was also observed with the other membranes. For CO_2 the results were not that uniform, with the dependence on temperature ranging from $T^{0.3}$ to $T^{1.3}$.

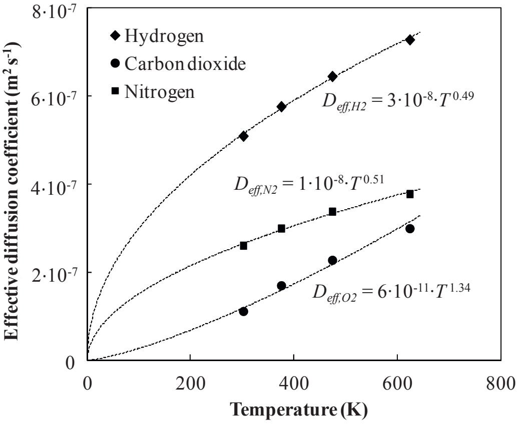

Figure 2. *Plot of effective diffusion coefficient vs. temperature for PC2+SF(0.25)*

The temperature dependence of the $D_{i,eff}$ gives an indication of which of the three principle diffusion mechanisms, viz. bulk diffusion, Knudsen diffusion or surface diffusion, prevails in the samples. Knudsen diffusion is characterized by the dominance of molecule-wall collisions, while for bulk diffusion molecule-molecule collisions are prevalent; the term surface diffusion describes the successive “hopping” of molecules from one surface site to the next. The present findings indicate that the governing gas transport mechanism in the membranes was Knudsen diffusion, since the coefficient of Knudsen diffusion, $D_{K,i}$, in a cylindrical pore is given by [20]

$$D_{K,i} = \frac{d_P}{3} \cdot \sqrt{\frac{8 \cdot RT}{\pi \cdot M_i}} \tag{2}$$

where d_P is the diameter of the pore, R is the universal gas constant, T is the temperature and M_i is the molar mass of the gas species. On the contrary, the coefficient of bulk diffusion is dependent on temperature by about $T^{1.65}$ to $T^{2.0}$ (for ideal gases: $T^{1.5}$) [20]. Further, since the pastes contained no mensurable micropores and their specific surface areas were low, the importance of surface diffusion for the gas transport is negligible.

3.2 Separation factors and Knudsen numbers

From the compositions of the outflowing gases at the feed and permeate side, the separation factor, $\alpha_{H2,CO2}$, of the membranes was calculated as is usual from

$$\alpha_{H2,CO2} = (x_{H2}''/x_{CO2}'')/(x_{H2}'/x_{CO2}') \tag{3}$$

where x_{H2}'' and x_{CO2}'' are the mole fractions of H_2 and CO_2 in the permeate gas (at the outlet), respectively, and x_{H2}' and x_{CO2}' are the mole fractions of H_2 and CO_2 in the feed gas, respectively.

The values of $\alpha_{H2,CO2}$ of the pastes ranged between 1.42 and 3.43. As can be seen from Table 2, the highest separation factors were exhibited by pastes with low w/b and incorporation of slag and/or pozzolans, which also possessed the finer pore structures.

Fig. 3 [19] shows the relation between the threshold radii of the pastes (after heating) and the separation factors of the corresponding membranes. As can be seen, smaller threshold radii led to higher separation factors for all temperatures.

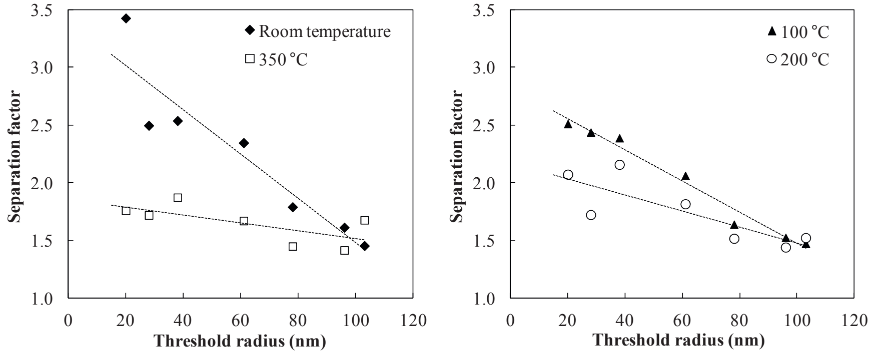

Figure 3. *Plot of separation factors vs. threshold radii after heat treatment*

In contrast, the separation factors showed no dependence on the hydraulic radii of the pastes – which is a measure of their average pore width –, calculated from their open porosities and specific surface areas [11]. These results can be rationalized by calling to mind that the threshold radius of cement paste is a measure of the width of the constrictions in the pore system which control the ingress of mercury into the sample during mercury porosimetry, i.e. they represent the size of bottlenecks which limit the flow of mercury in the pore channels that traverse the sample [12]. It is reasonable to assume that also the flow of gases in cement paste is controlled by these constrictions, which is supported by the dependence of the separation factors on the threshold radii.

This further implies that the gas molecules travelling through the membranes had to pass these constrictions. Therefore the Knudsen numbers of the membranes were calculated on the basis the threshold radii. The Knudsen number, *Kn*, of a pore is defined by

$$Kn = \lambda / d_p \tag{4}$$

where λ is the mean free pass of the gas molecules, i.e. the distance travelled on average by a gas molecule between two successive collisions with other gas molecules. For *Kn* << 1 bulk diffusion dominates, while for *Kn* >> 1 Knudsen diffusion prevails. In the intermediate region both mechanisms combine, however, the higher *Kn* is, the more important is the influence of Knudsen diffusion. For a single gas, λ can be straightforwardly estimated by applying the kinetic theory of gases [21]; since here we deal with a mixture, the collision diameter, σ, of the single gas in the pertinent formula was replaced by

$$\sigma_{ave} = \sum_{i=1}^{3} \sum_{j=1}^{3} \left\{ \left(\frac{\sigma_i}{2} + \frac{\sigma_j}{2} \right) \cdot x_i x_j \right\} \tag{5}$$

where σ_i is the collision diameter of the gas species' and x_i their mole fraction in the mixture; $i,j = 1,2,3$ indicate the gas species H_2, CO_2 and N_2, respectively. The mean free path thus calculated ranged between 96.1 nm (at 32 °C) and 195.6 nm (at 350 °C).

The resulting Knudsen numbers of the pastes, calculated by Eq. (4) and using $2 \cdot r_{thr}$ for d_P, lay in the range from 0.47 to 4.89, indicating a large influence of Knudsen diffusion, in particular at higher temperatures. The results thus are consistent with the conclusion drawn from the temperature dependence of the diffusion coefficients of the membranes.

Returning to Fig. 3 and Table 2, it can be seen that the separation factors of all membranes were strongly dependent on temperature, higher temperatures leading to smaller $_{\mathrm{H2,CO2}}$. This is unexpected because in theory the separation factors should be independent of temperature if Knudsen diffusion were the sole gas transport mechanism, given all other conditions are unchanged. In the present case, however, the fluxes and concentration gradients varied with sample and temperature. Therefore, the theoretical separation factors for sole Knudsen diffusion were calculated for each measurement [11]. For this, the simplifying assumption on the concentration gradients as used for the diffusion coefficients was applied as well. The separation factors thus calculated ranged from 2.99 to 3.78, i.e. they were significantly higher than the measured ones (except for PC+SF(0.25) at room temperature). We tentatively conclude that the deviations from the theoretically expected separation factors and the temperature dependence of the measured separation factors were caused by (temperature dependent) concentration polarization at the surfaces of the membranes. Concentration polarization is often encountered in gas separation and denotes the effect of depletion of the faster diffusing gas component and the accompanying accumulation of the slower diffusing component at the surface of the membrane on the feed side, and the opposite effect on the permeate side, which lead to lowered separation factors [3, 4]. A related phenomenon is channeling, which means that part of the feed gas does not come into contact with the membrane [3].

Concentration polarization and channeling can be counteracted by proper dimensions and arrangement of the membranes in the membrane module and adjustment of the fluxes on both sides of the membrane. This can enhance the separation factors considerably and will be subject of further studies.

4. Conclusions

Hardened cement pastes of differing mixture compositions have been analyzed regarding their pore structure and tested for their use as membranes for gas separation in a Wicke-Kallenbach cell. Low water to binder ratios (w/b) as well as the use of supplementary cementitious materials (slag, fly ash, silica fume) led to finer pore structures and lower porosities. The effect of lowering w/b is simply related to the decrease of water-filled space between the solid particles, while the effect of the slag and pozzolans is attributed to a change in the morphology of the C-S-H, the main binding phase in hardened cement paste.

With finer pore structures higher separation factors occurred. In particular, an approximately linear correlation between the separation factors and the threshold radii of the pastes was found. The highest measured value of $_{\mathrm{H2,CO2}}$ was 3.43. The Knudsen numbers of the pastes, calculated from their threshold radii, as well as the temperature dependence of the effective diffusion coefficients indicated that Knudsen diffusion is the prevailing transport mechanism in the membranes. However, the separation factors were lower than theoretically expected for sole Knudsen diffusion and depended on the temperature (with higher temperatures leading to lower separation factors), which is tentatively ascribed to the occurrence of concentration polarization and channeling effects in the diffusion cell.

Acknowledgements

This work was funded by the Fachangentur nachwachsende Rohstoffe e.V. (Agency for Renewable Resources) under grant no. 22010502.

References

1. Bridgwater AV (1995) The technical and economic feasibility of biomass gasification for power generation. Fuel 74:631–653
2. Gerber S, Behrendt F, Oevermann M (2010) An Eulerian modeling approach of wood gasification in a bubbling fluidized bed reactor using char as bed material. Fuel 89:2903–2917
3. Baker RW (2004) Membrane technology and applications, 2nd edn. Wiley, Chichester
4. Melin T, Rautenbach R (2007) Membranverfahren: Grundlagen der Modul- und Anlagenauslegung, 3rd edn. Springer, Berlin
5. Caro J, Noack M, Kölsch P, Schäfer R (2000) Zeolite membranes – state of their development and perspective. Microporous Mesoporous Mater 38:3–24
6. Bernardo P, Drioli E, Golemme G (2009) Membrane gas separation: a review/state of art. Ind Eng Chem Res 48:4638–4663
7. Abbas A, Carcasses M, Ollivier J-P (1999) Gas permeability of concrete in relation to its degree of saturation. Mater Struct 32:3–8
8. Farage MCR, Sercombe J, Gallé C (2003) Rehydration and microstructure of cement paste after heating at temperatures up to 300 °C. Cem Concr Res 33:1047–1056

9. Lion M, Skoczylas F, Lafhaj Z, Sersar M (2005) Experimental study on a mortar. Temperature effects on porosity and permeability. Residual properties or direct measurements under temperature. Cem Concr Res 35:1937–1942
10. Sercombe J, Vidal R, Gallé C, Adenot F (2007) Experimental study of gas diffusion in cement paste. Cem Concr Res 37:579–588
11. Gluth GJG (2011) Die Porenstruktur von Zementstein und seine Eignung zur Gastrennung. PhD Thesis, Technische Universität Berlin, Berlin
12. Diamond S (2000) Mercury porosimetry: an inappropriate method for the measurement of pore size distributions in cement-based materials. Cem Concr Res 30:1517–1525
13. Härdtl R (1995) Veränderungen des Betongefüges durch die Wirkung von Steinkohlen-flugasche und ihr Einfluß auf die Betoneigenschaften. Schriftenr Deutscher Ausschuss für Stahlbeton 448. Beuth, Berlin
14. Sing KSW (1967) Assessment of microporosity. Chem Ind (London) 829–830
15. Richardson IG, Groves GW (1992) Microstructure and microanalysis of hardened cement pastes involving ground granulated blast-furnace slag. J Mater Sci 27:6204–6212
16. Taylor HFW (1997) Cement chemistry, 2nd edn. Thomas Telford, London
17. Richardson IG (1999) The nature of C-S-H in hardened cements. Cem Concr Res 29:1131–1147
18. Hüttl R, Hillemeier B (2000) Hochleistungsbeton – Beispiel Säureresistenz. Betonwerk Fertigteiltech Int 66(1):52–60
19. Gluth GJG, Zhang W, Gaggl M, Hillemeier B, Behrendt F (2012) Multicomponent gas diffusion in hardened cement paste at temperatures up to 350 °C. Cem Concr Res 42:656–664
20. Bird RB, Stewart WE, Lightfoot EN (2007) Transport phenomena, revised 2nd edn. Wiley, New York
21. Wedler G (2004) Lehrbuch der Physikalischen Chemie, 5th edn. Wiley-VCH, Weinheim

Development of High-efficiency Cd-free $Cu(In,Ga)Se_2$ Solar Cells using Chemically Deposited ZnS Film

Dong Hyeop Shin[1], Seung Tae Kim[1], Luidmila Larina[1], Kyung Hoon Yoon[2], and Byung Tae Ahn[1]

[1] Department of Materials Science and Engineering, Korea Advanced Institute of Science and Technology, Yuseong-gu, Daejeon, 305-701, Koarea
[2] Solar Cell Research Center, Korea Institute of Energy Research, Yuseong-gu, Daejeon, 305-343, Koarea

Abstract

A ZnS film covered completely the CIGS surface without pinholes. The thickness of the ZnS film could be controlled according to the cycle number of the CBD process. As the thickness of the ZnS film increased, the J_{SC} value of a CIGS solar cell with the ZnS film decreased sharply due to the increase in the series resistance of the cell. The QE spectrum of the CIGS solar cell with a 50 nm-thick ZnS film consequently showed very small values through the whole wavelength range. On the other hand, the V_{OC} and FF values of the CIGS solar cell with a 27 nm-thick ZnS film were significantly influenced by the sputtering power for deposition of the ZnO:Al film. By decreasing the sputtering power during deposition of the ZnO:Al film, the V_{OC} and FF values of the CIGS solar cells with a 27 nm-thick ZnS film were sharply improved due to a reduction of sputtering damage at the ZnS surface and ZnS/CIGS interface. Additionally, the J_{SC} value of the CIGS solar cell with a 27 nm-thick ZnS film was improved by annealing the ZnS film. As a result of an annealing process, the QE value in a wavelength range of 400 to 700 nm increased. Finally, we achieved a conversion efficiency of 14.21% for a CIGS solar cell with a ZnS film by optimizing the fabrication conditions.

Keywords: *Cu(In,Ga)Se2 solar cell, ZnS buffer, chemical bath deposition*

W. Udomkichdecha et al. (eds.), *Materials Challenges and Testing for Manufacturing, Mobility, Biomedical Applications and Climate*,
DOI 10.1007/978-3-319-11340-1_21

1. Introduction

Several research groups have recently achieved a conversion efficiency of 20% for Cu(In,Ga)Se_2 (CIGS) solar cells [1]. The conventional structure of a high-efficiency CIGS solar cell is composed of n-ZnO/i-ZnO/CdS/CIGS/Mo. However, there has been strong pressure to replace the CdS buffer with a Cd-free buffer in CIGS solar cells in order to obtain an advantage over CdTe solar cells in the solar cell market. Over the past decade, much research has been undertaken to develop Cd-free CIGS solar cells and several candidate materials for a Cd-free buffer layer have been identified, including ZnS, ZnSe, ZnMgO, and In_2S_3 [2]. In addition, diverse deposition methods for a Cd-free buffer layer have been developed. At present, ZnS films grown via chemical bath deposition (CBD) are among the most promising materials in terms of the efficiency of CIGS solar cells. At the laboratory scale, CIGS solar cells with a ZnS buffer layer have achieved efficiency levels as high as 18.6% [3]. Nevertheless, the efficiency of the ZnS/CIGS solar cells remains much lower than that of CdS/CIGS solar cells.

While numerous research papers have been published on the subject, only a few groups have shown a high efficiency in CIGS solar cells with a ZnS buffer layer [3-5]. There are many factors to consider before high-efficiency CIGS solar cells can be realized. First, the quality of ZnS film is poor compared with that of CdS film. Secondary phases ($Zn(OH)_2$, ZnO) grow concurrently with ZnS during the CBD process. In particular, the existence of $Zn(OH)_2$ induces the creation of pinholes in the film [6].

Another problem is connected to the physical properties of ZnS films such as the high resistivity and the weak hardness of CBD-ZnS films. The potential for reducing the resistivity of ZnS films is limited by the lack of an effective dopant. Thus, it is extremely important to control the ZnS film thickness at the nano-scale level to form a desirable heterojunction. However, during the deposition of the ZnO:Al window layer by sputtering, high-energy negative oxygen ions or neutral particles in the plasma damage the ZnS surface and ZnS/CIGS interface [4].

To obtain high efficiency CIGS solar cells with a ZnS buffer layer, a uniform and pinhole-free ZnS film is essential. Additionally, a ZnO:Al film should be deposited softly on the ZnS film and efforts should be made it minimized damage by the sputtering process. In this study, we focused on optimizing the cell fabrication conditions to achieve high efficiency CIGS solar cells with a ZnS buffer layer.

2. Experimental Procedures and Methods

A CIGS film was deposited onto a Mo-coated soda lime glass substrate using a three-stage co-evaporation process. The experimental details of the deposition procedure have been described previously [7]. The composition of the CIGS film was adjusted to Cu($In_{0.7}Ga_{0.3}$)Se_2. In order to grow a ZnS film on the CIGS film via chemical bath deposition, an alkaline aqueous solution of zinc sulfate ($ZnSO_4·7H_2O$, 99.9%), thiourea ($((NH_2)_2CS$, 98%), and ammonia hydroxide (NH_4OH) was prepared. $ZnSO_4$ and $(NH_2)_2CS$ served as Zn^{2+} and S^{2-} sources for the growth of a ZnS film in the solution. The NH_3 of NH_4OH acts a complex agent and is used to control the heterogeneous precipitation of ZnS in the solution through a complexation reaction. The concentrations of $ZnSO_4$, $(NH_2)_2CS$, and NH_4OH in the bath solution were 0.1, 0.6, and 7.0 M, respectively. The ZnS film growth was carried out in a laboratory-made bath equipped with a Teflon substrate holder. The samples with the CIGS film were dipped in the solution, and the temperature of the solution was elevated from room temperature to 73 °C. ZnS films were grown on the CIGS films for 20 min. After growth of the ZnS films on the CIGS films, the samples were rinsed with deionized water and a 0.5 M NH_3 solution sequentially and dried under a nitrogen flow. The diluted NH_3 solution removes loosely-bonded homogeneous precipitates of large $Zn(OH)_2$ secondary nanoparticles from the surface of the ZnS films [6]. The thickness of the ZnS film grown by one cycle of the CBD process was approximately 27 nm. Thicker ZnS films were obtained by repeating the CBD process. After the ZnS film growth, the samples were annealed at 200 °C for 10 min in ambient air using rapid thermal annealing (RTA) equipment.

Al-doped ZnO (ZnO:Al) was deposited as a window layer on the ZnS film by radio-frequency (RF) magnetron sputtering. A RF magnetron sputtering system with a base pressure of $2x10^{-7}$ torr was used. Prior to the deposition of the ZnO:Al film, the Al (2.5 wt%)-doped ZnO target was cleaned by pre-sputtering for 10 min. The thickness of the ZnO:Al window layer deposited on the ZnS buffer layer was estimated to be 125-150 nm. To investigate the effect of sputtering damage on the performance of CIGS solar cells, the sputtering power was varied in a range of 200 to 400 W. Finally, a front grid of Al was deposited by vacuum evaporation using resistance heating. In order to activate and ensure good performance, light soaking was performed using a constant light solar simulator under a one-sun (AM 1.5 and 100 mW/cm^2 at 25℃) condition. The active area of ZnO:Al/ZnS/CIGS/Mo solar cells is 0.43 cm^2.

The morphology and thickness of the ZnS films were investigated by field-emission scanning electron microscopy (FE-SEM) without any coating. The chemical information of the ZnS films was investigated using X-ray photoemission spectroscopy (XPS). The current density-voltage characteristics were recorded at 25℃ in dark and under illumination with a Spectra Physics Oriel 300W Solar Simulator with an AM 1.5G filter set. Spectral quantum efficiency (QE) measurements were performed by one-source illumination (xenon lamp) combined with a monochromator. A calibrated Si-cell was used as reference for the J-V as well as the QE measurement.

3. Results and Discussion

Figure 1 shows SEM cross-sectional images of ZnS films grown on the CIGS films by one cycle (a), two cycles (b), and three cycles (c) of the CBD process. The surface morphology of the ZnS film showed a fine grain-accumulated structure without formation of pinholes. The ZnS film completely covered the CIGS surface. As the cycles of the CBD process were increased, the thickness of the ZnS film increased: 27 nm (one cycle), 50 nm (two cycles), and 83 nm (three cycles).

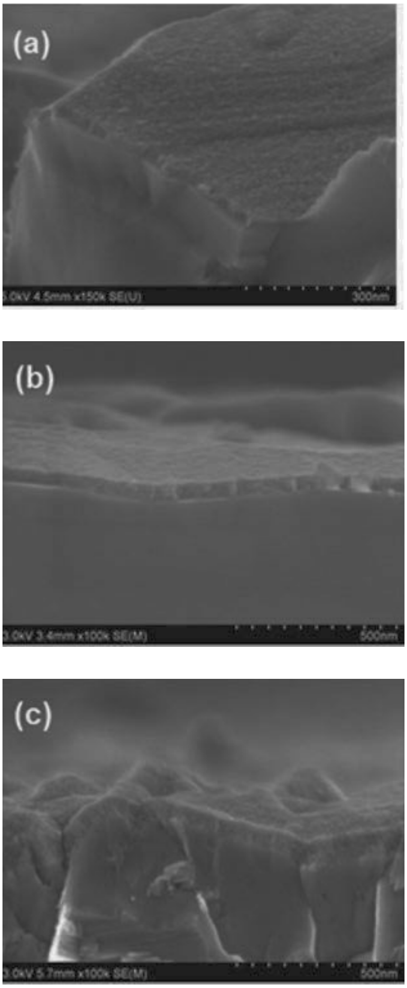

Figure 1. *SEM cross-sectional images of ZnS films grown on the CIGS films by one cycle (a), two cycles (b), and three cycles (c) of the CBD process.*

Figure 2 shows the atomic concentration of constituent elements at the ZnS/CIGS interfaces with the 27 nm-thick and 50 nm-thick ZnS films grown on the CIGS films. The composition of the 27 nm-thick ZnS film was similar to that of the 50 nm-thick ZnS film. The cycle number of the CBD process did not influence the composition of the ZnS film. The ZnS film contained a large amount of oxygen, which could be in the form of Zn-O and Zn-OH bonds [8]. The Zn-OH bond in the ZnS may originate from the basic solution of approximately pH 11. The high concentration of hydroxide ions in the basic solution can react with Zn complex ions during the ZnS film growth.

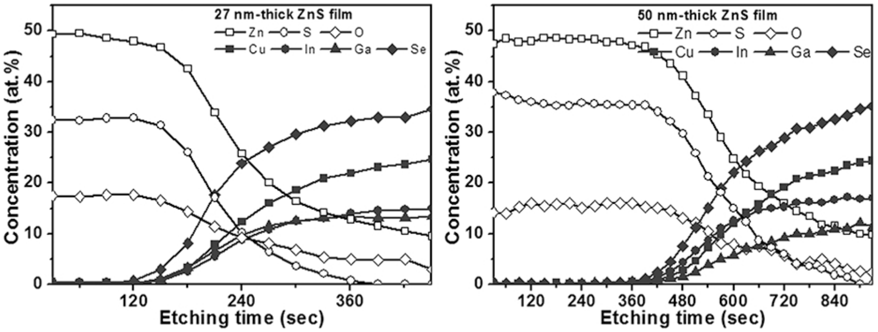

Figure 2. *Atomic concentration of constituent elements at the ZnS/CIGS interfaces with the 27 nm-thick and 50 nm-thick ZnS films grown on the CIGS films.*

Figure 3 shows the current density-voltage curves and QE spectra of CIGS solar cells fabricated with 27 and 50 nm-thick ZnS films using the CBD process. The cell efficiency of the CIGS solar cell with a 50 nm-thick ZnS film is much lower than that of the CIGS solar cell with a 27 nm-thick ZnS film. When the thickness of the ZnS film decreased, the Jsc value increased sharply from 8.22 to 26.85 mA/cm^2. The increase in the Jsc value can be clearly understood in terms of the series resistance of the CIGS solar cells with 27 nm and 50 nm-thick ZnS films. The series resistances of the CIGS solar cells with 27 nm and 50 nm-thick ZnS films were 3.2 and 9.5 Ω, respectively. Thus, the increase in the Jsc value of the CIGS solar cells with the 27 nm-thick ZnS film is strongly related to the decrease in the series resistance of the cell. To clarify the effect of the ZnS thickness on the performance of the CIGS solar cells, QE measurement was conducted. The QE spectrum of the CIGS solar cell with a 50 nm-thick ZnS film showed very small values through the whole wavelength range. This indicates that the 50 nm-thick ZnS film hinders the transport of electrons in the cell. To achieve a high efficiency CIGS solar cell with a ZnS film, the thickness of the ZnS film should be reduced.

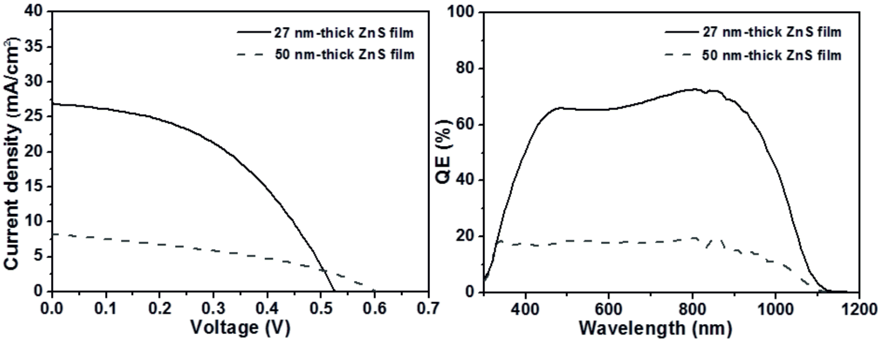

Figure 3. Current density-voltage curves and QE spectra of CIGS solar cells fabricated with 27 and 50 nm-thick ZnS films using the CBD process.

Figure 4 shows the photovoltaic parameters of ZnS/CIGS solar cells fabricated with a ZnO:Al film deposited at sputtering powers from 200 to 400 W. The increase in the CIGS solar cell efficiency was consistent with the decrease of the sputtering power. Most importantly, the Voc and FF values of the CIGS solar cells were sharply improved by decreasing the sputtering power. If the sputtering power is increased, high-energy negative oxygen ions or neutral particles during the sputtering process have high kinetic energy and bombard the ZnS surface. Thus, the 27 nm-thick ZnS film and ZnS/CIGS interface might be damaged during the sputtering process. The sputtering damage creates many defects at the ZnS film and ZnS/CIGS interface. To achieve a high efficiency CIGS solar cell with a thin ZnS film, the ZnO:Al film should be deposited at the lowest possible sputtering power.

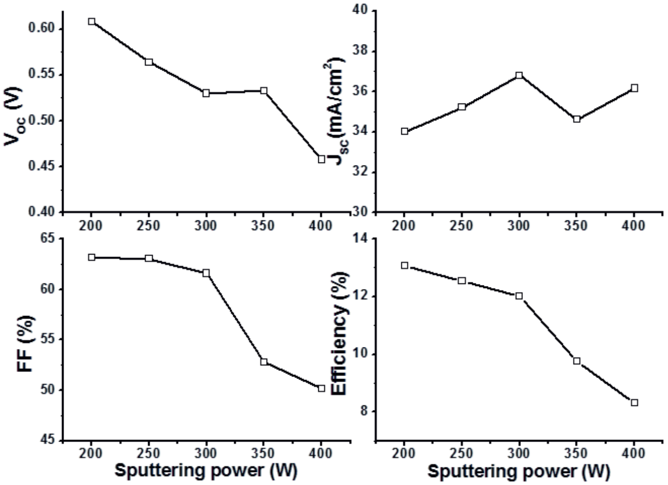

Figure 4. Photovoltaic parameters (Voc, Jsc, FF, Efficiency) of ZnS/CIGS solar cells fabricated with a ZnO:Al film deposited at sputtering powers from 200 to 400 W.

Figure 5 shows the current density-voltage curves and QE spectra of the CIGS solar cell with an as-grown ZnS film and a ZnS film annealed at 200℃ for 10 min in air. When the ZnS fim was annealed using rapid thermal annealing equipment, the conversion efficiency of the CIGS solar cells increased from 13.04 to 14.21 %. Note that the Jsc value of the CIGS solar cell with the annealed ZnS film increased by 3.2 mA/cm^2 compared with the as-grown ZnS film. However, the Voc was not improved by the annealing process. As seen in the QE spectra, the increase in the Jsc value of the CIGS solar cell is consistent with the increase in the short wavelength range of 400 to 700 nm. The increase in the wavelength range of 400 to 700 nm is related to the properties of the ZnS film. Thus, the aforementioned results suggest that the increase in the Jsc value of the CIGS solar cell can be attributed to the enhancement of the ZnS film quality. Finally, we were able to fabricate a high-efficiency CIGS solar cell with a ZnS film by optimizing the fabrication conditions.

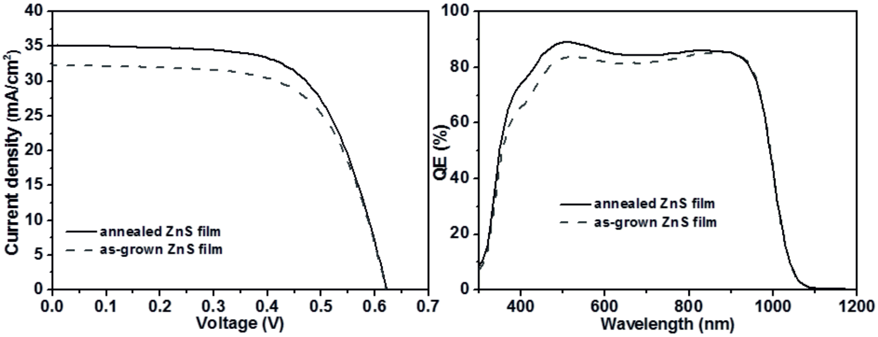

Figure 5. *Current density-voltage curves and QE spectra of CIGS solar cells with an as-grown ZnS film and a ZnS film annealed at 200℃ for 10 min in air.*

4. Conclusion

A uniform and pinhole-free ZnS film was grown on a CIGS film using the CBD process. According to the XPS depth profile, the ZnS film grown on the CIGS film contained a large amount of oxygen in the form of Zn-O and Zn-OH bonds, due to the basic solution used to grow the ZnS film. As the thickness of the ZnS film increased with repeated cycles of the CBD process, the Jsc value of the CIGS solar cell with the ZnS film decreased sharply due to the increase in the series resistance of the cell. Furthermore, the QE spectrum of the CIGS solar cell with a 50 nm-thick ZnS film showed very small values through the whole wavelength range. The 50 nm-thick ZnS film hindered transport of electrons in the cell.

Although the efficiency of the CIGS solar cell with a 27 nm-thick ZnS film is higher than that of cell with a 50 nm-thick ZnS film, the 27 nm-thick ZnS film and ZnS/CIGS interface could be damaged during sputtering for deposition of the ZnO:Al film. By decreasing the sputtering power for deposition of the ZnO:Al film, the Voc and FF values of the CIGS solar cells were sharply improved. Additionally, the Jsc value of the CIGS solar cell with the 27 nm-thick ZnS film was improved by annealing the ZnS film. The annealing process had positive effect on the quality of the ZnS film, as QE value was increased in the wavelength range of 400 to 700 nm. Finally, we achieved a conversion efficiency of 14.21% for a CIGS solar cell with a ZnS film through optimization of the fabrication conditions.

Acknowledgement

This work was supported by the Center for Inorganic Photovoltaic Materials (No. 2012-0001167), the KAIST EEWS Initiative program (EEWS-2012-N00120013), and the Priority Research Center Program (2011-0031407) funded by the Korean Ministry of Education, Science and Technology.

References

1. Jackson P, Hariskos D, Lotter E, Paetel S, Weurz R, Menner R, Wischmann W, Powalla M (2011) New world record efficiency for Cu(In,Ga)Se_2 thin-film solar cells beyond 20%. Prog Photovolt: Res Appl. 19:894–897
2. Hariskos D, Spiering S, Powalla M (2005) Buffer layers in Cu(In,Ga)Se_2 solar cells and modules. Thin Solid Films. 480-481:99–109
3. Contreras MA, Nakada T, Hongo M, Pudov AO, Sites JR (2003) ZnO/ZnS(O,OH)/Cu(In,Ga)se_2/Mo Solar Cell with 18.6% Efficiency. Proceeding of 3rd WCPEC. 570–573
4. Nakada T, Mizutani M (2002) 18% Efficiency Cd-Free Cu(In,Ga)Se_2 Thin-Film Solar Cells Fabricated Using Chemical Bath Deposition (CBD)-ZnS Buffer Layers. Jpn J Appl Phys. 41:L165–L167
5. Kyshiya K, Tanaka Y, Hakuma H, Goushi Y, Kijima S, Aramoto T, Fujiwara Y (2009) Interface Control to enhance the fill factor over 0.70 in a large-area CIS-based thin-film PV technology. Thin Solid Films. 517:2108–2110
6. Ennaoui A, Bar M, Klaer J, Kropp T, Saez-Araoz R, Lux-Steiner MC (2006) High-efficient Cd-free $CuInS_2$ Thin-film Solar Cells and Minimodules with Zn(S,O) Buffer Layers Prepared by an Alternative Chemical Bath Process. Prog Photovolt: Res Appl. 14:499–511

7. Kim KH, Yoon KH, Yun JH, Ahn BT (2006) Effects of Se Flux on the Microstructure of Cu(In,Ga)Se_2 Thin Film Deposited By a Three-Stage Co-evaporation. Electrochem Solid-State Lett. 9:A382–A385
8. Nakada T, Furumi K, Kunioka A (1999) High-Efficiency Cadmium-Free Cu(In,Ga)Se_2 Thin-Film Solar Cells with Chemically Deposited ZnS Buffer Layers. IEEE Tran. Electron Dev. 46:2093–2097

Performance and Stability of Organic Trimethine Cyanine Dye – C_{60} Heterojunction Solar Cells

Gaëtan Wicht[1*], **Etienne Berner**[1], **Timo Jäger**[2], **Hui Zhang**[1], **Roland Hany**[1] **and Frank Nüesch**[1]

Empa, Swiss Federal Institute for Materials Science and Technology, Ueberlandstrasse 129, CH-8600 Dübendorf
[1]*Laboratory for Functional Polymers, gaetan.wicht@empa.ch*
[2]*Laboratory for Thin Films and Photovoltaics*

Abstract

The performance and stability of cyanine dye – C_{60} heterojunction solar cells were investigated both in the regular and the inverted geometry. While active layers absorption was stable under inert environment (N_2), we observed a dependence on cell performances as a function of storage time for the regular geometry. This was attributed to the influence of the coating solvent on the cyanine dye film / buffer layer interface as well as the top electrode / buffer layer interface. Chlorobenzene as solvent and silver as low work function electrode were proposed as good candidates to improve stability. The inverted geometry was found to be another solution for the stability enhancement due to well protected active layers and more stable interfaces.

Keywords: *Organic photovoltaics; cyanine dyes; stability; interfaces.*

1. Introduction

The use of organic small molecules for photovoltaic applications is attractive due to their ease of synthesis, purification or monodispersity [1, 2]. Cyanine dyes are small semiconducting molecules that have initially been used as spectral sensitizers for silver halide emulsion photography, and that have recently attracted interest for biological, medical and optoelectronic device applications. Cyanine dyes have a number of interesting property characteristics such as a tunable wavelength of absorption by straightforward chemistry, very high light extinction coefficients or good film forming features from organic solvents [3]. Furthermore, cyanine

W. Udomkichdecha et al. (eds.), *Materials Challenges and Testing for Manufacturing, Mobility, Biomedical Applications and Climate*,
DOI 10.1007/978-3-319-11340-1_22

dyes are charged molecules that are accompanied by a counter anion. We demonstrated for cyanine bilayer thin film solar cells that the counter anions are relatively mobile and are displaced within the cyanine layer and into adjacent layers. Thereby, ionic charge could be used to control the flow of electronic current [4].

Until now efforts have been focused on enhancing device efficiency (≈ 3%) and improving processing methods for cyanine dye heterojunction solar cells [5]. Equally important from a practical point of view is the long term stability of an organic solar cell. Cyanine dyes are known to quickly decompose under the simultaneous influence of light, water and oxygen, but they are stable for years in our laboratories when kept as powder in the dark.

No work on the stability of organic cyanine dye solar cells has been reported so far. Solar cells degrade by extrinsic and intrinsic factors [6]. Extrinsic degradation factors are for example oxygen and water vapor that diffuse through the encapsulation barrier foil and react with the organic layers or the top metal electrode. Intrinsic device degradation can occur due to morphological changes in the active layers or secondary reactions due to chemical impurities with accompanied charge trap formation. Here, we report on the durability and intrinsic degradation processes of cyanine dye / C_{60} heterojunction solar cells using a trimethine cyanine dye with the counter anion PF_6^-. First, we systematically optimized solar cell performances as a function of layer thicknesses, top electrode materials and the cyanine dye solvent coating. Device stability was studied as a function of storage time under different inert conditions. We identified the buffer layer / cyanine dye film interface and the buffer layer / top electrode interface as the places where slight initial degradation processes were primarily taking place over a period of approximately 1 month; for longer storage times the cell performance stabilized. In preliminary work we finally found that cyanine dye solar cells fabricated in the inverted device architecture are much more stable than regular solar cells.

2. Experimental procedures and methods

1-Ethyl-2-[3-(1-ethyl-3,3-dimethyl-1,3-dihydro-indol-2-ylidene)-propenyl]-3,3-dimethyl-3H-indolium hexafluorophosphate (Cy3-P, FEW Chemicals), 1-Ethyl-2-[3-(1-ethyl-3,3-dimethyl-1,3-dihydro-indol-2-ylidene)-propenyl]-3,3-dimethyl-3H-indolium perchlorate (Cy3-C, FEW Chemicals), poly(3,4 ethylenedioxythiophene):poly(styrenesulfonate) (PEDOT:PSS, from Sigma-Aldrich, PEDOT:PSS Clevios P VP Al 4083, Heraeus, PEDOT:PSS Clevios HTL Solar, Heraeus), C_{60} (SES Research, 99.5%), tris-(8-hydroxyquinoline) aluminum (Alq_3, Sigma-Aldrich, 99.995%), molybdenum oxide (MoO_3, Sigma-Aldrich, 99.99%), aluminum (Al, Kurt J. Lesker company, 99.999%), silver (Ag, Cerac, 99.99%), 2,2,3,3-tetrafluoro-1-propanol (TFP, Sigma-Aldrich) and chlorobenzene (CB, Sigma-Aldrich) were used as received. Indium tin oxide-coated glass (ITO, ThinFilmDevices, 150 nm, resistivity 20 Ohms/square) were used as substrates and were sequentially cleaned in acetone, ethanol, detergent and de-ionized water. PEDOT layers were spin coated onto ITO followed by heating at 120°C for 15 min. TiO_2 (anatase phase) thin films were deposited on ITO by RF-magnetron sputtering at 200°C. Cy3-P and Cy3-C layers were spin coated inside a nitrogen filled glove box (< 5 ppm H_2O, < 6 ppm O_2) from filtered TFP or CB solutions. C_{60}, Alq_3, MoO_3, Al and Ag layers were deposited by thermal sublimation under vacuum at a pressure of $4 \cdot 10^{-6}$ mbar. The evaporation rate was 0.2 Å/s for C_{60}, Alq_3 and MoO_3 and 0.5 Å/s for Al and Ag.

Current-voltage (J-V) characteristics were measured using 100 mW/cm^2 simulated AM 1.5G solar irradiation on a calibrated solar simulator from Spectra-Nova. A homemade sample holder was used to transfer and measure samples J-V curves outside the glove box under N_2. Absorption spectra were measured on a Varian Cary 50 UV-Vis spectrophotometer.

3. Results and discussion

3.1 Optimization of solar cell performance

Solar cells were fabricated either in the regular (ITO (150nm) / PEDOT:PSS (70-90nm) / Cy3-P / C_{60} / Alq_3 (2nm) / Al or Ag (35nm)) or in the inverted geometry (ITO (150nm) / TiO_2 (40nm) / C_{60} / Cy3-P / MoO_3 (10-30nm) / Ag (60nm)). As cyanine dye coating solvents we used either CB or TFP. Best solar cell performances were experimentally found for 20 nm thick cyanine and 40 nm thick C_{60} films. This is in agreement with optical simulations which showed the maximum amplitude of the electric field at the donor-acceptor interface for this thicknesses couple (data not shown).

Table 3.1 shows a summary of initial performances for regular and inverted cells based on different PEDOT:PSSs, top electrodes and solvent combinations. While the electrode material (Al or Ag) in the regular geometry did not influence the overall cell performance, a marked dependence was observed when using different PEDOT:PSSs. For loss free hole extraction, the PEDOT:PSS work function has to match the cyanine HOMO level. This condition was fulfilled for both PEDOT:PSSs from Sigma Aldrich and Clevios P VP Al 4083 but not for the Clevios HTL Solar as it is evident from the V_{oc} values which directly reflect these energy levels alignments. As reported recently [3], solar cell performances were also dependent on the solvent used for the dye layer coating. Different degrees of dye intermolecular interactions and initial distributions of cyanine cations and counter anions throughout the film are indeed expected when comparing the polar solvent TFP, where the ions are fully dissociated, with the apolar CB, where they are mainly present as ion pairs [7-10]. It is well known that solar cell performance is strongly dependent on the film morphology and interfacial potential shifts that can build up due to non-equilibrium ionic distributions [11]. These effects were not studied systematically here, but we observed that TFP-produced cells initially performed better than when using CB. Overall, we were able to produce cells with efficiencies up to 2.3%. For the inverted geometry, encouraging efficiencies up to 2% could be reached without any further device optimization. Selected experiments with Cy3-C instead of Cy3-P did not succeed in higher efficiencies than 0.7%.

Table 3.1 *Solar cell performances for different cell configurations. For the regular geometry the layers sequence was ITO (150nm) / PEDOT:PSS (70 - 90nm) / Cy3-P (20nm) /* C_{60} *(40nm) /* Alq_3 *(2nm) / Al (35nm) or Ag (35nm). For the inverted geometry the layers sequence was ITO (150nm) /* TiO_2 *(40nm) /* C_{60} *(80nm) / Cy3-P (20nm) /* MoO_3 *(10 - 30nm) / Ag (60nm).*

CELLS CONFIGURATION	**V_{oc} [V]**		**J_{sc} [mA/cm^2]**		**FF [%]**		**η [%]**	
	TFP	**CB**	**TFP**	**CB**	**TFP**	**CB**	**TFP**	**CB**
Regular								
PEDOT:PSS Sigma Aldrich (70nm) / active layers / Al (35nm)	0.55 ± 0.08	0.3 ± 0.02	7.3 ± 0.6	6.75 ± 0.75	40.9 ± 2.5	61.5 ± 0.5	2.0 ± 0.3	1.3 ± 0.1
PEDOT:PSS Clevios HTL Solar (90nm) / active layers / Al (35nm)	0.15 ± 0.05	-	4.7 ± 0.2	-	49.7 ± 1.0	-	0.35 ± 0.1	-
PEDOT:PSS Clevios P VP Al 4083 (90nm) / active layers / Al (35nm)	0.7 ± 0.1	-	6.0 ± 0.15	-	36.7 ± 2.5	-	1.7 ± 0.3	-
PEDOT:PSS Clevios P VP Al 4083 (90nm) / active layers / Ag (35nm)	0.65	-	6.6	-	32.5	-	1.4	-
Inverted								
TiO_2 (40nm) / active layers / MoO_3 (10nm) / Ag (60nm)	0.72 ± 0.03	-	4.4 ± 0.3	-	39.0 ± 4.0	-	1.2 ± 0.2	-
TiO_2 (40nm) / active layers / MoO_3 (30nm) / Ag (60nm)	0.85 ± 0.05	-	4.7 ± 0.2	-	38.0 ± 10.0	-	1.7 ± 0.3	-

3.2 Solar cell stability

When cyanine solar cells are exposed to ambient, they degrade within one day (data not shown). That means the exclusion of oxygen and water is essential.

Fig. 3.1 shows normalized performance values over a period of one month for several regular cells stored under N_2 in the dark. The glove box, in which the samples were stored, is also used for spin coating the cyanine layers. This results in a constant background of solvent vapor, as we measured with GC-MS experiments (data not shown) [12]. Identical trends were measured for cells stored under high vacuum ($2 \cdot 10^{-6}$ mbar) or in a solvent-free glove box, confirming that this residual solvent vapor did not influence cell performances.

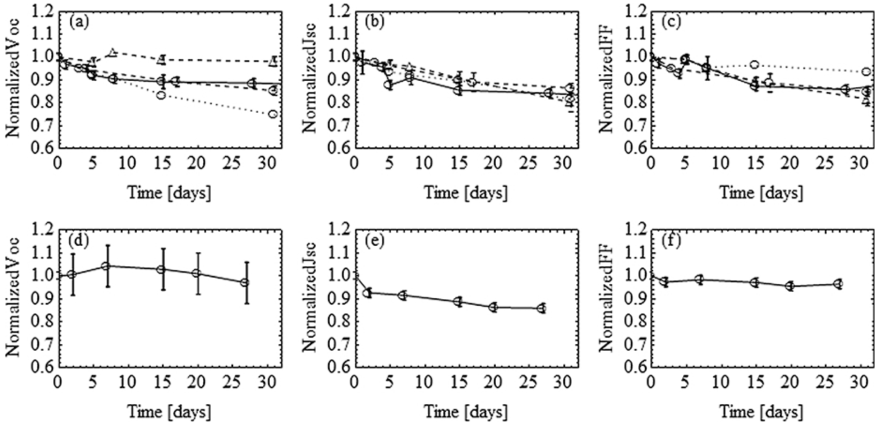

Figure 3.1 Normalized performance values of regular devices (ITO / PEDOT:PSSs / Cy3-P / C_{60} / Alq_3 / Al or Ag) as a function of storage time under N_2. In (a), (b) and (c) cyanine films were spin coated from TFP, in (d), (e) and (f) they were spin coated from CB.

—○—PEDOT:PSS Sigma Aldrich and Al
– –○– – PEDOT:PSS Clevios P VP Al 4083 and Al
•••○••• PEDOT:PSS Clevios HTL Solar and Al
– –Δ– – PEDOT:PSS Clevios P VP Al 4083 and Ag

Using 35 nm Al electrodes and TFP (Fig. 3.1 (a), (b) and (c)), V_{oc}, J_{sc} and FF decreased by about 15% after 30 days. The stability trends were independent of the PEDOT:PSS used and did not change when TFP was purified by column distillation immediately before use. For longer times, performance values seemed to stabilize. Indeed, measurements made on selected cells after more than 60 days of storage showed no real further decrease (not shown on the graph). Solar cells were more stable when fabricated with CB (Fig. 3.1 (d) – (f)). V_{oc} and FF values remained almost constant, and J_{sc} decreased by only 10% after 30 days.

Absorption spectra of cyanine films (coated from CB or from TFP) and ITO / PEDOT:PSS / Cy3-P / C_{60} samples stored in the glove box did not change over a period of more than 2 months. Therefore, the slight performance decrease (notably for the J_{sc}) cannot be attributed to distinct chemical reactions degrading the organic layers. It excludes as well any substantial water or oxygen ingress which leads to dye degradation and a decrease of the absorption spectra (Fig. 3.2). Details of the detrimental influence of TFP to cell stability are the subject of ongoing work. One reason might be a solvent-induced Cy3-P degradation due to the protic nature of TFP. The fraction of dye degradation must be very small, however, since no changes in film absorption spectra could be observed. We also suspect that the different degree of ion pairing in TFP or CB-based solution (see section 3.1) transforms into differences in solid-state packing in non-equilibrium upon rapid spin coating the dye into a thin film. For TFP and with the predominance of PSS^- at the surface of PEDOT:PSS layers [13], $Cy3^+$ ions might then be accumulated at the PEDOT:PSS surface. That would lead to an initial distribution of cyanine cations and anions in non-equilibrium that can build up electric fields that are known to strongly influence the cell performance. Upon storage, the ions possibly rearrange towards thermal equilibrium with an associated change in solar cell performance (much less pronounced with CB). To confirm the occurrence of such a "physical" cell aging effect, measurement are being carried out to determine the ionic distribution throughout a 20 nm thin cyanine film as a function of time.

In a further set of experiments we stored individual cell parts (ITO / PEDOT:PSS; ITO / PEDOT:PSS / Cy3-P; ITO / PEDOT:PSS / Cy3-P / C_{60} and ITO / PEDOT:PSS / Cy3-P / C_{60} / Alq_3 layers) for 10 days in the glove box before completion. No significant differences (within a realistic data variation of ± 10%, see Table 3.1) in performance values immediately after completion were found between cells fabricated from these stored films. Moreover, all cells followed the same performance trend over time as shown in Fig. 3.1. This indicates that, beyond the cyanine film / PEDOT:PSS interface role, degradation is also related to the top electrode deposition.

Compared to TFP-based cells with 35 nm Al electrodes (fig. 3.1), no change in stability was found for thicker Al electrodes (80 nm) or thin Al electrodes (35 nm) covered by a thin Ag layer (35 nm). Relevant processes must therefore also be identified at the Alq_3 / top electrode interface.

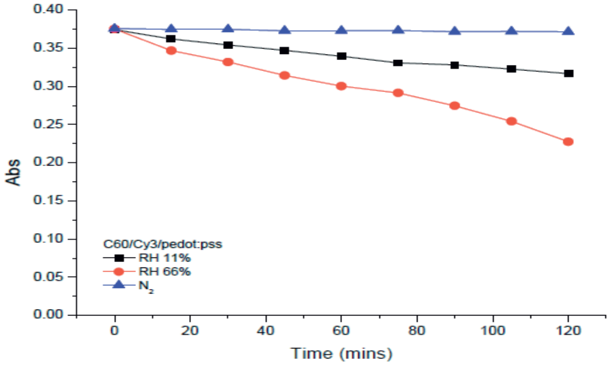

Figure 3.2 *Decrease in absorption at 578nm (cyanine peak absorption) for PEDOT:PSS / Cy3-C /* C_{60} *samples stored under* N_2 *(▲) and at relative humidity values of 11% (■) and 66% (●).*

Several studies [14-17] demonstrated improved device life times when using buffer layers in combination with Al. One role of such buffer layers is to block water and oxygen that diffuse through the thin Al layer [18, 19]. Another role is to protect the organic layer from the hot Al atoms impinging during evaporating [20]. For the very thin Alq_3 layers used here, the protection might only be partial.

Replacing Al by Ag in TFP-based cells stabilized V_{oc} at its initial value but the trend for J_{sc} and FF remained unchanged (Fig. 3.1). The beneficial influence of Ag over Al can result from the lower temperature deposition (softer impinging), a smaller grain size as well as a sharper metal-organic transition [21, 22], which makes the interface "cleaner". The low work function of silver makes it also less reactive [23]. Working solar cells over a period of three months in open air were demonstrated with a top Ag electrode [21]. Au was also demonstrated to be a much more stable electrode material than Al [24].

Fig. 3.3 shows solar cell performance values over a period of one month for two inverted cells stored under N_2 in the dark. In agreement with reports for other materials combination [25, 26], this device architecture improved the stability of cyanine dye cells and the initial performance decrease of the regular cells was not observed anymore. We suggest this to be a combination of two reasons: i) the critical interface between the cyanine film spin coated from TFP and PEDOT:PSS is now replaced by a cyanine / MoO_3 interface, and ii) the sensitive C_{60} layer is now protected during cathode evaporation and covered by the cyanine film and an additional MoO_3 layer, which is much thicker (at least 10 nm) as compared to the Alq_3 layer (2.5 nm).

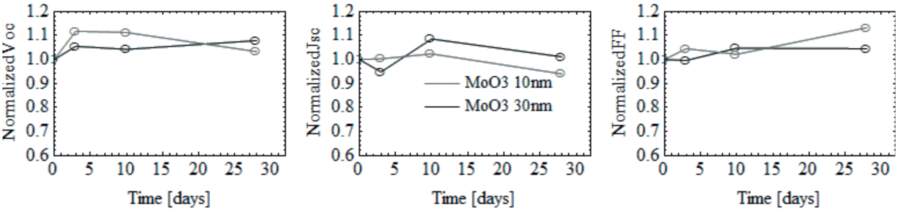

Figure 3.3 *Normalized performance values over a period of one month storage in the glove box of inverted solar cells (ITO / TiO2 / C60 / Cy3-P / MoO3 / Ag). Cy3-P films were coated from TFP, where C60 is insoluble.*

4. Conclusions

By a wise choice of components, cyanine cells with efficiencies up to, respectively, 2.3% and 2% for regular and inverted geometries could be reached.

In contrast to the often stated chemical instability of cyanine dyes we observed unchanged long term absorption of stored thin cyanine films. But when used as active layers in photovoltaic devices, an initial slight decrease in cells performances revealed in the regular geometry. After this burn-in period the cells were rather stable. For this architecture, the materials combination CB as coating solvent with Ag as top electrode might work the best. Considering more stable interfaces and better active layers protection, the inverted structure showed a radically improved stability. However, as it is the case with any other type of organic cells, any contact with oxygen and water has to be excluded otherwise degradation will inevitably occur. This reflects again the necessity to develop high performing barrier layers.

It is clear that only devices that are exposed to light for a long time are solar cells. This will be the subsequent step in this study of cyanine - C_{60} cells stability. Preliminary results on regular cells exposed to light for 15 hours tend to show a first burn-in period followed by a rather stable behavior. Long term durability investigations of the cells under more realistic conditions are on-going.

References

1. Lloyd MT, Anthony JE, Malliaras G G (2007) Photovoltaics from soluble small molecules. Mater Today 10:34-41
2. Walker B, Kim C, Nguyen T-Q (2011) Small molecule solution-processed bulk heterojunction solar cells. Chem Mater 23:470-482
3. Hany R, Fan B, Castro FA (2011) Strategies to improve cyanine multilayer organic solar cells. Prog Photovolt: Res Appl 19:851-857
4. Benmansour H, Castro FA, Nagel M et al (2007) Ionic space charge driven organic photovoltaic devices. Chimia 61:787-791
5. Fan B, Castro FA, Chu BT-T et al (2010) Improved performance of cyanine solar cells with polyaniline anodes. J Mater Chem 20:2952-2955
6. Brabec CJ, Gowrisanker S, Halls JJM et al (2010) Polymer-fullerene bulk-heterojunction solar cells, Adv Mater 22:3839-3856
7. Perez MD, Borek C, Forrest S R et al (2009) Molecular and morphological influences on the open circuit voltage of organic photovoltaic devices. J Am Chem Soc 131:9281-9286
8. Heier J, Steiger R, Nüesch F et al (2010) Fast assembly of cyanine dyes into aggregates onto [6,6]-Phenyl C-61-Butyric Acid Methyl Ester surfaces from organic solvents. Langmuir 26:3955-3961
9. Tatikolov AS, Ishchenko AA, Ghelli S et al (1998) Ion pairs of indobenzimidazolo cyanines: a structural study based on conductivity, absorption, fluorescence and H-1-NMR. J Mol Structure 471:145-159
10. Park J, Yang RQ, Hoven C V et al (2008) Structural characterization of conjugated polyelectrolyte electron transport layers by NEXAFS spectroscopy. Adv Mater 20:2491-2496
11. Lenes M, Bolink HJ (2010) Ionic space-charge effects in solid state organic photovoltaics. ACS Appl Mater & Interfaces 2:3664-3668
12. Chang LL, Lademann HWA, Bonekamp JB et al (2011) Effect of trace solvent on the morphology of P3HT:PCBM bulk heterojunction solar cells. Adv Funct Mater 21:1779-1787

13. Greczynski G, Kugler T, Keil M et al (2001) Photoelectron spectroscopy of thin films of PEDOT-PSS conjugated polymer blend: a mini-review and some new results. J Electron Spectrosc Relat Phenom 121:1-17
14. Jeon SO, Lee JY (2012) Improved lifetime in organic solar cells using a bilayer cathode of organic interlayer/Al. Sol Energy Mater Sol Cells 101:160-165
15. Yang L, Xu H, Tian S et al (2010) Effect of cathode buffer layer on the stability of polymer bulk heterojunction solar cells. Sol Energy Mater Sol Cells 94:1831-1834
16. Wang Y, Yang L, Yao C et al (2011) Enhanced performance and stability in polymer photovoltaic cells using lithium benzoate as cathode interfacial layer. Sol Energy Mater Sol Cells 95:1243-1247
17. Song QL, Li FY, Yang H et al (2005) Small-molecule organic solar cells with improved stability. Chem Phys Lett 416:42-46
18. Krebs FC, Norrman K (2007) Analysis of the failure mechanism for a stable organic photovoltaic during 10000 h of testing. Prog Photovoltaics 15:697-712
19. Norrman K, Gevorgyan SA, Krebs FC (2009) Water-Induced Degradation of Polymer Solar Cells Studied by (H2O)-O-18 Labeling. ACS Appl Mater Interfaces 1:102-112
20. Brabec CJ, Shaheen SE, Winder C et al (2002) Effect of LiF/metal electrodes on the performance of plastic solar cells. Appl Phys Lett 80:1288-1290
21. Tavakkoli M, Ajeian R, Badrabadi MN et al (2011) Progress in stability of organic solar cells exposed to air. Sol Energy Mater Sol Cells 95:1964-1965
22. Lloyd MT, Olson DC, Lu P et al (2009) Impact of contact evolution on the shelf life of organic solar cells. J Mater Chem 19:7638-7642
23. Jorgensen M, Norrman K, Gevorgyan SA et al (2012) Stability of polymer solar cells. Adv Mater 24:580-612
24. Vivo P, Jukola J, Ojala M et al (2008) Influence of Alq_3/Au cathode on stability and efficiency of a layered organic solar cell in air. Sol Energy Mater Sol Cells 92:1416-1420
25. Zhang F, Xu X, Tang W et al (2011) Recent development of the inverted configuration organic solar cells. Sol Energy Mater Sol Cells 95:1785-1799
26. Song QL, Wang ML, Obbard EG et al (2006) Degradation of small-molecule organic solar cells. Appl Phys Lett 89

Functionalised Adsorbents for Carbon dioxide Capture

Amit Bansiwal, Vivek Kumar, Pradnya Pillewan, Nitin Labhsetwar, Rajesh Biniwale, and Sadhana Rayalu*

Environmental Materials Division, National Environmental Engineering Research Institute (CSIR-NEERI)
Nehru Marg, Nagpur – 440020, India
**Corresponding author: email: s_rayalu@neeri.res.in, Telfax: +917122247828*

Abstract

Carbon dioxide is a green house gas and its emissions from large stationary sources like coal based power plants is a global catastrophe. Keeping in view the limitations associated with the reported adsorbents, development of new functionalised adsorbents based on immobilized amines is attempted in the present work. The synthesised adsorbents were thoroughly characterised using various techniques namely XRD, SEM, FTIR to determine the physico-chemical, structural and morphological properties before and after modification. The characterisation results have confirmed that the ordered porous structure of zeolite was retained after modification of only the surface and retaining the porosity and pore volume which is highly desired for an efficient adsorbent. These functionalised adsorbents were evaluated using continuous flow through packed bed reactors and simulated stream of ~15% CO_2 rest N_2 to determine adsorption capacity and other breakthrough parameters. It was observed that after incorporation of amines, the adsorption capacity of zeolite was significantly improved and was comparable to the benchmark adsorbents. The results clearly demonstrate high uptake of CO_2 in amine treated zeolite, almost in the temperature range of flue gas (50-120ºC). The investigations based on amine modified zeolites are promising showing better adsorption capacities and selectivities and are expected to overcome the limitations of conventional adsorbents.

Key words: *Carbon Dioxide Capture, Amines, Zeolites*

W. Udomkichdecha et al. (eds.), *Materials Challenges and Testing for Manufacturing, Mobility, Biomedical Applications and Climate*,
DOI 10.1007/978-3-319-11340-1_23

1. Introduction

The phenomenon of global warming can be attributed to the greenhouse effect caused by the major greenhouse gases such as carbon dioxide, chlorofluorocarbons (CFCs), N_2O, methane, etc.

Carbon dioxide is a major contributor to this global phenomenon. CO_2 gas molecules by virtue of their polar nature tend to trap the infrared radiations arising from the earth's atmosphere resulting in warming of the earth and rise in surface temperatures. This is similar to the warming effect produced in a greenhouse. It has been predicted that global warming can cause a 3 °C rise in surface temperature by 2050 AD [1]. As per the Third Assessment report of the Intergovernmental Panel on Climate Change (IPCC), the present ambient concentration of CO_2 is about 380 ppm, as compared to 280 ppm in the pre-industrial revolution period (early 1900) [2].

To tackle this alarming global phenomenon, there is a growing need to develop suitable carbon capture and sequestration (CCS) technologies. The developed CCS technologies must be capable to capture CO_2 arising from the combustion of fossil fuels, as in power generation, or from the preparation of fossil fuels, as in natural-gas processing. The technologies developed may be also applied to other related issues such as, the combustion of biomass-based fuels and in different industrial processes, such as the production of hydrogen, ammonia, iron and steel, or cement. Capturing CO_2 involves the separation of CO_2 from some other gases present in the flue gas stream of a thermal power plant. It is equally important that the CO_2 captured needs to be transported to a storage site where it can be stored for a long period of time [3].

1.1 Capture CO_2 through Adsorption

Adsorption is a surface phenomenon as compared to absorption which is a bulk phenomenon. It is caused by the interaction of intermolecular forces between the gaseous phase and the surface of certain solid materials. The gaseous phase is referred to as adsorbate whereas the solid surface is referred to as adsorbent. Selective adsorption of gases is dependent on many factors such as the pore size of the adsorbent, dipole moment of the adsorbate, temperature and partial pressure of the gas involved. Adsorption may again be classified as physisorption and chemisorption depending upon the nature of interaction of the gas molecules with the solid surface. Physisorption is generally due to weak van der Waals' forces of attraction between the gas and the solid. In case of chemisorption, the interaction is chemical in nature and thus stronger. Solid materials having porous nature and high surface area tend to be good adsorbents. In this process, the adsorbent adsorbs a particular adsorbate to a certain extent, which is referred to as the adsorption capacity of the material. As the adsorbent gets saturated with the adsorbate, the material is regenerated so as to repeat the cycle of adsorption. Depending upon the method of regeneration used, adsorption processes may be further classified as pressure swing adsorption (PSA), temperature swing adsorption (TSA) and electric swing adsorption (ESA).

In PSA processes, the regeneration is affected by reduction in pressure. In TSA processes, regeneration is achieved by raising the temperature of the adsorbent whereas in case of ESA processes, regeneration is achieved by passing a low - voltage current through the adsorbent. PSA and TSA processes are widely used in H_2 production, separation of O_2 and CO_2 from natural gas [6]. A combination of both these processes described as PTSA has been studied at pilot scale levels by the Tokyo Electric Power Company (TEPCO) & Mitsubishi Heavy Industries for zeolite Ca-X (β) [7].

Different adsorbent materials have been investigated which include zeolites, activated carbons, pillared clays and metal oxides [8-20]. Siriwardane et al. have reported high adsorption capacities to the tune of 160, 135 and 110 mg/g for zeolites 13X, 4A and activated carbon respectively at 25°C and 1 atm CO_2 partial pressure. However, it was observed that with increasing temperature, as comparable to that of flue gas streams this capacity drops down drastically. Thus, these adsorbents need to be modified so as to facilitate chemical adsorption and therefore there is an increasing demand to design highly selective adsorbents, which can operate at high temperatures [21]. Also, there is a need to develop adsorbents that may be able to perform in the presence of steam with improved selectivity towards CO_2 [22].

2. Methodology

Considering the acidic nature of CO_2 it is envisaged that incorporation of basicity in the adsorbent, can improve the adsorption behaviour for enhanced uptake of CO_2. This concept can be understood by the use of the conventional amine systems for absorption of CO_2. Amines have been used in the past, in liquid absorption systems to remove acidic gases like CO_2, SO2, etc. which is actually a chemical reaction. Therefore incorporation of basic molecules like amines on the conventional adsorbents like zeolite, activated carbon and alumina can promote the adsorption capacity of the support matrix. This may be attributed to the additional process of a weak chemisorption process taking place along with the physisorption process which may be attributed to the support matrix.

2.1 Synthesis of adsorbents

Synthesis of amine modified sorbents has thus become a research issue to be investigated by different researchers in the area of carbon capture. Several possible matrix-functionalization molecule combinations have been tried and reported by our group at CSIR-NEERI. A brief description of synthesized adsorbents is discussed in the following section.

2.1.1 Amine functionalized zeolite-13X

The immobilization of amines was also carried out using alcoholic solutions of amine. The amine solutions with different concentrations corresponding to 25, 50 and 80 weight percent loadings were prepared in methanol. The zeolite was wetted with methanol prior to agitation with amine solution by agitating zeolite 13X beads and methanol in solid liquid ratio of 1:2 for a period of 10 minutes in two stages. The wetted beads were then air-dried and then agitated with alcoholic amine solution for a period of 15 minutes and 4 hours on a rotary shaker at ambient temperature, keeping the solid liquid ratio at 1:2. The amine solution was decanted and stored for analysis whereas the zeolite beads were allowed to dry in air overnight.

2.2 Evaluation technique

Among several options for post combustion CO_2 capture, flow through column adsorption processes are considered to have high potential for capturing CO_2 gas from bulk flue gas. The bed is filled with sorbent, which is a material used to adsorb gases. The sorbent characteristics include the possession of high internal surface area, controlled pore size, stable network structure and ability of modify surface chemical to suit specific applications.

All the as prepared adsorbents were evaluated for CO_2 adsorption at different temperatures namely 30, 55 and 75 °C. These temperatures were chosen keeping in mind that the best location for adsorption of CO_2 in a coal-fired thermal power plant is after the flue gas desulphurization (FGD) unit before the stack. Thus, these temperatures were selected as they represented the post-FGD region, which is typically around 55-75 °C. The selected screening temperature was 55 °C. The shortlisted matrices were then also evaluated at lower and higher adsorption temperature of 30 and 75 °C respectively.

2-2.1 Dynamic flow through system

In this method, the gas stream to be treated is passed over a fixed bed of adsorbent. An unsteady state condition prevails, in that the adsorbent bed continues to take up increasing amounts of adsorbate gases. The composition of the gas stream at the outlet of the bed is monitored continuously. Then the amount of a particular gas is followed as the fraction of the concentration of that gas in the effluent gas from the adsorption column Ce over that of the gas concentration in the feed gas, Co. This method matches practical (actual end use) conditions like flow conditions, temperatures and multi-component streams and we can calculate the dynamic adsorption capacities of the materials.

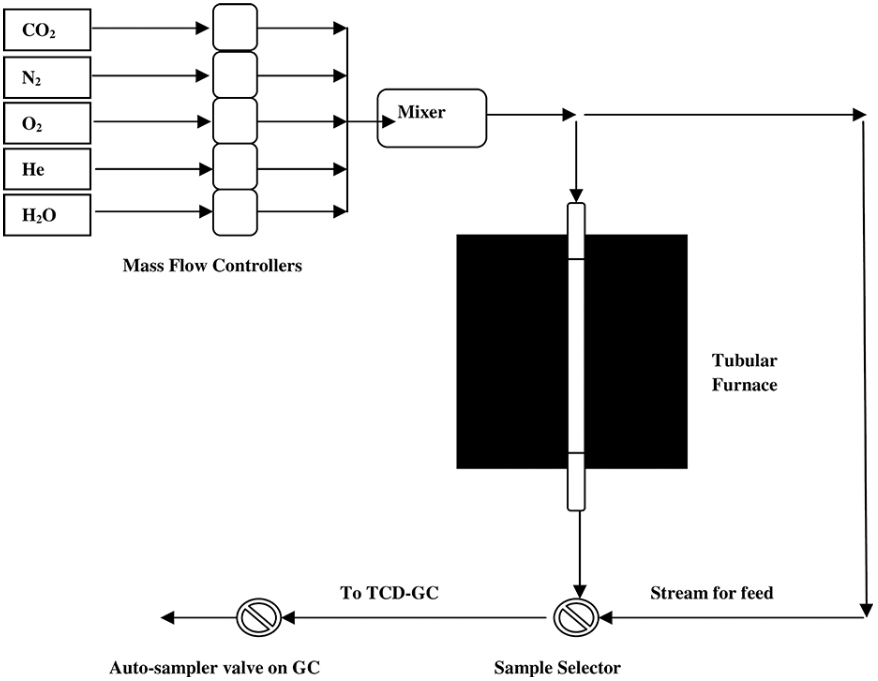

Figure 1. *Experimental setup used for breakthrough adsorption studies*

Table 1. *Adsorption bed (Column) configuration*

Parameters	**Values**
Bed length (mm)	340
Effective working length (mm)	300
Internal diameter (mm)	10
Wall thickness (mm)	2
Dead volume (ml)	25
Unused bed length (mm)	8
Unused bed volume (mm^3)	25

3. Characterization

The surface morphology of adsorbents needs to be investigated to suggest the role of adsorbent support and functionalization molecule towards CO_2 adsorption. Various adsorbent characterization techniques have been utilized to explain the possible happening over the surface of adsorbents due to functionalization and CO_2 adsorption.

3.1 X-ray diffraction (XRD) analysis

X-ray diffraction analysis was conducted to access the structural integrity of the adsorbent samples after incorporation of the amines. The low angle X-Ray diffraction patterns have been recorded using X-ray diffractometer, Model (Phillips: PW-1830). The radiations of Cu-Kα were generated using X-ray generator of model (PW 1729) of same make and the β radiation were filtered using monochromator. Rigaku: MiniflexII-DD34863 operated at 30 kV and 15 mA with a monochromator and using Cu-Kα radiation (k = 0.15418 nm) has also been used to obtain the XRD pattern of samples under the 2Θ range from 5 to 60°. The radiations of $Cu\text{-}K_\alpha$ were generated using X-ray generator of model of same make and the β radiation were filtered using monochromator.

3.2 Fourier transform infrared (FTIR) analysis

The IR spectra of the synthesized materials were recorded using a Perkin–Elmer spectrometer using the KBr pellet technique. The samples were analyzed in the wavelength region 4000–400 cm-1. This was done for confirming the formation of mainly the carbamate and bicarbonate groups which are formed as the adsorption product present in the adsorbent samples. The details of the functional groups before and after adsorption were an important tool to suggest the reaction mechanism taking place over the adsorbent with CO_2 interaction.

3.3 Flash Elemental analysis (EA)

The elemental analysis of the samples was determined by using a Thermo Flash EA 1112 fitted with a MAS 200R autosampler including instrument control. Data analysis was done with the help of Eager Xperience software package.

Elemental nitrogen (N), carbon (C), hydrogen (H), sulphur(S) content was analysed. Samples were measured in duplicate with laboratory standards and blanks. The instrument was first checked for helium pressure which was kept between 4 and 5 bars, and oxygen pressure at 4 bar. The gas pressure inside the instrument’s gauges, inside the detector compartment was also set accordingly.

3.4 Scanning Electron Microscopy (SEM) analysis

Scanning electron microscopy (SEM) analysis was used to investigate the structural transformations of adsorbents. It was carried out to provide information on the association and distribution of elements within particles of adsorbents. Analysis was carried out using Quanta 600 Scanning Electron Microscope by FEI Company. The Quanta 600 SEM produces enlarged images of a wide variety of specimens, using magnifications usually from 100x to about 100,000x.

3.5 Thermogravimetric analysis (TGA)

Isothermal analysis of adsorbents was performed using thermogravimetric analysis (TGA) on a Perkin Elmer TGA. The thermo gravimetric experiments were carried out in a Quadstar (Perkin Elmer Instruments). It was capable of heating at the rate of approximately 200 °C min-1. The sample temperature was measured with a thermocouple placed very close to the sample.

3.6 BET surface area and pore size analysis

The standard method of Brunauer, Emmett and Teller (BET) was used for measuring specific surface area of the adsorbent based on the physical adsorption of a gas on the solid surface. Specific surface area of the catalysts has been determined using BET Surface Area Analyzer of make Micromeritics: ASAP-2000. The samples were degassed at 70-110°C. This temperature range was chosen keeping in mind the boiling point of the various amines used in the present study.

4. Results and discussion

4.1 Amine functionalized zeolite-13X

Synergistic effect of loading of various amines over the 13X zeolite is shown in fig 2. The first Y-axis shows CO_2 adsorption capacity per unit weight of adsorbent. Whereas, additional adsorption of CO_2 because of amine loading is depicted on second Y-axis and by area graph. In all samples the targeted loading of amines was 50% by wt of zeolite. However the actual loadings obtained were between 11 to 19% as detailed in Table 2. It is apparent from the data that the loading of bulkier amines namely DEA and EDAN resulted in reduction of adsorption capacity of 13X. A promotional effect was observed in case of MEA, EDA, IPA and AMP. The effective promotion by IPA and AMP was about 60 and 62 mg of CO_2 per g of amine loaded respectively. In case of MEA and EDA the promotional adsorption was 22 and 25 mg of CO_2 per g of amine loaded respectively.

Table 2. *Breakthrough adsorption capacities at 75 °C of 13X modified by different amines*

Sr. No.	**Material**	**Adsorption Capacity (mg/g)**	**Amine loading (wt.%) (titrimetric)**
1	13X-Comm.	16.01	-
2	13X-MEA-50	19.98	17.76
3	13X-DEA-50	2.91	12.19
4	13X-EDA-50	20.15	15.79
5	13X-IPA-50	22.78	11.10
6	13X-AMP-50	25.86	15.64
7	13X-EDAN-50	5.26	19.19

Adsorption temperature = 7 °C; gas flow rate = 52 c.c/min; CO_2 concentration = 11%

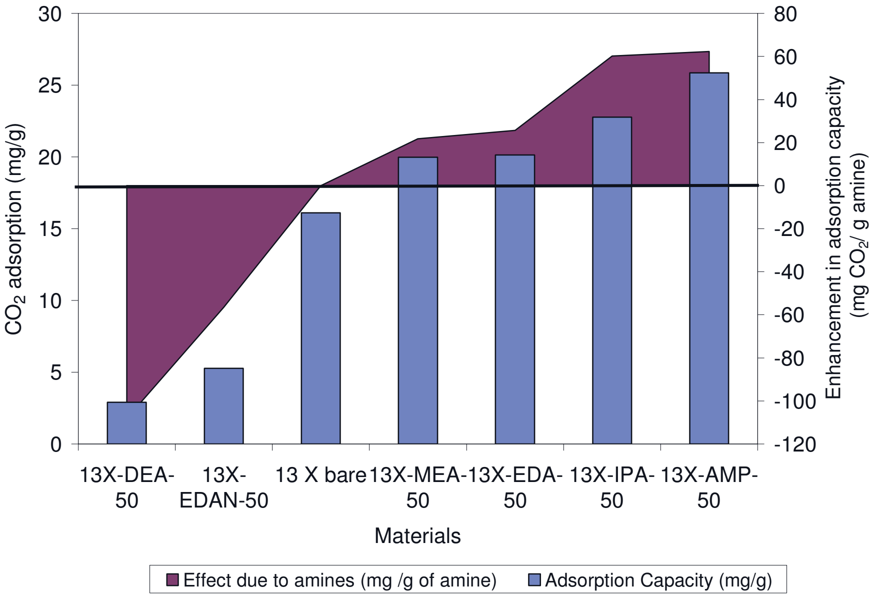

Figure 2. *Comparative adsorption capacities and amine efficiencies of different amines*

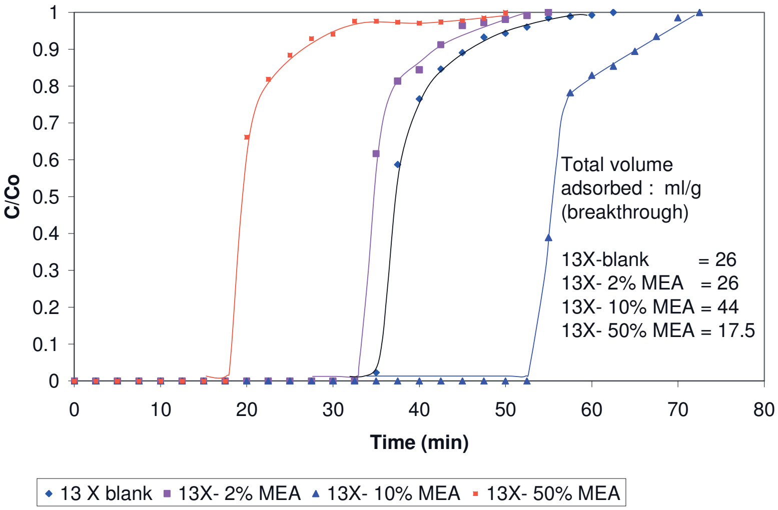

Figure 3. *Adsorption capacities of modified 13X at 30 ºC*

For adsorption at room temperature, 13X-10% MEA exhibited highest adsorption capacity 86.43 mg compared to 51.07 mg of blank. This proved enhancement in adsorption of acidic gas CO_2 with introduction of basicity with amine loading as reported by many researchers (Birbara, 1999 and 2000, Chang, 2003, Xu, 2005). As can be seen from Table 3, small loading (2%) had capacity unchanged. But even with very high loading (50%), capacity had dropped to 34.38 mg. This can be attributed to possible pore blocking and restricted access to adsorption sites for CO_2 at higher loadings.

Table 3. *Adsorption capacities of amine modified 13X at 30 ºC*

Material	**BT capacity**			**Saturation capacity**	
	c.c/g	**mmol/g**	**mg/g**	**mmol/g**	**mg/g**
13X-blank	26	1.16	51.07	1.44	63.33
13X-2% MEA	26	1.16	51.07	1.33	58.52
13X-10% MEA	44	1.96	86.43	2.08	91.73
13X-50% MEA	17.5	0.78	34.38	1.09	47.96

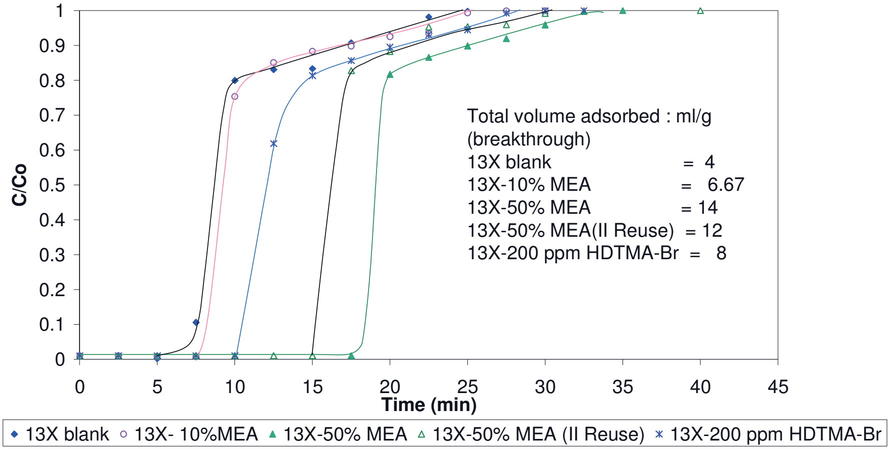

Figure 4. *Adsorption capacities of modified 13X at 120 ºC*

At 120 °C, higher loading (50%) proved to give highest adsorption capacity of 27.5 mg compared to 7.86 mg of blank and 13.1 mg for 13X-10% MEA. The surfactant modified 13X exhibited intermediate adsorption capacity of 15.71 mg.

Table 5. *Adsorption capacities of amine and surfactant modified 13X at 120 ºC*

Material	**BT capacity**			**Saturation capacity**	
	c.c/g	**mmol/g**	**mg/g**	**mmol/g**	**mg/g**
13X-blank	4	0.18	7.86	0.41	18.15
13X-10% MEA	6.67	0.30	13.10	0.47	20.76
13X-50% MEA	14	0.63	27.50	0.76	33.59
13X-50% MEA (II Reuse)	12	0.54	23.57	0.66	28.97

4.2 Representative characterization results

The select adsorbents from each category have been characterized to know about the surface morphological changes attributing towards improved CO_2 adsorption properties.

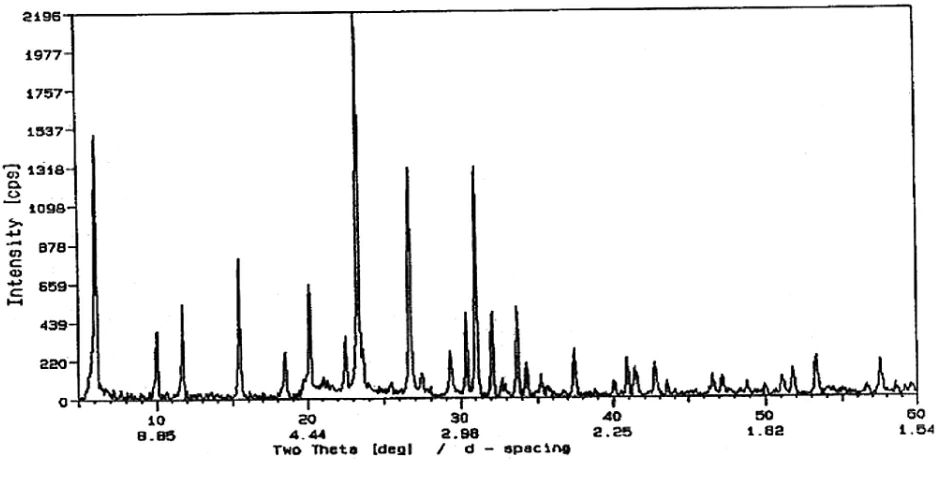

Figure 6. *X-ray diffraction pattern of 13X-AMP-25*

A representative characterization result pertaining to above explored adsorbents is provided as follows. The presence of carbamate species gets confirmed with the FTIR analysis at peak position 992.41 cm-1. This also supports the possible mechanism of amine CO_2 interaction towards carbamate formation reported in literature.

Table 10. *Surface area and pore volume of adsorbents*

S.N.	Adsorbents	BET surface area (m^2/g)	Pore volume (ml/g)
1.	13X zeolite matrix	359	0.22
2.	13X-AMP 25%	265	0.18

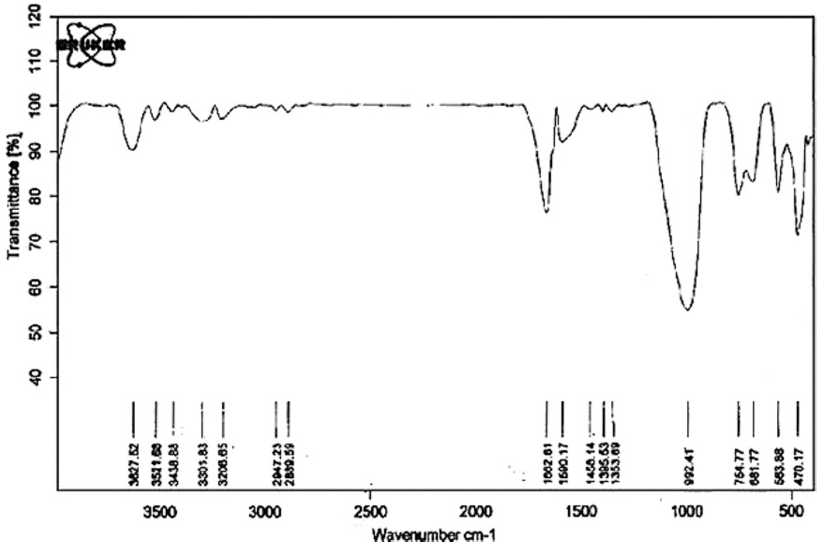

Figure 7. *FTIR spectrum of 13X-AMP-25 evaluated for adsorption of CO2*

5. Conclusions

The newly synthesized amine functionalised adsorbents based on zeolites have been evaluated and characterized for their adsorption performance in presence of binary CO_2/N_2 gas mixture. It was observed that the incorporation of amine significantly improves the adsorption properties of zeolite. Further, adsorption studies at different temperature indicate that the adsorption capacity of aminated zeolites decreases with increase in temperature. The functionalised zeolites also showed improved selectivity towards CO_2 in presence of water at temperatures of 55°C. Moreover, increase in adsorption capacity was observed in presence of moisture as compared to dry feed mixture and the functionlaised adsorbents showed adsorption capacities in range of 52 mg/g to 63 mg/g. The study has proved that functionisation of zeolites with amines overcomes the drawbacks namely low adsorption capacity, interference due to moisture and other gases, deleterious effect of temperature etc. associated with conventional adsorbents for CO_2.

Acknowledgements

The present work was performed at National Environmental Engineering Research Institute (CSIR-NEERI), Nagpur. The authors acknowledge the support extended by Director, NEERI for his encouragement. One of the authors Mr. Vivek Kumar would also like to kindly acknowledge the Council of Scientific and Industrial Research (CSIR), India for granting Senior Research Fellowship to him.

References

1. A.K. De, Environmental Chemistry - New Age International Publishers, 4th Edition (2003) 34
2. IPCC. J. T. Houghton , Y. Ding ,D. J. Griggs , M. Noguer , P. J. van der Linden , X. Dai ,. K. Maskell, C. A. Johnson. Climate Change 2001: The Scientific Basis. Intergovernmental Panel on Climate Change, Cambridge University Press, Cambridge, UK, (2001).
3. IPCC, 2001a: Climate Change 2001 - Mitigation. The Third Assessment Report of the Intergovernmental Panel on Climate Change. B. Metz, O. Davidson, R. Swart, and J. Pan (eds.).Cambridge University Press, Cambridge, UK.
4. K. Thambimuthu, Gas cleaning for advanced coal based power generation. IEA Coal Research. London, Report no. IEACR/53(1993).
5. K. Arthur, N. Richard, Alkanolamines for hydrogen sulfide and carbon dioxide removal. Chapter 2: Gas Purification, 5th Edition, Gulf Publishing Company.40-186(1997).
6. M. Barbara, Solutions for the 21st century, Zero emissions technologies for fossil fuels. Technology Status Report, IEA Working Party on Fossil Fuels, 1-47(2002).
7. Smith, CO_2 reduction-prospects for coal. IEA-Coal, CCC/26, 1-84(1999).
8. Y.H Ma, C. Mancel, Diffusion studies of CO_2, NO, NO_2, and SO_2 on molecular sieve zeolites by gas chromatography. AIChE J.18(1972)1148
9. Y.H. Ma, A.J. Roux, Multi-component rates of sorption of SO2 and CO_2 in sodium mordenite. AIChE J.19(1973)105
10. D. Valenzuela, A.L. Myers, in Adsorption equilibrium data handbook. Prentice-Hall: Engelwood, Cliffs, NJ, (1989)39.

11. R. J. Wilson, R.P. Danner, Adsorption of synthesised gas-mixture components on activated carbon. J. Chem. Eng. Data, 28(1983)14.
12. D. T. Hayhurst, Gas adsorption by some natural zeolites. Chem. Eng. Commun. 4(1980), 729
13. C. Han, D. P. Harrison, Simultaneous shift reaction and carbon dioxide separation for the direct production of hydrogen. Chem. Eng. Sci. 49(1994) 5875.
14. Kapoor, R. T. Yang, Kinetic Separation of Methane-Carbon Dioxide Mixture By Adsorption on Molecular Sieve Carbon. Chem. Eng. Sci. 44 (1989)1723.
15. Z. Yong, V. G. Mata, A. E. Rodrigues, Adsorption of Carbon Dioxide on Chemically Modified High Surface Area Carbon-Based Adsorbents at High Temperature. Adsorption 7(2001)41.
16. R. V. Siriwardane, M. S.Shen, E. P. Fisher, J. A. Poston, Adsorption of CO_2 on Molecular Sieves and Activated Carbon. Energy Fuels 15(2001) 279.
17. Y. Ding and E. Alpay, Equilibria and kinetics of CO_2 adsorption on hydrotalcite adsorbent. Chem. Eng. Sci. 55 (2000) 3461.
18. P. R. Pereira, J.Pires, M. B. Carvalho, Zirconium Pillared Clays for Carbon Dioxide/Methane Separation. 1. Preparation of Adsorbent Materials and Pure Gas Adsorption. Langmuir ,14(1998) 4584.
19. Z.Yong,V.Mata, A. E. Rodrigues, Adsorption of Carbon Dioxide on Basic Alumina at High Temperatures. J. Chem. Eng. Data, 45(2000) 1093.
20. M.Anand, J.Hufton, S.Mayorga, S.Nataraja, S.Sircar, T. Gaffney, APCI report for DOE,(1995)
21. N.D.Hutson,S.A.Speakman,E.A.Payzant,Structural Effects on the High Temperature Adsorption of CO_2 on a Synthetic Hydrotalcite. Chem.Mater.16(2004) 4135.
22. K. Thambimuthu, J. Davison, M. Gupta, CO_2 Capture and Reuse. IPCC workshop on carbon capture, Regina, Canada, (2002) 26.
23. J. Thote, R.Chatti, K. Iyer, V.Kumar, A. Valechha, N. Labhsetwar, R. Biniwale, M.Yenkie, S. Rayalu, N-doped mesoporous alumina for adsorption of carbon dioxide, J. Env. Sci, Accepted, 2012.
24. Valechha, J.Thote, N. Labhsetwar and S.Rayalu, Biopolymer based adsorbents for the post combustion CO_2 capture. International journal of knowledge engineering, ISSN: 0976-5816 & E-ISSN: 0976-5824, 3(2012) 103.
25. V. Kumar, N. Labhsetwar, S. Meshram and S. Rayalu, Functionalized Fly ash based alumino-silicates for capture of carbon dioxide. Energy & Fuels, ACS, 25(2011) 4854.
26. J. Thote, K. Iyer, R.Chatti, N. Labhsetwar, R. Biniwale, S. Rayalu, In-situ Nitrogen enriched carbon for carbon dioxide capture. Carbon, Elsevier, 48(2010)396.

27. R. Chatti, A. Bansiwal, J. Thote, V. Kumar, P. Jadhav, S. Lokhande, R. Biniwale, N. Labhsetwar and S. Rayalu, Amine loaded zeolites for carbon dioxide capture: amine loading and adsorption studies. Micro and Meso Mater, 121(2009) 84.
28. P. Jadhav, R. Chatti, R.Biniwale, N. Labhsetwar, S. Devotta, and S. Rayalu, Monoethanol amine modified zeolite 13-X for CO_2 adsorption at different temperatures. Energy & Fuels 21 (2007) 3555.
29. P. Jadhav, S. Rayalu, R. Biniwale, S. Devotta, CO_2 emissions and its mitigation by adsorption on zeolites and activated carbon. Curr. Sci., 92(2007)